UNIVERSITÀ DEGLI STUDI DI TRIESTE

XXXIV CICLO DEL DOTTORATO DI RICERCA IN

FISICA

COSMIC CHEMICAL AND DUST EVOLUTION

SETTORE SCIENTIFICO-DISCIPLINARE: FIS/05

Dottorando:

Marco Palla

Coordinatore:

Prof. Francesco Longo

Supervisore di tesi:

Prof.ssa Francesca Matteucci

Anno accademico 2020/2021

UNIVERSITÀ DEGLI STUDI DI TRIESTE

XXXIV CICLO DEL DOTTORATO DI RICERCA IN

FISICA

COSMIC CHEMICAL AND DUST EVOLUTION

SETTORE SCIENTIFICO-DISCIPLINARE: FIS/05

Dottorando:

Marco Palla

Coordinatore:

Prof. Francesco Longo

Supervisore di tesi:

Prof.ssa Francesca Matteucci

Anno accademico 2020/2021

Astronomy is much more fun when you are not an astronomer

Brian May

Abstract

In this Thesis, we investigate the chemical and dust evolution of the different galactic environments we encounter during the cosmic history, from the high-redshift Universe to the Milky Way (MW) and the solar vicinity.

The study of the evolution of galaxies is performed by means of detailed chemical evolution models that predict the abundances of single chemical elements in the interstellar medium (ISM), as well as the condensation into dust of the so-called refractory elements, i.e. those mostly depleted from the gas phase into dust. For this reason, the chemical evolution models distinguish the contributions to chemical and dust enrichment from different sources during the galactic evolution.
Given the substantial differences in the history of star formation suffered by the objects in our study, we develop different models for galaxies of different morphological types, i.e. dwarf irregulars, spirals and starbursts/local elliptical galaxies. In addition, detailed models are developed for the study of the MW Galaxy, which is the best studied system in the literature.

In the first part of the Thesis, we concentrate on the study of moderate to high-redshift (up to $z \sim 4$) systems. One of the main issues in studying these systems is accounting for interstellar dust, which deeply influences our view of the distant universe. Therefore, dust treatment was implemented in our models by taking into account all the processes that play a role in regulating the dust amount in the ISM, i.e., dust production by stars, accretion in the cold, dense ISM, and destruction by supernova (SN) shocks. This allows us to trace directly the gas abundance ratios inferred from ISM spectroscopy as well as to predict absolute dust quantities in galaxies.
In particular, we focus on high-redshift starburst galaxies, whose extreme conditions for

star formation pose questions on the universality of the stellar initial mass function (IMF) as well as on the processes regulating the ISM dust. We test the impact of the IMF shape on high-redshift environments by applying the so-called integrated galactic IMF (IGIMF) theory in models specifically suited to study starburst galaxies. By applying this IGIMF on dust evolution models for the first time in the literature, we look at the interplay between the IMF and dust processes in shaping the observed gas abundance patterns as well as global dust quantities, such as the dust mass. This analysis highlights the degenerate effect of the IGIMF and dust on abundance patterns and suggests that the IGIMF can explain the dust masses observed in some high-redshift star forming objects.
In order to get a more complete picture about dust cosmic evolution, we also investigate how dust quantities evolve on larger scales. To this aim, in this Thesis we present a novel method to compute the redshift evolution of dust mass in galaxy clusters. In brief, we integrate the predictions of chemical and dust evolution models for individual galaxies over the galaxy cluster luminosity function (LF), assuming suitable cosmological scenarios for the LF evolution. By applying this method, we reproduce the dust amounts observed in low and intermediate-redshift galaxy clusters and we answer still unresolved questions concerning dust in cluster. In particular, we find that spiral galaxies are the most important dust producers within clusters and that galactic ejecta can account alone for the observed intracluster dust.

In the second part of the Thesis, instead, we focus on study of the local Universe and in particular on the MW Galaxy. In fact, despite of the wealth of data from Galactic surveys and missions, many questions remain open on the formation and evolution of the four major Galactic components, i.e., the bulge, the halo, and the thick and thin discs.
To answer to at least part of these questions, we investigate the evolution of the MW thick and thin discs by comparing detailed models based on the two-infall paradigm with recent survey data. In particular, we discuss the formation of abundance gradients in the MW and the main physical parameters influencing this process, concluding that inside-out disc formation should act together with radial gas flows and/or variable efficiency of star formation. Moreover, we suggest that to reproduce the observed [α/Fe] dichotomy/bimodality (i.e., the presence of two distinct data sequences in the [α/Fe] vs. [Fe/H] diagram) at different Galactocentric distances, one should assume a prolonged gap between the formation of the thick and thin discs and a chemically enriched infall in the innermost thin disc. By running a specific model for the progenitor of Gaia-Enceladus-Sausage (GES) stars, we also find that the gas lost by GES progenitor could have concurred to the formation of the thick disc but not to that of the thin disc.
Finally, we study the impact of different Type Ia SN yields on the evolution of Fe-peak elements in our Galaxy. To this aim, we implement in the chemical evolution models presented above a large compilation of Type Ia SN yields from the recent literature, sampling different explosion mechanisms. The results are then compared with those obtained with classical Type Ia SN prescriptions. In addition, we allow combinations of Type Ia

SN yields from different progenitor classes. We find that the predicted chemical abundance patterns strongly depend not only on the explosion mechanism but also on the initial conditions at the time of the explosion and on the stellar model adopted. Moreover, the comparison with the observed abundance trends suggests that a combination of different classes of explosion is necessary to reproduce the data.

Contents

CHAPTER 1

Introduction

CHEMICAL ABUNDANCES are one of the most powerful tools we have to pin down the history of the objects we encounter in the Universe exploration, from the solar system to high-redshift galaxies. Interstellar dust also deeply influences our view of the Universe by constantly modifying the incoming radiation from astrophysical sources.
The goal of this Thesis is to use the constraints coming from chemical abundances and dust observations to develop chemical evolution models able to study the different galactic environments encountered during cosmic history, from the high-redshift Universe to local galaxies.

In this Chapter, we outline the framework in which this Thesis fits. First, we give a general introduction about the two key players mentioned above. We start from an overview of the cosmic origin of chemical elements, then we pass to a thoughtful introduction about dust in the interstellar medium. Finally, we introduce the model framework adopted in this Thesis, highlighting why and when dust treatment is necessary to provide a coherent comparison between models and observations.

1.1 Chemical elements in the Universe

The discovery of chemical elements by the human kind started in the prehistoric ages, with the usage of copper well before the first civilized societies. From this breakthrough event, the list of known elements has grown through the centuries, arriving to 118 chemical elements, from Hydrogen (H, the lightest element) to Oganesson[1] (Og, the heaviest element).

From the 18^{th} century, the progressively higher number of known elements pushed scientists to search for a proper classification scheme. In particular, the attention was focused on finding some patterns and regularities in the element properties.
Various trials were performed to reach this goal, highlighting a path full of obstacles. From Döbereiner triads (Döbereiner 1829) to Newlands octaves (Newlands 1865) important failures were found in the first tentative classifications. It was not until 1869 that the framework that became the modern periodic table was proposed by Mendeleev, where the chemical elements are arranged according to their atomic weight A, i.e. the sum of protons and neutrons (Mendeleev 1869). This framework was then revised following the discovery of the atomic number Z, i.e. the number of protons, at the beginning of the 20^{th} century, when finally Moseley reached our current formulation of the periodic table (Moseley 1913), with elements categorised in periods (rows) and groups (columns) according to their atomic number.

A similar story of trials and failures had been experienced in the understanding of the cosmic origin of the chemical elements. In particular, the question was: how did the Universe produce the elements of the periodic table?

The first attempts date back to the end of the 19^{th} century. To explain the abundance patterns observed in the solar system, named as cosmic abundances (see later), Clarke (1889) suggested that light elements, making up a primitive substance named "protyl" might assemble into heavier elements. On the other hand, Vernon (1890) proposed a sort of heavy primordial atom that would decompose into lighter elements.
These first ideas soon became outdated: with the advent of quantum mechanics and the nuclear theory, it became evident that chemical elements are produced through nuclear reactions, i.e. through the nucleosynthesis process. In this context, Alpher et al. (1948) (hereafter $\alpha\beta\gamma$) proposed that all the elements in the Universe formed from protons and neutrons soon after the Big Bang by neutron capture and subsequent β-decay processes, thanks to the very extreme conditions of the primordial Universe. This would imply that the abundance of the chemical elements should remain mostly static over time, with only a slight change in H and Helium (He) due to stellar nucleosynthesis[2]. On the other hand

[1] actually, all elements beyond Uranium (U) are unstable and are not present in nature.

[2] by that time, it was already known that conversion of H into He by nuclear fusion could provide the energy required to power stars (e.g. Bethe & Critchfield 1938)

Hoyle (1946, 1954) proposed an alternative theory in which all atomic nuclei heavier than Lithium (Li) are synthesized in star nuclear processes at well defined stages of stellar evolution.

The turning point of the story is represented by the observations of Merrill (1952), who reported the presence of Tc lines in the spectra of a S-class star, i.e. a peculiar red giant star. Tc does not have stable isotopes and its half-life time is $\tau_{1/2} = 4$ Myr: hence, its presence in stellar spectra may be explained only if stellar nucleosynthesis in the stars have produced this element.
This additional input drove the work of Burbidge et al. (1957) (hereafter B^2FH) and Cameron (1957), which are considered as the seminal papers for the current knowledge about element nucleosynthesis. By reviewing and improving Hoyle (1946, 1954) work, B^2FH and Cameron (1957) concluded that only the lightest nuclei (H, He and Li) were synthesised in the Big Bang, whereas all the others have been made by nuclear processes in stars[3].

1.1.1 Stars as chemical factories

The works by B^2FH and Cameron (1957) allowed the community to correctly understand the solar system/cosmic abundances in terms of the reactions producing the nuclides we are observing.
In Fig. 1.1 we show the cosmic abundance pattern of elements, that has not changed significantly since the one adopted in B^2FH. We see that H and He dominate the abundance budget in the solar system. In particular, they are estimated to make up roughly 74% and 24% of the total mass of the Sun. These abundances are quite universal, with H and He making up almost the total mass of baryons in the Universe. Concerning the other elements in the periodic table, only about 2% (by mass) of the Sun is composed of heavier elements. Despite of their small fraction , these elements have a crucial influence on various astrophysical phenomena. For example, they change the conditions for star formation and influence several processes stellar evolution.

In the rest of the Thesis, we refer to all these elements as metals. This definition has a clear meaning in Astronomy, since it comprises all the elements formed only through stellar nucleosynthesis (thus excluding ^{6}Li, Be and B, that are made by spallation processes). In fact, H and He (as well as very small amounts of D and ^{7}Li) are produced soon after the Big Bang , whereas heavier nuclei do not meet the temperature and density conditions necessary to be synthesised during the first moments of the Universe.

However, now the question is: which stars do produce the various elements? In other words, can we categorize the metals in terms of their stellar sources? And can we assess

[3] actually, Be, B and ^{6}Li are produced by cosmic ray spallation on interstellar atoms, but their fractions are negligible with respect to the others nuclei.

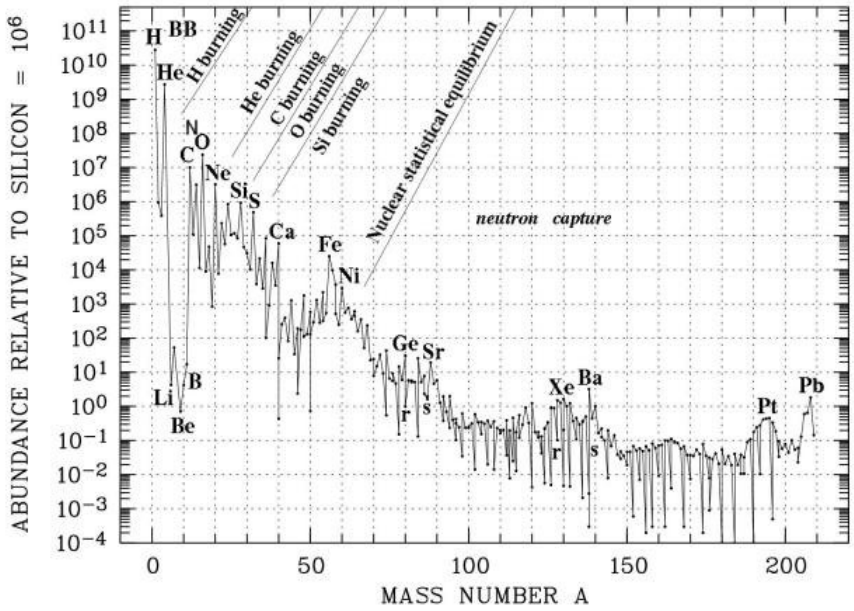

Figure 1.1: *From Cameron (1982). Cosmic abundances normalized to* $\log(N(Si)) = 6$*. The nucleosynthetic processes giving rise to the elements are shown in the Figure.*

the relative contribution of each stellar source? Thanks to the pioneering works by B^2FH and Cameron (1957) and later developments, we can now answer to these questions.
Even if stellar mass and metallicity (i.e. the fraction of mass in metals in an object, usually indicated with Z and not to be confused with atomic number) play a very important role in shaping elemental nucleosynthesis, for simplicity we can divide the stellar sources into low-intermediate mass stars (LIMS), that dye as white dwarfs, and massive stars, mostly exploding as core collapse supernovae (CC-SNe) and leaving a neutron star or a black hole. In addition, the binary condition is an important ingredient affecting the nucleosynthesis: LIMS can also give rise to Type Ia SNe, which are exploding white dwarfs in binary systems. Also other binary systems could play important roles in elemental production: among these, we highlight compact binary mergers (CBM), i.e. merging neutron stars and neutron star-black hole mergers.

In Fig. 1.2 we show a peculiar periodic table where the relative contribution of each group of stellar sources to cosmic abundances is displayed[4].
By comparing this periodic table with the abundances in Fig. 1.1, which represent the solar chemical composition, we note that the most abundant metals (i.e. those up to $Z \sim 30$, $A \sim 60$) are made concurrently by LIMS, CC-SNe and Type Ia SNe. These elements are

[4]it should be noted that Fig. 1.2 contains few errors. Half F should be produced by LIMS (colored in yellow), while Cu and Zn should not be produced in consistent amount by Type Ia SNe (colored in light blue). See Kobayashi et al. (2020b) for more information.

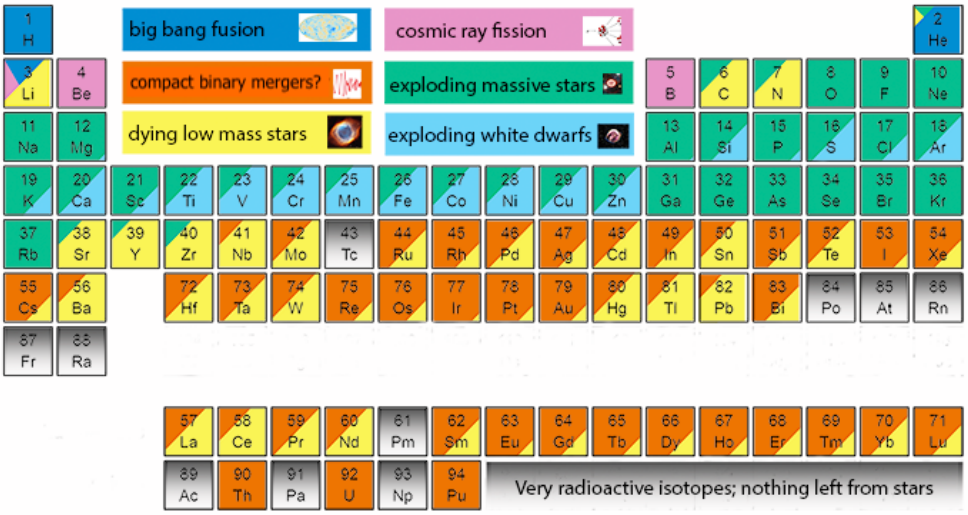

Figure 1.2: *Cosmic origin of elements in the Periodic table. Colors indicates different sources for element production, as shown on the top of the Table. Credits: (adapted from) J. Johnson 2017, http://www.astronomy.ohio-state.edu/∼jaj/ nucleo/*

the results of nuclear fusion processes (hereafter burnings) occurring during and at the end of stellar evolution. This is shown in Fig. 1.1, where the nuclear burnings corresponding to the element synthesis are shown. Concerning the most abundant elements, we note that Carbon (C) and Nitrogen (N) are the only ones with significant contribution by LIMS: this is because such stars do not have enough mass to trigger C burning. On the other hand, massive stars and Type Ia SNe are able to perform all nuclear burnings to produce Iron (Fe) and its neighbours (Fe-peak elements). In particular, the bulk of Fe-peak elements is produced by Type Ia SNe , whereas the so-called α-elements[5] are mainly made by massive stars.

The abrupt decline of the abundances after $Z \sim 30$ due to the fact that Fe has the highest binding energy per nucleon and thus other processes are needed to produce heavier nuclei (B^2FH). These processes consist of slow or rapid (relative to the timescale of the β-decay process) neutron captures on (mostly) Fe nuclei and explain the bottom part of the periodic table, where the contribution is dominated by LIMS and CBM. In particular, most of the slow neutron capture processes happen in the late stages of LIMS, i.e. in the Asymptotic Giant Branch (AGB) phase (e.g. Cristallo et al. 2009, 2011, but peculiar massive stars can also contribute), whereas rapid neutron captures occur in CBM (Rosswog et al. 1999) and, possibly, peculiar massive stars.

[5]elements whose nuclei have a mass number A multiple of 4 (He, i.e. the α particle). Examples are O, Mg, Si, S, Ca.

The Sun is not the Universe

Till now, we have named "cosmic abundances" the abundances measured in the solar system, though the term cosmic is not entirely correct because the chemical composition of the Sun does not reflect the chemical composition found everywhere in the Universe.
However, until the 60s there was the common misconception that solar system abundances roughly represent the typical abundance in all the Universe: this idea was the result of the comparison between the Sun and neighbouring stars, that show very similar abundance patterns (Matteucci 2012). The concept that the Sun should not be taken as an universal tracer for the abundances became clear only in relative recent times (e.g. Chamberlain & Aller 1951; Morgan 1956), with the observation of metal poor stars and globular clusters associated to the stellar halo of our Galaxy.

Now it is common knowledge that different galaxies and stellar populations within galaxies show different ratios between different abundances of heavy ($A \geq 12$) elements. A change in the abundance patterns also means that the relative contribution of each type of stellar source to element abundances is not the same in all cosmic environments. These quantities critically depend on the environment (i.e., the type of galaxy) and the stage of evolution we are looking at (e.g. Kobayashi et al. 2020b).
This is because different galaxies show different histories of star formation, which deeply impact the process of metal enrichment. Moreover, stars of different masses have different lifetimes so the products of nucleosynthesis are ejected into the interstellar medium on different timescales.

For these reasons, the adoption of galactic chemical evolution models is necessary to understand the general picture and provide stronger constraints on the chemical enrichment process as well as on the history of different environments in the Universe.

1.2 Dust in the Universe

Chemical abundances are obtained by means of spectra from very different type of sources, from stars to gas nebulae with different temperatures and compositions. Indeed, light at its different wavelengths is the most important source in Astrophysics and it is the main observable we have to obtain information about objects beyond the Solar System.
However, a correct vision of the Universe must account for another fundamental ingredient that constantly modifies the light from astrophysical sources, i.e. the dust in the interstellar and intergalactic medium.

The first hypothesis regarding the presence of dust dates back to the beginning of the 20^{th} century: Kapteyn (1909) suggested that the decreasing star counts with increasing distance from the Earth (Struve 1847) could arise from the light absorption of intervening material. However, the first evidence of interstellar dust can be attributed to Trumpler (1930), who discovered the wavelength dependent absorption of light, called "extinction", and concluded that it is caused by the scattering and absorption from solid grains in the interstellar medium (ISM).

With the passing of the years, it has become clear that these solid particles are fundamental players in our understanding of the Universe. Interstellar dust is involved in a great variety of physical processes. Dust absorbs the visble and ultraviolet (UV) light and re-emits it in the infrared (IR) band (e.g. Draine & Lee 1984; Calzetti 2001), thus deeply affecting the spectral energy distribution (SED) of galaxies (e.g. Silva et al. 1998; Granato et al. 2000). Dust also subtracts metals from the gas phase of the ISM and therefore modifies its chemical composition (e.g. Vladilo 2004; Jenkins 2009). In addition, dust grains are catalysts of numerous chemical reactions, including the formation of molecular hydrogen (H_2, e.g. Gould & Salpeter 1963) and they are involved in star (e.g. Matsuda et al. 1969; Hirashita et al. 2002) and planet formation (e.g. Safronov & Zvjagina 1969; Pollack et al. 1996) processes.

From what said above, it is natural to associate dust to different scales in our Universe. The zodiacal light demonstrates the presence of dust particles in our Solar System, with direct collection of dust grains performed by space missions such as *Ulysses*, *Galileo*, and *Stardust* (e.g. Grun et al. 1993; Landgraf et al. 1999; Altobelli et al. 2005), not to mention dust grain extraction from meteorites (e.g. Zinner 2014 and references therein). Beyond the Solar system, thermal emission of light caused by dust production has been detected in stellar cold envelopes (e.g. Knapp 1985; Matsuura et al. 2009). At Galactic scales, the presence of dust in the plane of the Galaxy is responsible for the high extinction when observing towards the Galactic center (e.g. Baade 1951; Becklin & Neugebauer 1968). Outside our Galaxy, dust properties have been intensively studied in local galaxies, such as Andromeda galaxy (M31) or the Magellanic Clouds (e.g. Schneider et al. 2014; Casasola et al. 2017) and now many effort are devoted to detect dust in high-redshift (up to $z \sim 9$)

galaxies (e.g. Watson et al. 2015; Laporte et al. 2017; Tamura et al. 2019). Moreover, the possible presence of dust in the intracluster medium (ICM) of galaxy clusters was claimed in several studies (e.g. Stickel et al. 2002; Gutiérrez & López-Corredoira 2017).

1.2.1 Dust observations and properties

We have seen that dust is an important player in a large number of astrophysical processes and that its understanding can cast light on objects evolution at different scales. But what is actually dust? And what is the dust composition?

Since its discovery in the first decades of the XX century, many models have been advanced to explain dust grain properties (e.g. Schoenberg & Jung 1934; Hoyle & Wickramasinghe 1962; Mathis et al. 1977; Draine & Li 2007; Galliano et al. 2011; Jones et al. 2017).
Our understanding of dust grain size distribution and composition comes primarily from the analysis of the spectral features observed in extinction curves, scattering, and thermal emission by interstellar grains. In fact, direct analysis of dust grains from meteorites (e.g. Clayton & Nittler 2004) or stratospheric balloons/airplanes (e.g. Sandford 1987) are subject to severe selection effects and these grains cannot be considered as representative of the global population (Draine 2003).

The study of the extinction curve has been one of the first observables available for probing interstellar dust (Trumpler 1930). In fact, extinction at a certain wavelength λ can be simply defined as $A_\lambda = 2.5 \log_{10}(F^0_\lambda / F_\lambda)$, where F_λ is the observed flux and F^0_λ is the flux in absence of extinction (Draine 2003). This latter quantity can be determined in different ways depending on the object we are looking at (see Galliano et al. 2018 and references therein). Despite of its rather simple determination, the dust extinction curve remains one of the most important constraints for the properties of the dust component, since curve features change with the composition and the size distribution of dust grains.
Examples of extinction curves are shown in Fig. 1.3. We see that the Milky Way (MW) and M31 show a clear "bump" at 217.5 nm that, even though not completely understood, has been associated to the presence of carbonaceous grains. However, this feature is not seen at all for the Small Magellanic Cloud and starburst galaxies, suggesting a lack of carbonaceous grains (Weingartner & Draine 2001) for these objects. This suggests that extinction curves vary depending on the line of sight (see also Steigman et al. 2007) and in different astronomical objects, and therefore that dust may vary depending on the physical conditions of the ISM.

On the other side, the study of the infrared (IR) and far-infrared (FIR) wavebands, that allow us to detect the dust thermal emission, has become available only in more recent years thanks to the launch of space observatories. From the first IR all-sky dust maps obtained by the *InfraRed Astronomical Satellite* (IRAS, Neugebauer et al. 1984) and

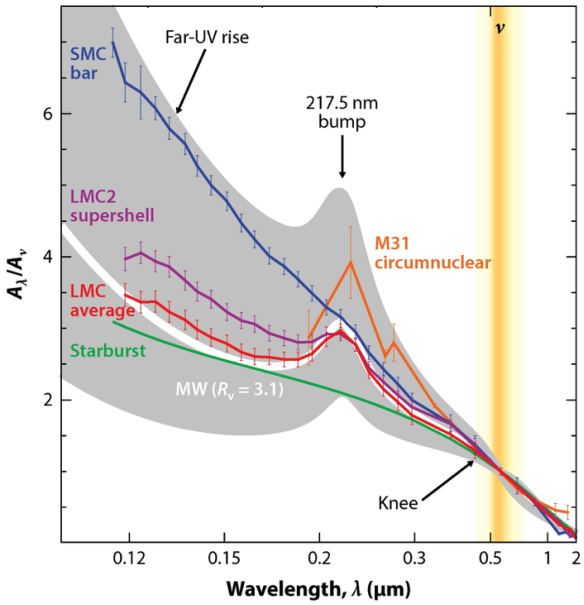

Figure 1.3: *Adapted from Galliano et al. (2018). Extinction A_λ normalised to the extinction in the V band (A_v) as function of the wavelength λ. Extinction curves are for the Magellanic Clouds (SMC, LMC, Gordon et al. 2003), starburst galaxies (Calzetti et al. 2000) and M31 circumnuclear region (Dong et al. 2014). These curves are compared with the one of the Milky Way for different values of $R_v = A_v/A_B - A_v = 2 - 5$ (grey area, $R_v = 3.1$ for the white curve).*

the *COsmic Background Explorer* satellite (COBE, Boggess et al. 1992), several missions were designed to investigate the IR-window, such as the *Infrared Space Observatory* (ISO, Kessler et al. 1996), *Spitzer* (Werner et al. 2004), *Akari* (Murakami et al. 2007). Recently, a great step forward has been made thanks to *Herschel* satellite (Pilbratt et al. 2010). Beyond orbiting satellites, first the *Submillimetre Common User Bolometer Array* (SCUBA, Holland et al. 1999) and nowadays the *Atacama Large Millimeter/submillimeter Array* (ALMA, Wootten & Thompson 2009) has also proved to be very useful in the understanding of dust features at the longest wavelenghts.

In fact, the study of rest frame[6] IR wavelengths is important because it provides information on both microscopic and macroscopic properties of dust. From mid-infrared (MIR) spectra we can get information of dust grain composition from emission lines as well as from additional absorption features (see Galliano et al. 2018 and references therein). Moreover, dust thermal emission in the IR is used to constrain macroscopic dust properties, such as dust masses in galaxies (e.g. Galliano et al. 2011; Jones 2014). However, it is worth mentioning that such macroscopic measures strongly depends on the assumptions on the microscopic dust properties, in particular the grain composition (Zubko et al. 2004;

[6]real wavelengths of emission/absorption, without considering the redshift effect.

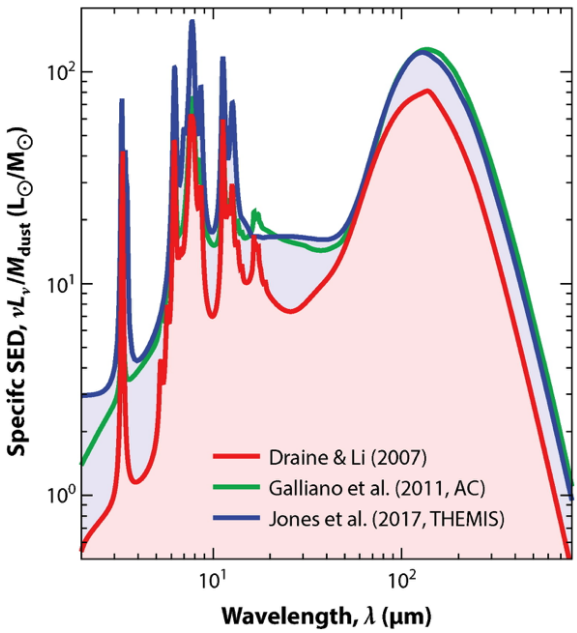

Figure 1.4: *Adapted from Galliano et al. (2018). Model SED for dust models with different grain compositions. Models are from Draine & Li (2007), Galliano et al. (2011) and Jones et al. (2017).*

Galliano et al. 2018). For example, in Fig. 1.4 we show the impact on a synthetic SED of models adopting different grain compositions, leaving unchanged the other parameters. By looking at this Figure, it is immediately seen how uncertainties in this single parameter affect the model predictions (see, e.g. Rémy-Ruyer et al. 2014).

The study of the chemical composition of the ISM is also useful to constrain the composition of dust grains. In fact, dust is made of the available metals produced and ejected by stars, which are present both in the gas and dust phases in the ISM. Since we can observe and estimate the chemical composition of the gas phase, we can estimate the fraction of missing elements from the gas, which is called depletion.

Depletion of different chemical elements has been studied in several systems, i.e. in the MW (e.g. Jenkins 2009), several nearby galaxies (e.g. Sembach et al. 2001; Jenkins & Wallerstein 2017) and damped Lyα systems[7] (DLAs, e.g. De Cia et al. 2016). In general, the depletion of an element X is defined as:

$$\log(\mathrm{X/H})_{dep} = \log(N(\mathrm{X})/N(\mathrm{H}))_{obs} - \log(\mathrm{X/H})_{ref}, \tag{1.1}$$

where $N(\mathrm{X})$ and $N(\mathrm{H})$ are the column densities of an element X and Hydrogen, respectively, and the last term of the equation represents the reference X/H abundance ratio. De-

[7]Gamma-Ray Bursts and Quasi Stellar Objects absorption systems characterised by a neutral hydrogen column density of $N_{\mathrm{HI}} > 2 \times 10^{20}$ cm^{-2} (Wolfe et al. 2005).

spite of the uncertainties related to the choice of the reference abundance ratios, these kind of studies have provided important information about dust. In particular, it appears that some elements are more depleted than others and that the depletion rate follows the trend of the condensation temperature T_c[8] (Field 1974; Savage & Sembach 1996): refractory elements (elements with a higher T_c) are more depleted than volatile elements (elements with a lower T_c).
In this way, it emerges that Mg, Si and Fe are the most depleted elements in the ISM (see Tab. 2 of Galliano et al. 2018): Si and Mg represent two of the major constituents of silicates, and their depletion give an idea of the total fraction of silicate-type dust (e.g. Kemper et al. 2004; Voshchinnikov & Henning 2010). Fe is another element locked up in silicates, but its even higher depletion factor suggests that it may be incorporated in other dust species (e.g. Wickramasinghe & Wickramasinghe 1993; Dwek 2004, 2016).

In addition, several other observables are used to constrain grain properties in the ISM. Among these, polarization studies are the most important. Dust grains are some of the main agents polarizing light in galaxies (see Galliano et al. 2018 and references therein). In particular, the dependence of the polarization fraction on the wavelength provides valuable information on the dust constitution and discriminates between dust models. For instance, polarization studies have been conducted on several local galaxies, such as the Magellanic Clouds, M31 and M82 (Clayton et al. 1996, 2004; Rodrigues et al. 1997; Kawabata et al. 2014). The results all point towards a grain size distribution shifted towards smaller grains relative to the MW, confirming the idea that dust properties may vary depending on the physical conditions of the ISM.

All these constraints have provided us the view of the dust we have today.
Thnaks to the present dust models, we can say that interstellar dust is composed by solid particles of sizes ranging from $\sim$ 1 μm down to molecules containing tens of atoms of $\sim$ 1 nm and it is composed by a mixture of silicates (mainly olivines and pyroxenes), graphite/amorphous carbon and small polycyclic aromatic hydrocarbon (PAHs) molecules separated in the ISM.

A "dynamic" picture of interstellar dust

The above picture of the interstellar dust is now widely accepted in the astrophysical community (e.g. Draine & Lee 1984; Draine & Li 2007; Galliano et al. 2018).
However, this is far away to give a complete explanation of the real composition of interstellar dust. Given the turbulent nature of the ISM, the dust materials become mixed into inhomogeneous assemblages. Moreover, evidences from extinction curves, elemental depletion, and polarization studies (see 1.2.1) highlight that dust composition strongly de-

[8] the condensation temperature T_c of a chemical compound is defined in many ways in the literature. In this Thesis, we define it as the temperature at which 50% of the element has been removed from the gas phase because of condensation (e.g. Lodders 2003).

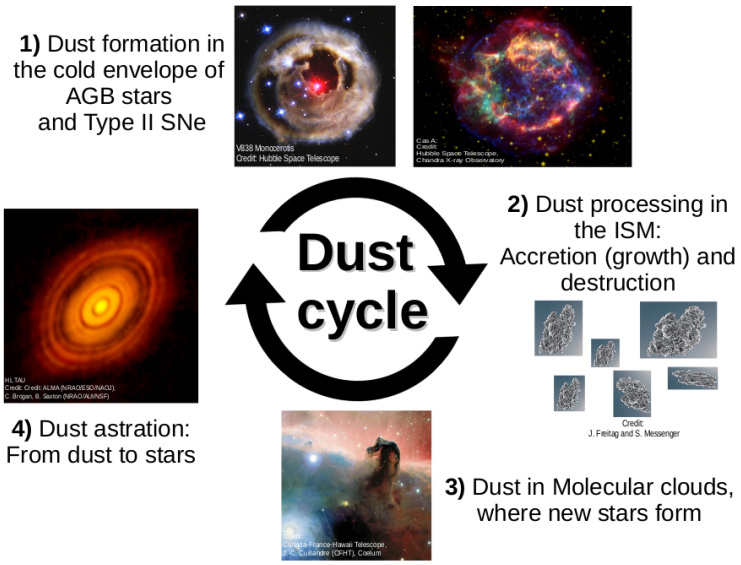

Figure 1.5: *From Gioannini (2017). Cartoon representing the "dust cycle" in the interstellar medium.*

pends on the physical conditions of the ISM and therefore that the properties of dust may be different from one region to another.

For these reasons, dust should be considered as a variable/evolving component of the ISM rather than a "static" one (Gioannini 2017): dust is produced, destroyed, changes its mass, its size distribution and its chemical composition according to different processes. In particular, the circumstellar environments of evolved LIMS, i.e., AGB stars, and SNe represent the first sites from where cosmic dust comes (see, e.g. Gall & Hjorth 2018 for a review). After the ejection by stellar sources into the ISM, dust experiences a lot of processes affecting its amount and nature. For example, SN shocks are the main responsible of cycling dust back into the gas phase and decreasing the grain size (e.g. Dwek & Scalo 1980; Jones et al. 1994). At the same time, grains grow in mass and size thanks to coagulation of other dust grains and metals in the gas phase in the densest ISM regions (e.g. Dwek 1998; Hirashita 2000). Most of these regions, i.e. molecular clouds, are the sites where star formation occurs: therefore, dust material will be used for the formation of the new stars (astration process). However, the new stars will form dust at the end of their life, starting again all the cycle. The ensemble of all these processes is often named as "dust cycle" and it is graphically presented in Fig. 1.5.

Although the great observational and theoretical effort to understand this "dust cycle", current literature is still divided about the relative importance of the different dust pro-

cesses, i.e., production, accretion and destruction (Gall & Hjorth 2018 and references therein).
This uncertainty actually reflects all the interstellar dust topic: despite the great advancement we have made in the understanding of dust grains, many open questions are still present and a lot of work is necessary to reach a thorough understanding of cosmic dust.

1.3 Chemical evolution of galaxies

The different abundances detected in different stars and galaxies are the final result of a complex and continuous process.

As we mentioned in Section 1.1, it is now well known that the Big Bang is responsible only for the production of the lightest elements (H, D, He, and part of Li) of the periodic table. All the elements from C to U and beyond are only formed inside stars.
Nuclear reactions occurring in stellar interiors then change the composition of the matter out of which these stars were born. The processed material, composed of both newly formed and already present elements, is then expelled in the ISM during and at the end of the star lifetime. Depending on the stellar properties (i.e. mass and metallicity), different types of stars eject different amounts of material (from a small fraction to almost their total mass) and different chemical elements, and this happens on different timescales depending on the stellar mass.
With the time passing by, more stellar generations succeed to one another, with new generations forming out of the ISM enriched in metals by the previous ones. In this way, stars progressively enrich and transform the chemical composition of the ISM and play the most important role in the evolution of chemical elements within galaxies: this is what we mean for "chemical evolution of galaxies".

In chemical evolution studies it is often convenient to use elemental abundance ratios X/Y, where X and Y are two chemical elements. The most common way to express abundance ratios in stars and galaxies is in terms of the solar chemical composition:

$$[\mathrm{X/Y}] = \log(\mathrm{X/Y}) - \log(\mathrm{X/Y})_{\odot}, \tag{1.2}$$

expressed in dex. Therefore, in this notation the abundances in the Sun are $[\mathrm{X/Y}]_{\odot}$=0. Eq. (1.2) is usually preferred because we can use equivalently abundance ratios either by number (as measured in stellar spectra) or by mass (as usually computed in models).
However, in this Thesis we also express abundance ratios in terms of absolute values, i.e. without any reference to the solar composition, which is usually adopted for gas phase abundance measurements. For the ratios over Hydrogen, the most abundant element, values are expressed in this way:

$$A(\mathrm{X}) = \log(\mathrm{X/H}) + 12, \tag{1.3}$$

where A(H)=12. In this notation, abundance ratios are expressed in number.

1.3.1 Chemical evolution models

As mentioned above, chemical evolution tries to explain how the chemical elements formed and their abundances have evolved in time and/or distributed in space.

In particular, chemical evolution models aim at following the evolution of the ISM and its chemical composition inside galaxies. Such an evolution depends on the stellar nucleosynthesis and on the star formation history of a galaxy, as well as on possible gas flows.

The first seminal papers on chemical evolution are from Schmidt (1963); Lynden-Bell (1975) and Pagel & Patchett (1975). In these pioneering works simple analytical models were built, with the studied systems represented as closed boxes (i.e. without any gas flow) and stellar lifetimes neglected in computing the relations between the global ISM metallicity Z and the fraction of gas. For this reason, several problems where encountered in reproducing the evolution of the MW, for which considerable amounts of data were already in place at that time. For example, Lynden-Bell (1975) and Pagel & Patchett (1975) discussed possible solutions for the G-dwarf problem, i.e., the excess of low metallicity stars predicted by the simple closed-box models when compared to observations.
However, the foundation of the field is often attributed to Tinsley (1980), who produced a seminal review paper on galactic chemical evolution. In that paper, she summarized all the basic ingredients and the basic equations that even nowadays chemical evolution models are built upon.

Since the foundational paper by Tinsley (1980), many models considering gas flows effects and solving numerically the basic equations of chemical evolution have appeared in the literature.
In particular, a great deal of work has appeared concerning MW galaxy (e.g. Matteucci & Greggio 1986; Matteucci & Francois 1989; Ferrini et al. 1992; Chiappini et al. 1997; Boissier & Prantzos 1999; Cescutti 2008; Schönrich & Binney 2009; Kobayashi et al. 2011; Haywood et al. 2013; Mollá et al. 2015), allowing us to understand many features about the evolution of our Galaxy. In fact, these models were following in detail the stellar lifetimes and thus the evolution of the abundance of individual chemical species.

Nonetheless, several uncertainties are still present even in the understanding of the solar vicinity, with different authors often reaching different conclusions (e.g. Grisoni et al. 2017; Spitoni et al. 2019; Sharma et al. 2021). Therefore, the study of the MW still deserves much work, also in consideration of the wealth of high-quality data that are accumulating in recent years (see Chapter 4).

The "time-delay model" for different galaxies

We know that the Universe contains thousands of millions of galaxies, spanning orders of magnitude in stellar masses ($\sim 10^6 - 10^{12}$ $M_\odot$) and luminosities ($\sim 10^4 - 10^{13}$ $L_\odot$)[9]. Moreover, different galaxies show peculiar morphological features. For this reason, Hub-

[9] in astronomy, it is common practice to express quantities in terms of solar units. In particular, $M_\odot \simeq 2 \times 10^{33}$ g and $L_\odot \simeq 3.8 \times 10^{33}$ erg s^{-1}.

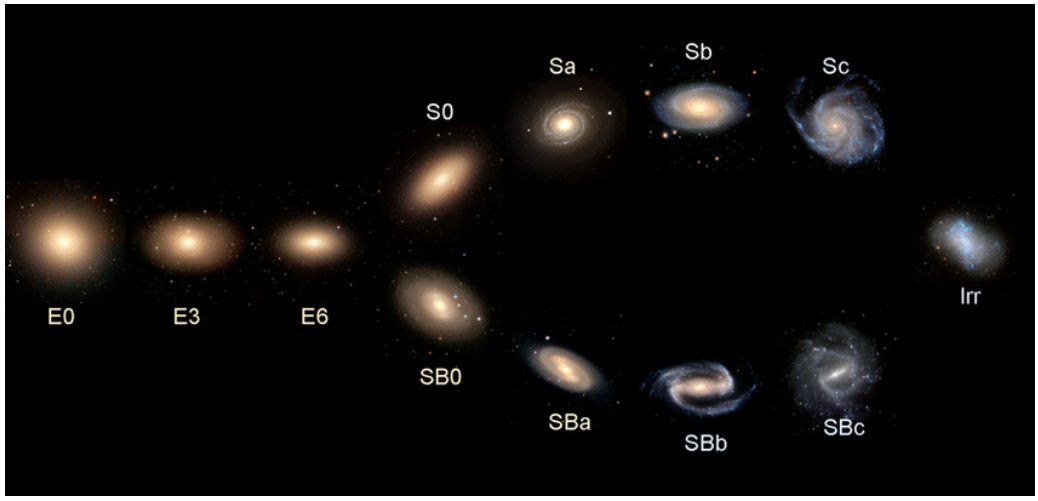

Figure 1.6: *From Cui et al. (2014). The Hubble sequence.*

ble (1926) proposed a galaxy classification basing on their morphology, now called the Hubble sequence. This sequence is shown in Fig. 1.6. Without entering in the details of Hubble classification, we highlight the main differentiation into three classes: elliptical galaxies (E0-E6, depending how much flattened the ellipsoid is), spiral galaxies (S or SB, depending if they contain a bar in their central part) and irregular galaxies (Irr).

The variations in the morphological structure of the different galaxy types are actually driven by variations of the gas and stellar content of these objects: elliptical galaxies show older and more metal rich stars relative to spirals, which in turn show older and metal rich stellar populations relative to irregulars. At the same time, irregular galaxies are much more gas rich than spirals, which however show a much larger gas content than that of elliptical galaxies. These differences in the characteristics of the galaxies are driven by the different histories of star formation they have experienced. Star formation is very fast in spheroids/ellipticals, moderate in spiral disks, and slow and perhaps gasping (Tosi et al. 1991) in irregular gas rich galaxies (see Matteucci 2012 for a review).
As already mentioned in 1.1.1, the different star formation histories also produce different chemical abundance patterns with respect to that observed locally. This is at the basis of the so-called "time-delay model" (Matteucci 2012).

The "time-delay model" explains the observed behavior of [X/Fe] vs. [Fe/H], with X being any chemical element, as due to the different roles played by different types of stars in the galactic chemical enrichment.
The most striking example regards the [α/Fe] vs. [Fe/H] diagram. α-elements are ejected mostly (where not entirely) by CC-SNe. On the other hand, the bulk of Fe is produced by

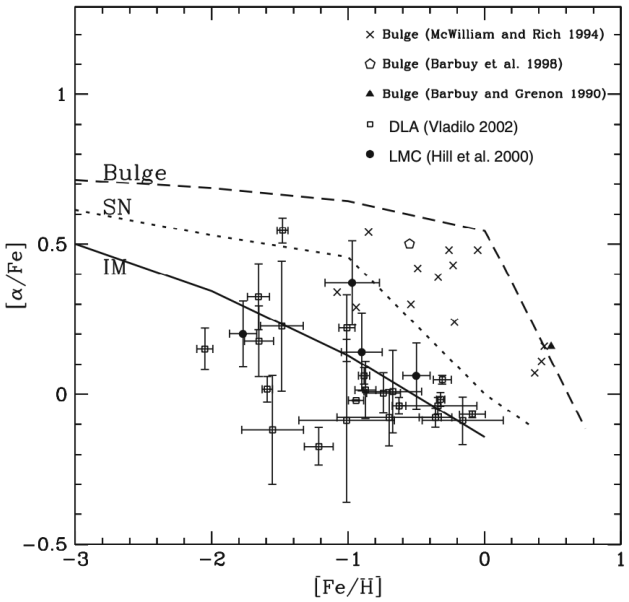

Figure 1.7: *From Matteucci (2012). Predicted [α/Fe] vs. [Fe/H] relations for the Large Magellanic Cloud (solid line), the solar vicinity (short dashed line) and the Galactic bulge (long dashed line). The plot show clearly the "time-delay model" for different galactic environments.*

Type Ia SNe, while the rest by CC-SNe. These different stars do not eject elements on the same timescales: CC-SNe originate from massive stars whose lifetime is typically below 30 Myr, whereas Type Ia SNe explosions are the product of binary systems containing LIMS, that live more than 30 Myr and up to billion years. The effect of the delayed Fe production by Type Ia SNe is to create an overabundance of α-elements relative to Fe ([α/Fe]> 0) at low [Fe/H] values, where the production of α and Fe is regulated only by CC-SNe, and a continuous decline at larger [Fe/H], i.e. when Type Ia SNe start exploding (Matteucci & Greggio 1986, see also Tinsley 1979 for the first approach to the problem).

But do all galaxies show the same [alpha/Fe] vs [Fe/H] trend?
In Fig. 1.7, we present a plot in which predictions of the [α/Fe] ratios as functions of [Fe/H] in galaxies of different morphological types are shown. In particular, this Figure gives predictions for the Galactic Bulge, i.e., a fast-evolving system, similar in this respect to an elliptical galaxy, for the solar vicinity region, that reflects the secular evolution of a typical disc region, and for the Large Magellanic Cloud, i.e. a prototype irregular galaxy. It is evident that the different star formation histories produce different behaviours in the abundance ratios. [α/Fe] ratios in elliptical galaxies are higher and remain almost constant for a large interval of [Fe/H]. This is due to the fact that, since star formation is very intense, ellipticals reach high metallicities only by means of CC-SNe. Also, CC-SN progenitors are likely favoured in elliptical/starburst galaxies (e.g. Matteucci 1992, 1994;

Henkel & Mauersberger 1993), thus leading to even higher [α/Fe] ratios. In this way, when Type Ia SNe start ejecting Fe into the ISM, the metallicity is much higher than that in spirals at the same time. In the case of an irregular galaxy, we have the opposite situation: the slower star formation implies that the gas is poorly enriched in Fe when Type Ia SNe start exploding. Therefore, the so-called knee in the [α/Fe] vs. [Fe/H] relation is placed at lower metallicities, implying that [α/Fe] ratios observed in irregular galaxies are lower than those in spirals, that in turn are lower than those observed in elliptical galaxies.

From the first prediction by Matteucci & Brocato (1990), the "time-delay model" has been adopted as the basis for the analysis of the different [X/Fe] ratios observed in external galaxies, from dwarf irregular galaxies to giant ellipicals (e.g. Lanfranchi & Matteucci 2003; Pipino & Matteucci 2004; Ballero et al. 2007; Calura et al. 2009a; Vincenzo et al. 2014, 2019; De Masi et al. 2018; Lacchin et al. 2020).
Moreover, this scheme can be used also to identify high-redshift galaxies with unknown morphology by looking at their abundance ratios (e.g. Calura et al. 2009b; Grieco et al. 2014; Palla et al. 2020c). In fact, galaxies of different morphologies differ for their different history of star formation, that is the main driver of the different abundance patterns.

1.3.2 Chemical evolution models with dust

Chemical evolution models study the evolution of the ISM metal content in a galaxy. As we have seen in 1.2, however, metals also represent the constituent of dust grains.
For this reason, chemical evolution models can be adopted to study the properties of dust in the ISM.

In order to compute the evolution of dust in galaxies, models have to follow the evolution of the abundances of the main metals and in particular those of refractory elements, i.e., those where dust depletion is more important, such as Fe, Si, Mg. Having computed the total ISM (gas+dust) evolution for these elements, the life cycle of dust grains, i.e. the "dust cycle", is computed by including the main processes affecting the dust abundances. In particular, dust production by stars and dust accretion and destruction processes in the ISM are accounted for in the models to follow the evolution of dust in the ISM.
In this way, chemical evolution models can also play a fundamental role in the study of interstellar dust, allowing a theoretical interpretation of the dust depletion patterns as well as of the most important dust-related scaling relations, such as the dust-to-gas mass ratio vs. metallicity (see Galliano et al. 2018 and references therein).

The first study in which the main processes of the "dust cycle" where accounted for dates back to Dwek & Scalo (1980), where chemical evolution models with dust were developed for the study of the solar neighbourhood. Later on, this approach was adopted by Dwek (1998), which is often considered one of the foundational works about dust

evolution in galaxies. In this paper, the evolution of dust was studied at Galactic scale and for the first time a detailed theoretical study on elemental dust depletion was performed. Beyond the MW, Calura et al. (2008) studied the dust evolution in galaxies of different morphological type: by adopting the same assumptions of Dwek (1998), they investigated the influence of the star formation history on the evolution of several dust properties and scaling relations.

Since these pioneering works, significant progress has been made both in dust observations (see 1.2.1) and in theoretical prescriptions. In particular, in the last decade several papers have appeared, both concerning stellar dust production (e.g. Piovan et al. 2011; Dell'Agli et al. 2017; Marassi et al. 2019) and other ISM dust processes (e.g. Hirashita & Kuo 2011; Asano et al. 2013; Bocchio et al. 2014). Moreover, the appearance of several galactic surveys specifically aimed at measuring dust masses in galaxies (e.g. Kennicutt et al. 2011; Madden et al. 2013; De Vis et al. 2017a; Saintonge et al. 2018; Clark et al. 2018) increased the need for dust models.
This led to a great development of chemical evolution models with dust, with a large number of papers published (e.g. Zhukovska et al. 2008; Zhukovska 2014; Gioannini et al. 2017a; De Vis et al. 2017b; Vladilo et al. 2018; Millán-Irigoyen et al. 2020).

In parallel to chemical evolution models, in the last years dust treatment started to be incorporated into hydrodynamical simulations that follow the dust evolution in galaxies in a multi-phase inhomogeneous ISM (e.g. Zhukovska et al. 2016; Aoyama et al. 2017; McKinnon et al. 2018; Graziani et al. 2020). In this way, the authors can benefit from a more physical treatment of the ISM, although sub-grid physics recipes still affect the final results.
Nonetheless, one-zone chemical evolution models are still widely adopted in the literature to study dust properties in galaxies (e.g. De Looze et al. 2020; Galliano et al. 2021; De Vis et al. 2021). In fact, hydrodynamical simulations are much more computationally expensive which makes hard to fully explore the parameter space, at variance with one-zone models, that allow much more flexibility.

We are thus at the right time to fully exploit the potential of chemical evolution models including dust. The development of new theoretical dust prescriptions has put the model framework on more solid physical grounds, although large uncertainties still affect the understanding of dust evolution.
This is especially true at high-redshift, where we cannot count on the large amount of data coming from dust-designed surveys. Moreover, observations of several very high-redshift galaxies (e.g. Watson et al. 2015; Laporte et al. 2017) have questioned if the main dust mechanisms thought to explain local observations are the same in the primordial Universe (see, e.g. Gall & Hjorth 2018 and references therein).

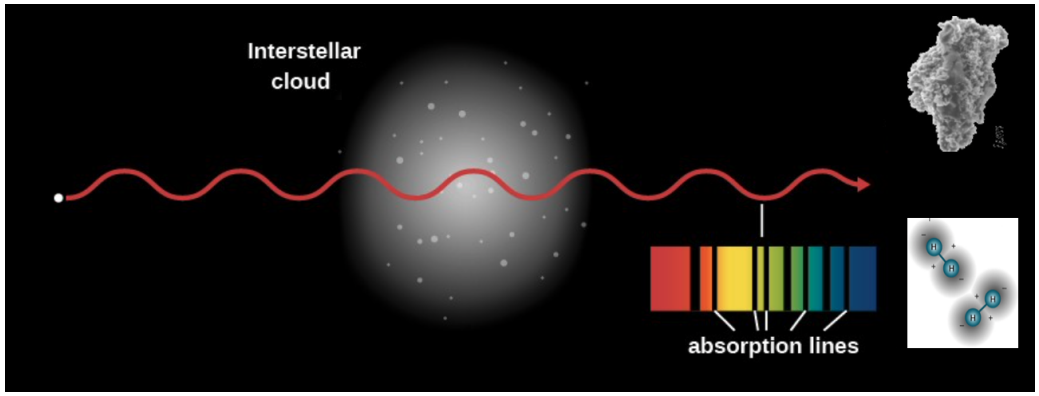

Figure 1.8: *Cartoon representing the composition of the ISM (gas and dust) and we get from optical/UV absorption spectroscopy (only gas). Credits: (adapted from) http://cnx.org/contents/2e737be8-ea65-48c3-aa0a-9f35b4c6a966@10.1*

Dust or not dust in chemical evolution models?

We have just seen that chemical evolution models including dust are fundamental tools in the progress of our understanding of dust evolution.
However, dust treatment also plays a fundamental role in the abundance analysis of external galaxies, especially at high-redshift (Gioannini 2017).

In general, standard chemical evolution models trace the total (gas+dust) abundances in the ISM. This approach allows us an immediate comparison with the abundances inferred from absorption lines in stellar spectra. In fact, stellar atmospheres reflect the composition of the total ISM at the time of stellar birth (e.g. Trimble 1996, although some exceptions exist for elements convoyed to the stellar surface by convection or affected by other physical mechanisms acting in the stellar atmospheres such as, for instance, atomic diffusion). Therefore, stars can be used as fossil records of the past star formation history of a galaxy and compared with the predictions of chemical evolution models.
However, this kind of comparison is possible only for our Galaxy and few other local galaxies. In order to adopt such an approach, in fact, we need either to resolve individual stars, which is possible only for the nearest stellar systems, also including M31 and its satellites, or rely on integrated stellar spectra, such as for elliptical galaxies.

Looking at more distant objects, observational diagnostics for chemical abundances base primarily on rest frame UV/optical absorption or emission line spectroscopy of the interstellar gas. However, at variance with stellar abundances, the chemical composition of ISM gas represents only part of the total ISM composition. This is well represented in the cartoon in Fig. 1.8, where we see that light from a background source is absorbed by atoms in the intervening medium resulting in absorption features in the spectrum. How-

ever, in this way the elemental abundances embedded in dust grains are left undetected. In particular, refractory metals can be severely depleted into dust grains. For example, in the solar neighbourhood ISM more than 95% of Fe is trapped into dust particles (e.g. Jenkins 2009).
For this reason, accounting for the elemental depletion in the ISM becomes fundamental to properly interpret the gas abundance patterns.

Therefore, chemical evolution models including dust need to be adopted in the comparison with observed abundance ratios, especially for the elements with different depletion fractions.
Examples of this approach are the studies of DLAs abundance patterns (e.g. Grieco et al. 2014; Gioannini et al. 2017a; Palla et al. 2020c), for which high resolution spectroscopy can be performed to infer precise column densities of the different gas atoms. However, the same approach can be adopted for any high-redshift object in the presence of high-quality abundance data.

1.4 Plan of the Thesis

The goal of this Thesis is to develop chemical evolution models able to study the different galactic environments encountered during cosmic history, from the high-redshift Universe to local galaxies and in particular the MW.

The description of the chemical evolution models adopted to describe these environments is committed to Chapter 2, where details about the basic ingredients and model equations are given. For the many issues related to dust, especially in high-redshift galaxies, detailed dust treatment is also implemented in the models.

Having described the models, in the subsequent Chapter we describe the original results of the Thesis work. In particular, the results are splitted into two Chapters, according to the objects of study. In Chapter 3, we show the results obtained in the study of high-redshift environments, for which dust evolution is also computed in the models (see 1.3.2). First, our focus is devoted to high-redshift starburst galaxies, whose gas abundance patterns are still poorly understood due to many open questions on the nature of these objects. After that, we move to the study of galaxy clusters and in particular to the computation of their dust evolution, whose understanding is a matter of debate.
For what concerns Chapter 4, we concentrate on our Galaxy, where chemical evolution models do not need dust treatment, at variance with those of the previous Chapter. In this case, we investigate the evolution of the MW disc under different aspects, trying to reproduce multiple observational constraints, such as present-day radial gradients and chemical evolution patterns at different radii. By means of these models, we also study the effects on the element nucleosynthesis implementing different recent prescriptions for Type Ia SNe.

Finally, in Chapter 5 we summarize the main conclusions of this Thesis and their possible implications. We also pay attention to future advancements in the fields covered throughout the Thesis.

CHAPTER 2

Chemical and dust evolution models

MATTER in the interstellar medium (ISM) in all galaxies is continuously astrated and reprocessed by stars and restored to the ISM through stellar winds and SN explosions. Chemical evolution models allow us to predict the evolution of the abundance of chemical elements in the ISM of a galaxy together with other crucial information on the galaxy star formation history (SFH).
In parallel, dust grains are astrated and produced by stars as well as accreted and destroyed in the ISM, constantly changing the dust depletion fraction of metals in the ISM gas. Thus, dust evolution models are also fundamental to uncover the evolution of the chemical elements both in the gas and dust phase.

In this Chapter, we present the adopted chemical and dust evolution models, which are the fundamental building blocks of this Thesis work. We start showing the basic ingredients of chemical evolution models, followed by a detailed explanation of the contents of the chemical evolution equations. Then, we concentrate on dust evolution models by describing their most important ingredients. Finally, we show the dust evolution equations together with their assumed prescriptions.

2.1 Basic ingredients for chemical evolution models

The basic physical ingredients for modelling galactic chemical evolution can be summarized in four points (Matteucci 2012):

- initial conditions;
- stellar birthrate function (product of the star formation rate with the initial mass function),
- stellar yields (nucleosynthesis);
- gas flows (infall, outflow);

We now look at these points more in detail.

2.1.1 Initial conditions

The initial conditions specify if:

- the chemical composition of the initial gas is primordial or pre-enriched (by pre-galactic processes, neighbour systems)
- the galaxy is considered as a closed-box (without any interaction with the outer environment) or an open system (with the possibility to have gas flows).

The standard assumption in models of chemical evolution is to have an initial primordial chemical composition: in this way, the initial ISM composition is made by the elements produced during the Big Bang nucleosynthesis (H and He isotopes, see Section 1.1). In addition, it is commonly assumed that model galaxies are formed by infall of gas onto a pre-existing dark matter (DM) halo and evolve suffering gas outflows.

During this Thesis, we make the above assumptions, adopting the primordial abundances by Pitrou et al. (2018) and gas flows laws as described in 2.1.4 , unless otherwise specified.

2.1.2 Birthrate function

The stellar birthrate function represents the number of stars formed in the mass interval $[m,\ m+dm]$ and in the time interval $[t,\ t+dt]$. The birthrate function is usually expressed as the product of two independent functions in this way:

$$B(m,t) = \psi(t)\phi(m), \tag{2.1}$$

where $\psi(t)$ is the star formation rate and $\phi(m)$ the initial mass function in number. We now present these two quantities in detail.

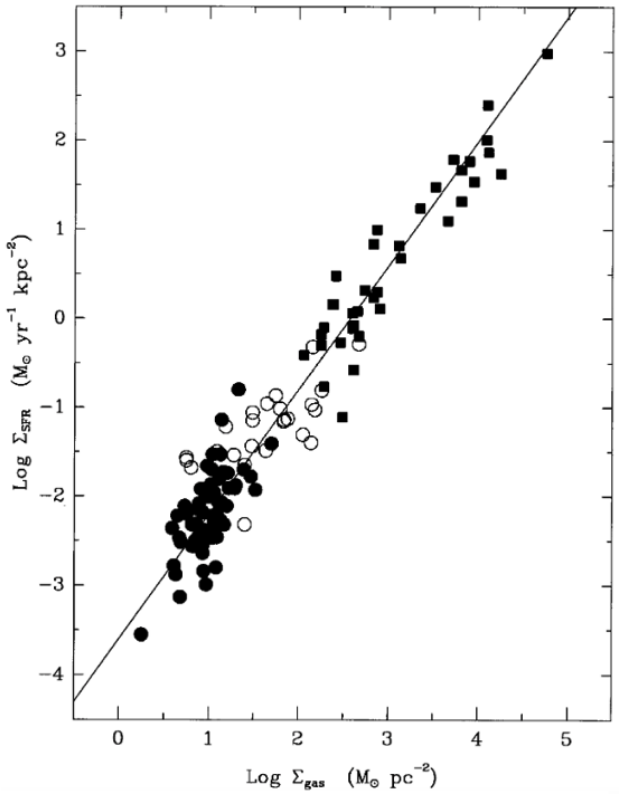

Figure 2.1: *Adapted rom Kennicutt (1998). The SFR in star forming galaxies. The continuous line represents the best fit to the data that can be achieved using Eq.* (2.2) *and* $k = 1.4$.

Star formation rate

The star formation rate (SFR) indicates the rate at which the interstellar medium is turned into stars per unit time. It is generally expressed in terms of $M_\odot$ pc^{-2} Gyr^{-1} or $M_\odot$ yr^{-1} (depending if we refer to the SFR density or not).
The most common parametrisation for the SFR is the Schmidt-Kennicutt law (Kennicutt 1998):

$$\psi(t) = \nu {\Sigma_{gas}}^k, \tag{2.2}$$

where Σ_{gas} is the gas surface density and $k = 1 - 2$, with a preference for $k = 1.4 - 1.5$ for star forming discs (see Fig. 2.1). ν is the star formation efficiency (SFE), which is a free parameter that represents the SFR per unit mass of gas and has the dimensions of the inverse of time.

To be precise, the original Kennicutt (1998) law refers to surface densities only. However, as noted in Romano et al. (2015), in star forming regions with roughly constant

scaleheights, the surface density in Eq. (2.2) can be turned into volume density (but see also Bacchini et al. 2019). By assuming that the Schmidt-Kennicutt law indicates that SFR is controlled by gas self-gravity, Eq. (2.2) can be rewritten as:

$$\psi(t) = \nu' {\rho_{gas}}^{k'}, \tag{2.3}$$

where ρ_{gas} is the gas volume density, ν' has the same meaning of Eq. (2.2) and $k' = 1$ is the equivalent of $k = 1.5$. Integrating over the volume, we can also write Eq. (2.3) as:

$$\psi(t) = \nu' M_{gas}^{k'}, \tag{2.4}$$

where M_{gas} is the gas mass within the galaxy.

Throughout this Thesis, we adopt both the surface and volume density expressions. We use Eq. (2.2) to model the Milky Way (MW) galaxy, while we adopt Eq. (2.3)/(2.4) for external galaxies.
Concerning the SFE, we adopt different values depending on the morphological type of galaxy we are modelling (see Section 3.1): for irregular, spiral and elliptical galaxies, we assume values of the order of 0.1 Gyr^{-1} (e.g. Lanfranchi & Matteucci 2003; Vincenzo et al. 2014), 1 Gyr^{-1} (e.g. Cescutti et al. 2007; Spitoni et al. 2019) and 10 Gyr^{-1} (e.g. Pipino & Matteucci 2004; De Masi et al. 2018), respectively.

Initial mass function

The initial mass function (IMF) represents the mass distribution of stars at their birth. It is usually parametrized as a one-slope or multi-slope power law, which is assumed to be constant in space and time. It is also normalized to unity in mass, in this way:

$$1 = \int_{m_{min}}^{m_{max}} \varphi(m)\, dm \;=\; \int_{m_{min}}^{m_{max}} m\, \phi(m)\, dm, \tag{2.5}$$

where m_{min} and m_{max} delimit the mass range in which the IMF is considered and $\varphi(m)$ is the IMF in mass.

The most common (and simple) example for this quantity is the Salpeter (1955) IMF, which is still widely used in chemical evolution studies and which is also adopted in this Thesis:

$$\phi_{Salp}(m) \propto m^{-(1+1.35)}, \tag{2.6}$$

generally extrapolated in the mass range 0.1-100 $M_\odot$[1].
Later on, several multiple power-law IMF were derived (Miller & Scalo 1979; Scalo 1986;

[1] Salpeter (1955) defined the IMF in a restricted mass range ($\sim$0.4-10 $M_\odot$).

Kroupa et al. 1993; Kroupa 2001; Chabrier 2003[2]). Among these, during this Thesis work we use the ones by Scalo (1986):

$$\phi_{Scalo}(m) \propto \begin{cases} m^{-(1+1.35)} & m \leq 2\mathrm{M}_{\odot} \\ m^{-(1+1.7)} & m > 2\mathrm{M}_{\odot}, \end{cases} \tag{2.7}$$

and Kroupa et al. (1993):

$$\phi_{Kroupa}(m) \propto \begin{cases} m^{-(1+0.2)} & m \leq 0.5\mathrm{M}_{\odot} \\ m^{-(1+1.2)} & 0.5 < m/\mathrm{M}_{\odot} \leq 1 \\ m^{-(1+1.7)} & m > 1\mathrm{M}_{\odot}. \end{cases} \tag{2.8}$$

The differences between the Salpeter (1955); Scalo (1986) and Kroupa et al. (1993) IMFs can be appreciated in Fig. 2.2, which clearly shows the main differences between single and multiple power-law IMFs. It is worth noting that the Kroupa et al. (1993) IMF is preferred for the MW disc according to chemical evolution studies (Romano et al. 2005) and accurate analysis of *Gaia* satellite DR2 data (Sollima 2019) in the solar neighbourhood. Moreover, some evidences in favour of an IMF disfavouring massive stars relative to the Salpeter (1955) (i.e. Scalo 1986; Kroupa et al. 1993) were found by looking at candidate spiral galaxies hosting high-redshift GRBs (Palla et al. 2020c).

For these reasons, in the next Chapters we adopt the Scalo (1986) IMF for generic spiral disc galaxies and the Kroupa et al. (1993) IMF for the solar neighborhood and the MW disc. For the other galaxy types (i.e. dwarf irregular, spheroids/elliptical) we adopt instead the Salpeter (1955) IMF, unless otherwise specified.

However, all the IMFs mentioned so far were derived from stellar counts in the solar vicinity (see Matteucci 2012 for more information): they are ideal for the study of our own Galaxy, but what about other galaxies?
Unfortunately, the same analysis on stellar counts cannot be performed in other galaxies (with few exceptions for the very nearby Magellanic Clouds, see, e.g. Schneider et al. 2018) so we cannot test directly if the IMF is the same everywhere. This topic has been the subject of a large debate in the scientific community for years (e.g. Kroupa 2002; Ferreras et al. 2016), but nowadays most of the observational probes point towards a dependence of the IMF on the environment (in particular on the SFR and the metallicity).

The integrated galactic initial mass function (IGIMF) theory (e.g. Kroupa & Weidner 2003; Weidner & Kroupa 2005; Jeřábková et al. 2018) places in this context. This IGIMF formulation is based on the empirical evidence that most stars in galaxies form in star clusters (e.g. Lada & Lada 2003) and that the IMF within stellar clusters can be well

[2]actually, the low mass domain ($m < 1$ M$_{\odot}$) in Chabrier (2003) has a log-normal form.

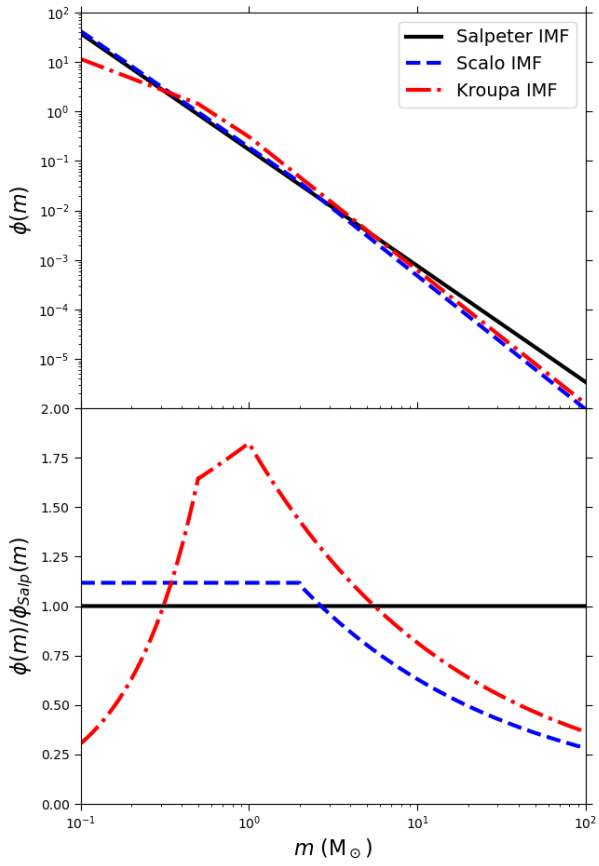

Figure 2.2: *Upper panel: the Salpeter, Scalo and Kroupa IMFs. Lower panel: difference between multi-slope IMFs and the Salpeter one.*

approximated by a power-law (e.g. Pflamm-Altenburg et al. 2007). However, the IMF integrated over a galaxy is generally different from the IMF in embedded stellar clusters, because it is integrated over the mass function of embedded stellar clusters (ECMF). In its more general form, the IGIMF can be expressed in this way (Jeřábková et al. 2018):

$$\xi_{\rm IGIMF}(m,t) = \int_{M_{\rm ecl,min}}^{M_{\rm ecl,max}(\psi(t))} \phi(m, M_{ecl}, [{\rm Fe/H}])\, \xi_{ecl}(M_{ecl}, \psi(t))\, dM_{\rm ecl}, \tag{2.9}$$

where here $\phi(m, M_{ecl}, [{\rm Fe/H}])$ is the IMF within stellar clusters, ξ_{ecl} is the ECMF and M_{ecl} the mass of the embedded cluster.

With such a formulation, an IMF dependence on SFR and metallicity[3] is derived, allowing top-heavier/bottom-lighter IMFs (i.e. favouring massive stars) for galaxies experiencing higher SFR (e.g. De Masi et al. 2018) and bottom-heavier/top-lighter IMFs (i.e. favouring low mass stars) in lower SFR environments (e.g. Vincenzo et al. 2015). This theory has gained important successes in explaining many of the IMF related features observed in external galaxies (e.g. Recchi et al. 2009; Meurer et al. 2009; Fontanot et al. 2017; De Masi et al. 2018; Watts et al. 2018), although it encountered several problems for some extreme, low star forming environments such as ultra faint dwarf galaxies (UFDs, see e.g. Lacchin et al. 2020; Prgomet et al. 2021, but see also Yan et al. 2020).
A more detailed discussion about the IGIMF formulation is given in Section 3.2, where we focus on the impact of this theory on starburst galaxies at high-redshift.

2.1.3 Stellar yields

The stellar yields are the amounts of newly formed elements that are ejected by stars into the ISM.
As mentioned in 1.1.1, elements with mass number A from 12 (C) to $\sim$60 (Fe-peak elements) are formed in stars during either quiescent and explosive burnings. Stars transform H into He and then He into heavier atoms until the Fe-peak elements, where the binding energy per nucleon reaches a maximum and the nuclear fusion reactions stop. Elements with higher mass number ($A >> 60$ up to U) are formed by means of slow or rapid (relative to the timescale of the β- decay process) neutron capture by Fe and other heavy seed nuclei. They are thus called s- and r-process elements, respectively.

Different stars produce different elements, depending primarily on their initial mass. Below, we focus on the main stellar categories and their nucleosynthesis products.

Low-intermediate mass stars (LIMS)

This group includes single stars in the mass range 0.8 $M_\odot$ $-$ 8-10 $M_\odot$. The 0.8 $M_\odot$ limit is driven by stellar lifetimes, since lower mass objects live well beyond the age of the Universe ($\sim$ 14 Gyr). At the same time, LIMS do not have enough mass to switch on all the nuclear burnings and die as core collapse supernovae (CC-SNe) and therefore end their lives as white dwarfs (WDs).The upper mass limit of this class is however quite uncertain: while for lower mass stars (<6-8 $M_\odot$, depending on metallicity) evolve through the asymptotic giant branch (AGB) phase and die as Carbon-Oxygen (CO) WD, the final outcome of higher mass stars, known as super AGB (sAGB) is uncertain: they may form a hybrid Carbon-Oxygen-Neon (CONe) WD, an Oxygen-Neon-Magnesium (ONeMg) WD but they could even undergo an electron capture induced collapse and produce electron capture (e-capture) SNe (see Kobayashi et al. 2020b and references therein).

[3] not all the IGIMF forms assume a metallicity dependence

LIMS contribute to the chemical enrichment through mass loss and, in their final stages of evolution, planetary nebula ejection. They enrich the ISM mainly with ^{4}He, ^{12}C and ^{14}N. Some other isotopes produced by CNO related chains (^{23}Na, Al) as well as heavy s-process elements ($A > 90$) can be also produced in significant amounts.

Throughout this Thesis, we adopt different mass and metallicity dependent LIMS yields from the literature. In Chapter 3, we take advantage of either yields by van den Hoek & Groenewegen (1997) (Sections 3.1, 3.2) or Karakas (2010) and Doherty et al. (2014a,b) (these latter for sAGB stars, Section 3.3). In Chapter 4 instead, we adopt only the Karakas (2010) yield set.

Massive stars

Stars within this group have masses larger than 8-10 $M_{\odot}$.
In the mass range 8-10 $M_{\odot}$ $-$ 10-12 $M_{\odot}$ they end their lives as e-capture SNe: oxygen ignites explosively in the ONeMg degenerate core together with the electron capture process. This prevents the total destruction of the progenitor, leaving a neutron star (NS). In the mass range 10-12 $M_{\odot}$ $-$ M_{WR}, where M_{WR} is the minimum mass for the formation of a Wolf-Rayet star, stars explode as CC-SNe, in particular Type II SNe. The M_{WR} values is rather uncertain, since it depends on the stellar mass loss, which in turn depends on the initial stellar mass and metallicity (e.g. for a solar chemical composition $M_{WR} \simeq$25 $M_{\odot}$). Also uncertain is whether these stars form a NS or a black hole (BH), which depends on the amount of the ejected material which falls back on the contracting core during the explosion (see Matteucci 2012; Kobayashi et al. 2020b and references therein).
For masses above M_{WR}, stars should still explode as CC-SNe, but of Type Ib/c for the lack of H in their spectra. There are evidences that these events are linked to gamma ray bursts (GRBs, see Palla 2018). For many of these SNe, higher explosion energies ($\epsilon_0 = 10^{52}$-10^{53} erg) than "regular" SNe ($\epsilon_0 = 10^{51}$ erg) are required to reproduce the observed lightcurves (see, e.g. Kobayashi et al. 2006). For this reason, they are often called hypernovae (HNe).

Massive stars are the main factories of most metals. They are responsible for most of α-element production, some Fe-peak elements, as well as light s-process elements ($A < 90$) and a non-negligible fraction of C. They may perhaps contribute also to r-process element production (see, e.g. Matteucci et al. 2014). As an example, in Fig. 2.3 we show the yield patterns produced for a 25 $M_{\odot}$ star by two different stellar models (Kobayashi et al. 2006; Limongi & Chieffi 2018).

In this Thesis, different yield sets are adopted for massive stars. In particular, we use the yields of François et al. (2004) (i.e. Woosley & Weaver 1995 yields except for Mg, which is artificially increased to fit solar abundance) in Sections 3.1 and 3.2, while in Section 3.3

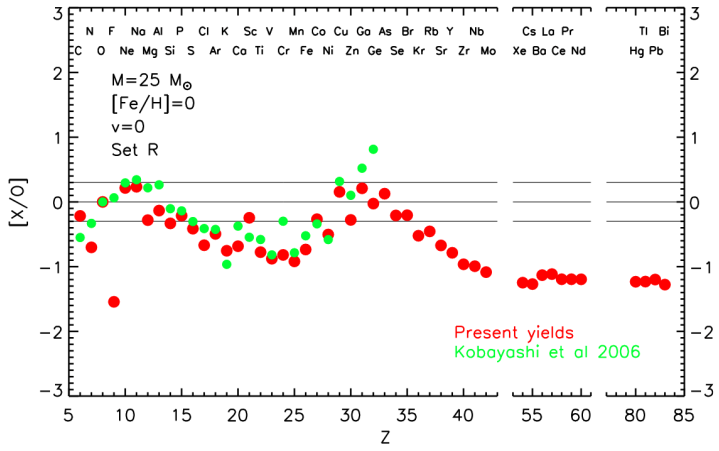

Figure 2.3: *From Limongi & Chieffi (2018). Comparison between the [X/O] produced by Limongi & Chieffi (2018) yields for non rotating, 25$M_{\odot}$, solar metallicity star (red points) and analogous yields provided by Kobayashi et al. (2006) (green points).*

and Chapter 4 we adopt the yields by Kobayashi et al. (2006)/Nomoto et al. (2013)[4]. For both sets, the yields are extrapolated to the upper limit of the IMF by keeping constant the last computed masses ejected as newly produced elements.

Type Ia Supernovae

Type Ia SNe are assumed to be thermonuclear explosions of WDs in binary systems. Nonetheless, the physics governing Type Ia SNe is still largely debated (see, e.g. Ruiter 2020 for a review). In particular, the main concerns regard the progenitor system and the explosion mechanism.

For the progenitor system, the two main evolutionary scenarios are: i) the single degenerate (SD) scenario, where the WD accretes material from a normal star; ii) the double degenerate (DD) scenario, where two WDs merge due to the loss of angular momentum caused by gravitational wave emission.

With regards to the explosion mechanism, C-deflagration in near-Chandrasekhar mass (near-M_{Ch}, M_{WD} $\sim$1.4 $M_{\odot}$) WD had been for long time considered as the favoured models for Type Ia SN explosions (Seitenzahl & Townsley 2017). These models were recently overcome by delayed-detonation models (i.e. initial C-deflagration followed by detonation) of near-M_{Ch} WD. Moreover, different evidences (e.g. Maoz et al. 2014; Kirby et al. 2019) suggest at least a fraction of Type Ia SN with sub-Chandrasekhar mass (sub-M_{Ch}, $0.8 \lesssim M_{WD}/M_{\odot} \lesssim 1.2$) progenitors is contributing to the whole population. For this subclass, double detonation models (i.e. initial He detonation in shell that triggers C

[4]the yields table are identical except for three models which show different ^{13}C and N values.

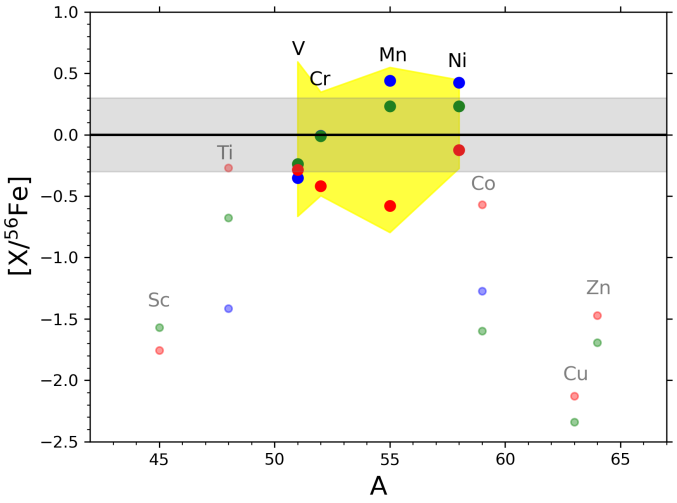

Figure 2.4: *Solar metallicity [X/^{56}Fe] Type Ia SN yields of most abundant stable isotope for Fe-peak elements. The yellow area cover the values spanned in the model tested in Palla (2021). Blue, green and red points indicate the yields a pure deflagration model, a delayed detonation model (from Leung & Nomoto 2018) and double detonation model (from Leung & Nomoto 2020a), respectively.*

detonation) were developed.

Type Ia SN systems are responsible for the production of the bulk of Fe, with both near-M_{Ch} and sub-M_{Ch} progenitors contributing with more than 0.5 $M_{\odot}$ of Fe per event. They are also very relevant for the production of other Fe-peak elements, for which instead a clear difference in the yields is seen for near-M_{Ch} and sub-M_{Ch} models. This can be seen in Fig. 2.4, especially for Mn and Ni. The contribution to α-elements is instead minor with respect to massive stars, even if Type Ia SNe are non negligibly contributing to some of these elements, such as Si, S, Ca.

During this Thesis, we mostly adopt the near-M_{Ch}, pure-deflagration model dubbed as W7 by Iwamoto et al. (1999). We show in Section 4.3 that the W7 model can still be safely adopted in chemical evolution models if the main goal of the study are not Fe-peak elements other than Fe itself, despite of being less physical than more recent Type Ia SN models. In fact, Fe yields are not particularly different from the most recent near-M_{Ch} and sub-M_{Ch} yields
However, in Section 4.3 we test the other yield sets of both near-M_{Ch} (Seitenzahl et al. 2013a; Fink et al. 2014; Leung & Nomoto 2018) and sub-M_{Ch} (Shen et al. 2018; Leung & Nomoto 2020a) channels to see their effects on chemical evolution models.

2.1.4 Gas flows

Gas flows in and out of galaxies are fundamental ingredients for studying the chemical evolution, since they are required to explain several important features in galaxies and galaxy clusters. In the subsequent paragraphs, we briefly discuss gas infall and outflows.

Gas infall

Since Oort (1970), the possibility of baryonic matter infalling onto spiral discs was supported by several observational evidences. Analyses of intermediate, high, and very high velocity clouds (IVC, HVC, VHVC) by means of UV, optical and radio measurements seem to rule out a local origin for these clouds, suggesting instead an intergalactic origin. On the other hand, it has also been suggested that HVCs and IVCs could be galactic fountains, i.e. gas expelled out of the disc by SN explosions which later falls back (Wakker & van Woerden 1997; Fraternali et al. 2015). The analysis of the chemical composition of all these clouds would be an important discriminant, but available data do not allow to draw firm conclusions.

From a theoretical point of view, gas infall was claimed as a natural consequence of a realistic galaxy formation process from extended haloes. Moreover, gas infall is the most promising solution to explain the G-dwarf problem in the solar vicinity (Chiappini et al. 1997). Infall is also desirable to prevent gas consumption in spiral discs, allowing them to form stars until the present day. Finally, infall of primordial gas is needed to explain significant presence of deuterium in the MW disc (Romano et al. 2006).

In chemical evolution models, we are forced to parametrise the infall rate because of the lack of a real dynamical treatment. Several parametrisations are adopted for the rate of infall in the the literature. In this Thesis, we adopt the exponentially decaying law:

$$\dot{\Sigma}_{inf}(t),\ \dot{M}_{inf}(t) \propto e^{-\frac{t}{\tau}} \tag{2.10}$$

where τ is the infall timescale, depending on the morphological type of galaxy we are dealing with. In particular, we have timescales of the order of 10 Gyr for late type galaxies (spiral discs, irregular galaxies), whereas for early type galaxies (elliptical galaxies) we adopt timescales of the order of 1 Gyr or less.
With regard to the chemical composition of the incoming flow, we normally assume a primordial composition (from Pitrou et al. 2018). However, in some cases we also consider the possibility of a metal enriched infall (see Section 4.2).

Gas outflow

Gas outflows or galactic winds are also likely to play a fundamental role in the evolution of galaxies, and their existence is indicated by several observational constraints. In

fact, outflows are observed in both local and high-redshift starbursts and irregular galaxies (Veilleux et al. 2005). At the same time, the chemical composition of the intra cluster medium (ICM) shows almost solar abundance for some heavy elements, indicating that galaxies in clusters should loose a substantial amount of their ISM (see Matteucci & Vettolani 1988) and especially of their SN ejecta (e.g. Martin et al. 2012).

Aside from AGN feedback driven wind (which treatment is out of the scope of this Thesis, see e.g. Fabian 2012 for a review), the main causes for galactic winds are SN explosions and (usually in minor part) stellar winds from massive stars. Part of SN blast energy ($\epsilon_0 = 10^{51}$ erg) is converted into thermal energy of the ISM, which can trigger gas outflows when the thermal content of the gas equals or is larger than its binding energy:

$$(E_{th})_{ISM} \geq (E_{bind})_{ISM}. \tag{2.11}$$

An important condition to satisfy Eq. (2.11) is that SNe should overlap in energy: second generation explosions happen in a hot, rarified medium, which allows a maximum thermal energy transfer to the ISM, since the radiation is proportional to the square of the gas density (see Matteucci 2012). On the other side, $(E_{bind})_{ISM}$ describes the potential well of the considered galaxy and therefore depends strongly on the DM amount and distribution (Matteucci 1992).
Concerning the chemical composition of the outflow, ordinary galactic wind abundances should reflect those of the ISM, since the metals produced and ejected by stars are normally well-mixed with the pre-existing medium. However, SN explosions can produce "chimneys" which eject outside the galaxy mostly the SN ejecta and hence more metal enriched material (e.g. Mac Low & Ferrara 1999). We refer to these winds as metal-enhanced or differential winds (see also Marconi et al. 1994).

As it happens for gas infall, galactic winds have to be parametrised because of the lack of dynamical treatment. Except for the specific MW models presented in Chapter 4 that do not include winds (see 4.1.1), in this Thesis we adopt two different wind parametrisations:

- a continuous wind rate proportional to the SFR:

  $$\dot{\Sigma}_{wind}(t),\ \dot{M}_{wind}(t) = \omega\,\psi(t), \tag{2.12}$$

  where ω is the wind mass loading factor, a free parameter regulating the wind efficiency. This parametrisation is adopted for the study of external irregular and spiral galaxies. The wind mass loading factor is chosen to reproduce the galaxy features and exhibits values between 0 and of the order of 1. We do not adopt any differential wind formulation, assuming an equal ω for all chemical elements;

- a sudden wind occurring when Eq. (2.11) condition is satisfied and all the gas present is lost, making the galaxy to evolve passively. This formulation is devoted to the study of elliptical and high-redshift starburst galaxies.

For the DM halo, we assume a diffuse ($R_e/R_{DM} = 0.1$, where R_e is the effective radius of the galaxy while R_{DM} the radius of the DM core) and massive ($M_{DM}/M_{lum} = 10$, with M_{DM} the dark matter mass and M_{lum} the mass set for the galaxy in a model, i.e. the infall mass) DM halo for all galaxies, accordingly to previous studies (e.g. Pipino & Matteucci 2004; Grieco et al. 2014; De Masi et al. 2018).

2.2 Chemical evolution equations

Having described the fundamental ingredients, we need now to write a set of equations describing the evolution of the gas and its chemical abundances which include all these ingredients. These equations describe the temporal variation of the gas content and its abundances by mass.

Analytical models need to adopt the instantaneous recycling approximation (IRA, Tinsley 1980), in which all the stars with mass $m \geq 1$ $M_\odot$ die instantaneously while all the stars with mass $m < 1$ $M_\odot$ live forever. These models fail in reproducing a large number of observational constraints: in particular, they are unable to follow the observed trend of [X/Fe] abundance ratios as functions of [Fe/H], which is not constant as they predict. For this reason, in this Thesis we drop the IRA and solve the complete set of integro-differential equations of chemical evolution, taking into account stellar lifetimes.

Let us define $G(t)$ as the surface mass density/mass at the time t in the ISM normalized to the infall surface mass density/mass[5] :

$$G(t) = \frac{\Sigma_{ISM}(t)}{\Sigma_{inf}(t_f)} = \frac{M_{ISM}(t)}{M_{inf}(t_f)}. \tag{2.13}$$

In this way, we can describe $G_i(t)$ as the normalized surface mass density/mass of the element i at a time t:

$$G_i(t) = G(t)X_i(t). \tag{2.14}$$

Here, the quantity $X_i(t)$ represents the abundance fraction in mass of a given element i, with the summation over all elements in the gas mixture being equal to unity.
In this way, the evolution of an element i can be described by this expression (Matteucci 2001, 2012):

$$\dot{G}_i(t) = -\psi(t)X_i(t) + R_i(t) + \dot{G}_{i,inf}(t) - \dot{G}_{i,w}(t), \tag{2.15}$$

where the terms on the right hand side can be summarized in this way:

- $\psi(t)X_i(t)$ represents the rate at which the element i is removed by the ISM due to SF process;
- $R_i(t)$ is the rate at which the element i is restored into the ISM from stars. Within this term the particular nucleosynthesis prescriptions of the specific element i are taken into account (for a better description, see 2.2.1);
- $\dot{G}_{i,inf}$ is the rate of gas infall of the i-th element;
- $\dot{G}_{i,w}$ refers to the outflow rate of the element i, caused by galactic winds.

In what follows, we focus on the $R_i(t)$ term, which is the core of Eq. (2.15).

[5] total surface mass density/mass accreted to the galaxy at the present time t_f.

2.2.1 Element processing in stars

$R_i(t)$ represent the rate of restitution of matter from the stars into the ISM in the form of the element i. This term takes into account the nucleosynthesis prescriptions for the i-th element together with the models for progenitors of dying stars.

As shown in Matteucci & Greggio (1986), $R_i(t)$ takes the following form:

$$\begin{aligned} R_i(t) = & \int_{M_L}^{M_{Bm}} \psi(t-\tau_m)\, Q_{mi}(t-\tau_m)\, \varphi(m)\, dm + \\ + A_{Ia} & \int_{M_{Bm}}^{M_{BM}} \varphi(m) \left[\int_{\mu_{min}}^{0.5} f(\mu)\, \psi(t-\tau_{m2})\, Q_{mi}(t-\tau_{m2})\, d\mu \right] dm + \\ & + (1-A_{Ia}) \int_{M_{Bm}}^{M_{BM}} \psi(t-\tau_m)\, Q_{mi}(t-\tau_m)\, \varphi(m)\, dm + \\ & + \int_{M_{BM}}^{M_U} \psi(t-\tau_m)\, Q_{mi}(t-\tau_m)\, \varphi(m)\, dm. \end{aligned} \tag{2.16}$$

Here, $Q_{mi}(t-\tau_m)$ contains all the information about stellar nucleosynthesis of a star of mass m dying at the time t. In fact, $Q_{mi}(t-\tau_m)$ corresponds to $\sum_j Q_{mij}(m) X_j(t-\tau_m)$, where Q_{mij} corresponds to the element production matrix (Talbot & Arnett 1971). This matrix takes into account both newly formed (originating from elements $j \neq i$) and pre-existing elements in a star of initial mass m, while $X_j(t-\tau_m)$ represents the abundance of the element j in the star at its birth.
τ_m is the function which describes stellar lifetime as functions of stellar mass. It allows to integrate in m Eq. (2.16), thus resulting fundamental in the computation of the integro-differential chemical evolution equation. Throughout this Thesis, we adopt the two relations suggested by Schaller et al. (1992) and Kodama (1997), which show very similar behaviours (see Romano et al. 2005).

Concening the four integrals in Eq. (2.16), we now list their meanings:

- the first integral refers to single stars in the mass interval $[M_L, M_{Bm}]$, namely stars dying as CO WDs. M_L represents the minimum mass of dying stars at a certain time t (for $t \simeq 14$ Gyr, $M_L \simeq 0.8$ $M_\odot$). M_{Bm} is the minimum mass for binary systems giving rise to a Type Ia SN: in our calculations we adopt $M_{Bm} = 3 M_\odot$, after Matteucci & Greggio (1986);
- the second term refers to Type Ia SNe. In this formulation, we consider the binary system as a unique star with the mass given by the sum of the primary and secondary star. The two extremes of the integral are M_{Bm} and M_{BM}, with $M_{BM} = 16$ $M_\odot$,

requiring that the mass of each component cannot exceed $m = 8\mathrm{M}_{\odot}$ (i.e. the upper mass limit for a star to end its life as a WD).
In Eq. (2.16) the Type Ia SN rate is calculated by assuming a SD scenario (Matteucci & Recchi 2001). In this framework, a second internal integral in the variable $\mu = m_2/m_B$, namely the ratio between the mass of the secondary component (m_2) and the total mass of the binary (m_B), is computed. The integral goes from μ_{min} (i.e. the minimum mass fraction producing to the Type Ia SN at the time t) and 0.5 and contains the distribution function of the secondary mass fraction, $f(\mu)$:

$$f(\mu) = 2^{1+\gamma}(1+\gamma)\mu^{\gamma}, \tag{2.17}$$

where $\gamma = 2$ in order to favour μ values towards 0.5 (see Matteucci & Recchi 2001 for more details).
Outside of the integrals, the constant A_{Ia} is a free parameter representing the fraction of binary systems able to produce a Type Ia SN and it is set to reproduce the observed rate of Type Ia SNe in different galaxies. As can be seen in Eq. (2.16), in the SD formalism the clock for the explosion is given by the lifetime of the secondary star (τ_{m_2});

- the third integral represents the enrichment given by stars in the range $[M_{Bm}, M_{BM}]$ which do not produce Type Ia SNe . They can be either LIMS that end their lives as WDs or, if $m > 8$ $\mathrm{M}_{\odot}$, CC-SNe;
- The last integral term refers to stars more massive than M_{BM}: all these stars end their lives as CC-SNe. In our models, we assume an upper mass limit for stars contributing to the chemical evolution M_U, in agreement with the adopted IMF.

It is worth noting that in the adopted formulation we assume that all Type Ia SNe systems come from the SD scenario. However, as noted in 2.1.3, not all Type Ia SN systems explode through this channel: for this reason, different formulations for the delay time distribution (DTD) have been proposed in the past years, derived either from theoretical principles (e.g. Greggio 2005) or observations (e.g. Totani et al. 2008).
In Matteucci et al. (2009) it has been shown that the adopted SD DTD by Matteucci & Recchi (2001) is very similar to that related to the DD scenario of Greggio (2005). The same happens for observationally inferred $t^{\sim -1}$ DTDs (e.g. Totani et al. 2008; Maoz & Graur 2017). In fact, Totani et al. (2008) showed that a t^{-1} DTD is very similar to that of Greggio (2005).
For this reason, even though the Matteucci & Recchi (2001) DTD is only representative of the SD scenario, it can be considered an acceptable compromise to describe the delayed pollution from the entire Type Ia SN population.

2.3 Basic ingredients for dust evolution models

In addition to the basic ingredients for chemical evolution (see Section 2.1), dust modelling requires few other fundamental building blocks. In particular, we need to take into account:

1. stellar dust production, i.e. dust yields;
2. dust processing in the ISM, i.e. dust growth and destruction.

In the next Subsections we look at these points in more detail.

2.3.1 Dust yields

AGB stars and SN explosions are fundamental players in the building up of dust mass and represent the first environments where dust form. Depending on the physical structure of the progenitor (type of star, mass, metallicity), different dust amounts and species can originate.

In the following, we discuss the yields of dust by AGB stars, CC-SNe and Type Ia SNe in the context of the most recent studies in the literature.

Dust from AGB stars

The amount of dust produced during most of the lifetime of LIMS is negligible: the low amount of material in their ejecta and the physical conditions of their winds do not favor dust formation (Gail et al. 2009). Hence, the formation of dust in LIMS can be restricted to the final stages of their evolution and in particular to the AGB phase. In fact, the cold envelope of AGB stars is a good environment to allow nucleation and formation of the first dust-seeds, which can then escape from the star by means of a dust-driven wind (Höfner & Olofsson 2018).
The dust species formed during the AGB-phase strongly depend on the surface composition of the star during this evolutionary phase (Ferrarotti & Gail 2006) and in particular on their C/O ratio (Nanni et al. 2013). The surface composition is determined by the interplay of complex physical processes which critically depend on the stellar mass and the metallicity of the star (e.g. Ventura et al. 2012; Nanni et al. 2013; Dell'Agli et al. 2017).

In Fig. 2.5, we show the masses of dust and the main species produced in AGB models by Dell'Agli et al. (2017) for different stellar masses and metallicities. For masses below 3-4 $M_{\odot}$ carbon dust is mostly produced, since the third dredge-up (TDU) brings some of the C processed in the internal layers to the stellar surface, favouring high C/O ratios and hence a lot of carbon dust seeds. On the other hand, silicates are mostly produced by massive AGB stars. The minor production of carbon dust is caused by the activation of the hot bottom burning (HBB) process, in which the CNO cycle is activated at the base of the convective envelope, thus decreasing the number of ^{12}C nuclei and favouring lower

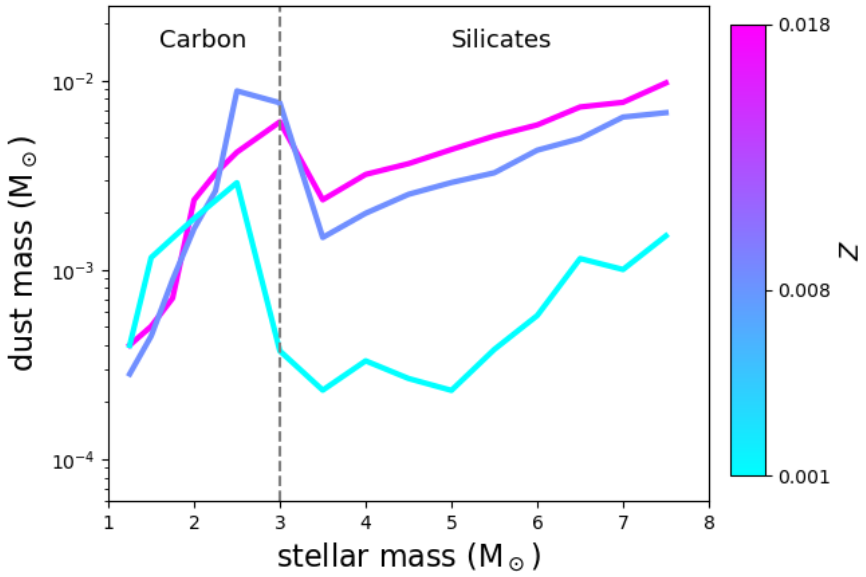

Figure 2.5: *Mass of dust produced by AGB models by Dell'Agli et al. (2017) at various metallicities. The colorbar indicates the metallicity Z of the model. The thin, dashed line separates models producing mostly silicates from those producing carbon-dust.*

surface C/O ratios (Nanni et al. 2021).
Another difference between low-mass and high-mass AGB dust is the metallicity dependence on the dust mass. This is also the effect of the different surface composition. For low-masses, the C condensed into dust is primary[6] and thus no previously formed seeds are needed to form dust, resulting in rather similar dust yields for different metallicities. For masses above 3-4 $M_{\odot}$ instead, the low surface C abundance and the lower yields for elements heavier than C (see Romano et al. 2010) indicate that metals already in place are needed to produce dust.

To account for all these effects on AGB dust production, in this Thesis we adopt the mass and metallicity dependent dust yields by Piovan et al. (2011) and Dell'Agli et al. (2017).

Dust from CC-SNe

Massive stars and CC-SNe have been known to produce dust for a long time (e.g. Cernuschi et al. 1967; Hoyle & Wickramasinghe 1970; Clayton 1979; Danziger et al. 1991).

[6] a primary element is directly synthetised from H and He. A secondary element needs metal seeds in the star to be produced.

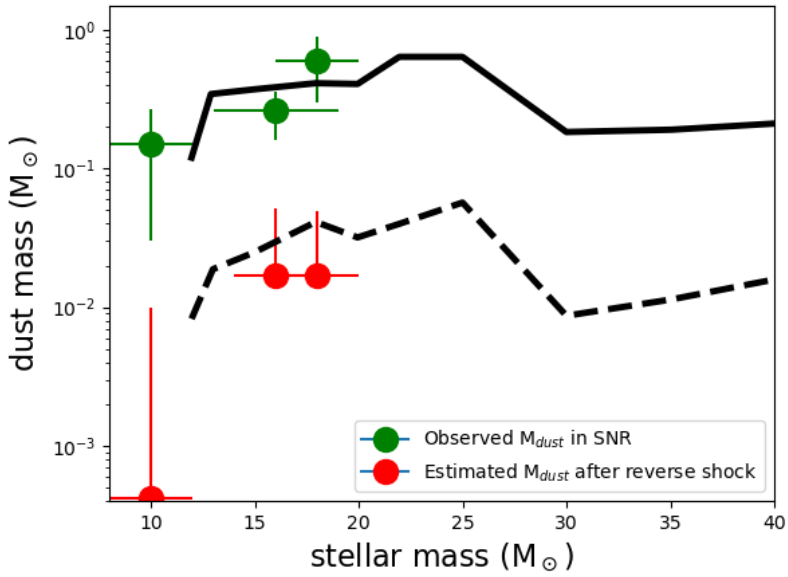

Figure 2.6: *Total dust masses produced by Type II SN models by Bianchi & Schneider (2007) with (dashed line) and without reverse shock (solid line) compared to observed cold dust masses in SN remnants (green points) and models for individual SN remnants after the reverse shock passage. Data are from Gomez et al. (2012); Temim & Dwek (2013) (Crab), Matsuura et al. (2011); Indebetouw et al. (2014) (SN 1987A) and De Looze et al. (2017) (Cas A). Models for individual remnants are taken from Bocchio et al. (2016).*

CC-SNe are believed to be prolific dust factories. For instance, the large dust masses found in high-redshift QSO hosts (e.g. Michałowski et al. 2010; Marrone et al. 2018) and some high-redshift star forming galaxies (e.g. Laporte et al. 2017; Tamura et al. 2019) can be explained by sources able to inject large amounts of dust in much less than 1 Gyr of cosmic evolution. These timescales are in agreement with the typical timescales of SNe, suggesting these sources as valuable candidates for the production of the observed dust masses (with several indications of subdominant AGB contribution, see e.g. Schneider et al. 2015).

However, we are far from having a clear picture on the exact mass of dust ejected from these SNe. Despite the large number of measurments made in the past, there are still only a few accurate estimations of dust masses in SNe and SN remnants (SNRs, e.g. Matsuura et al. 2011; Gomez et al. 2012; De Looze et al. 2017).

Moreover, it is still unknown what is the real effect of the SN reverse shock, which can destroy much of the dust produced in the same SN explosion. In fact, this shock has a typical timescale of 10^4-10^5 yr, much longer than the lifetime of the historical SNe (e.g.

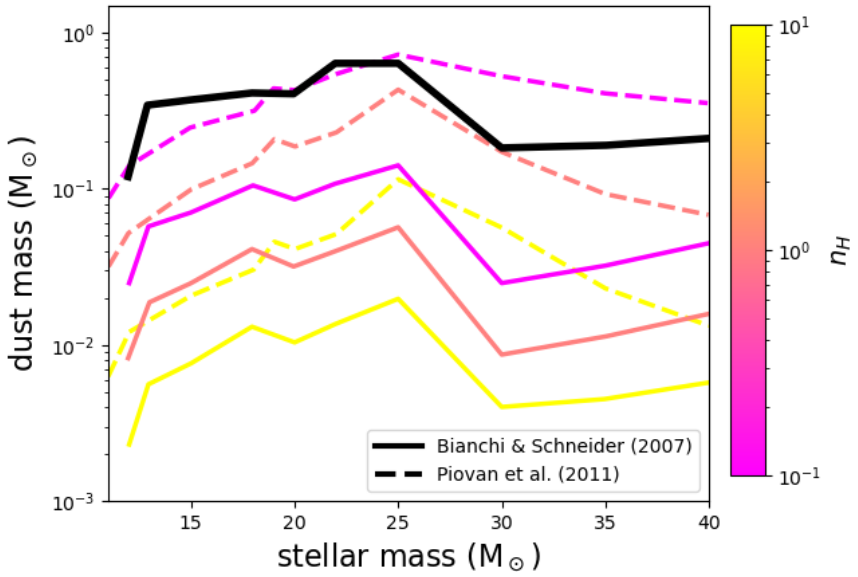

Figure 2.7: *Total dust masses produced by Type II SN models including the reverse shock mechanism by Bianchi & Schneider (2007) (solid lines) and Piovan et al. (2011) (dashed lines) as function of stellar mass. The colorbar indicates the ambient density in which the SN reverse shock develops. The black line represent the Bianchi & Schneider (2007) without reverse shock.*

Bianchi & Schneider 2007).

In Fig. 2.6, we show the detected dust mass in SNe and SNRs (green points) compared with the predictions of the final dust mass in these SNRs after the reverse shock passage (red points). The range of dust masses varies between $\sim$0.5 $M_\odot$ and $\lesssim$0.01 $M_\odot$ and reflects the variations in the models by Bianchi & Schneider (2007) without and with reverse shock.

On the other hand, the dust destruction rates in reverse shocks depend on many factors, such as: i) the ambient density, ii) the assumed destruction mechanisms, iii) the morphology of the SNR and surrounding material, iv) the dust grain size distribution in the input model. This leads to very different survival rates, from much more than 50% to much less than 10% (see Gall & Hjorth 2018 for a review).

In order to account for these uncertainties, in this Thesis we adopt either models with or without the reverse shock mechanism. In the case of the reverse shock, we test the impact of different ambient densities n_H, between 0.1 and 10 cm^{-3}: the lower the density, the higher the dust survival rate. This is clearly seen in Fig. 2.7, where we show the dust masses produced by CC-SNe by the SN dust models adopted in this work, i.e. Bianchi &

Schneider (2007) and Piovan et al. (2011) (solid and dashed lines, respectively).

Dust from Type Ia SNe

Type Ia SNe have been considered as contributors to dust enrichment of the ISM on theoretical bases in past chemical evolution models including dust treatment (e.g. Dwek 1998; Calura et al. 2008; Zhukovska et al. 2008), where Fe dust yields from these sources were considered.
However, during the last decade, observational data and theoretical studies have progressively changed the role of Type Ia SN dust production. The search for newly-formed dust in Type Ia SNRs has been performed by *Spitzer* and *Herschel* satellites, but most of the observations do not detect any newly formed dust, attributing the IR emission to shocked interstellar dust (Blair et al. 2007; Williams et al. 2012; Gomez et al. 2012). Also from a theoretical point of view, net dust production by Type Ia SNe is unlikely: in the context of the W7 model for Type Ia SNe, Nozawa et al. (2011) predicted that the dust formed in the explosions is destroyed before it can be injected into the ISM.

For the reasons explained above, in this Thesis we generally assume that Type Ia SNe are not producing dust, as already done in other recent works (e.g. Gioannini et al. 2017a,b). However, we make an exception on this assumption in Section 3.3, where we allow Type Ia SN producing dust in some galaxies. The reason of such an unrealistic assumption is to put an extreme upper limit to dust mass contribution in these galaxies.

2.3.2 Dust processing in the interstellar medium

Dust is not only produced by stars, but experiences several processes in the ISM that change its mass and the dimension of the grains, giving rise to the so-called "dust cycle" (see Section 1.2). On the one hand, processes are either acting in increasing the dust mass (dust growth/accretion, e.g. Savage & Sembach 1996) or cycling dust back to the ISM gas (dust destruction, e.g. McKee 1989). At the same time, other mechanisms affect the grain size distribution, increasing (coagulation of grains, e.g. Chokshi et al. 1993) or decreasing (shattering of grains, e.g. Biermann & Harwit 1980) dust grain dimensions.
Here we consider only the evolution of the total amount of dust and its chemical composition during the cosmic time. Hence, in this work we do not take into account all the processes affecting the grain-size distribution.

In what follows, we describe in detail the different events responsible for dust accretion and destruction, introducing the formalism adopted in the models for dust evolution.

Dust accretion

During galactic evolution, dust grains in the ISM can grow in mass and size owing to the accretion of metal particles in the gas onto the surface of the grains. This process occurs mostly in the coldest and densest regions of the ISM, i.e. in molecular clouds, and has the effect of increasing the global amount of interstellar dust.
For this reason, dust accretion is believed to be a fundamental ingredient in dust chemical evolution both in the local Universe and at high redshift, as pointed out by many studies (e.g. Dwek 1998; Hirashita & Kuo 2011; Asano et al. 2013; Mancini et al. 2015; Ginolfi et al. 2018). In particular, grain growth in the ISM is required to explain the large observed depletion rates of Fe, since the main producers of this element (Type Ia SNe) do not seem to contribute to dust production (e.g. Nittler et al. 2018).

Since the pioneering work of Dwek (1998), the dust growth has been treated in terms of a typical accretion timescale τ_{accr}:

$$\dot{M}_{dust,accr} = \frac{M_{dust}}{\tau_{accr}}. \tag{2.18}$$

To find this timescale, we should consider the conditions in which accretion takes place. Since more efficient accretion happens in cold dense regions of the ISM, the higher the mass of ISM within molecular clouds, the higher the rate of dust accretion. At the same time, the higher the fraction of metals in dust in the ISM the less the gas available to be accreted. Moreover, τ_{accr} has to take into account the characteristic growth timescale within a cloud, which depends on the physical conditions found in these regions and on the typical dust grains dimension (Asano et al. 2013).

In this Thesis, we consider all these ingredients by adopting well-tested prescriptions from the literature (Hirashita 2000; Asano et al. 2013), already adopted in chemical evolution models by Gioannini et al. (2017a,b).

Dust destruction

Dust grains do not only grow, but also experience destruction in the ISM. Thermal sputtering, evaporation in grain-grain collision, thermal sublimation, or desorption are some examples of the various dust destruction processes. However, the most important mechanism for cycling dust back to the gas phase resides in the sputtering of the ISM in high velocity SN forward shocks (Dwek & Scalo 1980; McKee 1989; Jones et al. 1994). Ongoing dust destruction of swept-up ISM dust grains has in fact been observed in several SNRs (e.g. Arendt et al. 2010; Dopita et al. 2016).

Similarly to what is assumed for dust accretion, chemical evolution models express the

dust destruction in terms of a typical timescale for grain destruction τ_{destr}:

$$\dot{M}_{dust,destr} = \frac{M_{dust}}{\tau_{destr}}. \tag{2.19}$$

Since only SNe are considered to be able to destroy grains, the timescale will be inversely proportional to the total SN rate (here including both CC and Type Ia SNe). At the same time, the amount of dust destroyed by a SN shock depends on the mass swept by the shock itself and on the efficiency of grain destruction by this mechanism.
The product of these two latter values depends on the physical conditions of the ISM, such as the temperature and the density of the medium (McKee 1989; Zhukovska et al. 2008). In this scenario, the ISM metallicity plays a role in setting the destruction timescale: for higher metallicities, the line cooling of metals is more efficient, leading to a lower temperature and higher density and thus limiting the amount of swept gas (Asano et al. 2013).

For this reason, in this Thesis we take advantage of the detailed, metallicity dependent, prescriptions by Asano et al. (2013), previously tested by the works of Gioannini et al. (2017a,b).

2.4 Dust evolution equations

In this Thesis, we use the same approach first used by Dwek (1998) and Calura et al. (2008) and later adopted by Grieco et al. (2014) and Gioannini et al. (2017a). The equation for the dust evolution is similar to Eq. (2.15), but it includes other terms describing all the physical processes changing the mass distribution of dust in the ISM, besides dust production by stars. By defining:

$$G_{i,dust} = G(t)X_{i,dust}(t) \tag{2.20}$$

as the normalized mass of the element i at the time t in the dust phase, with $X_{i,dust}$ as the dust mass fraction of the element i, we can write:

$$\begin{aligned}\dot{G}_{i,dust} = -\psi(t)X_{i,dust}(t) + R_{i,dust}(t) + \dot{G}_{i,dust,accr}(t) + \\ -\dot{G}_{i,dust,destr}(t) - \dot{G}_{i,dust,w}(t).\end{aligned} \tag{2.21}$$

We note in Eq. (2.21) the absence of the infall term: the assumption of no dust infall is naturally explained by the usual primordial composition for infall in the models and that dust is composed by metals.
As said above, the dust evolution equation considers all the processes governing the "dust cycle" for a given element. We now summarize Eq. (2.21) right hand side terms meaning:

- $\psi(t)X_{i,dust}(t)$ concerns the process of dust astration, i.e. the process of removal of dust from the ISM by star formation;
- $R_{i,dust}(t)$ is the rate at which the element i is restored into the ISM from stars in the dust phase. The term is also called dust production rate (DPR);
- $\dot{G}_{i,dust,accr}$ refers to the dust accretion rate (DAR) for the element i, i.e. dust mass enhancement due to grain growth by accretion processes in the ISM;
- $\dot{G}_{i,dust,destr}$ is the dust destruction rate (DDR) for the i-th element, namely the rate of dust mass decrease by SN forward shock destruction;
- $\dot{G}_{i,dust,w}$ indicates the rate of dust in the form of element i expelled by galactic winds. In our models, we assume a coupling between ISM dust and gas, assuming the same mass loading factor ω for the gas and dust models.

In what follows, we focus on the three terms regulating the dust cycle, i.e. the dust production, accretion and destruction rates.

2.4.1 Dust production rate

$R_{i,dust}(t)$ represents the rate of dust production of a given element i by stellar sources at a certain time t. In the context of Eq. (2.21), it takes the following form:

$$\begin{aligned} R_{i,dust}(t) = & \int_{M_L}^{M_{Bm}} \psi(t-\tau_m)\delta_i^{AGB} Q_{mi}(t-\tau_m)\varphi(m)\,dm + \\ & + A_{Ia}\int_{M_{Bm}}^{M_{BM}} \varphi(m)\left[\int_{\mu_{min}}^{0.5} f(\mu)\,\psi(t-\tau_{m2})\,\delta_i^{Ia} Q_{mi}(t-\tau_{m2})\,d\mu\right] dm + \\ & + (1-A)\int_{M_{Bm}}^{8M_\odot} \psi(t-\tau_m)\delta_i^{AGB} Q_{mi}(t-\tau_m)\varphi(m)\,dm + \\ & + (1-A)\int_{8M_\odot}^{M_{BM}} \psi(t-\tau_m)\delta_i^{CC} Q_{mi}(t-\tau_m)\varphi(m)\,dm + \\ & + \int_{M_{BM}}^{M_U} \psi(t-\tau_m)\delta_i^{CC} Q_{mi}(t-\tau_m)\varphi(m)\,dm. \end{aligned} \tag{2.22}$$

Recalling Eq. (2.16), we note that the above expression is very similar, but with some crucial differences. The terms δ_i^{AGB}, δ_i^{Ia} and δ_i^{CC} are added relative to Eq. (2.16). These δ terms are the condensation efficiencies, namely the fraction of the element i expelled by stars (AGB, Type Ia and CC-SNe) which goes into the ISM in the dust phase. Combined with $Q_{mi}(t-\tau_m)$, they give the dust yields as described in the previous Section (Bianchi & Schneider 2007; Piovan et al. 2011; Dell'Agli et al. 2017), which depend on the mass and the metallicity of the progenitor star. The adoption of such literature values represents a big step forward relative to older model prescriptions (Dwek 1998; Calura et al. 2008), in which δ values were arbitrary and based on very simple assumptions.
It is also worth reminding that we generally set to zero the condensation efficiencies by Type Ia SNe, except for some special cases in Section 3.3. In the case we set $\delta_i^{Ia} = 0$, the term describing the dust output by Type Ia SNe can be totally neglected.

2.4.2 Dust accretion and destruction rates

As already mentioned in 2.3.2, the terms describing the rates of dust accretion and destruction of a given element i in the ISM can be written in terms of typical timescales.

For the DAR (Eq. (2.18)), we have $\tau_{i,accr}$ as the typical timescale of accretion for the i-th element in the dust phase. For this term, we adopt the formalism introduced by Hirashita (2000):

$$\tau_{i,accr} = \frac{\tau_g}{X_{cl}(1-f_i)}. \tag{2.23}$$

where X_{cl} is the mass fraction of dense cold clouds in a galaxy and $f_i = G_{i,dust}/G_i$ the dust-to-gas ratio (DGR) for the i-th element. We set X_{cl} increasing from irregular to spiral and spheroidal galaxies, according to the increasing star formation efficiency (and hence the presence of cold gas available for star formation) in these galaxy types. Concerning the characteristic dust growth timescale within a molecular cloud τ_g, we take the expression from Asano et al. (2013):

$$\tau_g = 2.0 \cdot 10^7 \times \left[\frac{a}{0.1\mu m} \cdot \left(\frac{n_H}{100 cm^{-3}} \right)^{-1} \cdot \left(\frac{T}{50K} \right)^{-1/2} \cdot \left(\frac{Z}{0.02} \right)^{-1} \right] [\mathrm{yr}], \quad (2.24)$$

which allows us to link τ_g with the metallicity Z. To reproduce the physical conditions encountered in molecular clouds as well as the properties of typical dust grains, the physical parameters in Eq. (2.24) are set to $T = 50$ K for the temperature, $n_H = 100$ cm^{-3} for the cloud density and $a = 0.1$ μm for the typical size of grains.

For the DDR (Eq. (2.19)), τ_{destr} is the typical timescale of dust destruction. For the computation of this timescale, we rely on the expression reported by Calura et al. (2008) describing the relation of $\tau_{i,destr}$ with the SN rate:

$$\tau_{destr} = \frac{M_{ISM}}{(\epsilon \cdot M_{swept}) SN_{rate}}, \quad (2.25)$$

where M_{swept} is the ISM mass swept and ϵ is the efficiency of grain destruction in the ISM by a SN shock. For these terms, we adopt the values proposed by Asano et al. (2013), in which it was suggested a destruction efficiency $\epsilon = 0.1$ and a swept mass by the SN shock decreasing with metallicity (see 2.3.2):

$$M_{swept} = 1535 \cdot n^{-0.202} \cdot (Z/Z_\odot + 0.039)^{-0.289} [\mathrm{M}_\odot], \quad (2.26)$$

where we assume $n = 1$ cm^{-3} as the ISM density surrounding the SN environment. Although different densities are expected in different galactic environments, we decide to keep this value fixed, since order of magnitude variations in n provide much less than factor 2 differences in M_{swept}.

CHAPTER 3

Elements and dust through cosmic evolution

THE UNIVERSE is made of billions of galaxies that show different morphological properties, which correspond to different stars and gas content.
Therefore, it is of great interest to study the process of galaxy evolution in different systems. Apart from the Milky Way (MW) and few other galaxies of the Local Group, this can be done by looking at distant galaxies, that probe the Universe up to its earliest times. However, one of the main issues in studying these systems is that one needs to account for the presence of interstellar dust, which deeply influences our view of the distant universe.

Therefore, in this Chapter we focus on the study of intermediate and high-redshift systems by means of chemical evolution model including dust. First, we describe the basic constraints for chemical and dust evolution models in different types of galaxies. Then, we focus on high-redshift starburst galaxies, i.e. extreme systems with very high star formation rates: in particular, we analyse the complex interplay between the initial mass function and dust in these objects. The results presented here are also described in the published paper Palla et al. (2020a). Finally, we concentrate on a much larger spatial scale: in particular, we study the evolution of dust masses and dust-to-gas ratios in galaxy clusters volumes. The obtained results have been published in a refereed paper by Gjergo, Palla et al. (2020).

3.1 Modelling chemical evolution and dust in different galaxies

As mentioned in 1.3.1, at the time of discovery of external galaxies in the early 20^{th} century, it was already clear that these show a different morphological structure (Hubble 1926). In particular, the galaxy population can be divided into three main groups, i.e. i) spheroids/elliptical galaxies, ii) spiral galaxies and iii) irregular galaxies. Since then, further photometric and spectroscopic observations allowed us to understand that these differences in morphology correspond to variations in their stellar populations (age and metallicity) as well as in their gas content.
It is now widely accepted that the variations of the gas and the stellar content between these galaxies, with progressively older, metal rich stellar populations and lower gas content from irregulars to spheroids/ellipticals, are driven by the different star formation history (SFH) experienced by the galaxies. In fact, star formation (SF) has a central role in the formation and in the evolution of galaxies (Matteucci 2001; Pagel 2009; Matteucci 2012).

Therefore, we have to develop different chemical evolution models for different galactic morphological types, in order to follow the different SFH experienced by the different galaxies. However, as seen in 1.3.2, interstellar dust deeply influences our view of the distant universe (e.g. Hauser & Dwek 2001) by affecting the chemical abundances we are collecting for these objects.
Hence, dust evolution must be taken into account to properly trace these objects. This can be used either for computing global dust quantities, such as dust masses and dust-to-gas ratios in galaxies, as well as to predict the evolution of chemical abundances in the gas phase only, which may suffer by dust depletion.

In the following, we describe the main parameters of models meant to follow both chemical and dust evolution of galaxies of different morphological type. The set up is chosen to reproduce the most important observables about the SFH (e.g. star formation and supernova rates, gas fraction) and dust evolution (e.g. dust-to-gas ratios, total dust masses). In this Section we also compare the predictions of the models with relevant data from the literature.

3.1.1 Chemical evolution parameters

We adopt specific chemical evolution models for the different galaxy types (i.e. irregular, spirals, spheroids/ellipticals) in order to reproduce the major observational constraints for the different objects.

All the models developed in this Chapter drop the instantaneous recycling approximation and assume that galaxies formed by primordial gas infall which accumulates into a preexisting dark matter halo on different timescales and evolve suffering galactic winds.

Table 3.1: *Input parameters for typical reference chemical evolution models adopted for galaxies of different morphological type.*

Model	$M_{inf}(\mathrm{M}_\odot)$	$\tau_{inf}(\mathrm{Gyr})$	$\nu(\mathrm{Gyr}^{-1})$	ω
Irregular (I)	5×10^9	10	0.1	0.5
Spiral (Sp)	5×10^{10}	7	1	0.2
Spheroid (E)	10^{11}	0.3	15	-$^{(1)}$

Notes: $^{(1)}$ adopted the "sudden wind" formulation (see 2.1.4).

The main differences among the models for different galaxy types are the assumed star formation efficiency (SFE, see Eq. (2.4)), the timescale for gas infall (see Eq. (2.10)), which determine the history of star formation, i.e. the main driver of galaxy evolution, the wind mass loading factor (see Eq. (2.12)) and the infall mass.
We start our work by building reference models for typical galaxies of each morphological type. In this way, we are confident of adopting realistic models for each galaxy morphology and to be able to follow the galaxy evolution of each type since the beginning and until the present time. In Tab. 3.1 the basic assumptions (galaxy mass, infall timescale, SFE, galactic wind parameter) are shown for the reference models. We adopt the same IMF (an extrapolation of Salpeter 1955, see 2.1.2) for all these reference models and focus only on variations in the above mentioned parameters.

In Fig. 3.1, we show the variation in the star formation rate (SFR, upper panel), gas fraction (M_{gas}/M_{tot}, central panel) and metallicity relative to the solar value ($\mathrm{Z/Z}_\odot$, lower panel) for these reference chemical evolution models.
We see in Fig. 3.1 upper panel that for the spheroidal/elliptical galaxy model we have a very high initial SFR ($\gtrsim 100$ $\mathrm{M}_\odot$ yr^{-1}). This burst of star formation drives a very fast build-up of metals (Fig. 3.1 lower panel) that reaches supersolar values within few 0.1 Gyr (see also, e.g. Calura et al. 2014). The burst is then followed by an abrupt decline due to the occurrence of a galactic wind, which devoids the galaxy of the gas residual from star formation (Fig. 3.1 central panel). This wind occurs approximately 1 Gyr after the beginning of star formation: this is a good approximation for elliptical galaxies, as real early-type galaxies have less than 1 per cent of their stellar population younger than 3 Gyr (Salvador-Rusiñol et al. 2019), and ensures to reproduce several observational constraints of local ellipticals (e.g. Matteucci 1994; Pipino & Matteucci 2004). In the case of the spiral and irregular galaxies, instead, star formation lasts until the present time, with progressively lower SFR values, higher gas fractions and slower metals build-up in the ISM gas from spirals to irregulars. As it can be seen in Fig. 3.1 upper panel, we check that the present time absolute SFRs for the reference spiral and irregular galaxy models do reproduce the values found for the MW disc ($SFR_{MW} = 1.9 \pm 0.4$ $\mathrm{M}_\odot$ yr^{-1}, Chomiuk & Povich 2011) and the Small Magellanic Cloud (SMC, $SFR_{SMC} = 0.053^{+0.03}_{-0.02}$ $\mathrm{M}_\odot$ yr^{-1}, Rubele et al. 2015), which are two typical examples of a spiral disc and an irregular galaxy. More-

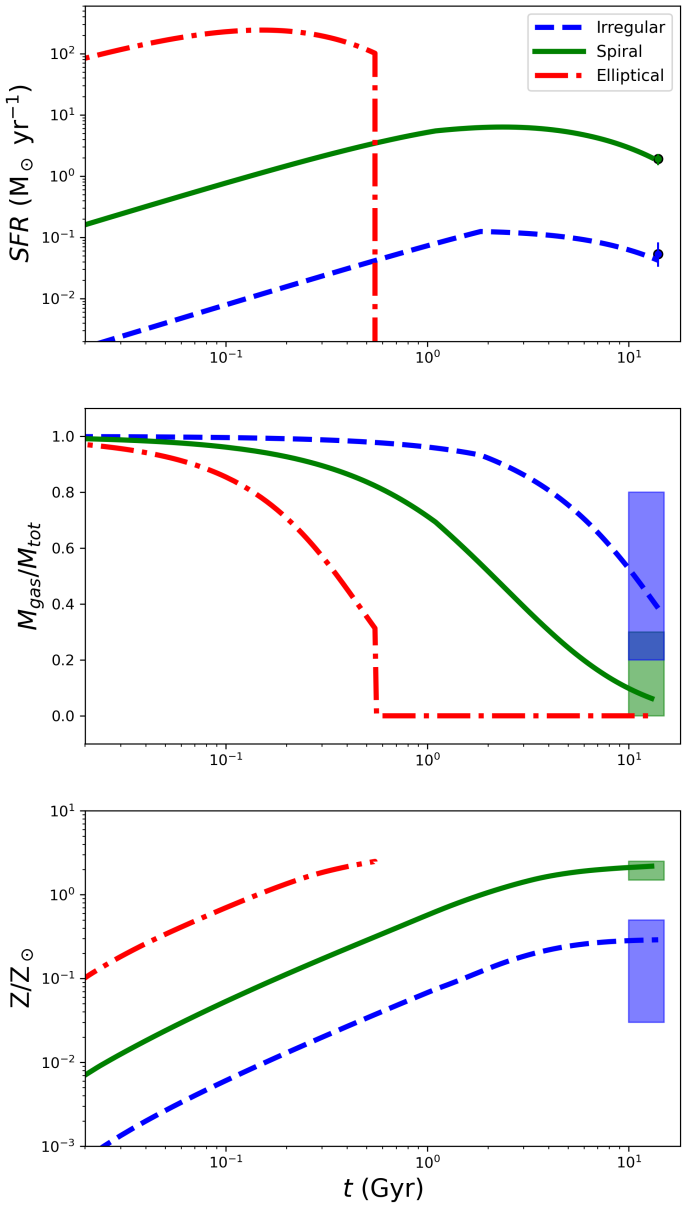

Figure 3.1: *SFR (upper panel), gas fraction (middle panel) and metallicity (lower panel) as function of evolutionary time for typical models of different galaxy types. Present time SFR data are taken from Chomiuk & Povich (2011) (green point) and Rubele et al. (2015) (blue point) for the Galaxy disc and for the Small Magellanic Cloud, respectively. Observed present day gas fraction and metallicity (normalised to Asplund et al. 2009) are taken from Grieco (2015).*

Table 3.2: *Ranges of input parameters explored for the chemical evolution models for galaxies of different morphological types.*

Models	$M_{inf}(\mathrm{M}_\odot)$	$\tau_{inf}(\mathrm{Gyr})$	$\nu(\mathrm{Gyr}^{-1})$	ω
Irregulars	$5 \times 10^7 < M < 5 \times 10^9$	$1 < \tau < 12$	$0.01 < \nu < 0.25$	$0.5 < \omega < 2$
Spiral discs	$10^{10} < M < 10^{11}$	$4 < \tau < 8$	$1 < \nu < 3$	$0.1 < \omega < 0.5$
Spheroids	$3 \times 10^{10} < M < 10^{12}$	$0.2 < \tau < 0.5$	$5 < \nu < 20$	-(1)

Notes: (1) adopted the "sudden wind" formulation (see 2.1.4).

over, it is worth noting that such histories of star formation were already tested in previous chemical evolution papers (e.g. Grieco et al. 2012; Gioannini et al. 2017b) and ensure that we can reasonably reproduce the characteristics of a galaxy of a given galactic morphological type (see Fig. 3.1).
As explained in 1.3.1, the different SFHs shown in Fig. 3.1 give rise to different behaviours in the [X/Fe] vs. [Fe/H] diagram as a consequence of the so-called "time-delay model" (Matteucci 2001, 2012). In this way, we can discriminate between the different types of galaxies by means of their observed chemical abundance ratios, which can be accurately predicted by our detailed chemical evolution models.

However, since real galaxies show a distinctive spread in their properties, we can allow variations in the main parameters describing the SFH of galaxies. In particular, during this Thesis we also consider ranges of values for the parameters expressed in Tab. 3.1 (galaxy mass, infall timescale, SFE, galactic wind parameter) for irregular, spiral and elliptical galaxy models. These ranges are shown in Tab. 3.2 and are chosen in such a way to still reproduce the main chemical properties of local ellipticals (e.g. Pipino & Matteucci 2004; De Masi et al. 2018), spiral (e.g. Cescutti et al. 2007) and irregular galaxies (e.g. Lanfranchi & Matteucci 2003, see also Calura et al. 2009a). Moreover, different IMFs can be adopted to better describe the behaviour of different galaxies. As for example, the Scalo (1986) IMF fits better the features of spiral discs than the Salpeter (1955) IMF (Chiappini et al., 2001; Romano et al., 2005), while for more massive spheroids an overabundance of massive stars (i.e. a top-heavy IMF) at early times is necessary to explain multiple features (e.g. Gibson & Matteucci 1997; De Masi et al. 2018; Zhang et al. 2018, see Section 3.2 for more information).
Despite of the differences relative to the reference models, it is worth noting that the parameter variations as well as the changes in the IMFs preserve the typical SFHs for the different type of galaxies and allow the "time-delay model" working.

Despite *Gaia* mission results (Gaia Collaboration et al. 2018) suggested that mergers may play a significant role in the MW first phases of evolution, in our work we do not consider galaxy interactions. Several chemical evolution papers have demonstrated that

interactions can be simulated by enriched gas infall from a companion galaxy (Spitoni, 2015; Spitoni et al., 2016a) and it was demonstrated (e.g. Spitoni 2015) that external, primordial infall is more important than enriched one, especially in the early phases of galaxy evolution. We will come back to this point also in Section 4.2.

3.1.2 Dust evolution parameters

The different SFH experienced by different galaxies is not the only thing we have to deal with in this Chapter. Dust is a key player in both the observations and the evolution of these astrophysical systems.

From our point of view, dust depletes the galactic ISM by important amounts of their gaseous metals, changing the elemental abundance ratios in the ISM gas due to the different depletion rates of different elements (i.e. refractory and volatile, see 1.2.1, 1.3.2). This deeply affects our knowledge of the chemical composition of distant galaxies. In fact, the ISM abundances are inferred by means of absorption or emission line features in rest frame UV/optical spectra: these observations reveal only the chemical composition of the gas phase, leaving undetected the elemental particles embedded in the dust phase. Hence, without dust modelling our interpretation of observational data would risk to be partially or, in the worst case, totally wrong, leading to deceptive conclusions.

On the other hand, many issues regarding overall dust quantities are far from being completely understood. The substantial progress made in the interstellar dust field in the past years has allowed a more thorough understanding of galactic dust especially in local galaxies, even if some issues still remain (e.g. De Looze et al. 2020; Galliano et al. 2021). However, the situation is more critical when we look at high-redshift galaxies (e.g. Graziani et al. 2020) as well as at larger volume scales (Gioannini et al. 2017b; Gjergo et al. 2018), where the uncertainties concerning the evolution of dust are hampering the building of a global, consistent picture of this ISM component. For this reason, it is also vital to look at the global behaviour of dust relations in different astrophysical objects to pin down important constraints on dust evolution.

In order to do so, we build dust evolution models considering the main processes affecting the dust amount in the ISM, i.e. astration by SF, production by stars, accretion in cold dense regions of the ISM and destruction by SNe shocks. These processes are accounted by adopting well tested dust prescriptions form the literature (see Section 2.3). In particular, we adopt either dust yields from Piovan et al. (2011) or Dell'Agli et al. (2017) and Bianchi & Schneider (2007) or Piovan et al. (2011) for AGB and CC-SNe, respectively, whereas accretion and destruction terms are taken from the work by Asano et al. (2013). Most of these prescriptions have been already tested in previous works (e.g. Gioannini et al. 2017a,b; Vladilo et al. 2018; Palla et al. 2020c). However, in the light of more recent

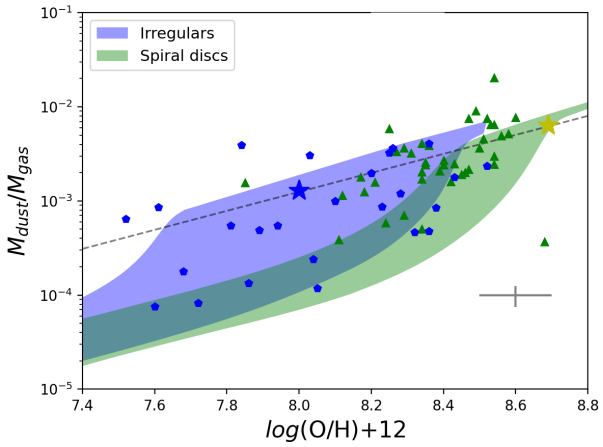

Figure 3.2: *Dust-to-gas ratio vs.* log*(O/H)+12 achievable by our chemical evolution models for irregular (blue area) and spiral (green area) galaxies. Data for irregulars are from the DGS survey (blue pentagons) whereas those of spiral discs form the KINGFISH survey (green triangles). Yellow and blue stars represent the dust-to-gas ratio observed in the solar neighbourhood (Zubko et al. 2004) and in the Small Magellanic Cloud (Leroy et al. 2007), respectively. The gray dashed line expresses a linear relation between the dust-to-gas ratio and the metallicity. Typical data errors are expressed by the grey cross in the bottom-right corner.*

dust data, we further check whether our chemical evolution models are able to reproduce the most important constraints coming from the observed dust-related scaling relations. For this reason, in Fig. 3.2 and 3.3 we compare the results of the models with current data for irregular, spiral and spheroidal/local elliptical galaxies. In order to account for the distinctive spread in the properties of the different galaxy types, the models in these Figures follow the SFH prescriptions as described in Tabs. 3.2 and 3.2. The same is done for stellar dust production prescriptions, which allows for different dust masses produced by stars depending on the efficiency of the reverse shock density (see 2.3.1). On this side, it is worth noting that in these Figures we adopt stellar dust production yields by Piovan et al. (2011). However, we check that similar results are obtained by using Bianchi & Schneider (2007) and Dell'Agli et al. (2017) prescriptions.

In Fig. 3.2, we show the comparison of a bunch of models which reproduce the main physical and chemical properties of irregular and spiral galaxies with recent literature data for the dust-to-gas ratios (DGRs) in local samples of galaxies. In particular, we use for this comparison selected subsamples of the Dwarf Galaxy Survey (DGS, Madden et al. 2013, blue points), that consists of mostly dwarfs galaxies, and the KINGFISH survey (Kennicutt et al. 2011, gas and dust masses are from Rémy-Ruyer et al. 2014, 2015, green points), which is composed by more metal-rich, spiral galaxies.

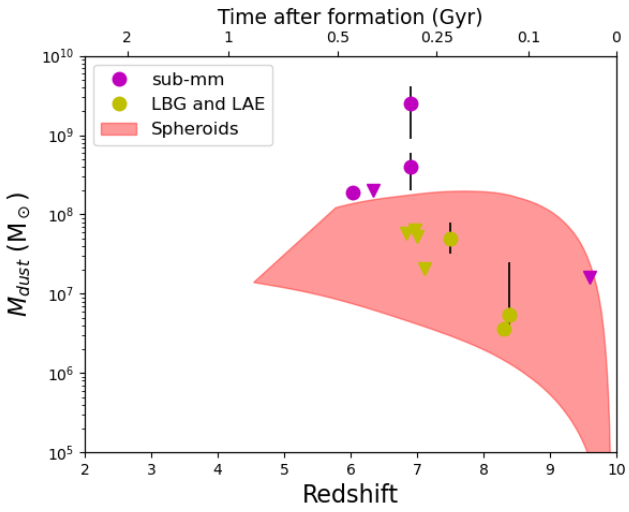

Figure 3.3: *Dust mass in proto-spheoids (local ellipticals) galaxies as a function of redshift (lower x-axis) and time from galaxy formation (upper x-axis). Red area covers the dust mass values predicted by models. Data are dust masses (filled circles) and upper limits (triangles) for Lyman Break Galaxies and Lyman-α Emitters (yellow, Maiolino et al. 2015; Watson et al. 2015; Ota et al. 2014; Knudsen et al. 2017; Laporte et al. 2017; Tamura et al. 2019) and sub-mm galaxies (magenta, Cooray et al. 2014; Zavala et al. 2015, 2018; Marrone et al. 2018).*

By looking at this Figure, our models for irregular and spiral disc galaxies successfully reproduce the general behaviour of DGRs in local galaxies. Moreover, the regions covered by the spiral and irregular models reproduce the DGR of the solar neighborhood (BARE-GR-S model of Zubko et al. 2004, yellow star) and the one measured in the SMC (Leroy et al. 2007, blue star), respectively.

For what concerns spheroids/local elliptical galaxies, we compare the dust masses predicted by our models with high-redshift data, as shown in Fig. 3.3. Here, we assume that galaxies form at redshift $z = 10$ and evolve in a flat Λ-cold dark matter (ΛCDM) cosmology with $H_0 = 70$ Km s^{-1} Mpc^{-1} and $\Omega_m = 0.3$.
The adopted chemical and dust evolution prescriptions allow us to reach very high dust masses (i.e. up to $\gtrsim 10^8$ M$_\odot$) already at redshifts $z \sim 8$: this is due to a very fast metal formation driven by a very strong burst of star formation (see Fig. 3.1), that triggers a very fast dust mass buildup. As it can be seen in Fig. 3.3, the predicted trend reproduces the observed dust masses in very high-redshift Lyman Break Galaxies (yellow symbols), that are thought to be the star forming progenitors of local elliptical galaxies (e.g. Matteucci & Pipino 2002; Pipino et al. 2011). However, we also see that the predictions are generally lower than what observed in sub-mm galaxies (magenta symbols), even wehen adopting the most efficient CC-SN dust production prescriptions (see Fig. 2.7). However, the strug-

gling of the galaxy models to reproduce these extremely high dust masses is well known in literature and it is named as the "dust-budget crisis" problem (e.g. Rowlands et al. 2014). For this reason, in Section 3.2 we try to give a possible interpretation and solution to this issue.

3.2 Starburst galaxies at high-z: an IMF or dust matter?

3.2.1 Introduction

The stellar IMF influences most observable properties of stellar populations, as it regulates the relative fractions of low- and high-mass stars within them. Massive stars (i.e. the stars with mass > 8 $M_{\odot}$) are known to be the main producers of α-elements over short (≤ 30 Myr) timescales. On the other hand, the bulk of Fe in a galaxy is known to be produced by Type Ia SNe (originating from low and intermediate mass stars) over timescales that can even reach or exceed the Hubble time (Matteucci & Greggio 1986; Matteucci & Recchi 2001). Additionally, even when not entering in the cycle of production and recycling of elements, low mass stars affect the chemical evolution by locking baryonic matter away from the ISM. Owing to these differences, chemical abundance ratios have been used as powerful instruments for reconstructing the star formation history of galaxies and the shape of the prevailing IMF (e.g. Matteucci 1994, 2012).
However, the implications of IMF variations go well beyond chemical abundances and affect many other properties of a galaxy. Low mass stars are the main contributors to the present time stellar mass budget (Kennicutt 1998), while massive stars dominate the integrated light of galaxies (Conroy & van Dokkum 2012a). Furthermore, these latter strongly influence the amount of energetic feedback produced by stellar winds and SNe.

At present, a complete theory able to explain the origin of the IMF does not exist yet. In fact, previous works concentrate on single aspects of the star formation process, such as the effect of molecular flows and protostellar winds (e.g. Silk 1995; Krumholz et al. 2011), of the Jeans mass (Larson 1998, 2005), of gravitational fragmentation and of the thermal physics (Bonnell et al. 2007; Hopkins 2013; Chabrier et al. 2014).

Another fundamental issue not yet clarified concerns the universality of the IMF. As mentioned in 2.1.2, direct star counts in star forming regions and clusters support the adoption of an invariant IMF in the form of a power-law, with a turn-off at masses < 1 $M_{\odot}$ (e.g. Kroupa et al. 1993; Kroupa 2001; Kroupa et al. 2013, but see Schneider et al. 2018). The invariance of the local IMF has been invoked for a long time to support claims for its universality, but a direct confirmation of this through star counts in external galaxy is precluded by our observational capabilities.
However, there are plenty of observational evidences supporting variations in the IMF relative to the solar vicinity. As for example, gravity sensitive features (e.g. NaI $\lambda\lambda$8183,8195 doublet, Wing-Ford FeH band at 9900 Å; CaT at λ8498,8542 and 8662 Å) in galaxy integrated spectra are powerful tools to constrain IMF variations in the low-mass end in local elliptical galaxies. By using these features, several works agree in observing a trend of the IMF becoming bottom-heavier (i.e. favouring the presence of low mass stars) in more massive galaxies (e.g. Saglia et al. 2002; Cenarro et al. 2003; Conroy & van Dokkum 2012a,b;

La Barbera et al. 2013; Spiniello et al. 2014). On the other hand, various other studies indicate that a high-redshift top-heavy IMF seems to be required to explain several properties of massive galaxies. These properties include the observed evolution of the optical luminosity density (Larson 1998), the integrated [α/Fe] ratios (Calura & Menci 2009; De Masi et al. 2018) and the colour-luminosity relation (Gibson & Matteucci 1997) in local spheroids, the observed galaxy number counts in the infrared (IR) band and at submillimetric wavelengths (Baugh et al. 2005), the isotopic ratios in high-z starbursts (Romano et al. 2017; Zhang et al. 2018) and the discrepancy between the observed present-day stellar mass density and the integral of the comoving SFR density (Davé 2008). Arguments in favour of a top-heavy IMF in high-redshift starbursts are provided also on independent grounds by Papadopoulos et al. (2014). Such results are supported by observations of star-forming galaxies at low-to-moderate redshift (Gunawardhana et al. 2011), with the high mass slope of the IMF becoming flatter (hence providing a top-heavier IMF) in objects with higher star formation activity, as it might be the case for the progenitors of more massive galaxies.

The IGIMF

In this complex framework, a significant role is played by the integrated galactic initial mass function (IGIMF) theory (see Kroupa & Weidner 2003; Weidner & Kroupa 2005 for earlier formulations, while latter developments are presented in Yan et al. 2017; Jeřábková et al. 2018).

As mentioned in 2.1.2, this formulation is based on few basic empirical evidences related to the birth of stars in local star-forming environments, which include the facts that: (i) stars form in a clustered mode (Lada & Lada 2003; Megeath et al. 2016), i.e. in groups of at least a few stars in local over-densities, called embedded star clusters; (ii) within each embedded cluster, the stellar/canonical IMF can be derived from observations and it is well approximated by a multiple power-law form (Massey & Hunter 1998; Pflamm-Altenburg et al. 2007; Yan et al. 2017 and references therein); (iii) stellar clusters are distributed according to a single-slope power law (Lada & Lada 2003) and (iv) the upper mass end of the embedded cluster mass function has been found to depend on the SFR of the galaxy (Weidner & Kroupa 2004).
A schematic view of the IGIMF formulation is shown in Fig. 3.4: as it is evident from the Figure, the IGIMF is just the sum of all the IMFs of star-forming regions (i.e. embedded clusters) belonging to a given galaxy.

An important consequence of this particular formulation is that the integrated IMF in disc galaxies (e.g. the MW) is generally steeper than the stellar IMF within each single star cluster (Kroupa & Weidner 2003), with evident implications in the chemical evolution for the solar neighbourhood (see Calura et al. 2010).
In the last years various studies have been carried out to assess the effects of the IGIMF on

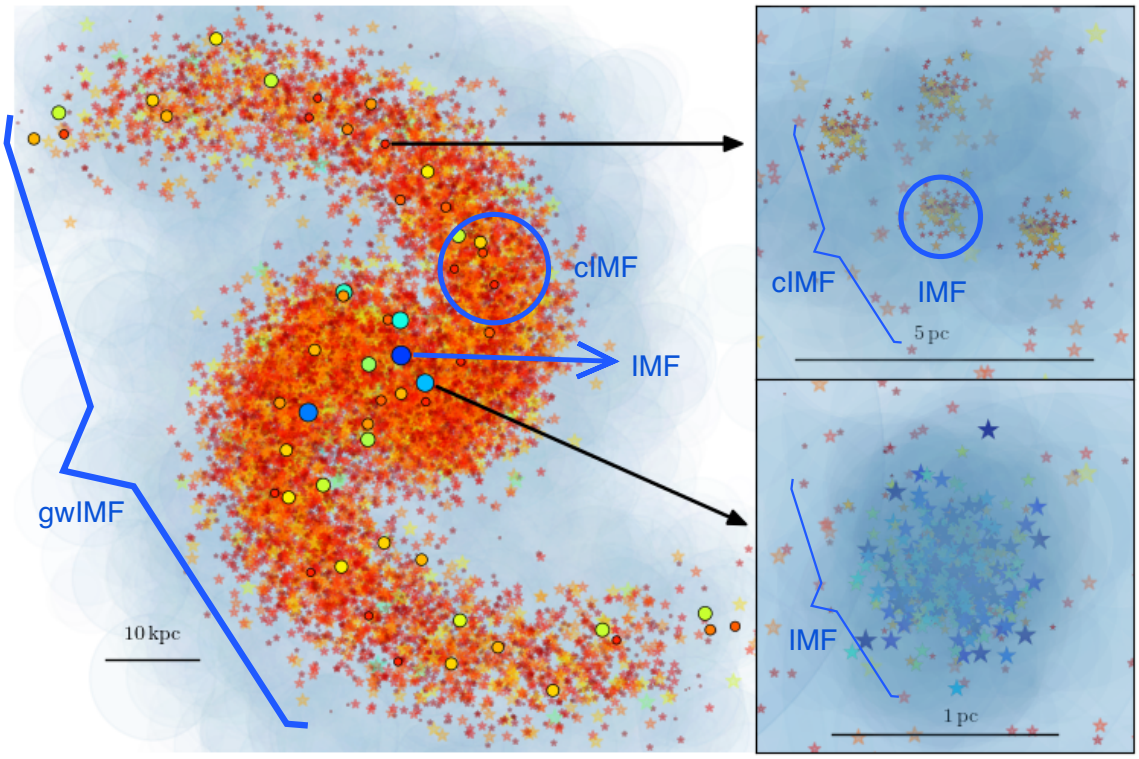

Figure 3.4: *Adapted from Jeřábková et al. (2018). Schematic showing of the IGIMF (here gwIMF) formulation. Galaxy field population is represented by red and orange stars. The newly formed stellar populations are indicated by circles that represent the embedded star clusters, with colour and dimension according to the stellar cluster mass. Here, IMF stands for the stellar/canonical IMF within an embedded clusters, while cIMF is the sum of the IMFs over larger regions within the galaxy.*

galactic chemical evolution in different environments characterised by different star formation histories, ranging from dwarf galaxies (Vincenzo et al. 2015; Lacchin et al. 2020; Yan et al. 2020) to local elliptical galaxies (Recchi et al. 2009; De Masi et al. 2018; Yan et al. 2019).

In this Section, we follow on these studies and apply the IGIMF suggested by Weidner et al. (2011) to the study of high-redshift starburst galaxies, i.e. objects that are experiencing a very strong burst of star formation. It is worth noting that this IGIMF formulation is specifically built for such objects: in fact, Weidner et al. (2011) extended the original Kroupa & Weidner (2003); Weidner & Kroupa (2005) theory to systems characterised by high star formation rates ($SFR > 10$ $M_\odot$ yr^{-1}), showing that in the most active star-forming objects, i.e. in very massive and compact systems, the resulting IMF becomes top-heavy, with strong consequences on chemical enrichment and stellar feedback.
We point out that a novel SFR and metallicity dependent formulation of the IGIMF was recently proposed by Yan et al. (2017) and Jeřábková et al. (2018). However, we reserve the implementation of such new formulation to future work.

Dust at high-redshift: SN production or grain growth?

Unfortunately, the IMF is not the only concern when dealing with starburst galaxies at high-redshift. In fact, the origin and composition of dust grains at high-redshift is highly uncertain and current literature is divided on the origin of cosmic dust. Dust formation by AGB stars (e.g. Valiante et al. 2011), SNe (e.g. Gall et al. 2011a; Ferrara et al. 2016; Gall & Hjorth 2018) or accretion of dust in the ISM (e.g. Draine 2009; Hirashita 2012; Graziani et al. 2020) have been alternatively claimed as major dust sources. The different conclusions reached by advanced chemical evolution models and large scale cosmological simulations suggest that their output is highly dependent on the still uncertain physical prescriptions adopted for the formation, growth and destruction of dust.

In the understanding of the most important dust factory, a crucial role is played by the impact of the reverse shock mechanism in dust production by CC-SNe (see 2.3.1).
Under the assumption of efficient SN reverse shock dust destruction, we need efficient dust accretion in the ISM (e.g. Draine 2009; Mancini et al. 2015) to regain the very large dust masses observed in high-redshift galaxies (see Fig. 3.3), if AGB stars are not efficient dust producers on short timescales (e.g. Leśniewska & Michałowski 2019). However, dust accretion in the ISM encounters some theoretical problems at high-redshift. In particular, the physical conditions are far from similar to those seen today in the MW (Ceccarelli et al. 2018): as demonstrated by Ferrara et al. (2016), grain growth cannot happen efficiently in dense molecular clouds (MC) in these environment, and also accretion in the cold neutral medium poses severe theoretical challenges due to the higher cosmic microwave background (CMB) temperature (see also Zhukovska et al. 2018).

For this reason, some works claim that the observed dust masses at high-redshift can be simply explained by dust production from SNe at a rate that is consistent with the dust masses measured in SN remnants (e.g. Gall & Hjorth 2018). Even if the reverse shock passage is far from being complete in these objects (see, e.g. Bocchio et al. 2016), they claim that this SN remnant dust-dust production correlation sets at least a strong constraint for other dust mechanisms (i.e. dust accretion and destruction in the ISM), that must obey to this relation. On the other hand, it has to be said that grain growth in the ISM is required to explain the large depletion rates of Fe, whose main producers (Type Ia SNe) do not seem to contribute to dust production (e.g. Nittler et al. 2018).

It is worth noting that the present work is the first in which a detailed treatment of dust is included in chemical evolution models with the IGIMF.
The inclusion of dust is particularly insightful for many reasons. First, we can test directly the interplay between various parameters, including the environmental dependent IMF, in determining the abundance pattern in high-redshift galaxies and how these parameters influence the growth of the dust mass. Moreover, differential dust depletion can solve the discrepancy between previous chemical evolution models and the observed [α/Fe] ratios in high-redshift starbursts (Matteucci & Pipino 2002; Pipino et al. 2011). Furthermore, the inclusion of models where different dust processes in the "dust-cycle" (i.e. SN reverse shock, dust growth, dust destruction) can be switched on and off can provide important insights on the behaviour of dust in high-redshift galaxies.

The remainder of this Section is organized as follows. In 3.2.2 we describe the galaxies and the observational data considered for our analysis. The detailed presentation of the IGIMF theory and the chemical and dust evolution models adopted here is deferred to 3.2.3. Our results on the SFHs, abundance patterns and dust quantities of high-redshift starburst galaxies are presented in 3.2.4, while some conclusions are drawn in 3.2.5.

3.2.2 Observational data: starburst galaxies at high-z

Several evidences support the idea that local spheroids/elliptical galaxies must have experienced a starburst phase at high-redshift. This is inferred from the properties of their stellar populations, in particular from their integrated ages and integrated abundances (e.g. Matteucci 1994; Spolaor et al. 2010 and references therein). In principle, high-redshift starbursts might also present the physical conditions required for a top-heavy IMF, whose signature might be encoded in their interstellar abundance pattern.

Therefore, the turbulent, strongly pressurized ISM of starbursts represents an ideal laboratory to probe the IMF in the progenitors of local spheroids, and in particular to test the hypothesis of a top-heavy IMF during the starburst phase.
Moreover, the extreme ISM conditions of these objects are the perfect testbed for varia-

tions of the different dust prescriptions .

For these reasons, we consider a sample of several starburst galaxies, mainly composed by Lyman Break Galaxies (LBGs) and Lyman-α Emitters (LAE), at redshift $z \gtrsim 2$.
Most of the considered objects in this Section benefit of gravitational lensing magnification. In fact, the magnification due to gravitational lensing allows one to perform high quality, high signal-to-noise (S/N) spectroscopy, from which physical properties and chemical abundances can be derived (Bayliss et al. 2014 and references therein). In addition, we extend our sample of high-redshift star-forming systems by considering also two cases where 'composite' spectra from sizable sets of high-z systems were obtained with observations in non-lensed fields. These samples include high-redshift systems, with average stellar masses and SFR values comparable to the ones of the lensed objects.

All the data from the lensed objects and the 'composite' samples are presented in Tab. 3.3 and 3.4, where we list the main features (redshift, SFR, stellar mass) and the chemical abundances observed in the selected systems.
In the following, we give a brief description of each of the objects considered in our analysis.

MS 1512 - cB58

MS 1512-cB58 (hereafter, cB58) is a lensed LBG first discovered by Yee et al. (1996), with redshift $z = 2.7276$ (Pettini et al., 2002). It is magnified by a factor ~ 30 by the cluster MS 1512+36 at $z = 0.37$ (Pettini et al., 2000).
Several SFR estimates were performed for this object in the past years, leading to different results depending on the adopted SFR estimator (e.g. IR, Hα, UV). The available values span the range $\sim$ 25 - $\sim$ 150 $M_\odot$ yr^{-1} (Siana et al., 2008). However, the highest SFR values might represent upper limits due to overestimated extinction corrections (Siana et al., 2008). The estimated baryonic mass is of $\sim 10^{10}$ $M_\odot$ (Pettini et al. 2000; Baker et al. 2004), whereas the effective radius is $R_{eff} \sim 2$ kpc (Seitz et al., 1998).

The observed abundances in Tab. 3.4 are from Teplitz et al. (2000) and Pettini et al. (2002). The log(O/H)+12 and log(N/O) abundances were estimated by Teplitz et al. (2000) from interstellar emission lines. The O abundance was calculated by means of the R_{23} indicator[1]. The abundances obtained by Pettini et al. (2002) were computed from interstellar absorption lines, and in particular from the measured column densities using the apparent optical depth method[2]. The N/O values from both sets will be compared with the models, in order to appreciate the differences in the measures as obtained from emission and

[1] metallcity dependent "strong-line ratio", i.e. ratio between intensities of strong emission lines, that is empirically calibrated to give the element abundance. Other examples are the N_2 and N_3O_2 indicators.

[2] the column density is inferred by measuring the ratio between observed intensity and the continuum (i.e. the apparent optical depth) in each velocity bin where the absorption line takes place and then summing the contribution of each bin. The term apparent is because of the assumption that intrinsic line properties are negligibly affected by instrumental effects.

Table 3.3: *Main features of the sample of starburst galaxies included in our sample. Objects in the upper part of the table are lensed galaxies. Objects in the lower part are stacked ('composite') spectra of galaxies.*

Object	Redshift	SFR ($M_\odot$ yr^{-1})	M_* ($M_\odot$)	Notes	References
MS 1512-cB58	2.7276	∼25-150	$\sim10^{10}$	(1), (2), (3)	Pettini et al. (2000, 2002); Teplitz et al. (2000); Siana et al. (2008)
8 o'clock arc	2.7350	∼270	$\sim10^{11.6}$	(2), (3)	Dessauges-Zavadsky et al. (2010); Finkelstein et al. (2009)
Cosmic Horseshoe	2.3812	∼95-190	$\sim10^{10}$	(1), (2), (3)	Quider et al. (2009); Hainline et al. (2009)
SGAS J105039.6+001730	3.6252	∼90-140	$\sim10^{9.7}$	(2)	Bayliss et al. (2014)
RCSGA 032727-132609	1.7037	∼130-360	$\sim10^{10.3}$	(2)	Wuyts et al. (2010); Rigby et al. (2011)
SMACS J0304.3-4402	1.96	∼20-90	$\sim10^{10.8}$	(2)	Christensen et al.(2012a); Christensen et al. (2012b)
SMACS J2031.8-4036	3.51	∼15-30	$\sim10^{9.4}$	(2)	Christensen et al.(2012a; Christensen et al. (2012b)
KBSS-LM1	2.396±0.111	∼50-55	$\sim10^{10}$	(2), (4)	Steidel et al. (2016)
Shapley LBG	∼3	>50	-	(2)	Shapley et al. (2003); Pettini et al. (2001)

Notes: *SFR and M_* estimates were derived adopting a Salpeter (1955) IMF.*
(1) M_* is the baryonic mass; (2) abundances from emission lines; (3) abundances from absorption lines; (4) median values of the sample, except for redshift (medium value with rms of the sample).

Table 3.4: *Abundance ratios of starburst galaxies included in our sample. Lensed galaxies and stacked spectra are organised as in Tab. 3.3. In parentheses, the method for* $\log$*(O/H)+12 estimation is indicated.*

Object	log(O/H)+12	log(N/O)	log(C/O)	[Fe/H]	[Si/H]	[Mg/H]
MS 1512-cB58	8.39±0.10 (R_{23})	-1.24±0.14[1]	-	-1.15±0.1	-0.37±0.1	-0.32±0.1
		-1.89±0.14[2]				
8 o'clock arc	8.58±0.18 (N_2)	-	-	-0.93±0.15	-0.19±0.14	-
Cosmic Horseshoe	8.38±0.18 (N_2)	-	-	$-1.17^{+0.18}_{-0.15}$	$-0.29^{+0.18}_{-0.15}$	-
SGAS J105039.6+001730	≥8.05 (direct)	-1.59±0.2	-0.79±0.06	-	-	-
	8.17±0.12 (R_{23})					
RCSGA 032727-132609	≥8.14 (direct)	1.7±0.02	-	-	-	-
	8.20±0.08 (R_{23})					
	8.20±0.04 (N_2)					
SMACS J0304.3-4402	8.07±0.09 (direct)	-1.64±0.05	-	-	-	-
	8.16±0.01 (R_{23})					
SMACS J2031.8-4036	7.76±0.03 (direct)	-	-0.80±0.09	-	-	-
	7.74±0.03 (R_{23})					
KBSS-LM1	8.38±0.05 (direct)	-1.24±0.04	-0.60±0.09	-	-	-
	8.20±0.1 (R_{23})					
	8.32±0.05 (N_2)					
Shapley LBG	[7.64,8.73] (R_{23})	-	[-0.81,-0.56]	-	-	-

Notes: *For [X/H] values, solar abundances are from Asplund et al. (2009).*
[1] *from Teplitz et al. (2000);* [2] *from Pettini et al. (2002).*

absorption lines.

8 o'clock arc

8 o'clock arc is a LBG at redshift $z = 2.7350$, lensed by the luminous red galaxy (LRG) SDSS J002240.91+143110.4 at $z = 0.38$ (Allam et al., 2007).
The arc has an inferred stellar mass of $4.2 \cdot 10^{11}$ $M_\odot$ and a SFR of $266 \pm 74 M_\odot$ yr^{-1} (corrected for a lensing magnification of $\mu = 8$, Finkelstein et al. 2009). Analysis of the Baldwin-Phillips-Terlevich (BPT) diagram excludes substantial AGN contamination (Finkelstein et al., 2009).

In Tab. 3.4, we show the O abundances from the Keck/LRIS emission spectrum (Finkelstein et al. 2009) and the Fe, Si abundances obtained from the VLT/X-SHOOTER absorption spectrum of Dessauges-Zavadsky et al. (2010). O abundances are obtained from the N_2 indicator, whereas Fe, Si abundances by means of the apparent optical depth method (as in Pettini et al. 2002).

Cosmic horseshoe

Cosmic Horseshoe is a gravitationally lensed LBG discovered by Belokurov et al. (2007), with redshift $z = 2.3812$. It is magnified by a factor $\mu = 24 \pm 2$ by a massive LRG at $z = 0.444$ (Dye et al., 2008).
The inferred baryonic mass and effective radius are of the order of 10^{10} $M_\odot$ and 2.5 kpc (Hainline et al., 2009). Its H_α and UV luminosities yield SFR values of 95 $M_\odot$ yr^{-1} (Quider et al., 2009) and 190 $M_\odot$ yr^{-1} (Hainline et al., 2009), respectively.

The absorption lines from its Keck II/ESI spectrum (Quider et al. 2009) and the emission lines from Keck II/NIRSPEC (Hainline et al. 2009) give the abundances presented in Tab. 3.4. Fe and Si abundances were obtained by means of the apparent optical depth method, whereas O abundance from the N_2 indicator.

SGAS J105039.6+001730

SGAS J105039.6+001730 LBG at redshift $z = 3.6252$ is a system lensed by a foreground galaxy cluster at $z = 0.593$. The lensing magnification is of the order of ~ 30.
By taking into account the magnification factor, Bayliss et al. (2014) derived for the galaxy a stellar mass of $5 \cdot 10^9$ $M_\odot$ and values of the SFR between 90 and 140 $M_\odot$ yr^{-1} (depending if based on [OII] or H_β luminosity, respectively). The Magellan/FIRE interstellar emission spectrum ruled out a substantial AGN contribution for this LBG.

Abundances in Tab. 3.4 are taken from Magellan/FIRE spectrum of Bayliss et al. (2014). As for the O abundance, both the direct method[3] measure and the value inferred

[3] abundance measurement directly inferred from emission line intensities, without the adoption of a calibrated indicator. Since the strength of metal lines is also the product of the temperature states of the gas, the ratio of auroral to strong lines is used to estimate the electron temperature T_e and thus the abundace of the gas.

via the R_{23} indicator are presented.

RCSGA 032727-132609

RCSGA 032727-132609 is a bright lensed galaxy (at the time of its discovery, it was the most luminous lensed galaxy ever known) at redshift $z = 1.7037$, magnified by a factor $\mu = 17.2 \pm 1.4$ by RCS2 032727-132623 galaxy cluster at $z = 0.564$.
From spectral energy distribution (SED) fitting, the stellar mass was found to be $2 \cdot 10^{10}$ $M_\odot$ (Wuyts et al., 2010). Different methods give SFR values between $\sim$ 130 $M_\odot$ yr^{-1} (Wuyts et al., 2010) and $\sim$ 360 $M_\odot$ yr^{-1} (Rigby et al., 2011). As noted in Rigby et al. (2011), the highest SFR value is to be regarded as an upper limit. The BPT diagram for this object is consistent with no AGN contribution.

The abundances in Table 3.4 are taken from Keck II/NIRSPEC emission spectrum of Rigby et al. (2011). The $\log$(O/H)+12 values reported in Table 3.4 refer to the direct, R_{23} and N_2 methods. Other abundance indicators (e.g. N_3O_2) were also used to estimate its metallicity (Rigby et al. 2011), with derived values which are similar to the ones shown in Table 3.4.

SMACS J0304.3-4402

This LAE at redshift $z = 1.963$ is magnified by a factor $\mu = 42.0 \pm 8.0$ by a galaxy cluster placed between redshift 0.3 and 0.5 (Christensen et al., 2012a).
SED fitting reveals a stellar mass of $6.3 \cdot 10^{10}$ $M_\odot$. The inferred SFR from emission lines lies between $\sim$ 20 $M_\odot$ yr^{-1} (from the H_α-detection) and $\sim$ 90 $M_\odot$ yr^{-1} (from the [OII]-detection). The rest frame UV spectrum shows no AGN contribution.

The abundance ratios presented in Table 3.4 are from the VLT/X-SHOOTER emission line spectrum of Christensen et al. (2012a,b). O/H have been measured using both direct and R_{23} methods.

SMACS J2031.8-4036

SMACS J2031.8-4036 is a LAE at redshift $z = 3.51$. It is magnified by a factor $\mu = 15.8 \pm 7.0$ by a galaxy cluster at $z = 0.331$ (Christensen et al., 2012a).
SED fitting reveals a stellar mass of $2.4 \cdot 10^9$ $M_\odot$. Its VLT/X-SHOOTER emission line spectrum indicates no AGN contribution and a SFR between $\sim$ 15 $M_\odot$ yr^{-1} and $\sim$ 30 $M_\odot$ yr^{-1}, inferred via [OII] and H_α detection, respectively (Christensen et al. 2012a,b).

The abundance data in Table 3.4 are drived from the VLT/X-SHOOTER spectrum of Christensen et al. (2012a,b). The values shown for $\log$(O/H)+12 are estimated by means of the direct and the R_{23} methods.

KBSS - LM1 (composite)

This 'composite' spectrum is the result of the combined analysis of Keck/LRIS and Keck-/MOSFIRE observations of a sample of 30 galaxies from the KBSS-MOSFIRE survey (Steidel et al., 2014).
Galaxies of this subsample lie in the redshift range $2.113 \leq z \leq 2.572$, which is optimal to get access to nebular lines as well as integrated OB stars light. Median values of the stellar mass and the SFR are $\log(M_*/\mathrm{M}_\odot) \simeq 10.0$ and ~ 50 $\mathrm{M}_\odot$ yr^{-1}, respectively, as traced by UV and H_α indicators.

The abundances shown in Table 3.4 are taken from Steidel et al. (2016). The three (O/H) values are from different estimators, namely the direct, the R_{23} and the N_2 methods. The direct measurement value is consistent with the one constrained from SED fitting (Steidel et al., 2016).

Shapley+03 LBG (composite)

Shapley et al. (2003) consider a sample of almost 1000 LBGs at redshift $z \sim 3$ with spectra taken with Keck/LRIS.
In general, the emission line stacked spectrum shows vigorous SF. All the four subsamples in which the full sample of galaxies is divided show SFR > 50 $\mathrm{M}_\odot$ yr^{-1}. No evidence of AGN emission is found in the composite spectrum.

In Table 3.4 we show the abundances derived by Shapley et al. (2003). The O/H abundance is actually taken from a sample of LBGs originally presented in Pettini et al. (2001).

3.2.3 Modelling the starbursts: chemical evolution and IGIMF

In the following, we describe the models adopted to probe high-redshift starburst galaxies. In particular, we first describe the main features of the chemical and dust evolution models aimed at describing the starburst phase of massive proto-spheroids. After that, we present the basic ingredients of the Weidner et al. (2011) IGIMF and we describe its behaviour following variations in its input parameters.

Chemical and dust evolution models for starbursts

The chemical evolution models adopted in this Section have been orginally designed to study the evolution of elliptical galaxies (Matteucci 1994; Pipino et al. 2011; Calura et al. 2014; De Masi et al. 2018). Here, we briefly resume the main characteristics of the models, also listing the adopted prescriptions for stellar yields and dust. In any case, we address the reader to Chapter 2 for more detailed information.

In our scheme, elliptical galaxies form from the rapid collapse of a gas cloud with primordial chemical composition, described by an exponential infall law as in Eq. (2.10).

Table 3.5: *Main parameters assumed for our chemical evolution models for starburst galaxies.*

Model name	M_{inf} ($M_\odot$)	R_{eff} (kpc)	ν (Gyr^{-1})	τ_{inf} (Gyr)
M3E10	3×10^{10}	2	5	0.5
M1E11	1×10^{11}	3	10	0.4
M1E12	1×10^{12}	10	20	0.2

The initial rapid collapse triggers an intense and rapid SF episode, i.e. a starburst, which lasts until a galactic wind, powered by the thermal energy injected by stellar winds and SN explosions, occurs (see Eq. (2.11)). After that time, the galaxy evolves passively, i.e. with no more SF (see 2.1.4).
With regards to the stellar feedback prescriptions, here we assume the same set up as De Masi et al. (2018): in particular, we assume that only a small, variable fraction (generally of the order of a few percent) of the initial blast wave energy of CC-SNe, $\epsilon_0 = 10^{51}$ erg, is deposited in the ISM (see Pipino et al. 2002; Pipino & Matteucci 2004 for details), whereas all the initial blast wave energy of Type Ia SNe (the same as for CC-SNe) is restored into the ISM, as suggested by Recchi et al. (2001): in fact, when Type Ia SNe explode, the ISM is already hot beacause of the explosion of CC-SNe. Moreover, we assume that stellar winds by massive stars can inject into the ISM 3% of the typical energy of stellar winds ($\sim 10^{49}$ erg, see Bradamante et al. 1998 for details).

The main features of the models used in this Section are summarised in Tab. 3.5. In the first column, the name of the model, which identifies also its mass, is shown. The second column shows the adopted total baryonic-infall mass. The third, the fourth and the fifth columns indicate for each model the adopted effective radius, the star formation efficiency (see Eq. (2.4)) and the infall timescale, respectively.
As in the "inverse wind model" of Matteucci (1994), here the star formation efficiency is increasing and the infall timescale is decreasing with galactic mass. This is important, because it allows us to reproduce fundamental observational constraints in local elliptical galaxies. In particular, the "inverse wind model" reproduces the "downsizing" behaviour of galaxies, with a galactic wind occurring at earlier times in more massive systems, thus producing higher α-elements relative to Fe abundance ratios in the dominant stellar population of the most massive galaxies (see also De Masi et al. 2018).

Nucleosynthesis prescriptions

The contribution to chemical enrichment by different stellar sources, i.e. LIMS, Type Ia and CC-SNe is computed by means of the following sets of stellar yields:

- for LIMS ($0.8 < m/M_\odot < 8$), we use the yields by van den Hoek & Groenewegen

(1997);

- for massive stars exploding as CC-SNe ($m > 8\mathrm{M}_{\odot}$) we adopt the yields by François et al. (2004), a revised version of those by Woosley & Weaver (1995). Yields for nitrogen are taken from Meynet & Maeder (2002) or Matteucci (1986) (see below);
- for Type Ia SNe we use the yields by Iwamoto et al. (1999).

In this Section we run the model twice for N, due to the uncertain origin of this element at low metallicity. In fact, Matteucci (1986) yield set assumes that all massive stars produce primary N. This is an ad hoc assumption which allows us to reproduce some important observational trends, such as [N/Fe] ratios in the MW halo stars (Israelian et al. 2004; Spite et al. 2005), as well as in low metallicity QSO-DLAs (Pettini et al. 2002, 2008) and in low metallicity star forming galaxies (e.g. Berg et al. 2012; James et al. 2015). On the other hand, Meynet & Maeder (2002) yields allow for the production of primary N only in rotating, massive, very low metallicity stars. In general, this leads to a deficiency of N between low and intermediate metallicities (Romano et al. 2010; Vincenzo et al. 2016), at variance with observations. Concerning rotating massive stars, Limongi & Chieffi (2018) recently published new yield sets for a wide range of metallicities and rotational velocities. However, in this work we just want to separate between primary and secondary N production scenarios, without adding other variables such as the distribution of rotational velocities (see, e.g. Prantzos et al. 2018; Romano et al. 2019).

We also point out that for very massive stars (i.e. with $m > 40\ \mathrm{M}_{\odot}$), we adopt C yields suggested by Chiappini et al. (2003). These yields consider rotation for this class of stars and are able to reproduce the C evolution observed in MW stars.

Dust prescriptions

To describe dust evolution, we follow the formalism of Eq. (2.21). As for dust production, we adopt the following mass and metallicity dependent condensation efficiencies:

- for AGB stars, we adopt the prescriptions from Dell'Agli et al. (2017);
- for CC-SNe, we use the prescriptions from Bianchi & Schneider (2007). To test the role of the SN reverse shock in the final dust yields, we run the models using either Bianchi & Schneider (2007) dust yields with reverse shock included (with $n_H = 1$ cm^{-3}) or Bianchi & Schneider (2007) dust yields without reverse shock effect.

Concerning the dust accretion and destruction terms in Eq. (2.21), we adopt the prescription by Asano et al. (2013) tested in previous works (see 3.1.2). Actually, we run models either with or without dust growth, as well as models with or without SN forward shock destruction for the ISM dust. This is due to the severe uncertainties related to dust accretion processes (e.g. Ferrara et al. 2016; Nittler et al. 2018) and dust survival rate in the

Table 3.6: *Dust prescriptions tested for our chemical evolution models for starburst galaxies.*

Model label	SN dust production	Dust Accretion	Dust Destruction
R	Bianchi & Schneider (2007), rev. shock	-	-
DR	Bianchi & Schneider (2007), rev. shock	-	Asano et al. (2013)
ADR	Bianchi & Schneider (2007), rev. shock	Asano et al. (2013)	Asano et al. (2013)
NR	Bianchi & Schneider (2007), no rev. shock	-	-
DNR	Bianchi & Schneider (2007), no rev. shock	-	Asano et al. (2013)
ADNR	Bianchi & Schneider (2007), no rev. shock	Asano et al. (2013)	Asano et al. (2013)

ISM (e.g. Gall & Hjorth 2018).

In the plots of this Section, the results of the models which include the various processes of dust production, growth and destruction are dubbed as described in Tab. 3.6. All the models which include reverse shocks in SNe are labelled with 'R', and models in which reverse shock is turned off are labelled 'NR'. Models which include growth (accretion) and destruction are labelled with 'A' and 'D', respectively. As for examples, a model which includes reverse shock, growth and destruction will be 'ADR', whereas a model in which growth and destruction are absent but reverse shock is present will be dubbed 'R'.

The Weidner et al. (2011) IGIMF

As already mentioned in 2.1.2 the IGIMF is defined by weighting the canonical IMF, $\phi(m)$, with the mass distribution of the embedded stellar clusters (called embedded cluster mass function, ECMF), $\xi_{ecl}(M_{ecl})$ (where M_{ecl} is the cluster mass). In fact, the IGIMF theory starts from the assumption that star formation takes place in molecular cloud cores, i.e. in embedded stellar clusters.
For sake of clarity, we show again the IGIMF expression (Eq. (2.9)), but for the specific version of Weidner et al. (2011) (hereafter W11):

$$\xi_{\rm IGIMF}(m,t) = \int_{M_{\rm ecl,min}}^{M_{\rm ecl,max}(\psi(t))} \phi(m \leq m_{\rm max}(M_{\rm ecl}))\, \xi_{ecl}(M_{ecl})\, dM_{\rm ecl}. \tag{3.1}$$

Here, the IGIMF adopted has a time dependence, which is due to the star formation rate $\psi(t)$ of the parent galaxy, following W11. As for standard IMFs (see Eq. (2.5)), the IGIMF is normalized in the models as

$$\int_{m_{min}}^{m_{max}} m\, \xi_{\rm IGIMF}(m,t)\, dm = 1. \tag{3.2}$$

In the following, we list the assumptions, based on empirical evidence, on which the IGIMF theory is based:

- the ECMF is represented by a single-slope power law:

$$\xi_{\rm ecl}(M_{\rm ecl}) \propto \left(\frac{M_{\rm ecl}}{M_{\rm ecl,max}}\right)^{-\beta}, \tag{3.3}$$

  where the slope β can vary between $\beta = 0.5$ and $\beta = 2.35$.
  In this work, the adopted minimum cluster mass is $M_{\rm ecl,min} = 10^3$ M$_\odot$. This choice is due to the fact that with high SFR values, the formation of low mass molecular cloud cores may be suppressed due to the intense stellar feedback (see W11). However, for $\beta \leq 2$ (as adopted in this paper) the ECMF is not much sensitive to the adopted $M_{\rm ecl,min}$ value.

  As for the upper mass limit $M_{\rm ecl,max}$, following Weidner et al. (2004) it can be expressed as:

$$M_{\rm ecl,max} = 8.5 \cdot 10^4 \left(\frac{\psi(t)}{\rm M_\odot\,yr^{-1}}\right)^{0.75} {\rm M_\odot}, \tag{3.4}$$

  which holds for both low and high SFRs (Bastian 2008). We fix a maximum value for this upper mass limit at 10^7 M$_\odot$, coherently with Weidner et al. (2004);

- within each embedded stellar cluster of a given mass $M_{\rm ecl}$, the IMF is assumed to be invariant. Following W11, we adopt the multi-component canonical IMF (Kroupa, 2001, 2002), which in its general form is expressed as:

$$\phi(m) = k \begin{cases} k' \left(\frac{m}{m_{\rm H}}\right)^{-\alpha_0} & 0.01 \leq m/{\rm M_\odot} < 0.08 = m_{\rm H}, \\ \left(\frac{m}{m_{\rm H}}\right)^{-\alpha_1} & 0.08 \leq m/{\rm M_\odot} < 0.50 = m_0, \\ \left(\frac{m_0}{m_{\rm H}}\right)^{-\alpha_1} \left(\frac{m}{m_0}\right)^{-\alpha_2} & 0.50 \leq m/{\rm M_\odot} < 1.00 = m_1, \\ \left(\frac{m_0}{m_{\rm H}}\right)^{-\alpha_1} \left(\frac{m_1}{m_0}\right)^{-\alpha_2} \left(\frac{m}{m_1}\right)^{-\alpha_3} & 1.00 \leq m/{\rm M_\odot} < m_{\rm max}, \end{cases} \tag{3.5}$$

  with the following exponent values:

$$\alpha_0 = +0.30, \quad \alpha_1 = +1.30, \quad \alpha_2 = +2.35, \quad \alpha_3 = +2.35.$$

  k and k' are normalisation constants whereby the brown dwarf regime needs not be a continuous extension of the stellar regime (Thies et al. 2015). In previous chemical evolution studies involving the IGIMF formalism, the quantity α_3 has been kept equal to 2.35, independently from the cluster mass (e.g. Recchi et al. 2009; Calura et al.

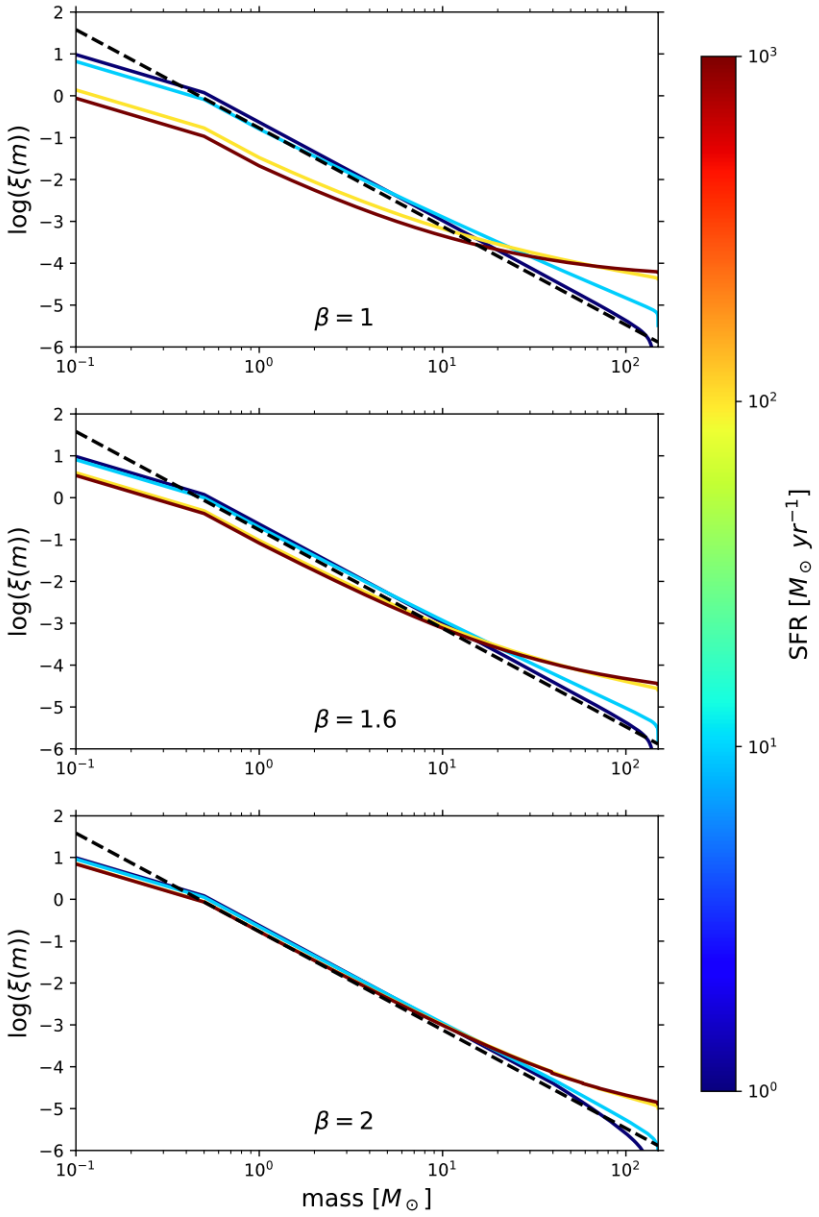

Figure 3.5: *Behaviour of the IGIMF adopted in this paper as a function of stellar mass and SFR for different values of β, namely the slope of the ECMF. Upper panel: $\beta = 1$; central panel: $\beta = 1.6$; lower panel: $\beta = 2$. In each panel, the four solid lines are the IGIMFs computed considering a SFR of $1\ M_\odot\ yr^{-1}$,10 $M_\odot\ yr^{-1}$, 100 $M_\odot\ yr^{-1}$, 1000 $M_\odot\ yr^{-1}$. The black dashed lines indicate the standard Salpeter (1955) IMF.*

2010). As in W11, for clusters with masses $M_{\rm ecl} > 2 \cdot 10^5$ M$_\odot$, the exponent α_3 is parametrised as:

$$\alpha_3(M_{\rm ecl}) = \begin{cases} -1.67 \log_{10}\left(\frac{M_{\rm ecl}}{10^6 M_\odot}\right) + 1.05 & M_{\rm ecl} \leq 10^6 {\rm M}_\odot, \\ +1 & M_{\rm ecl} > 10^6 {\rm M}_\odot. \end{cases} \quad (3.6)$$

The upper stellar mass limit $m_{\rm max}$ is computed from the mass of the embedded cluster $M_{\rm ecl}$. In any case, it is always assumed $\leq 150 M_\odot$ (see Weidner & Kroupa 2004 for more details).

IGIMF behaviour as a function of β and SFR

In Figure 3.5, we show the IGIMF obtained with the prescriptions shown in 3.2.3 for different values of the SFR, in which we have selected three values of β among those adopted in W11: $\beta = 1$, $\beta = 1.6$ and $\beta = 2$.

As it can be noted, we do not consider the most extreme values such as $\beta = 0.5$ and $\beta = 2.35$. By adopting an ECMF with $\beta = 1$ we obtain, for $\psi \gtrsim 10$ M$_\odot$ yr^{-1}, an IMF comparable or even more top-heavy to the single-slope IMF of Gibson & Matteucci (1997), a quite extreme top-heavy IMF, characterised by an index $x = 0.8$ ($x = \alpha - 1$, where $\alpha = 2.35$ is the Salpeter (1955) IMF index) over the whole stellar mass range. On the other hand, the IGIMF adopting $\beta = 2$ is very similar to the Salpeter (1955) (hereafter Salpeter) IMF over most of the stellar range, except at very high SFR values (> 100 M$_\odot$ yr^{-1}).
Concerning the IGIMF calculated at low SFR values (1 M$_\odot$ yr^{-1}), it shows an uniform decline with mass and the shape of a double-power law, with a knee located at 0.5 M$_\odot$. At low SFR values, a cut-off is visible at masses larger than ~ 100 M$_\odot$, where the decrease is steeper and where the behaviour is similar to the IGIMF as shown in, e.g. Recchi et al. (2009).

In general, the higher the SFR value, the flatter IGIMF, the higher the relative number of massive stars, as due to increasing $M_{ecl,max}$ values with increasing SFR. Moreover, the lower the β value, the stronger the IGIMF dependence on the SFR.

3.2.4 Results

In the following, we show the results of our tests on the effects of the IGIMF on the main global properties of galaxies of various masses, including the SF and the SN rates, the evolution of the gas, stellar and dust mass budget and the metal abundances. The calculated elemental abundance ratios are also compared to the values observed in high-redshift starburst galaxies. This comparison can be used also to better constrain the nature of these galaxies and to analyse the interplay between IMF and dust in shaping the abundance patterns.

The effects of the IGIMF

In this first part, we focus on the effects that the W11 IGIMF has on the evolution of the main physical properties and chemical abundance patterns in the modelled starburst galaxies. We dedicate a first paragraph to the description of the changes produced by the IGIMF on the history of star formation, while a second paragraph is devoted to the analysis of the resultant total (gas+dust) interstellar abundance patterns for these objects.

Star formation history

In Figs. 3.6, 3.7 and 3.8 we show the impact of the IMF on the evolution of the SFR, Type Ia and CC-SN rates, as well as gas, stellar mass and energetic budget for the starburst models of Tab. 3.5.
All the models presented in Figs. 3.6, 3.7 and 3.8 are characterised by star formation efficiencies of 5, 10 and 20 Gyr^{-1}, respectively. The fact that in each figure the SF efficiency is constant allows us to single out the effects of the IMF on the global properties of a galaxy of a particular mass.

It is evident that the star formation histories reported in Fig. 3.6, 3.7 and 3.8 are strongly dependent on the adopted IMF. In general, the models computed adopting the W11 IGIMF exhibit larger SFR values than the ones computed with a Salpeter IMF. This can be explained by the fact that a top-heavy IMF implies larger mass ejection rates from evolved stellar populations, and in particular from massive stars, with consequently larger gas mass reservoirs at any time, which also imply larger SFR values (for Eq. (2.4)).

The differences in star formation histories determine also the conditions for the onset of a galactic wind, and consequently the time at which the star formation stops. We note that the steepest IGMFs ($\beta = 1.6$ and $\beta = 2$) produce winds at the earliest times. In the case $\beta = 1$, the galactic wind occurs later than in the cases with $\beta > 1$ because of the larger binding energy of the gas compared to the other models. This happens in spite of the very high number of CC-SNe, which is roughly proportional to the SFR value.
By comparing Fig. 3.6 and 3.7, it is worth noting that a later occurrence of galactic winds in less massive galaxies, i.e. the downsizing in star formation as obtained by Matteucci (1994) by means of the "inverse wind model", cannot be reproduced by adopting the IGIMF with $\beta = 1$, and this occurs despite of a higher efficiency of star formation for the larger mass model. The "inverse wind" effect is instead visible in the models adopting the Salpeter IMF as well as for the case $\beta = 2$ and $\beta = 1.6$ IGIMF. It is worth reminding that the in Matteucci (1994) the winds occuring at earlier times in massive galaxies were obtained by increasing the efficiency of SF with galactic stellar mass, as we assume here, and with a constant Salpeter IMF, and that this scenario allows us to reproduce the observed increase of the integrated [α/Fe] with galactic stellar mass in ellipticals (see Thomas et al. 2010).

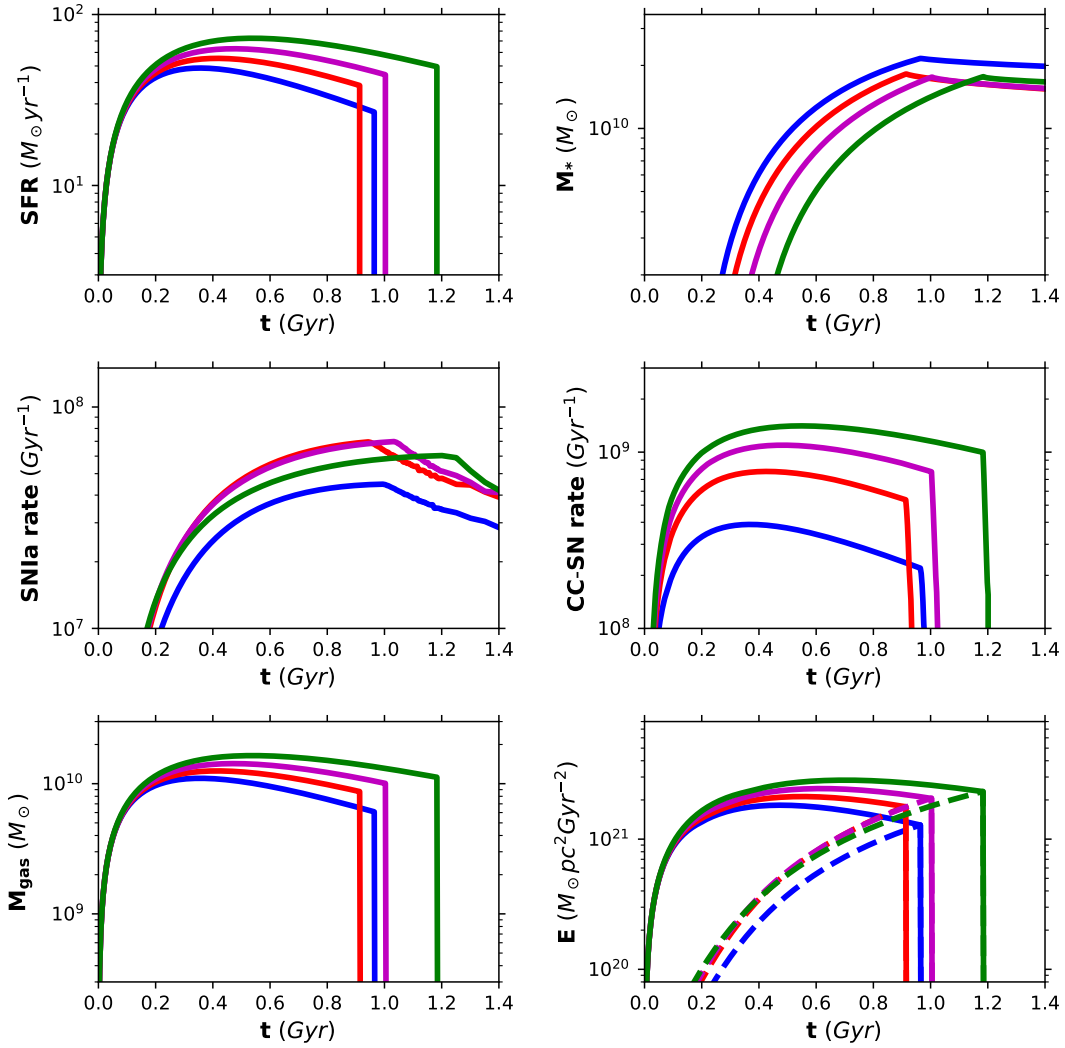

Figure 3.6: *From top-left corner, clockwise: time evolution of the SFR, stellar mass, CC-SN rate, energetic budget, gas mass and Type Ia SN rate obtained for the M3E10 model (see Tab. 3.5) with a Salpeter IMF (blue lines) and W11 IGIMF calculated for $\beta = 1$ (green lines), $\beta = 1.6$ (magenta lines) and $\beta = 2$ (red lines). The sharp truncation in the SFR, CC-SN rate and gas mass are due to the onset of the galactic wind, which devoids the galaxy from the residual gas. In the energetic budget plot, the solid lines represent the binding energy and the dashed lines the thermal energy in all the different models.*

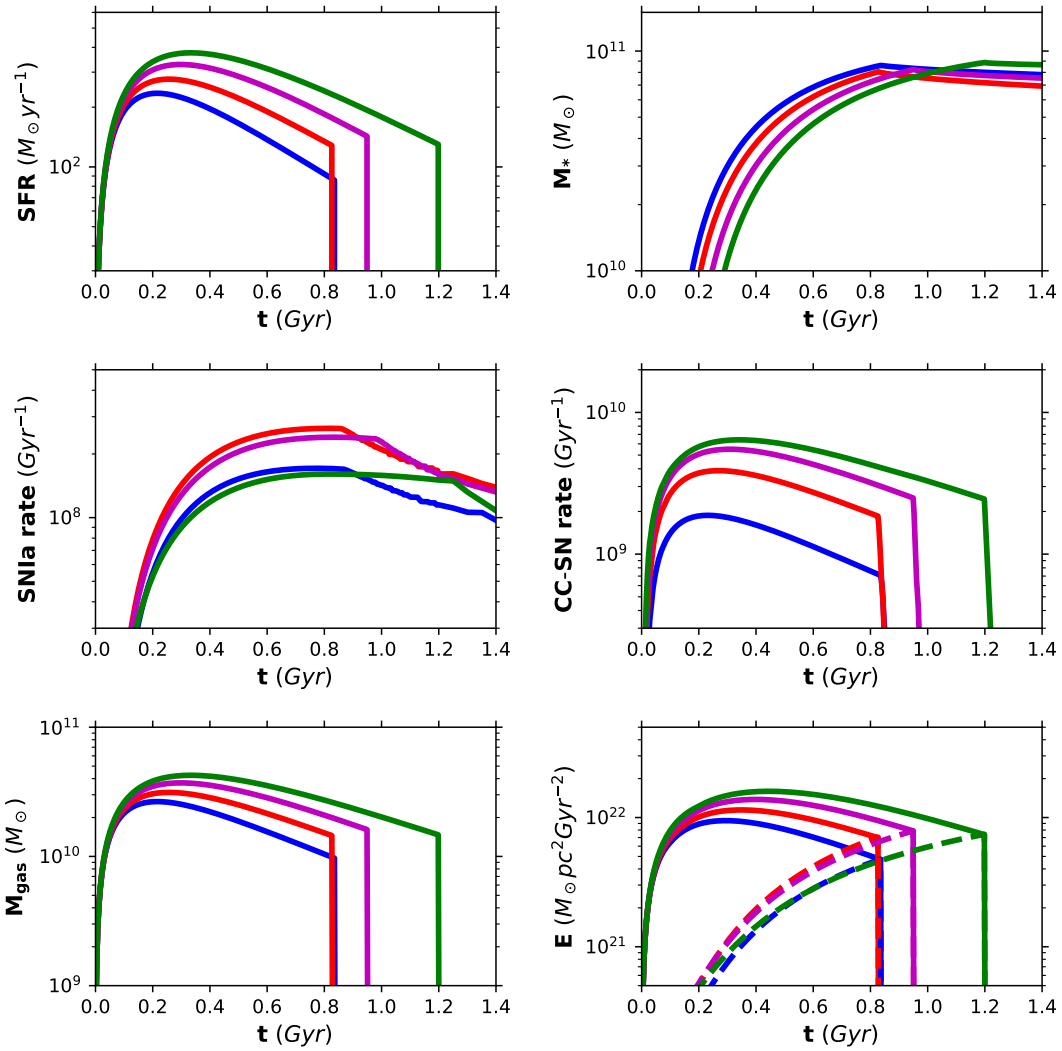

Figure 3.7: *Lines are as in Fig. 3.6, but computed for the M1E11 model of Tab. 3.5.*

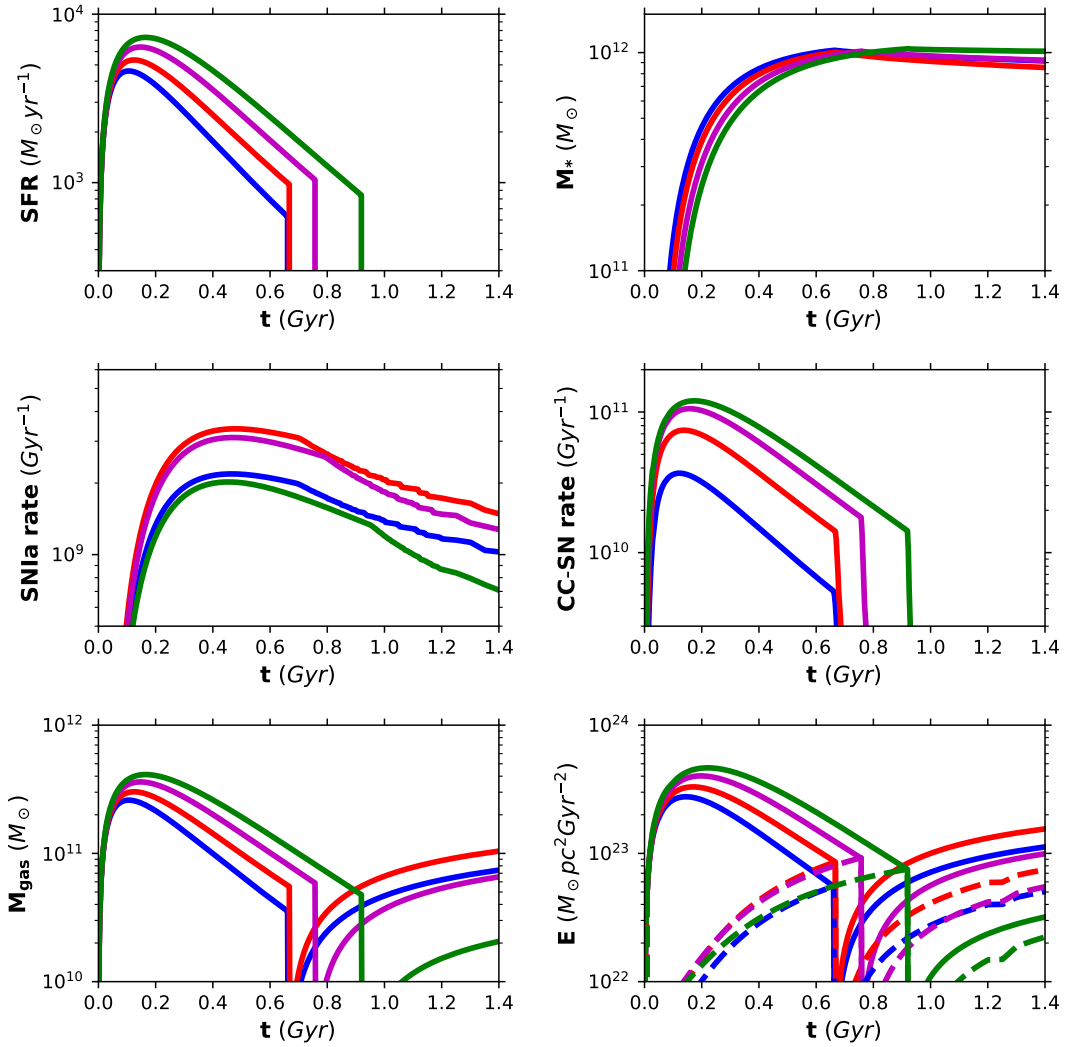

Figure 3.8: *Lines are as in Fig. 3.6, but computed for the M1E12 model of Tab. 3.5.*

In Fig. 3.8 the behaviour of M1E12 models is shown. The results are very similar to what found for M1E11 models. The same trends shown by the M1E11 and M1E12 models are explained by the similar IGIMFs, in particular at SFRs $\psi > 100$ M$_\odot$ yr^{-1} (see Figure 3.5). In fact, the adopted assumption of an upper mass limit for the maximum mass of stellar clusters ($M_{ecl,max}$) attenuates the dependence of the IGIMF on the SFR at very high ψ values ($\gtrsim 500$ M$_\odot$ yr^{-1}).

Looking at the lower left panel in Fig. 3.8, it can be seen that large amounts of gas are restored into the ISM after the onset of the galactic wind. The same behaviour is not shown by the lower mass models (Figs. 3.6 and 3.7), where the thermal energy of the gas after the galactic wind is always larger than its binding energy (i.e. situation of a continuous wind, see 2.1.4).

Another interesting aspect of Fig. 3.8 is that the model with $\beta = 1$ gives a Type Ia SN rate which is much lower than the one obtained with the Salpeter IMF, at variance with what shown in Fig. 3.6 and, although to a lesser extent, 3.7. However, this is expected from Fig. 3.5, where we have seen that the most extreme differences between the Salpeter IMF and the IGIMF were found when the lowest value for β was adopted together with the highest SFR values. Under such extreme conditions, an IMF remarkably light in low-intermediate mass stars, i.e. in the mass range of Type Ia SNe progenitors, is possible, thus balancing the much larger SFR obtained by adopting such an IMF relative to the Salpeter one.

Chemical abundances

In Fig. 3.9, we show the predicted [O/Fe] vs. [Fe/H] plots computed for the M3E10 models with the IGIMF for different values of β (green, red and magenta lines) as well as for the M3E10, M1E11, M1E12 models with a Salpeter IMF (blue lines).

A striking feature of Fig. 3.9 is that at a certain metallicity [Fe/H] W11 IGIMF produces larger [O/Fe] values than the Salpeter IMF. This is evident by looking at the different levels of the plateau in the [O/Fe] vs. [Fe/H] relation obtained with the M3E10 model assuming different IMFs: at low metallicity ([Fe/H] ≤ -1.5), higher [O/Fe] values are obtained assuming lower β values (i.e. with IMFs heavier in massive stars). Also the slope of the [O/Fe] vs. [Fe/H] relation is dependent on the IMF, with a progressively steeper decrease from $\beta = 1$ to the Salpeter IMF. These two features can be attributed to the O yield dependence on stellar mass: the larger the mass, the larger the O yield (e.g. Woosley & Weaver 1995; Limongi & Chieffi 2003). Therefore, a top-heavier IMF favours a larger overabundance of oxygen over iron.
A larger extension of the [α/Fe] plateau for lower β values is also seen in the Figure. This is again due to a larger number of massive stars, which are the first to enrich the ISM with Fe. As explained by the "time-delay model" (Matteucci 2001, 2012, see 1.3.1), the larger

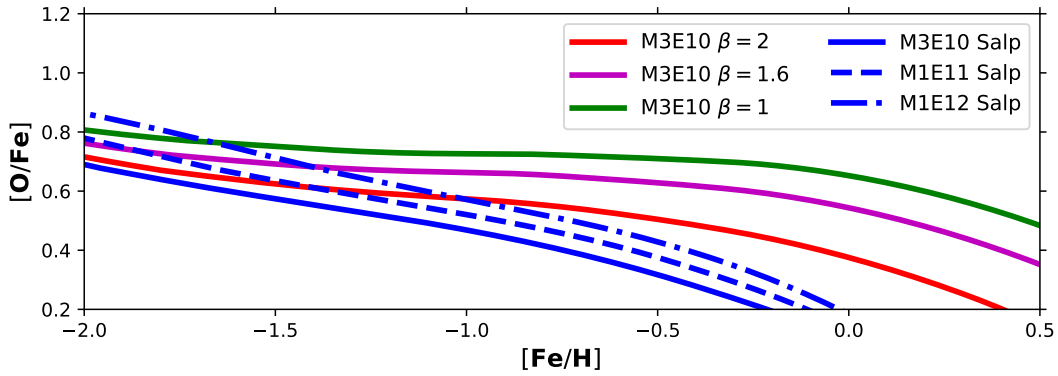

Figure 3.9: *Predicted evolution of the interstellar [O/Fe] vs. [Fe/H] relation. Lines are computed for: M3E10 models (solid) with Salpeter IMF (blue) and W11 IGIMF calculated for $\beta = 1$ (green), $\beta = 1.6$ (magenta) and $\beta = 2$ (red); M1E11 model with Salpeter IMF (dashed blue); M1E12 model with Salpeter IMF (dash-dotted blue).*

the fraction of massive stars, the higher the metallicity value (as traced by [Fe/H]) at which Type Ia SNe start to contribute significantly to the Fe enrichment, thus the higher is the [Fe/H] value for the change in slope of the [O/Fe] vs. [Fe/H] relation.
We also note that in the models adopting the IGIMF, [α/Fe]> 0.2 dex, as traced by O, extends to much higher metallicity than the Salpeter IMF, reaching values much larger than the solar metallicity.

As mentioned above, in Fig. 3.9, we also show the results of the M1E11 and M1E12 models obtained for a Salpeter IMF. An increase in galactic mass and SF efficiency leads to larger [O/Fe] values at low metallicity ([Fe/H]~ -2). On the other hand, the much larger SFR values in these models do not affect substantially the slope of the [O/Fe]-[Fe/H] relation: in spite of the fact that the [α/Fe] value of the most metal-rich extreme of the plateau is progressively shifted towards higher metallicity, the changes produced by the adoption of the IGIMF are of much larger extent.
This latter observation is quite important, because it rules out that the increase of the SFR caused by the W11 IGIMF is playing a significant role in shaping the abundance patterns. The key role in this task is done by the shape of the IMF itself.

A direct comparison with high-z starbusts: IMF or dust?

Having described the main effects of the W11 IGIMF on the predicted main physical and abundance properties of starburst galaxies, we now compare the model abundance patterns with the observed abundances of Table 3.4.

We divide the discussion into two parts. First, we study the behaviour of abundance ratios of volatile elements, namely the elements which are not negligibly depleted from

the gas phase by dust (e.g. N and O, see Jenkins 2009[4]) that do not need any particular dust treatment in the models (but see also Steigman et al. 2007). Then, we compare the data with model abundance ratios for refractory elements, i.e. elements more affected by dust depletion, such as C, Mg, Si, Fe. For these latter, the diverse dust prescriptions setups described in Tab. 3.6 are adopted: in this way, we can possibly better understand the issue of dust in high-redshift galaxies (see 3.2.1).

Volatile elements

We start our analysis by looking at the (N/O) vs. (O/H) relation, visible in Fig. 3.10. As described in 3.2.3, the analysis of N deserves special attention, since its primary or secondary nature at low metallicity is still debated. For this reason, in Fig. 3.10 we show models computed with different N yields: the Matteucci (1986) ones (thick lines), assuming that all massive stars produce primary N, and the Meynet & Maeder (2002) yields (thin lines), that allow for the production of primary N only in rotating massive low metallicity stars.
As for observational data, it is worth stressing that the variation in $\log$(O/H)+12 for a given system due to a different metallicity indicator is typically ≤ 0.2 dex. As for the theoretical abundances, here we show only the results obtained for the M3E10 and M1E11 models. We omit the the M1E12 model as it is characterised by SFR values much larger than the ones observed in the systems of our dataset.

In Fig. 3.10 we see that in the case of the yields for primary N of Matteucci (1986) (thick lines), the adoption of the IGIMF leads to lower (N/O) values at metallicity $\log$(O/H) +12 $\gtrsim 7$ with respect to the Salpeter IMF. The variations between the abundances obtained with the Salpeter IMF and the ones obtained with the IGIMF increase with metallicity, and in general the lower the β, the larger the variation. Looking at Fig. 3.10 left panel, a maximum variation of ~ 0.4 dex between the Salpeter and IGIMF models is visible at $\log$(O/H)+12$= 9$ in the case of $\beta = 1$ for the M3E10 model. However, the M3E10 model shows very limited variations at lower metallicities ($\log$(O/H) +12$\lesssim 7$).
On the other hand, larger (N/O) variations between the Salpeter IMF and IGIMF are visible at all metallicities in the case of the M1E11 model. In particular, the predicted $\log$(N/O) values span a range of ~ 0.6 dex at $\log$(O/H)+12$= 9$, as visible from Fig. 3.10 right panel. Moreover, we also see that at $\log$(O/H)+12$\lesssim 7.5$ larger $\log$(N/O) are obtained by adopting the M1E11 model with the IGIMF, at variance with the M3E10 model in the left panel.

By looking at the chemical evolution tracks predicted by means of the Meynet & Maeder (2002) yields (thin lines in Fig. 3.10), we can draw similar conclusion to those obtained with the yields of Matteucci (1986): a metallicity-dependent increase of the vari-

[4]for O, Jenkins (2009) estimated dust depletion up to ∼0.25 dex. However, the reference solar value that he adopted is ∼0.1 dex larger than the current adopted value (Asplund et al. 2009). This may suggest lower dust depletion.

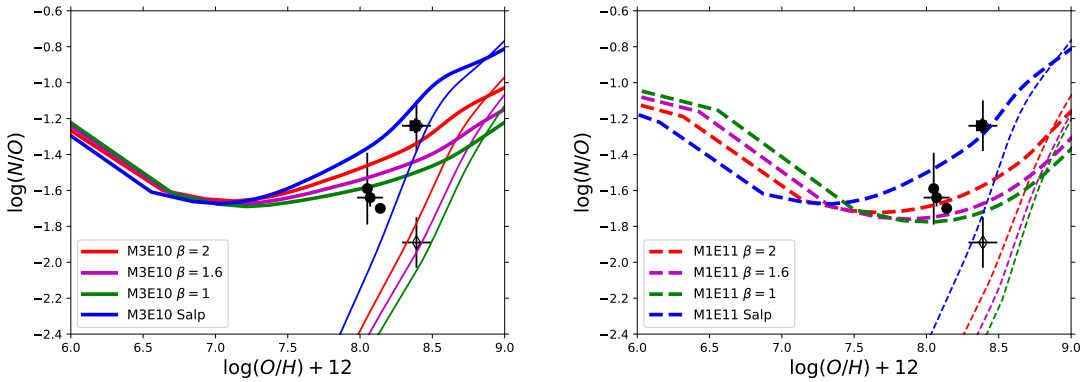

Figure 3.10: *Predicted* log*(N/O) vs.* log*(O/H)+12 adopting Matteucci (1986) (thick lines) and Meynet & Maeder (2002) (thin lines) yields for N compared with abundances measured in galaxies of the sample of Tab. 3.4. Left panel: lines are computed for M3E10 models (solid) with Salpeter IMF (blue) and W11 IGIMF calculated for* $\beta = 1$ *(green),* $\beta = 1.6$ *(magenta) and* $\beta = 2$ *(red). Right panel: lines are computed for M1E11 models (dashed) with a Salpeter IMF (blue) and W11 IGIMF calculated for* $\beta = 1$ *(green),* $\beta = 1.6$ *(magenta) and* $\beta = 2$ *(red). For both panels: data are from Steidel et al. (2016) stacked spectum (filled square); Rigby et al. (2011), Bayliss et al. (2014), Christensen et al. (2012a, 2012b) (filled circles); Pettini et al. (2002) (thin diamond) and Teplitz et al. (2000) (thick diamond).*

ation between the (N/O) obtained with the Salpeter and the IGIMF is observed also in this case. However, this increment is less evident, especially in the case of the M1E11 models (Fig. 3.10 right panel).

As for the comparison between the abundances observed in the high-redshift sample of Tab. 3.4 and models, we observe that without the primary N yields as suggested by Matteucci (1986) it would be very difficult to explain the (N/O) values measured in four out of the five systems whose data are shown in Fig. 3.10. Furthermore, we note that only for cB58 (Pettini et al. 2002, thin diamond) the yields of Meynet & Maeder (2002) produce a better agreement. For this galaxy, N/O ratio is also derived by adopting different spectral features (Teplitz et al. 2000, thick diamond), finding values in agreement also with the models computed using Matteucci (1986) prescriptions.
This reinforces the results found in previous studies, i.e. the need of at least a non-negligible primary N component in massive stars to reproduce the (N/O) values measured in star-forming galaxies in the Local Universe (e.g. Israelian et al. 2004; Vincenzo et al. 2016).

For what concerns the IMF issue, Fig. 3.10 outlines the role of the adopted IMF in determining the interstellar abundance pattern. However, it is still difficult to disentangle between the effects due to the IMF and due to nucleosynthesis prescriptions.

In summary, the comparison between the data and models discussed here provides useful suggestions regarding the nucleosynthesis of the volatile elements N and O. However, the analysis of the observational data is not conclusive on whether the W11 IGIMF should be preferred over the Salpeter IMF to reproduce these particular abundance ratios. To this purpose, more insights are provided by the study of the abundance ratios between refractory elements, described in the following.

Refractory elements

Figs. 3.11, 3.12, and 3.13 show the predicted (C/O) vs. (O/H), [Si/Fe] vs. [Fe/H], [Mg/Fe] vs. [Fe/H] and [O/Fe] vs. [Fe/H] relations, respectively, each one computed without taking into account dust depletion in the ISM. In Figures left and right panels, we plot the results for M3E10 and M1E11 models, compared to the observed abundances from the dataset presented in 3.2.2 .
As for volatile elements, we do not show the results of the M1E12 model computed using the IGIMF. Nonetheless, in this case we show in right panels the results obtained by means of the M1E12, Salpeter IMF model for the sake of clarity.

In Fig. 3.11 left panel the (C/O) vs. (O/H) relation of the M3E10 models is shown. Here we see that varying the IMF does not produce any significant change in the predicted abundance pattern: the effects produced by adopting different IMFs tend to cancel out, thus producing a very similar behaviour of the abundance ratio vs. metallicity. Similar conclusions can be drawn from the analysis of the results for the M1E11 models (Fig. 3.11 right panel), with the only difference that in this case the IGIMF produces higher (C/O) values than the Salpeter IMF only at low metallicity (log (O/H)+12$\lesssim$7.5), e.g. in the case of $\beta = 1$ higher by up to a few 0.1 dex at $\log$(O/H)+12 $\sim$ 6.7, with decreasing differences at increasing metallicity.

The data-model comparison of Fig. 3.11 highlights that all the models fall in the confidence region derived by stacked spectra by Shapley et al. (2003) and the sample of $z \sim 3$ LBGs of Pettini et al. (2001). In fact, the differences between models with Salpeter and IGIMF, where present, fall outside of the observational data range, which does not allow us to prefer any model in particular.

A disagreement between data and models is instead observed in Fig. 3.12, where the observed and predicted [Si/Fe] vs. [Fe/H] relations are shown. In the left panel of Fig. 3.12, the theoretical abundances predicted by M3E10 models lie below the error bar of two out of three data points by at least 0.1 dex. Only the M3E10 model with the most extreme IMF ($\beta = 1$ IGIMF) lies slightly below the highest metallicity point. The same point shows a marginal overlap between its errorbar and the M1E11 model with $\beta \leq 1.6$, as shown in Fig. 3.12 right panel. However, the remaining data cannot be explained by

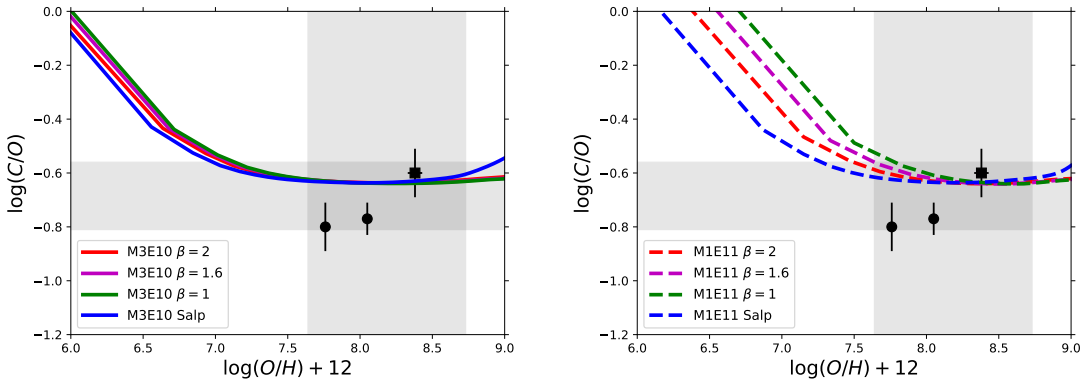

Figure 3.11: *Predicted* $\log(C/O)$ *vs.* $\log(O/H)+12$ *computed without taking into account dust depletion and compared with abundances measured in galaxies of the sample of Table 3.4. Left panel: lines are computed for M3E10 models (solid) with Salpeter IMF (blue) and W11 IGIMF calculated for* $\beta = 1$ *(green),* $\beta = 1.6$ *(magenta) and* $\beta = 2$ *(red). Right panel: lines are computed for M1E11 models (dashed) with Salpeter IMF (blue) and W11 IGIMF calculated for* $\beta = 1$ *(green),* $\beta = 1.6$ *(magenta) and* $\beta = 2$ *(red). For both panels: the shaded regions indicates the* $\log(C/O)$ *confidence region derived from the composite LBG spectrum of Shapley et al. (2003) and the* $\log(O/H)+12$ *characterising the sample of LBGs of Pettini et al. (2001). Other data are from Steidel et al. (2016) stacked spectum (filled square), Bayliss et al. (2014) and Christensen et al. (2012a, 2012b) (filled circles).*

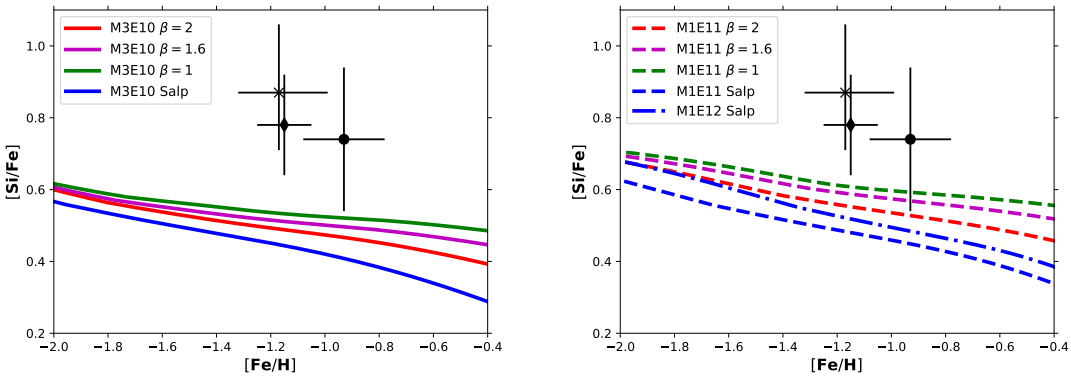

Figure 3.12: *Same of Fig. 3.11, but for [Si/Fe] vs. [Fe/H]. Left panel: lines are computed for M3E10 models (solid) with Salpeter IMF (blue) and W11 IGIMF calculated for* $\beta = 1$ *(green),* $\beta = 1.6$ *(magenta) and* $\beta = 2$ *(red). Right panel: lines are computed for M1E11 models (dashed) with Salpeter IMF (blue), W11 IGIMF calculated for* $\beta = 1$ *(green),* $\beta = 1.6$ *(magenta) and* $\beta = 2$ *(red); M1E12 model with Salpeter IMF (blue dash-dotted). For both panels: data are from Pettini et al. (2002) (diamond); Quider et al. (2009) (cross); Dessauges-Zavadsky et al. (2010) (filled circle).*

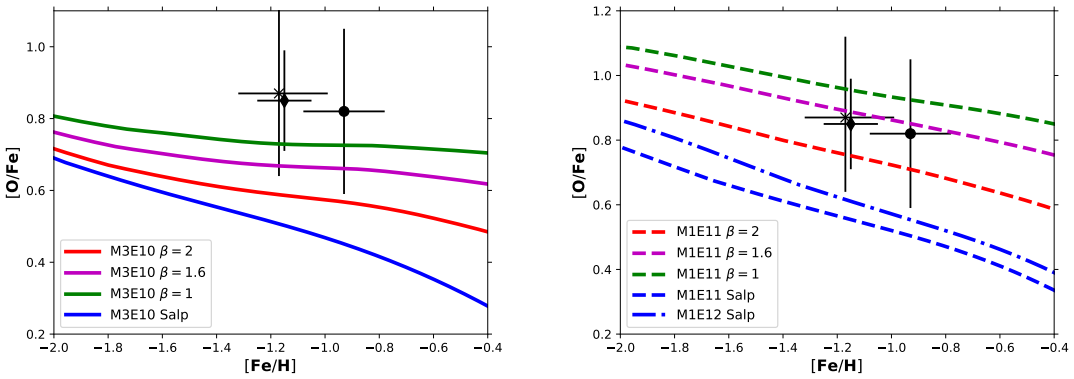

Figure 3.13: *Same of Fig. 3.11, but for [O/Fe] vs. [Fe/H]. Left panel: lines are computed for M3E10 models (solid) with Salpeter IMF (blue) and W11 IGIMF calculated for $\beta = 1$ (green), $\beta = 1.6$ (magenta) and $\beta = 2$ (red). Right panel: lines are computed for M1E11 models (dashed) with Salpeter IMF (blue), W11 IGIMF calculated for $\beta = 1$ (green), $\beta = 1.6$ (magenta) and $\beta = 2$ (red); M1E12 model with Salpeter IMF (blue dash-dotted). For both panels: data are from Pettini et al. (2002) (diamond); Quider et al. (2009) (cross); Dessauges-Zavadsky et al. (2010) (filled circle).*

any of the models in the panel.

As for Fig. 3.12, an evident disagreement between the model results and the data is also present for the [Mg/Fe] vs. [Fe/H] relation. However, we have to say that the availability of [Mg/Fe] for only one system places some limits in the analysis of this abundance ratio. For this reason, we decide to avoid plotting the [Mg/Fe] vs. [Fe/H] abundance diagram.

For what concerns [O/Fe], the comparison between data and models is shown in Fig. 3.13. In the left panel, we see that the observed [O/Fe] values are generally higher than the ones predicted by the M3E10 models. However, the results obtained with the IGIMF adopting $\beta \leq 1.6$ lie within the observational errors. The abundances predicted by the M1E11 models adopting the IGIMF are instead in good agreement with the observed [O/Fe] values, as shown in Fig. 3.13 right panel. On the other hand, the Salpeter IMF produces [O/Fe] values outside of the error bars of the data for all the three tested models. Even the sligthly α-enhanced ratios predicted by the M1E12 models are inconsistent with the data.

In summary, as for the [α/Fe] vs. [Fe/H] diagrams, the Si and Mg abundances computed with any of our models without taking into account dust production are generally lower than the ones observed in high-redshift lensed galaxies, whereas the O abundances derived with the models which include the IGIMF are in rather good agreement with the data.

In Figs. 3.14, 3.15 and 3.16 we show instead the results of our models computed taking into account the effects of dust depletion for the (C/O) vs. (O/H), [Si/Fe] vs. [Fe/H] and [O/Fe] vs. [Fe/H] diagrams, respectively. In each figure, the top and bottom rows show the results of the chemical tracks derived from the M3E10 and M1E11 models, respectively, with each column reflecting one of the prescriptions listed in Tab. 3.6. The tracks in these Figures trace the evolution of abundance ratios in the gas phase only, since these models are able to trace separately the abundances in the gas and dust phases. In this way, for the first time in literature, we can study the effects of dust on chemical evolution models adopting an IGIMF.
As for Figs. 3.11, 3.12 and 3.13, the models in Figs. 3.14, 3.15 and 3.16 are compared with abundance data presented in Tab. 3.4.

In Figs. 3.14, 3.15 and 3.16, we observe that the effects of dust depletion increase as one moves from left to right. In fact, in each figure the leftmost plot shows the results of our 'minimal dust' models, which take into account dust destruction and the reverse shock in SNe dust yields, dubbed DR, with all the other processes switched off. The middle plot shows results for models in which dust depletion has moderate effects and which includes accretion, destruction and no reverse shock (ADNR). The rightmost plot shows the results for our 'maximal dust' models, which include only dust production from stars with no reverse shock in SNe (NR).
We have tested also the other models of Tab. 3.6. These are not shown here because of their similar behaviour to models of Figs. 3.14, 3.15 and 3.16. In particular, the models including dust production in stars with reverse shock in SNe (R) and accretion, destruction and reverse shock (ADR) have small differences in comparison with data points relative to the DR model. Another case in which dust depletion has intermediate effects is the model with destruction but no reverse shock (DNR), which produces results similar to the ADNR model.

In Fig. 3.14, the minimal dust DR models show a small but yet appreciable difference with respect to the ones of Fig. 3.11. An evident consequence of including dust depletion is to decrease the (C/O) ratio, as C is refractory and O is not. For this reason, the (C/O) values of the DR models of Fig. 3.14 are at maximum ~ 0.1 dex lower than the ones of Fig. 3.11, with a small dependence on metallicity, i.e. with increasing depletion effects at larger values of $\log$(O/H)+12.

The ADNR and NR models show larger C depletion effects and lower (C/O) values. In particular, the ADNR M3E10 models fall below the dark gray confidence region defined by the range of abundance values from the composite LBG spectra (Shapley et al. 2003), but are still consistent with the values measured in the lensed galaxies SGAS J105039.6+001730 and SMACS J2031.8-4036 (Bayliss et al. 2014; Christensen et al. 2012a,b). As for the M1E11 models, the abundances obtained in most of the ADNR

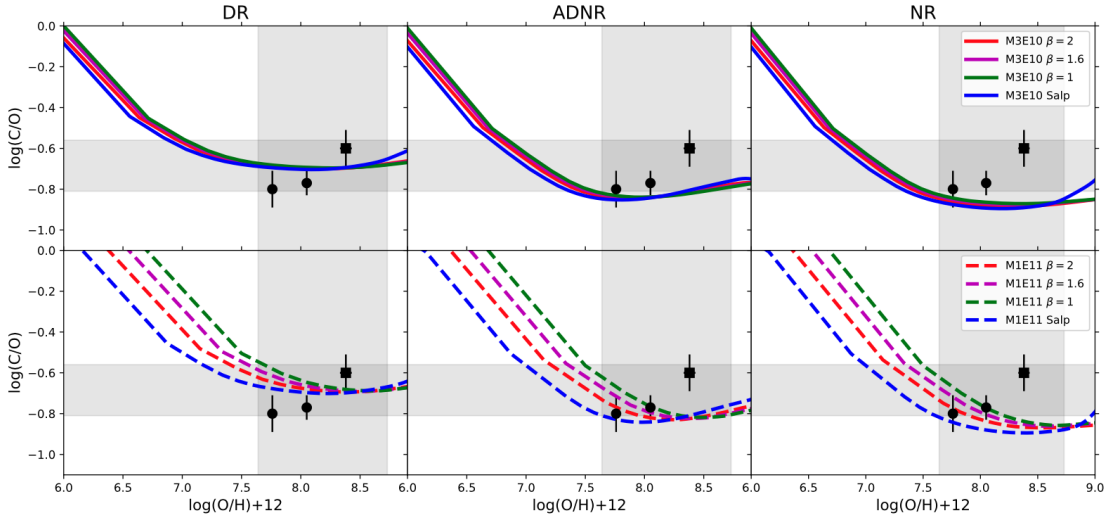

Figure 3.14: *Same of Figure 3.11, but with models considering dust.*

models are by 0.1-0.15 dex lower than the DR models, all still consistent with the composite spectra confidence region. The results for the NR models are globally similar to the ones obtained in the case of the ADNR models.

As for the [Si/Fe] vs. [Fe/H] relation, Fig. 3.15 upper left panel shows that all the M3E10 minimal dust models still underestimate the observed abundances. The models with the IGIMF show higher [Si/Fe] ratios, with the difference from the data decreasing with decreasing β values, thus indicating that the abundance pattern of lensed high-z systems might show some signatures of a top-heavy IMF. However, it is possible that the IMF is rather Salpeter-like and the effects of dust are important. If this is the case, these latter are clearly underestimated by our DR models.

All the ADNR models account satisfactorily for the observed abundances, in particular the Salpeter and the IGIMF, $\beta = 2$ model. On the other hand, all the NR models in which the IGIMF is adopted overestimate the observed abundances, although the abundances of the $\beta = 2$ model are within the $1 - \sigma$ error bars of two systems.
Similar suggestions come from the analysis of the M1E11 model results on Fig. 3.15 lower row. ADNR and DR models show more enhanced [Si/Fe] abundance ratios but still support a Salpeter-like IMF, or suggest that an IGIMF with $\beta < 2$ in the observed systems should be excluded.

Also in the case of the [O/Fe] vs. [Fe/H] diagram (Fig. 3.16), all the minimal dust M3E10 models underestimate the observed abundances. However, $\beta < 2$ IGIMF models

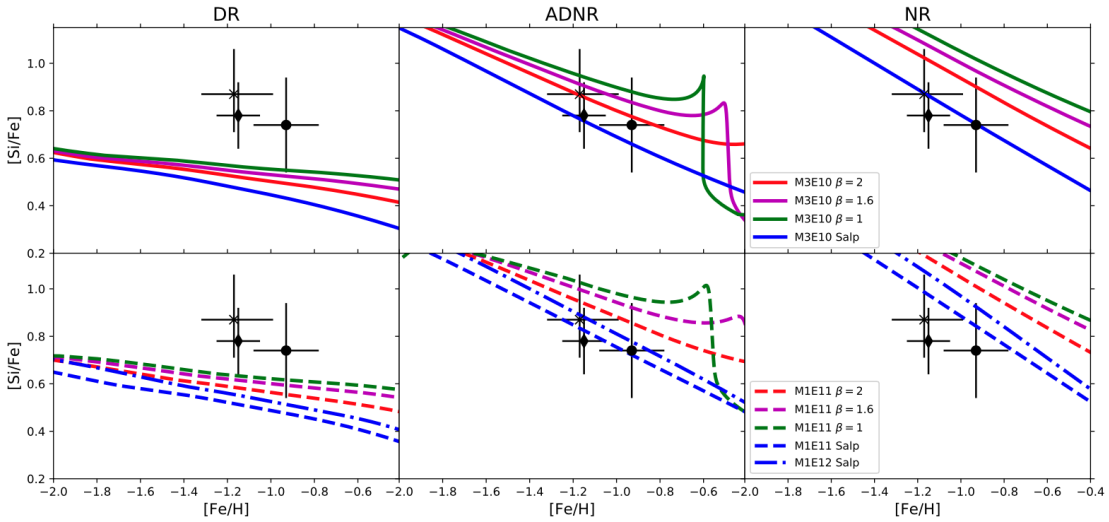

Figure 3.15: *Same of Figure 3.12, but with models considering dust.*

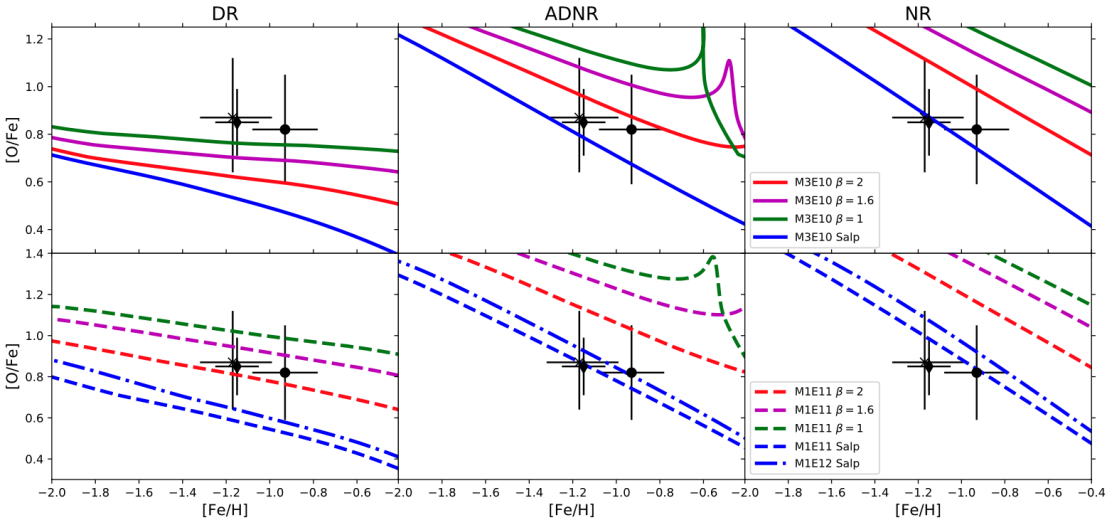

Figure 3.16: *Same of Figure 3.13, but with models considering dust.*

yield abundance values within the error bars, at variance with Fig. 3.15. On the other hand, all the M1E11 IGIMF models show abundance ratios consistent with the observations. In both cases, the models with the Salpeter underestimate the observed abundance pattern.

In all the other models, where the effects of dust are more significant, the M3E10 models support a Salpeter IMF or a moderate top-heavy (IGIMF with $\beta < 2$) in high-redshift galaxies, whereas all the M1E11 models with dust exclude the IGIMF.

Discussion on the interplay between dust and IMF

By looking at Figs. 3.11-3.16, we note that either the effects of the IGIMF or dust can explain the observed abundances in our sample of high-redshift starbursts. In particular, if one focuses on a single mass model (M3E10 or M1E11), our study shows that the effects of dust may produce variations in the abundance ratios even larger than the ones driven by a different IMF.
If the effects of dust are marginal in our sample of high-redshift galaxies, our IGIMF models account for the observed abundance pattern better than the ones with a Salpeter IMF. On the other hand, if the effects of dust are moderate or high even in the very first stages of evolution, the models with a Salpeter IMF or with the IGIMF with $\beta = 2$ allows us to reproduce the data, whereas the others with more extreme IGIMF assumptions (i.e. $\beta \leq 1.6$) do not.

It is worth noting that previous chemical evolution studies including dust failed in reproducing the observed gas abundances in high-redshift starbursts by adopting a Salpeter IMF (e.g. Pipino et al. 2011 with cB58). However, these previous results are not against our conclusion that significant dust depletion can explain the observed abundance patterns without invoking a top-heavy IMF.
In fact, previous works did not consider dust differential depletion, i.e. different elements depleted in dust in different proportions. In this work, instead, the use of elemental dust yields dependent on the mass and metallicity of the stars allows us to account for the differential dust depletion effect.
It has also to be highlighted that in this Section we compare for the first time an extended database of measured abundances of different chemical elements from lensed galaxies with results from detailed chemical evolution models. More observations are certainly needed in the future to shed more light on how the combined effects of dust depletion and IMF determine the abundance pattern of high-redshift galaxies.

To look at the interplay between dust and the IMF more in detail, in Fig. 3.17 we show the time evolution of the dust mass for our models with the Salpeter IMF and with the W11 IGIMF, all computed adopting dust prescriptions as in the ADNR model (i.e. the model with moderate dust depletion effects in Figs. 3.14-3.16). Fig. 3.17 is useful to assess the timescale for the buildup of dust and what is the role of the IMF in this process.

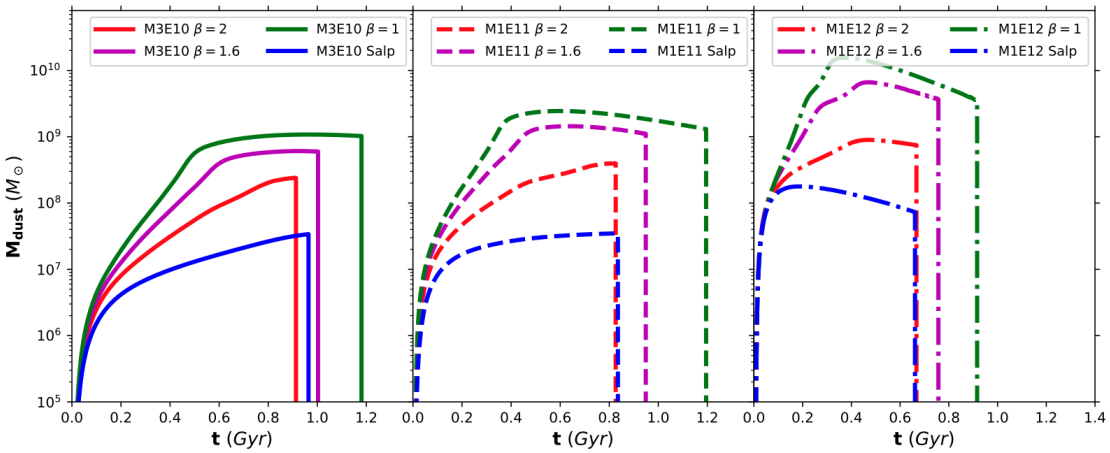

Figure 3.17: *Dust mass as a function of time for our models computed with a Salpeter IMF (blue lines) and with W11 IGIMF with $\beta = 1$ (green lines), $\beta = 1.6$ (magenta lines) and $\beta = 2$ (red lines). In the left, middle and right panel we show our results computed for the M3E10 (solid lines), M1E11 (dashed lines) and M1E12 (dash-dotted lines) models, respectively.*

In all models, a progressively steeper increase of the dust mass as a function of time is found for the IGIMF as the value of β decreases. This highlights that a top-heavy IMF produces not only a larger dust content, but also a faster dust mass buildup.
As discussed in previous works (Mattsson 2011, 2015; Gall et al. 2011b; Gioannini et al. 2017b), a fast growth of dust goes in lockstep with a rapid buildup of refractory elements, and this is clearly strongly dependent on the history of star formation. In particular, in starburst galaxies the buildup of metals occurs on a particularly rapid timescale, with a supersolar metallicity reached already at $\sim$0.1 Gyr (e.g. Calura et al. 2014). In fact, also in the case of a Salpeter IMF, in the M1E11 and M1E12 models the bulk of dust mass is already present at $\sim$0.25 Gyr after the beginning of star formation: clearly, the rapid buildup of the dust also depends on the infall timescale, shorter in larger systems.

With these particular prescriptions for dust, however, the dust mass values attained with a Salpeter IMF after a few 0.1 Gyr are generally between $\sim 10^7$ and $\sim 10^8$ M$_\odot$, lower than the values observed in a large fraction of galaxies in the *Herschel* sample at comparable redshift, which in many cases show dust masses larger $> 10^8$ M$_\odot$ (Calura et al. 2017; Pozzi et al. 2020), as well as in extremely high-redshift sub-mm galaxies (e.g. Marrone et al. 2018; Zavala et al. 2018). The same does not happen for the models adopting the IGIMF. For these models, dust masses in excess of 10^8 M$_\odot$ are generally predicted. For the lowest β values (i.e. top-heaviest IMF), these masses are reached in considerably small times of around 0.2 Gyr.
This latter result is apparently in contrast with what found for abundance patterns. How-

ever, uncertainties in the abundance data and in the elemental dust yields (e.g. Gall & Hjorth 2018 and references therein) have to be considered. Furthermore, in general, models with a moderate top-heavy IGIMF (i.e. β=2) reasonably satisfy both the abundance and dust mass constraints.

The necessity to adopt a top-heavy IMF to solve the "dust-budget crisis" (Rowlands et al. 2014) was already discussed by other authors (Mattsson 2011; Gall et al. 2011b; Valiante et al. 2014 and references therein). However, this aspect was never highlighted before in the context of the IGIMF.
Moreover, in this study we analyse in detail the interplay between various parameters, including the IMF, in determining the abundance pattern in high-redshift galaxies and how these parameters influence the growth of the dust mass.

Unfortunately, at present, IR-based determinations of the dust mass in LBGs and LAEs in the sample considered in this work are lacking, but it will be valuable in the future to better single out the role of such parameters in determining the properties of high-redshift starbursts.

3.2.5 Conclusions

In this Section, we have analyzed the effects of the integrated galactic IMF (IGIMF, as defined in Weidner et al. 2011) as well as dust condensation on the chemical evolution of high-redshift starburst galaxies.

In the IGIMF theory, in a galaxy the maximum mass of a stellar cluster increases with the SFR. In general, the higher is the SFR value, the larger is the fraction of massive stars (and the flatter is the IGIMF). This can affect several basic properties of galaxies, such as mass return from stellar populations and supernova rates, thus changing the star formation history.
Starburst galaxies, with their intense star formation activity, are ideal candidates to test such an IMF formulation.

We have thus compared the abundance patterns predicted by our chemical evolution models with the abundances observed in the spectra of high-redshift starburst galaxies, mainly Lyman Break Galaxies and Lyman-α Emitters.
To this aim, our models take into account the effects of dust depletion, which can have a strong impact on interstellar abundances and which are fundamental to interpret the observed abundance pattern of these objects.

It is worth noting that the application of dust to chemical evolution models including the IGIMF in this work is the first recorded in the literature.

To conclude, the results obtained can be summarised as follows:

- in all our models, the adoption of the IGIMF causes the increase of the rate of star formation with respect to the Salpeter IMF. In particular, the highest SFRs are obtained with the lowest values for the slope of the embedded cluster mass function β. This is a consequence of the behaviour of the IGIMF: the lower is β, the more top-heavy is the IMF. A high percentage of massive stars, due to a top-heavy IMF, causes large quantities of gas to be restored into the ISM with CC-SN explosions, which in turn favours higher star formation rates (as SFR $\propto$ M_{gas}). On the other hand, we find a longer duration of the star formation phase for lower β values, due to later galactic winds which quench star formation.
  In general, the higher the β value, the smaller the difference in the models with respect to the Salpeter IMF. As for example, in the models with $\beta = 2$, the occurrence of the galactic wind is comparable to the one obtained with a Salpeter IMF.
  For the most extreme assumptions of the β value ($\beta = 1$), we have found a reduced Type Ia SN rate with the IGIMF relative to the Salpeter IMF in model galaxies with 10^{11} and 10^{12} $M_{\odot}$. Moreover, we have found that with $\beta = 1$ the downsizing in star formation, i.e. winds occurring at earlier times in more massive galaxies, is not reproduced in model galaxies between 3×10^{10} and 10^{11} $M_{\odot}$, despite of the adopted higher star formation efficiency for the higher galactic masses;

- the different star formation histories obtained with different IMFs have an impact on the evolution of chemical abundances. For a given galaxy mass, the more top-heavy the IMF (lower β values), the faster is the growth of the metal content. As for the [α/Fe] vs. [Fe/H] diagram, the lower the β, the higher the overabundance of α-elements, and the higher the metallicity at which the [α/Fe] starts to deviate from the initial plateau.
  Our study also highlights the interplay between the IMF and the star formation efficiency in defining the insterstellar abundance pattern. In particular, when the IGIMF is adopted, the lowest mass model can be characterised by values for the α-enhancement larger than what obtained with the Salpeter IMF in the most massive galaxy model, in which a much larger star formation efficiency is adopted;

- we have collected a dataset of chemical abundances measured in high-redshift, strong star forming galaxies. The sample consists of high-quality abundances of several elements (C, N, O, Mg, Si, Fe) as measured in lensed galaxies at $2 \lesssim z \lesssim 3$ and two 'composite' spectra from sizable sets of high-redshift systems, obtained by means of observations in non-lensed fields. These data have been compared with our model results.
  Some of the measured abundance ratios between volatile elements (O, N) are in agreement with our results in which the IGIMF is adopted. However, a large scatter in the data and large uncertainties in the stellar yields, in particular for N, makes the interpretation of the abundance ratios difficult and the degeneracy between the ef-

fects of the IMF and the ones of stellar nucleosynthesis calculations prevents us from reaching any firm conclusion;

- to interpret the abundances for refractory elements, we have used models which can account for differential dust depletion (i.e., different elements depleted into dust in different proportions), and we have tested various assumptions regarding the processes that regulate the evolution of dust grains.
  All the models with minimal dust production tend to underestimate the observed pattern in the [Si/Fe] vs. [Fe/H], [Mg/Fe] vs. [Fe/H] and [O/Fe] vs. [Fe/H] diagrams. Under these conditions, the models with the IGIMF predict [α/Fe] values in better agreement with the observations with respect to the ones with a Salpeter IMF. On the other hand, if the effects of dust are important, our analysis suggests a Salpeter or an IGIMF with $\beta \geq 2$, i.e. only slightly top-heavier than the Salpeter;

- we have also predicted the evolution of the dust mass with time for galaxies of different stellar mass and IMF, showing that a top-heavy IGIMF may allow us to solve the "dust budget crisis" problem (e.g. Valiante et al. 2014).

Other works support a top-heavy IMF in high-redshift starbursts, in particular few studies based on the interpretation by means of chemical evolution models of the abundances of rare isotopes such as ^{13}C, ^{17}O and ^{18}O ratios, detected in the IR band and free from dust depletion effects (Romano et al., 2017; Zhang et al., 2018).
In the future, it will be important to take into account the IGIMF in models to interpret such measures, and possibly better understand the nature of star formation in such systems.

On the observational side, the *Multi Unit Spectroscopic Explorer* (MUSE, Bacon et al. 2010) instrument mounted on the VLT has allowed the identification and spectroscopic confirmation of hundreds of lensed galaxies in the redshift range $2 \leq z \lesssim 7$ (e.g., Vanzella et al. 2017 and references therein). This has also enabled the production of highly accurate lens models, useful to determine and interpret absolute physical quantities such as luminosity, stellar mass, star formation rate, and abundances of high-redshift galaxies (e.g., Meneghetti et al. 2017).
In the future, it will be important to perform high-resolution spectroscopic follow-ups of the most magnified sources, in order to derive precise abundance ratios and to extend the observational sample presented in this work.

3.3 Dust evolution in galaxy clusters

3.3.1 Introduction

Galaxies are not uniformly distributed in the Universe, at least on scales of the order of Mpc. Most galaxies are found in galaxy groups and galaxy clusters. Galaxy groups are small and low density ensembles of galaxies, whereas clusters are huge groups of galaxies with very high concentration.
The classification in one or the other category is rather arbitrary: a galaxy cluster is normally defined as an ensemble of galaxies where at least 50 members have luminosities within 2 magnitudes from the third most luminous galaxy of the cluster.

Concentrating on galaxy clusters, these are the largest gravitationally-bound cosmic structures in the Universe.
They contain galaxies, intacluster medium (ICM) gas and large amounts of dark matter (DM), i.e., roughly 90% of galaxy cluster mass. For this reason, they are valid cosmological probes of the DM: cosmological models tracing only the dissipationless DM provide accurate predictions of cluster properties (e.g. Kaiser 1986). At the same time, baryonic physics starts to become important on cluster scales. This places galaxy clusters at a key position also for the study of smaller-scale mechanisms such as gas flows or galaxy evolution.
At variance with smaller structures such as galaxies, clusters are dynamically younger. In some cases, external galaxies are still collapsing to the centre for the first time, indicating that these systems are not fully virialized.

Going more into detail, galaxy clusters have typical masses of 10^{13} - 10^{15} $M_{\odot}$ and may contain from 10^2 to 10^3 galaxies. These show very large velocity dispersions ($\sigma_v \sim 800 - 1000$ km s^{-1}) and are contained in a radius of a few Mpc. Within this radius, elliptical galaxies are more concentrated in the denser centre of the cluster whereas spirals in the more diffuse outskirts, producing the so-called morphology-density relation (Dressler 1980). The radial distribution of galaxies in clusters is similar to that of stars in elliptical galaxies and for this reason can be approximated by the "$R^{1/4}$ law".
X-ray observations reveal that galaxies in clusters are permeated by a very hot (10^7-10^8 K), bright (10^{43}-10^{45} erg/s) and sparse (10^{-2}-10^{-4} cm^{-3}) plasma (Kellogg et al. 1972), namely the ICM. As for example, in Fig. 3.18 we show the distribution of the gas X-ray emission within the galaxies of the Coma cluster (Abell 1656). Thermal Bremsstrahlung/free-free radiation (see Sarazin 1988 for a review) is the major responsible of this emission: the extreme conditions in the ICM allow hydrogen and helium to be fully ionized, thus providing the source for the free-free emission.
Heavy metals are also present in this plasma, being partially ionized. Their abundance decreases with radius and it is roughly a third of the solar metallicity (see Werner et al.

Figure 3.18: *Superposition of X-ray image by XMM-Newton European Photon Imaging Camera (EPIC) and optical image by the Sloan Digital Sky Survey (SDSS) for the Coma galaxy cluster (Abell 1656). Credits: ESA/XMM-Newton/SDSS/J. Sanders et al. 2019*

2008 for a review). This latter fact is a proof of the importance of galactic contribution from ellipticals to this medium (see, e.g. Matteucci & Vettolani 1988).

Dust in galaxy clusters: a still controversial picture

As mentioned in the beginning of this Chapter, many issues are still open regarding dust in galactic environments. Nonetheless, the substantial progress made in the field in the past years has allowed us to unveil much of the dust properties (i.e., composition, size distribution) within local galaxies.
However, much less is known regarding dust in galaxy clusters, including their diffuse ICM component.

The understanding of dust distribution in galaxy clusters is important for a number of reasons.
First of all, it affects galaxy cluster catalogue completeness: for example, up to $\sim$9 per cent of clusters in a redshift range of $0.5 < z < 0.8$ might be undetected in the Planck survey due to the presence of dust (Melin et al. 2018). On the other side, dust can also become an efficient cooling agent at the hot temperatures ($T > 10^7$ K) typical of the ICM (Montier & Giard 2004). Furthermore, a proper understanding of dust properties will be essential

in the analysis of protoclusters at redshift $z > 2$ (e.g. Casey 2016; Cheng et al. 2019), since their lower ICM temperatures are still not able to trigger efficient dust destruction mechanisms (i.e. thermal sputtering).

Since Stickel et al. (2002), several attempts (e.g. Bai et al. 2007; Kitayama et al. 2009) have been performed to estimate the dust-to-gas ratios in the ICM of local galaxy clusters. However, there is still no definitive evidence of the presence of dust in the ICM of individual local clusters.
Evidence of the presence of dust in clusters may instead have been found in the statistical analysis of large data sets at redshifts $z \lesssim 1$. Chelouche et al. (2007) and Muller et al. 2008 both obtained comparable ICM DGR measures of 10^{-4}, i.e. a DGR smaller than < 5 per cent of the typical galactic ISM values. Later on, Giard et al. (2008) found more stringent upper limits for ICM dust, finding DGRs not larger than 10^{-5} in low-redshift ($z < 1$) clusters. However, the follow-up work by Roncarelli et al. (2010) suggested larger ICM DGRs of $\sim 5 \times 10^{-5}$. In more recent times, Gutiérrez & López-Corredoira (2014, 2017) (hereafter GLC14 and GLC17) and Planck Collaboration (XLIII) et al. (2016) (hereafter, PlanckXLIII-16) provided some of the more accurate estimates about dust in galaxy clusters. In particular, PlanckXLIII-16 estimated the total dust mass, i.e., including both galaxy (ISM) dust and ICM dust, thus providing important additional informations to constrain the models.

However, only sporadic theoretical works have attempted to estimate ICM dust.
Dwek et al. (1990) already predicted that dust should exist mostly far away from the cluster center ($\mathrm{R} > 2$ Mpc) and in low abundances. A decade later, Popescu et al. (2000) proposed that any IR emission by diffuse ICM dust would originate from current dust injection in the ICM, and hence it would indicate the dynamical state and maturity of the cluster. More recently, Polikarpova & Shchekinov (2017) determined that dust may survive in the ICM for 100-300 Myr if it resides in isolated dense and cold gas filaments surviving the outflow. This would lead to an ICM DGR of about 1-3 per cent of the typical Galactic values ($\sim 10^{-2}$).
Some hydrodynamical simulations and semi-analytical models (SAMs) of galaxies and galaxy clusters have already included dust evolution (e.g. Bekki 2015; Zhukovska et al. 2016; McKinnon et al. 2017; Popping et al. 2017; Gjergo et al. 2018; Vogelsberger et al. 2019). Among these, both Gjergo et al. (2018) and Vogelsberger et al. (2019) cosmological simulations of galaxy clusters slightly underproduced dust compared to recent observational data (i.e. PlanckXLIII-16). In particular, they were able to alleviate the tension between model and data by relaxing the sputtering timescale, i.e., by allowing dust to survive longer in the harsh intracluster environment.

In this Section we present a novel approach to treat the evolution of dust within galaxy clusters.

In particular, we base our approach on the method proposed by Matteucci & Vettolani (1988) (hereafter MV88). This method consists in integrating, at the present time, the contribution of metals by models of elliptical/S0 galaxies over the luminosity function (LF), and in this way it was predicted that the bulk of the metal mass is produced by elliptical/S0 galaxies at the break of the LF (Gibson & Matteucci 1997).

Here we implement the same technique as in MV88, but using dust masses produced by galaxies in a cluster. Unlike MV88, we differentiate among the three main morphologies: elliptical, spiral, and dwarf irregular galaxies. For each of these types, we separate the dust component residing within the ISM of galaxies from the other component ejected into the ICM. Moreover, aside from the scenario where different galaxies form quickly at early times and evolve independently ("monolithic scenario"), we expand the model to account for a hierarchical galaxy formation scenario.
In this way, we predict the evolution of total dust mass in galaxy cluster, as well as of its galactic and intracluster component, in different galaxy formation scenarios. The results are also compared with recent dust mass estimates to test the reliability of our predictions.

In order to describe in detail the adopted method, the results and the comparison with dust data for galaxy clusters, we organize the rest of the Section as follows: in 3.3.2 we overview the relevant observational papers that investigated the presence of dust in galaxy clusters and in particular we focus on the data adopted in our work. Section 3.3.3 describes in detail the methodology employed, covering both aspects of the integration method and the chemical and dust evolution models employed. In 3.3.4, we present our predictions for the dust evolution within a typical galaxy cluster and we compare it against the latest observations. Finally, in 3.3.5 we discuss the results obtained and we draw some conclusions.

3.3.2 Dust observations in galaxy clusters

Literature about dust observation in galaxy clusters contains different approaches to this topic.
Some works investigated individual clusters (e.g. Stickel et al. 1998, 2002; Bai et al. 2007; Kitayama et al. 2009), whereas some others took a statistical average over large data sets investigating optical extinctions (Chelouche et al. 2007; Muller et al. 2008; McGee & Balogh 2010) or dust IR emission (Giard et al. 2008; GLC14; GLC17; PlanckXLIII-16). Furthermore, Roncarelli et al. (2010) reconstructed the SED of various galactic morphologies in order to isolate a galactic SED signal from the ICM dust.

Usually, dust abundances are estimated either through dust emission in the IR or through the extinction of objects on the background of the observed medium in UV-optical wavebands.
Typically, the IR dust emission technique consists in fitting the IR fluxes on modified

blackbody spectra of dust thermal emission (e.g. Hildebrand 1983). On the other hand, UV-optical extinction by dust is obtained by measuring the flux of objects (i.e. galaxies and quasi stellar objects) located in the background of a given cluster and comparing the obtained flux to a reference flux of similar objects located at a similar redshift but located in the field (e.g. Ostriker & Heisler 1984).

In general, dust abundances in the ICM of large cluster samples at redshift $z < 1$ are not too well constrained, but most estimates limit the ICM DGR to around 10^{-5}, which is around three orders of magnitude lower than the typical MW values.
Such low dust abundances are attributed to the short dust destruction timescales in the harsh ICM environment, which is permeated with X-ray radiation and highly energetic ions. For this reason, ICM dust is believed to be of recent origin (e.g. Dwek et al. 1990; Popescu et al. 2000; Clemens et al. 2010): it can be either newly ejected from galaxies by stellar winds, or stripped from the galactic ISM by merging events and ram pressure stripping.

Another important feature about dust in clusters is its preferred location in the outskirts of the clusters, where late-type galaxies (i.e. spirals and dwarf irregulars) are dominant, and where the environment is contaminated by small groups of galaxies. This hypothesis is corroborated by several studies investigating dust profiles in clusters (Chelouche et al. 2007; Muller et al. 2008) in combination with the low dust abundances observed around cluster centres (Stickel et al. 2002; Bai et al. 2007; Kitayama et al. 2009).

A summary of the existing observational literature is presented in Tab. 3.7. In this Section, we compare the results of our new methodology with the data by Stickel et al. (2002), GLC17, and PlanckXLIII-16, which are written in bold for clarity.

Stickel et al. (2002) measured the Coma cluster ICM dust. For this reason, we take their obtained value as an upper limit for dust content in the ICM of local galaxy clusters.

For what concerns GLC17, we need to go back to the work by GLC14. In this paper, the authors employed two methods on the SDSS-DR9 (Ahn et al. 2012) sample of galaxy clusters located in a redshift range of $0.05 < z < 0.68$. The first method is a statistical approach to extinction. Their average prediction for total dust mass is $M_d < 8.4 \times 10^9$ M$_\odot$ within a cluster radius of 3 Mpc. The second method is instead an estimate of the emission by cluster dust to the FIR sky from optical extinction maps, which leads to a lower prediction of $\lesssim 2 \times 10^9$ M$_\odot$. The conservative DGR upper limit from the combination of the two methods is $\sim 8 \times 10^{-5}$.
GLC17 is a follow-up of GLC14 which employed newer data from Herschle HerMES project. In this work, GLC17 binned the estimates for their selected sample of 327 clusters in redshift ($0.05 - 0.24$, $0.24 - 0.42$, and $0.41 - 0.71$), cluster mass ($< 10^{14}$ M$_\odot$ and $> 10^{14}$ M$_\odot$), aperture ($1 - 5$ arcmin), and observed frequency (250, 350, and 500 μm). For our purposes, we adopt the 350 μm channel detections (which provide the most restrictive

Table 3.7: *List of observational papers for dust in galaxy clusters. Besides the dust-to-gas ratio (DGR), other columns show the radius (in arcmin or Mpc) within which the estimate is computed, the redshift spanned by the sample/name of the individual cluster, the instrument and the wavelengths/bands used to gather data and the method employed to extrapolate the dust estimate.*

Paper	DGR (component)	r_{max}	z range / cluster name	λ / band (instrument)	Method
Stickel et al. (2002)	$\sim \mathbf{10^{-6}}$ **(ICM)**	**0.2 Mpc**	**Coma +**	**120, 180 μm (ISO)**	$\mathbf{I_{120}/I_{180}}$ [1]
Chelouche et al. (2007)	$< 5 \times 10^{-4}$ (ICM)	~ 1 Mpc	$0.1 - 0.3$	u-g-r-i-z (SDSS)	Bkg. extinction [2]
Muller et al. (2008)	$\lesssim 2 \times 10^{-4}$ (ICM)	1.5 Mpc	< 0.5	650,910 μm (CFHT)	Bkg. extinction
Giard et al. (2008)	$\lesssim 10^{-5}$ (ICM)	$10'$	$0.01 - 1$	12-100μm/ 0.1-2.4keV (IRAS/RASS)	Stacked emission
Bovy et al. (2008)	$\lesssim 2 \times 10^{-5}$ (ICM)	2 Mpc	~ 0.05	u-g-r-i-z (SDSS-DR4)	Bkg. extinction
Kitayama et al. (2009)	$< 10^{-5}$ (ICM)	0.1 Mpc	Coma	24,70,160 μm (Spitzer)	MIR/FIR emission
Roncarelli et al. (2010)	$\lesssim 5 \times 10^{-5}$ (ICM)	$< 12'$	$0.1 - 0.3$	u-g-r-i-z (SDSS-maxBCG)	SED-reconstruction
McGee & Balogh (2010)	$\sim 3 \times 10^{-4}$ (ICM)	$\lesssim 43$ Mpc	$0.1 - 0.2$	g-r-i-z/ 12-100 μm (SDSS/IRAS)	Bkg. extinction
GLC14	$\lesssim 2 \times 10^{-5}$ (ICM)	3 Mpc	$0.05 - 0.68$	g-r-i (SDSS-DR9)	Stk. em. + Bkg. ext.
PlanckXLIII-16	$\mathbf{1.93^{+0.92}_{-0.92}} \times 10^{-4}$ **(Full)**	**15′**	$\mathbf{0.01 - 1.}$	**850-60 μm (IRAS/Planck)**	**Stacked emission**
GLC17	$< \mathbf{9.5 \times 10^{-6}}$ **(ICM)**	**1-5′**	$\mathbf{0.06 - 0.7}$	**250, 350, 500 μm (Herschel)**	**Stk. em. + Bkg. ext.**

Notes: [1] *surface brightness ratios in the FIR;* [2] *reddening of galaxies and quasars located in the background of galaxy clusters.*

limits) within 1 arcmin of massive cluster centers, binned into three redshift intervals.

PlanckXLIII-16 considered a selection of 645 clusters within a redshift of $z < 1$. For these clusters, they combined the Planck-HFI maps (6 beams between 100 and 857 GHz) with the IRAS (Miville-Deschênes & Lagache 2005) maps (60 and 100 μm), integrating the stacked signal for each beam out to an aperture of 15 arcmin. In particular, they fitted the Planck and IRAS 100 μm data to the IR SED dust emission, following the approach suggested in Hildebrand (1983). 60 μm data were ignored in the SED fit because at this wavelength the contribution by small grains, that are not in thermal equilibrium, becomes prominent and would skew the fit.
For the full sample, each cluster is estimated to have, within 15 arcmin, a dust mass of around 10^{10} $M_\odot$ (with small variations depending on the choice of dust emissivity index β). The full sample ($\langle z \rangle = 0.26 \pm 0.17$, $M_d = 1.08 \pm 0.32 \times 10^{10}$ $M_\odot$) is split in two redshift bins ($z < 0.25$ and $z > 0.25$) and two mass bins (M_{200}[5]$= 5.5 \times 10^{14}$ $M_\odot$). The average dust mass for the two redshift bins is of $0.34 \pm 0.17 \times 10^{10}$ $M_\odot$ for the low z and $2.56 \pm 0.91 \times 10^{10}$ $M_\odot$ for the intermediate z, respectively. For the less and more massive clusters, the average dust mass is of $0.21 \pm 0.14 \times 10^{10}$ $M_\odot$ and $3.48 \pm 0.99 \times 10^{10}$ $M_\odot$, respectively. In our work, we compare our results with both the full sample and the two subsamples split according to redshift bins.

3.3.3 Modelling dust in galaxy clusters

In the following, we describe the adopted method to compute the total amount of dust produced and ejected by galaxies in clusters. As mentioned earlier in this Section, we follow the method proposed in MV88, in which they integrated over the LF of clusters the masses of given chemical species i produced by galaxies at the present time.
However, unlike MV88 which employs only chemical evolution models of early-type galaxies (Matteucci & Tornambe 1987), we take advantage of dust evolution models of irregular, spiral, and elliptical galaxies. Moreover, we extend the MV88 method across the entire evolutionary history of the cluster, assuming different scenarios of galaxy formation: a "monolithic scenario", where the three galaxy morphologies evolve independently and the number density of galaxies remains constant in time, and a "hierarchical scenario", in which the number densities of different morphologies change in time.

For simplicity, we assume that the first galaxies start evolving at the same time at redshift $z = 5$. The adoption of larger galaxy formation redshifts (e.g. $z = 10$, as in Section 3.1) does not affect our results significantly, in particular in the comparison with low-intermediate redshift ($z \lesssim 1$) data.
We also remark that in this study we adopt a flat ΛCDM cosmology with a Hubble constant

[5] M_{200} (R_{200}) is the mass enclosed by (radius that encloses) a sphere whose mean density is 200 times the critical density ρ_{crit} at a given redshift.

of $H_0 = 70$ km s^{-1} Mpc^{-1} and $\Omega_m = 0.3$.

The revised Matteucci & Vettolani (1988) method

In order to compute the evolution of dust amount in clusters, we first need to find the relationship between the evolution of dust masses M_d across the cosmic time t for galaxies of a given morphology and total baryonic galaxy mass/infall mass M_G.
We thus iterate our chemical and dust evolution code over a range of masses $M_{G,X}$ for each of the three morphologies X. In the case of elliptical galaxies, $M_{G,ell}$ has a lower limit of 5×10^9 M$_\odot$ and does not extend beyond 10^{12} M$_\odot$. For the other galaxy types, 5×10^9 M$_\odot$ $< M_{G,spi} < 5 \times 10^{11}$ M$_\odot$ is the range for spirals and 10^7 M$_\odot$ $< M_{G,irr} < 5 \times 10^9$ M$_\odot$ for irregulars. For each iteration, we are able to separate an ISM dust component, residing within galaxies, and an ICM dust component, ejected by stellar winds.
In this way, we fit the following relation between galaxy mass and dust mass:

$$M_d\,(t) = E_d\,(t)\,{M_{G,X}}^{\beta_d(t)}, \tag{3.7}$$

where $E_d(t)$ and $\beta_d(t)$ are the time-dependent fit parameters. We check these fits and we find that they are stable across cosmic time.

With the relation between dust and galaxy mass established, we need to convert galaxy masses into luminosities, because our ultimate goal is to use Eq. (3.7) as a weight function on the LF. We consider the mass-to-light ratio $K = M_G/L$, where the galaxy mass M_G and luminosity L are both expressed in solar units. We take a fiducial value of $K = 5$, but we test also variations up to $K = 15$. This range of K is typical of several studies in literature (e.g., Portinari et al., 2004; Spiniello et al., 2012; De Masi et al., 2019) for both early and late-type galaxies.
It is then possible to normalize Eq. 3.7 by the respective quantities at the break (*) of the LF:

$$M_d/M_d^* = (M_G/M_G^*)^{\beta_d} = (L/L^*)^{\beta_d}\,, \tag{3.8}$$

where M_d^* is the dust mass associated to a galaxy of mass M_G^* and luminosity L^* at the break.

With these tools, we can consider the distribution function of galaxies across luminosity (or mass). The most reasonable choice is the Schechter LF (Schechter, 1976): $\Phi\,(L) = n^*(L/L^*)^\alpha e^{-L/L^*}$, where L^* is the luminosity of a galaxy at the break of the Schechter Function, n^* is a measure of the cluster richness (in Mpc^{-3}), and α is the dimensionless slope of the power law. In this way, we weight the normalized Eq. (3.8) on $\Phi\,(L)$.
However, since our work includes galaxies of all morphologies, at variance with MV88 $\Phi\,(L)$ includes all galaxy types. For this reason, we need to rescale the integration by the number fraction f_X of each morphology X compared to the total number of galaxies. For example, $f_{ell} = 0.82$ in the Coma cluster, but lower values are found in dynamically young clusters such as Virgo, with $f_{ell} = 0.43$. The spiral number fraction is then defined

as $f_{spi} = 1 - f_{ell}$. To ensure that we do not count galaxies in multiple morphologies, we impose the same value for the upper mass limit of irregular galaxies and the lower mass limits of spiral and elliptical galaxies. In this way, we have that $f_{irr} = 1$.
The integrand that produces the cluster dust mass for a given morphology then takes the form of:

$$(L/L^*)^{\beta_{d,X}}\Phi\left(L\right) = f_X n^* (L/L^*)^{\beta_{d,X}+\alpha} e^{-L/L^*}, \tag{3.9}$$

which can be integrated as an upper incomplete Gamma function $\Gamma(a,x) = \int_x^\infty t^{a-1}e^{-t}\,dt$, where x is the lower limit of the integral. This is appropriate in the case of elliptical galaxies. For spiral and irregular galaxies, instead, we impose an upper limit to the integration by subtracting a second incomplete Gamma function to remove the regions of the LF where we do not observe this morphology. The cluster dust mass for each morphology X within the galaxies ISM (and similarly the ejected ICM component) is then derived as:

$$M_{d,ell}^{ISM}(< R_{200}) = f_{ell} M_{d,ell}^{*,ISM} n^* \Gamma(1 + \beta_{d,ell}^{ISM} + \alpha, L_{min,ell}/L^*) \tag{3.10}$$

$$M_{d,spi}^{ISM}(< R_{200}) = f_{spi} M_{d,spi}^{*,ISM} n^* [\Gamma(1 + \beta_{d,spi}^{ISM} + \alpha, L_{min,spi}/L^*) - \Gamma(1 + \beta_{d,spi}^{ISM} + \alpha, L_{max,spi}/L^*)] \tag{3.11}$$

$$M_{d,irr}^{ISM}(< R_{200}) = f_{irr} M_{d,irr}^{*,ISM} n^* [\Gamma(1 + \beta_{d,irr}^{ISM} + \alpha, L_{min,irr}/L^*) - \Gamma(1 + \beta_{d,irr}^{ISM} + \alpha, L_{max,irr}/L^*)], \tag{3.12}$$

where $L_{min,X}$ is the lowest luminosity observed in a given cluster, $M_{d,X}^* = E_{d,X} M_G^{*\beta_{d,X}(t)}$ is the dust mass for a galaxy at the break of the LF for the X morphology and M_G^* is the break galaxy baryonic mass.
Observational constraints on magnitude will define our luminosity integration limits, but also our galaxy masses. As derived in MV88, $M_G^* = KL^* = h^2 K \times 10^{-0.4(\mathrm{Mag}^* - \mathrm{Mag}_\odot)}$, with $\mathrm{Mag}_\odot = 4.83$ and Mag^* the V-band magnitude of the Sun and of a galaxy at the break.

Aside from the original Schechter LF, we test also a double Schechter LF. In the rest of the Section, we will refer to them as single LF and double LF, respectively. The double LF (e.g. Popesso et al., 2006), is presented in Moretti et al. (2015) as the best fit to the WIde-field Nearby Galaxy-clusters survey (WINGs, Fasano et al., 2006).
This function has the form of:

$$\Phi(L) \propto \Phi_b + \frac{L_b^*}{L_f^*}\Phi_f = \left(\frac{L}{L_b^*}\right)^{\alpha_b} e^{-L/L_b^*} + \frac{L_b^*}{L_f^*}\left(\frac{L}{L_f^*}\right)^{\alpha_f} e^{-L/L_f^*}, \tag{3.13}$$

where Φ_b and Φ_f are single Schechter functions calibrated on the bright end (b) and on the faint end (f) of the LF. Each of Φ_b and Φ_f have their own bright and faint break point,

identified with respective break luminosities L_b^* and L_f^* and power-law coefficients α_b and α_f.

Here, we weight spiral and elliptical galaxies with the bright component. For what concerns irregular galaxies, we treat the bright component as we treat irregulars in the single LF, and we add to it the incomplete gamma function integration of the faint component. In fact, by steepening its slope at fainter luminosities, the double LF predicts the existence of more dwarf irregular galaxies than the normal Schechter function.

The parameters α for the single LF (or α_b and α_f for the double LF) and L^* (or L_b^* and L_f^*) are taken from the WINGs (Moretti et al., 2015) median parameters unless otherwise specified: $\alpha = -1.15$ (or $\alpha_b = -0.97$ and $\alpha_f = -0.6$ for the double LF). and median V-band break magnitude $\mathrm{Mag}_V^* = -21.30$ (or -21.15 and -16.30 for the bright and faint end of the double LF). $fell = 0.74$ is the average elliptical fraction for WINGs, as extrapolated from Mamon et al. (2019).
To obtain the cluster richness, we take advantage of the richness-to-cluster-mass relation $n_* \propto M_{clus}^{0.92}$ found by (Popesso et al., 2007) and we rescale the Coma cluster richness to WINGs masses. Since Coma cluster has a mass of $M_{clust} \sim 1.1 \times 10^{15}$ $\mathrm{M}_\odot$ (Geller et al. 1999) and a richness of $n_* = 107$ (Schechter 1976), while WINGs clusters average mass is $M_{clust} \sim 5 \times 10^{14}$ $\mathrm{M}_\odot$, it follows that that $n_* = 52$ for the average WINGs cluster sample.

We do not report here numbers for other well-known local clusters, but we test a reasonable range of the parameter space to test what the dust evolution might look like in other clusters.
The parameters just presented are summarized in Table 3.8, where we also show our chosen integration limits. Regarding these values, we highlight that the irregular galaxy lower integration bound of 10^7 $\mathrm{M}_\odot$ corresponds to the WINGs faintest magnitude limit of $\mathrm{Mag}_{min} \simeq -15.5$ (Moretti et al. 2015). In Table 3.9 we report instead the adopted double LF parameters.

With these calculations, we obtain the evolution of dust mass in clusters for a "monolithic scenario", where galaxies of different morphological types do evolve separately, not changing in number.

Including the "hierarchical scenario"

In the "hierarchical scenario", the number of galaxies of different morphological types evolves with redshift.
To compute the evolution of dust mass in galaxy clusters within this context, we employ the technique presented in Vincoletto et al. (2012) and already coupled to chemical and dust evolution models in Gioannini et al. (2017b).

Table 3.8: *Fiducial model parameters from the single LF based on the median values of the full WINGs cluster sample (Moretti et al. 2015; Mamon et al. 2019). The upper table indicate the lower ($M_{G,min}$) and upper ($M_{G,max}$) mass limits for irregular, spiral, and elliptical galaxies (Irr, Spi, Ell). On the bottom Table, f_{ell} is the fraction of galaxies that are early-type, α is the slope of the single LF, n^* is the richness and Mag* is the V-band magnitude identifying the break luminosity.*

	Irr	Spi	Ell
$M_{G,min}$	10^7 M$_\odot$	5×10^9 M$_\odot$	5×10^9 M$_\odot$
$M_{G,max}$	5×10^9 M$_\odot$	5×10^{11} M$_\odot$	—

f_{ell}	n^*	α	Mag*
0.74	52	-1.15	-21.30

Table 3.9: *Fiducial model parameters from the double LF based on the median values of the full WINGs cluster sample (Moretti et al. 2015). The subscripts $_b$ and $_f$ represent the bright and faint end of the double LF, respectively.*

α_b	α_f	Mag$^*_b$	Mag$^*_f$
-0.97	-0.6	-21.15	-16.30

Instead of assuming that all moprhological types are born simultaneously and evolve separately as in the "monolithic scenario", we let the number density of galaxies of morphological type X evolve with redshift in this way:

$$n_X(z) = n_{X,0}(1+z)^{\theta_X}, \tag{3.14}$$

where $n_{X,0}$ is the number density at redshift $z = 0$ for a morphological type X and θ_X characterise the number density evolution of different galaxy types with redshift. This parameter is calibrated as in Gioannini et al. (2017b) to be 0.0, 0.9, and -2.5 for irregular, spiral, and elliptical galaxies, respectively.

From this definition of number density, we can thus derive the rescaled elliptical fraction:

$$f_{ell} = f_0 \frac{(1+z)^{-2.5}}{f_0(1+z)^{-2.5} + (1-f_0)(1+z)^{0.9}}, \tag{3.15}$$

where f_0 is the elliptical fraction at the present time. Similarly, we can also derive the spiral fraction f_{spi}. By doing this, we note that the relation $f_{spi} = 1 - f_{ell}$ is preserved across cosmic history.

The evolution of f_{ell} and f_{spi} with redshift is visible in Fig. 3.19. In this Figure, we show the evolution of the mass fraction contribution of the three different morphologies with both the single LF (upper panel) and double LF (lower panel), adopting the present

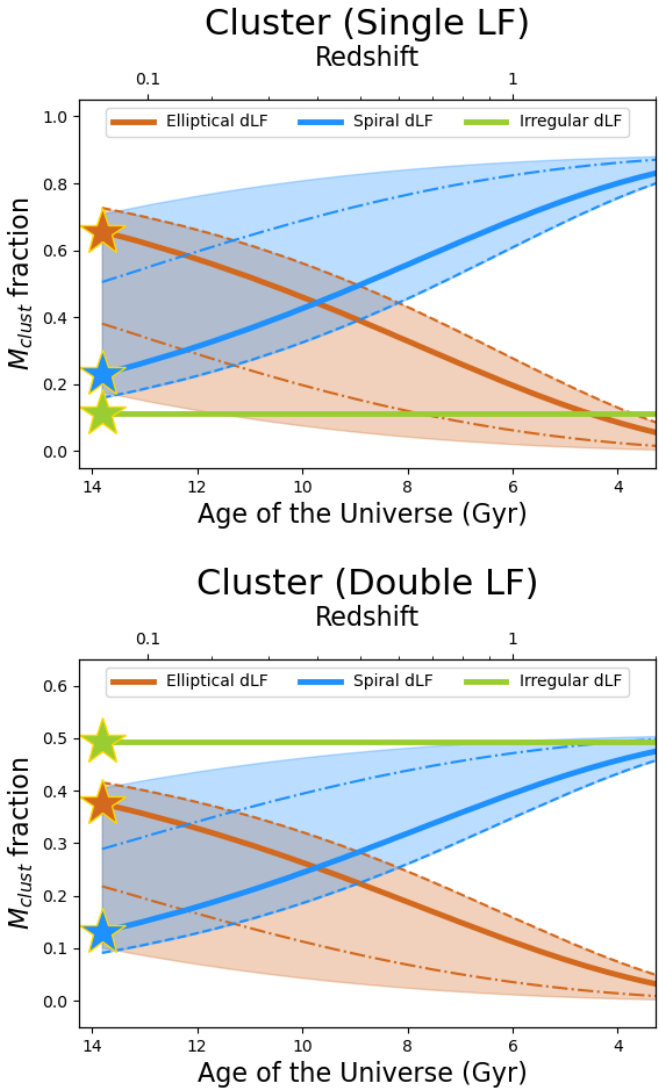

Figure 3.19: *M_{clust} mass fraction evolution within the "hierarchical scenario" adopting a single LF (upper panel) and a double LF (lower panel). Brown, blue and green solid lines refer to the evolution for elliptical, spiral and dwarf irregular fractions adopting present day WINGs cluster parameters ($f_{0,ell} = 0.74$), which are highlighted with colored stars. Dashed lines assume $f_{0,ell} = 0.82$, as in the Coma cluster, whereas dash-dotted lines $f_{0,ell} = 0.43$, as in the Virgo cluster. Shaded regions enclose $f_{0,ell}$ between 0.2 and 0.82, which are the extreme values considered in this study.*

day fractions taken from WINGs average (Moretti et al. 2015; Mamon et al. 2019, solid lines). The WINGs present day values, which are the ones adopted at all times in the independent evolution scenario, are highlighted with colored stars. In this Figure, we also plot the evolution considering the present day elliptical fraction of the Coma cluster (dashed lines), indicative of a mature cluster, and the one obtained with present day in Virgo cluster (dash-dotted lines), typical of dinamically young clusters.

From Fig. 3.19, it is evident the progressively higher fraction of ellipticals at lower redshift, independently of the adopted present day parameters. This is typical of the hierarchical clustering scenario for galaxy formation, where the baryon assembly mirrors the hierarchical buildup of dark matter structures and spheroids/ellipticals formed as a series of subsequential mergers between smaller galaxies (Vincoletto et al. 2012).
On the other hand, we keep the dwarf irregular contribution constant over time: these galaxies span a different mass range relative to other morphologies (see Tab. 3.8) and therefore $f_{irr} = 1$ at all times irrespective of the galaxy evolution scenario. However, Fig. 3.19 highlights a substantial difference in the mass contribution by irregulars with the two LFs and this provides a perfect benchmark to test dwarf irregular galaxies contribution to the total dust mass.

Scaling the LF with radius

Up to now, we present a method that is valid for calculations within R_{200}. Actually, the LF fits provided in Moretti et al. (2015) are valid within $0.5R_{200}$; in any case, previous works showed that the shape of the Schechter function does not vary from from $0.5R_{200}$ to R_{200} (Annunziatella et al., 2017).

However, in order to obtain a fair comparison with observations (i.e. PlanckXLIII-16), we need to calculate the integrated dust mass at radii larger than R_{200}.
Since we are interested in radii of 15 arcmin, we apply the method described below only at redsfhits $z \gtrsim 0.1$, where $R_{200} \sim 15'$; in fact, we are not interested in a profile at smaller radii than R_{200} as our goal is to compute the total dust cluster mass.

To rescale our integral to larger radii, we take advantage of the NFW model (Navarro et al., 1996). The mass contained within a radius $t = r/r_s$ is given by:

$$M_{scaled} = M_{vir} \frac{\ln(1+t) - t/(1+t)}{\ln(1+c) - c/(1+c)}, \tag{3.16}$$

where $r_s \rightarrow 15'$ is the redshift dependent scale radius that will rescale our integration to the 15 arcmin observed by PlanckXLIII-16. For the computation, we assume that the virial mass M_{vir} is roughly represented by M_{200}. Concerning the concentration c, it varies depending on the morphology: elliptical galaxies are well described with a concentration of $c \sim 4$, whereas spiral galaxies with $c = 0.85$ (see Tab. 2 of Cava et al., 2017).

Chemical evolution models and dust prescriptions

To reproduce the dust mass M_d evolution within galaxies of the three morphologies, we need to adopt detailed chemical evolution models for galaxies including dust evolution.

We develop models for typical galaxies of each morphological types. In particular, we build models for i) typical spheroids (local elliptical galaxies), ii) typical spirals and iii) typical irregulars.
In addition to the galaxy mass (M_G, see Tab. 3.8 for ranges of values adopted), the main differences among the models for different galaxy types are the assumed star formation efficiency (SFE, see Eq. (2.4)) and the timescale for gas infall, which are set according to the values adopted in Section 3.1. For what concerns the IMF, we adopt a Salpeter (1955) elliptical and irregular galaxy models and a Scalo (1986) IMF for spiral galaxies, in agreement with indications from previous studies (e.g. Romano et al. 2005; Yin et al. 2011; Gioannini et al. 2017b, but see e.g. Jeřábková et al. 2018 in the context of the IGIMF theory).
In this way, we are confident of adopting realistic models for each galaxy morphology and to be able to follow the galaxy evolution of each type since the beginning and until the present time. In fact, the resulting SFHs reproduces the majority of the observable properties of local galaxies, such as the present time SFR, the SN rates and the chemical abundances (Grieco et al., 2012; Gioannini et al., 2017b).

It should be noted that even though these models have been calibrated mainly on field galaxies, it is safe to apply them to cluster galaxies.
In fact, it was shown in several studies that dust properties such as the DGR and dust-to-stellar mass ratio vary little or not at all from field to cluster environments (e.g. Davies et al., 2019). Instead, morphology, age, and other physical processes predict the dust variables in which we are interested much more stringently.

Nucleosynthesis prescriptions

The contribution to chemical enrichment of LIMS, Type Ia and CC-SNe (Type II, Ib/c), is computed by taking advantage of detailed stellar yields for these stars (see Section 2.1.3).

In particular, the following mass and metallicity dependent stellar yields are adopted:

- for LIMS ($0.8 < m/\mathrm{M}_\odot < 9$) we use yields by Karakas (2010) for stars with mass lower than $6M_\odot$, while for super-AGB (SAGB) stars and e-capture SNe, with mass between 6 $\mathrm{M}_\odot$ and 9 $\mathrm{M}_\odot$, we use yields by Doherty et al. (2014a,b);
- for massive stars that explode as CC-SNe ($m > 9\,\mathrm{M}_\odot$), we adopt yields by Kobayashi et al. (2006)/Nomoto et al. (2013);
- for Type Ia SNe we use the yields by Iwamoto et al. (1999).

Dust prescriptions

The formalism adopted to describe dust evolution within galaxies (i.e., ISM component) is described in Section 2.4: we consider astration by SF, production by stars, accretion in cold dense regions of the ISM and destruction by SNe shocks (see Eq. (2.21)).

Concerning the dust production term, we follow these prescriptions:

- for AGB stars, we adopt the condensation efficiencies dependent on both mass and metallicity computed by Piovan et al. (2011), already tested by Gioannini et al. (2017a,b);
- for CC-SNe, we also adopt the condensation efficiencies provided by Piovan et al. (2011), that take into account the processes of both dust production and reverse shock destruction by the SN (see Section 2.3.1). These prescriptions give us the possibility to choose between different scenarios for the surrounding environment (low density, intermediate density and high density), which affects the efficiency of the reverse shock dust destruction (the higher the density, the higher the dust destroyed by this shock, see Fig. 2.7). Among the different possibilities, we adopt the values obtained for the intermediate density environment for spirals and spheroids/ellipticals and the low density environment for irregulars. We make this choice following Gioannini et al. 2017b, who well reproduced observed dust masses in high-redshift starbursts as well as DGR vs. metallicity relations in local spiral and irregular galaxies (see also 3.1.2);
- at variance with the other Sections of this Chapter, here we allow Type Ia SN dust production in models for spheroidal/elliptical galaxies. In particular, we adopt the prescriptions by Dwek (1998) as implemented by Calura et al. (2008): a dust condensation efficiency of 0.5 is taken for C, whether a value of 0.8 is taken for Si, Mg, Fe, Si, Ca. It is then assumed that for each atom of these elements, one oxygen atom is also condensed, i.e. $M_O = 16 \sum_i 0.8 M_i/\mu_i$, where M_i is the mass and μ_i is the atomic weight of each of the elements i.

The assumption of Type Ia SN dust production is made despite of recent observational and theoretical results that claim no effective dust production from Type Ia SNe (e.g. Nozawa et al. 2011; Gomez et al. 2012, see also Section 2.3.1).

We make this choice since dust evolution in elliptical/S0 galaxies is heavily affected by considering or not Type Ia SN dust production. In fact, this morphology will otherwise host only low-mass AGBs that will produce little dust mass (even at supersolar metallicity, see Ventura et al. 2020) .

While there could be other mechanisms of dust production within elliptical/S0 galaxies, such as dust growth in shielded shocked gas, e.g. in AGB winds (Li et al. 2019), these

processes cannot be easily included in our models and rough estimates show that their contribution to dust masses in ellipticals would be smaller than what would be produced by Type Ia SNe. For this reason, the inclusion of Type Ia SN dust production can be also seen as an upper limit to what elliptical galaxies would be capable of contributing to the total cluster budget.

In addition to dust processes within individual galaxies, we accurately model the fate of the dust ejected by galaxies into the ICM (i.e. ICM component).

To this aim, we apply thermal sputtering to this component, as prescribed in Tsai & Mathews (1995). Assuming a fixed grain size of 0.1μm, the initial sputtering timescale is taken to be $\tau_{sp} = 5.5 \times 10^7$ yr, as derived by Gjergo et al. (2018).
Specifically, they compute the dust destruction rate by sputtering in this way:

$$\dot{M}_{dust,sp} = M_{dust}^{ICM}/\tau_{sp}, \tag{3.17}$$

We highlight that this treatment of sputtering is reliable for virialized clusters whose ICM has become hot, diffuse, and highly ionized, therefore up to redshifts between 1 to 2 (i.e. well above the redshift of the data sets adopted).

3.3.4 Results

Having provided the detailed description of our method aimed at computing the dust mass evolution in galaxy clusters, we now describe the results of the integration procedure.

We divide the discussion into three main paragraphs.
We first show the prediction of dust mass evolution for every ISM and ICM cluster components (i.e., elliptical, spiral, irregular) in the case of single and double LFs and "monolithic" and "hierarchical" evolution scenarios.
After that, we try to reproduce PlanckXLIII-16 observations by rescaling our computed total dust masses to a fixed aperture of 15 arcmin (see 3.3.3 for more details) and normalising the obtained curves to cluster M_{200}.
Finally, we explore the parameter space by varying the main LF function parameters for each of the ISM and ICM components with both the "monolithic" and the "hierarchical" scenarios.

Component evolution in a cluster

In Fig. 3.20, we present the results of our integration method within R_{200} of a cluster of average WINGs LF (Moretti et al., 2015) and cluster (Mamon et al., 2019) parameters (see Tab. 3.8 and 3.9).
As can be seen from the labels, in the top panel we employed a single LF, whereas in the bottom panel we adopt a double LF. In the panels, both "monolithic" evolution (shaded

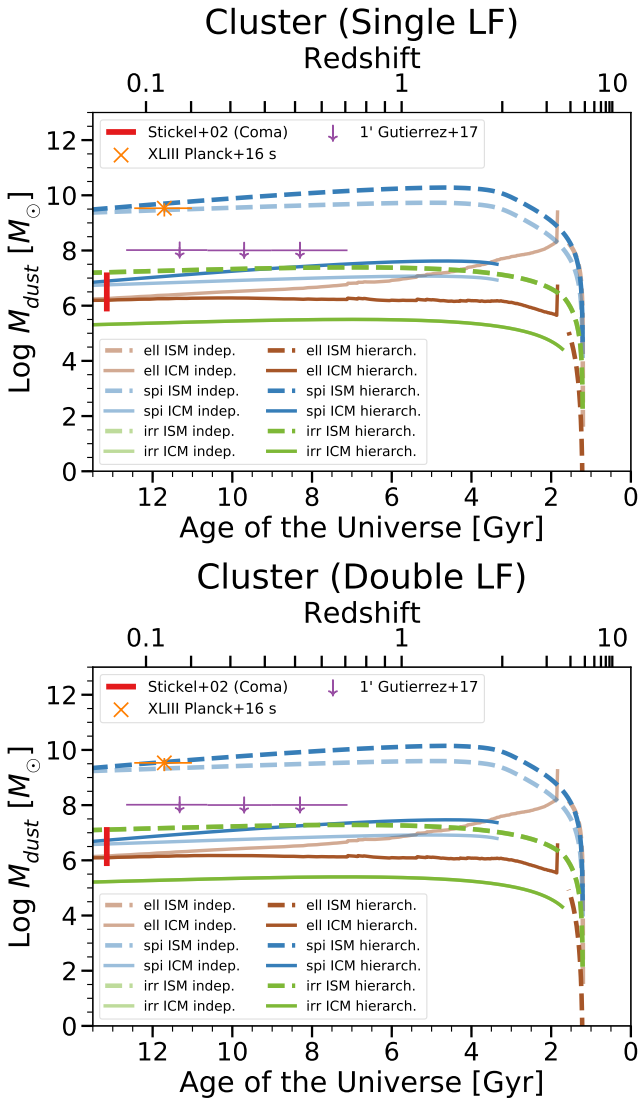

Figure 3.20: *Evolution of dust mass components within a WINGs-like average cluster ($M_{200} \sim 5 \times 10^{14}$ $M_\odot$, $f_{ell} = 0.74$) adopting a single LF (upper panel) and a double LF (lower panel). The brown, blue, and green lines represent elliptical, spiral and dwarf irregular galaxies, respectively. The dashed lines identify the integrated dust component residing within galaxies (ISM), whether the solid lines identify the ejected components (ICM). Shaded lines are computed assuming that "monolithic scenario", whether the fully opaque lines are computed assuming a "hierarchical scenario". Orange cross is the PlanckXLIII-16 low mass subsample at low redshift. Purple downward arrows are the upper limits found in GLC17 for the redshift bins are centered around redshift $z = 0.173$, 0.338, and 0.517. Red bar is the dust estimate from Stickel et al. (2002) for the Coma cluster.*

lines) and "hierarchical" evolution (fully opaque lines) scenarios of galaxy formation are shown.

By looking at both panels, we see that the dominant component for both galaxy evolution scenarios and LFs is the ISM dust in spirals. This is in agreement with the interpretation proposed by Roncarelli et al. (2010) that late-type galaxies should dominate the overall dust IR emission in galaxy clusters. For either scenarios and LFs, at a redshift $z < 2$ the next most abundant dust mass component appears only 2 dex below the ISM spiral component.
As we can expected, the choice of single or double LF does not affect significantly the most massive galaxies, if not by a marginal decrease in dust mass. In fact, the double LF differentiates from the classical Schechter function particularly in the low luminosity end. More surprisingly, the choice of the LF does not seem to affect the dwarf irregular ISM and ICM components. However, this can be expected since the additional faint LF component is dominated by very low mass ($< 10^8$ $M_\odot$) and poorly chemically evolved galaxies. For both LFs, we also see that below $z \lesssim 0.5$ the dust mass within irregular galaxies exceeds the dust mass ejected in the ICM by spirals.
Coming back to spiral components, there is a minimal but steady dust mass loss within the ISM of spiral galaxies in both "hierarchical" and "monolithic" evolution scenarios after the peak at a galaxy age of ~ 3 Gyrs. The negative slope traced by the spiral ICM dust line is instead steeper in the hierarchical scenario due to the higher spiral fraction at earlier times. For elliptical galaxies, we note in the panels that the ISM component is instantaneously ejected into the ICM as soon as stellar winds ignite (see 2.1.4). In this case, the ICM dust trend is flipped relative to spiral galaxies, with a flatter slope for the hierarchical evolution: elliptical galaxies were less numerous in the past for this scenario.

By comparing the model predictions in Fig. 3.20 with cluster observational data, we see that our results satisfactorily reproduce the total cluster dust mass by PlanckXLIII-16. In particular, here we employ the low mass, low-redshift bin with average cluster mass of $\langle M_{200} \rangle = 4.3 \times 10^{14}$ $M_\odot$ and average redshift $\langle z \rangle = 0.139$ (see 3.3.2).
For what concerns ICM dust estimates, we compare the results of our model with the data by Stickel et al. (2002) and GLC17. In particular, Stickel et al. (2002) represents a good upper limit for ICM dust of local quiescent clusters. On the other hand, GLC17 dust mass upper limits provide measurement for clusters with total masses $> 10^{14}$ $M_\odot$ up to $z \sim 0.7$. Both Fig. 3.20 panels show good agreement between ICM dust measurements and our computed cumulative ICM dust.

Summarising, within ~ 2 Gyr since galactic birth, the overall ISM of cluster galaxies with WINGs sample parameters contains already about 10^{10} $M_\odot$ in dust mass. This corresponds to a dust-to-gas ratio of DGR$\sim 5 \times 10^{-4}$. The ICM components are between 2 to 4 dex lower, around or below a dust mass of 10^7 $M_\odot$, which corresponds to a low DGR of

the order of 10^{-6}. These values are in agreement with estimates both for total dust mass (PlanckXLIII-16) and ICM dust mass (Stickel et al. 2002; GLC17).

Comparison with Planck observations

In Fig. 3.21 we rescale our total dust mass predictions in clusters out to a radius of 15 arcmin, in order to mimic PlanckXLIII-16 observations (see 3.3.3 for more details).

These dust mass estimates are displayed in the three data points of Fig. 3.21. In particular, the middle full square represents the whole sample of stacked clusters in the redshift range $0.01 < z < 1.00$ (645 clusters, $\langle M_{200} \rangle = (5.6 \pm 2.1) \times 10^{14}$ $M_{\odot}$), whereas the cross and the hollow diamond represents the subsamples with redshift $z \leq 0.25$ (307 clusters, $\langle M_{200} \rangle = (4.3 \pm 1.7) \times 10^{14}$ $M_{\odot}$) and $z > 0.25$ (254 clusters, $\langle M_{200} \rangle = (7.0 \pm 1.5) \times 10^{14}$ $M_{\odot}$), respectively.
It is worth noting that both these data and model curves are normalized to their respective M_{200}, which time evolution is taken from the D2 run by Gjergo et al. (2018).

Concerning the models, here we show the evolution for both the independent evolution scenario (blue curves) and the hierarchical clustering iteration (red curves), as well as for single LF (solid curves) and double LF (dashed curves). We adopt, just like Fig. 3.20, LF and cluster parameters coming from the WINGs average. However, we allow to vary the elliptical fraction $f_{0,ell}$ from the initial value of $f_{0,ell} = 0.74$ (Mamon et al. 2019, thick lines). In particular, we span an elliptical fraction from 0.2 to 0.82, indicated by the blue and red shaded regions for the "monolithic" and "hierarchical" scenarios. To better display the variation in the $f_{0,ell}$ parameter, we show the results for $f_{0,ell} = 0.43$ (thin lines): this value is representative of dynamically young local clusters, such as Virgo. On the other hand, the extreme value of $f_{0,ell} = 0.82$ is indicative of mature local clusters, such as Coma.

We see from the Figure that varying the elliptical fraction in the range between ~ 0.2 to ~ 0.8 changes the dust mass by less than an order of magnitude. In particular, the estimates vary by not more than a factor of 4 within scenarios, and 6 overall.
As f_{ell} (and so also f_{spi}) is time-dependent in the "hierarchical scenario", we note that at higher redshifts the curves for this scenario converge to higher dust-to-M_{200} ratios. The difference between the constant elliptical fraction of the "monolithic" evolution and the same fraction for the "hierarchical" evolution widens at high final elliptical fraction values because the spiral number density falls more steeply (and the elliptical number density grows more rapidly).
More in general, the quite steep slope seen for all the curves in Fig. 3.21 is mainly driven by the fixed aperture of 15 arcmin that progressively leads to larger encompassed radii. However, by $z \sim 0.5$ to 0.6, the 15 arcmin angular size has already reached 3 Mpc, and the NFW rescaling does not increase the dust mass by much, due to the low galaxy

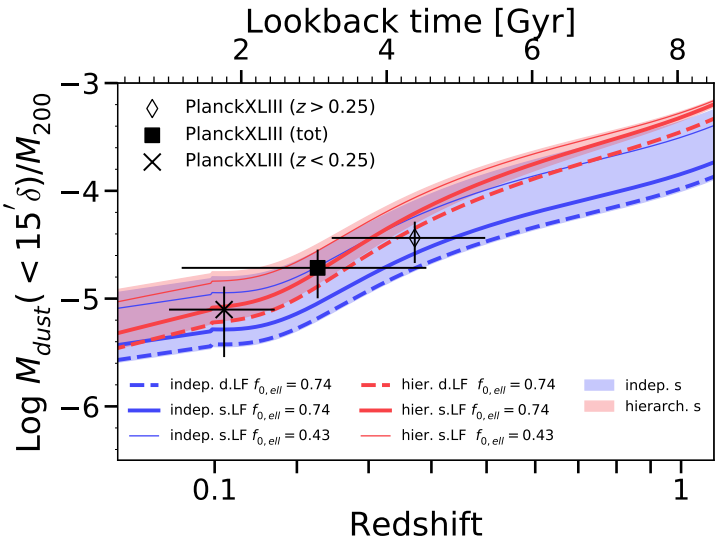

Figure 3.21: *Evolution of dust mass at low-intermediate redshift in comparison with average dust mass measured within 15 arcmin of a stacked cluster sample (PlanckXLIII-16). Black full square, cross and hollow diamond represent the full sample, the nearby subsample and the distant subsample, respectively. The blue curves identify the "monolithic scenario", whether the red curves show the "hierarchical scenario" case. The solid curves assume a single LF, the dashed curve a double LF. The thick curves assume an elliptical fraction of $f_{0,ell} = 0.74$, as in the WINGs clusters. The fainter curves assume instead a $f_{0,ell} = 0.43$. The shaded red and blue bands span an $f_{0,ell}$ between 0.2 and 0.82. Both theoretical curves and data are normalized to their respective M_{200}.*

density out to these outskirts. Therefore, the increase at higher z is mainly caused by the normalization to M_{200}.

For what concerns the data-model comparison, this seems to weakly favour a "hierarchical scenario" with the WINGs average elliptical fraction of 0.74, with no significant preference between the single or double LF (as expected from Fig. 3.20). The better suitability of the hierarchical scenario to explain PlanckXLIII-16 data is confirmed by a χ^2 test performed over different LFs and scenarios of galaxy evolution. In particular, for $f_{0,ell} = 0.74$ we obtain a χ^2 of 0.07 for the double LF and 0.21 for the single LF in the hierarchical scenario, whereas 1.10 and 0.40 are the values obtained letting the different morphologies evolve independently.
Another interesting aspect regards the comparison with other works in the literature in the reproduction of PlanckXLIII-16 data. In fact, our curves fall right between the observational points without any need of model calibration. This was instead necessary in several previous papers (e.g. Gjergo et al. 2018; Vogelsberger et al. 2019), where dust sputtering timescales where tuned to reproduce the data.

Further exploring the parameter space

In order to probe the robustness of our integration method, we test how the obtained results change by varying the LF parameters described in 3.3.3. In Fig. 3.22 we show the dependence of our model to single LF parameters. In fact, by testing all the dependencies on double LF parameters, we find only minor differences relative to the single LF case.

The parameters varied are those listed in Tab. 3.8: the elliptical fraction $f_{0,ell}$, the LF slope α, the V-band magnitude at the break of the LF Mag* , the cluster richness n_*, the mass-to-light ratio in K, the lower $M_{l,X}$ and upper $M_{u,X}$ mass integration limits for each of the three morphologies X.
Each parameter encompasses the typical average ranges of known clusters: $f_{0,ell}$ spans from 0.43 to 0.82, which is the elliptical fraction of the Virgo Cluster and of the Coma cluster, respectively. α and Mag* test ranges which include $\sim 1.5\sigma$ of the LF slope and break V-band magnitude in Moretti et al. (2015). Specifically, α ranges between -0.9 and -1.4, and Mag* ranges between -20.5 and -22.5. For the richness, we once again refer to the WINGs sample: we vary n_* between 115 (highest richness considered in Schechter 1976) and 52 (average WINGs richness). The K mass-to-light ratio spanned range is instead between 5 and 15: typical K values in early-type galaxies range from ~ 5 to ~ 13, while in late-type galaxies it ranges between 5 and 10 (De Masi et al. 2019).

The results of these tests reveal that our model depends linearly only on n_* and on $f_{0,ell}$. The richer and younger the cluster, the more dust there is, but the cluster richness does not vary the cumulative dust mass if not by a factor of 3. A factor of 3 is also the extent to which the variation of $f_{0,ell}$ changes the dust mass for the spiral and elliptical components. This leads to variations of this order also on the total dust mass, as seen in Fig. 3.21.
In each case at low redshifts, the spiral ICM dust component is between 3 and 30 times larger than the elliptical ICM component. Thus, we can safely conclude that spiral galaxies are more efficient than elliptical/S0 galaxies at contaminating the ICM with dust.

A little more complicated is the issue of the contribution to ICM dust by smaller galaxies. These faint irregular galaxies are difficult to resolve, so the emission and extinction from dust within these systems may be confused as newly ejected ICM dust. In order to compare how much dust there is within irregular galaxies against ICM upper limits, we add GLC17 data points to the third row of the plot. As expected, the irregular-born dust mass has little dependence on most parameter variations.
The only significant differences are generated by the choice of the α LF slope and of the upper mass integration limit $M_{u,irr}$: these are the only cases where parameter changes in a certain scenario span more than a factor 6 (instead of a factor 3, as in most of the other cases). The increase in dust mass in the α variation is mostly due to the excess in number density on the more massive end of the integration limits, closer to the break magnitude. In fact, when we test these variations on the double LF function, we find that a steeper

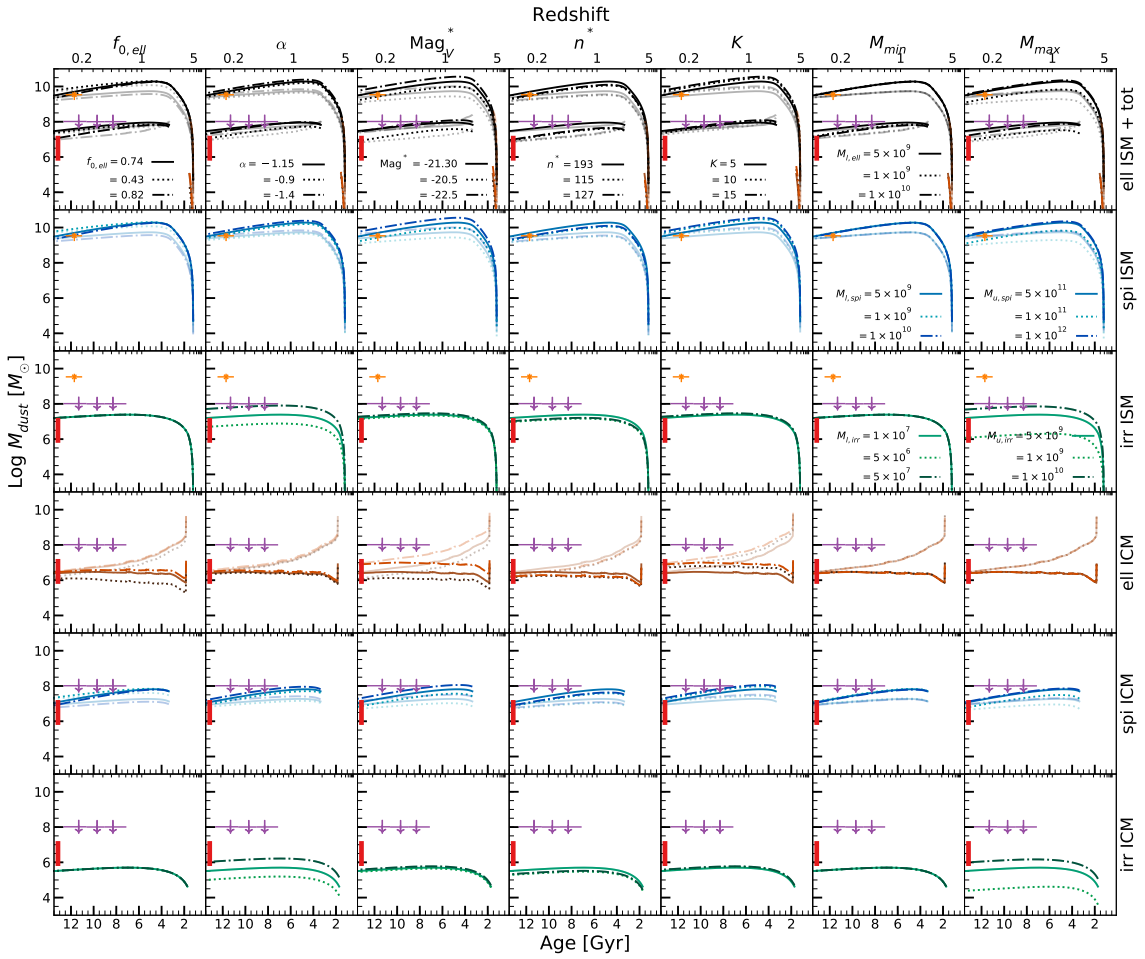

Figure 3.22: *Dependence of dust mass components evolution on parameter variations. ISM dust components are shown in the top three rows, whereas ICM dust components are shown in the bottom three rows. Columns identify the variation of a cluster parameter. From left to right, the parameters are: the final fraction of elliptical galaxies $f_{0,ell}$, the slope of the LF α, the V-band magnitude at the break of the LF Mag^*_V, the cluster richness n^*, the mass-to-light ratio K, and the lower and upper mass integration limits M_{min} and M_{max}. For each column, the parameter variation is labelled and identified with dotted and dash-dotted lines, whereas solid lines represent the calculations with fiducial values. Line colors and shading are as in Fig. 3.20. In addition, black lines display the total ISM dust and total ICM dust with the addition of the irregular ISM. Data points are from Stickel et al. (2002); PlanckXLIII-16; GLC17 as in Fig. 3.20.*

increase of α_f provides only a marginal gain in dust mass. On the other hand, the upper bound for irregular galaxies is dictated by observations (e.g. Vaduvescu et al. 2007; Yin et al. 2011). Therefore, it is not realistic to extend the upper integration limit for irregulars above our fiducial value of 5×10^9 $M_\odot$.

Except for the latter morphology, the lower and upper mass bounds of our integration matter little. Unless the infall mass is of the same order or larger than the break infall galaxy mass ($M^*_G = 6.94 \times 10^{10}$ $M_\odot$ for the single LF), the integration is not very sensitive to either mass bounds.
This is because of the dominance over the mass budget of galaxies at the break of the LF. In the case of spiral galaxies, $M_{u,spi} = 10^{11}$ $M_\odot$ (i.e. an upper bound five times smaller than the fiducial one) decreases the dust mass only by a factor of 3, whereas a larger upper bound of $M_{u,spi} = 10^{12}$ $M_\odot$ hardly makes a difference: this is because the dust mass has nearly reached its limiting value. A dependence on the upper limit does not exist for elliptical galaxies, because we integrate them over a single upper incomplete gamma function having only a lower bound. However, even if we want to impose an upper limit, it would not affect the stability of our results. In fact, as long as this limit has to be much larger than M^*_G (e.g. $M_{u,ell} = 10^{12}$ $M_\odot$), the variation are minimal as it happens for spiral galaxies.

Concluding, both in the case of the ISM and of the ICM components, spiral galaxies are the dominant dust producers and sufficient to explain the observed dust abundances within our model. After spiral galaxies, the ISM of irregular galaxies is a major dust source. This dust mass from irregulars comes mainly from the bright end of the single LF, as the dust mass is nearly independent of the lower integration limit.

It must be reminded that our results are obtained even assuming a strong dust production by Type Ia SNe in elliptical galaxies, which can be also seen in the context of other mechanisms acting in these galaxies as an upper dust production limit (e.g. Li et al. 2019). This means that elliptical/S0 galaxies, despite of their dominant contribution in the ICM metal enrichment (Gibson & Matteucci 1997), can be definitely ruled out as major dust producers in galaxy clusters.

3.3.5 Conclusions

In this Section, we aim at breaking down the galaxy-born total cluster dust mass into its various components.

We differentiate the three main morphologies (i.e., elliptical, spiral, and irregular) that contribute to the dust budget and we separate dust residing within galaxies from the dust ejected in the ICM by applying sputtering to the dust ejected out of galaxies. By revising the integration method developed by Matteucci & Vettolani (1988) we integrate galaxy dust over a parametrization of cluster luminosity function (LF). Our LF parameters are chosen from medians and average values of large local galaxy clusters (WINGs, Moretti

et al. 2015; Mamon et al. 2019). We test the cluster dust evolution both in a "monolithic" (i.e. galaxies evolve as a whole and independently of other galaxies) and in a "hierarchical" scenario of galaxy formation (Vincoletto et al. 2012).
Our prediction are compared with some of the latest and most advanced observations of dust in galaxy clusters (e.g. Planck Collaboration (XLIII) et al. 2016; Gutiérrez & López-Corredoira 2017) that provide total (ISM and ICM together) and ICM dust mass estimates.

Our main conclusions are as follows:

- spiral galaxies account for most of the dust contained within clusters in any assumed galaxy formation scenario. We estimate that a typical cluster should have around 10^{10} $M_{\odot}$ in total dust mass, mainly residing within its spiral galaxies, or alternatively a dust-to-gas ratio of $\sim 5 \times 10^{-4}$.
  Dust mass in the ICM of a cluster should be of the order of 10^{7} $M_{\odot}$. Concerning this component, dust ejected by spiral galaxies (~ 2.5 dex less abundant than the ISM dust component) is comparable in mass to the dust component residing within irregulars. In turn, these predictions are consistent with the dust abundance upper limits measured in the ICM of local galaxy clusters (Stickel et al. 2002; Bai et al. 2007; Kitayama et al. 2009) regardless of the assumed spiral fraction;

- without any need for model parameter calibration, we are able to produce dust abundances analogous to observational data. Galaxy-born dust is likely the main source of cluster dust, even in the ICM: it is not necessary to rely on dust sources aside from those of galactic origin (e.g. dust growth in cold filaments of the ICM, dust generated around intracluster stars) to explain where the bulk of cluster dust comes from. Unless the LF of such smaller sources dramatically spike at the faintest luminosities, these sources cannot produce sufficient dust mass to account for the ICM dust upper limits reported by Gutiérrez & López-Corredoira (2017).
  Furthermore, our integration method is able to reproduce total dust masses and their redshift evolution as observed by Planck Collaboration (XLIII) et al. (2016). In particular, we find a marginal improvement of the dust mass redshift dependence by letting our model evolve according to a "hierarchical scenario";

- galaxies close to the break of the LF dominate the cluster dust mass, and the method has little dependence on the integration limits. A similar result was found in Gibson & Matteucci (1997) for the gas-phase metals in the ICM, where galaxies at the break of the LF dominate the ICM metal enrichment.
  However, at variance with metals where early-type galaxies (elliptical/S0) dominate the chemical enrichment, here spiral galaxies govern the mass budget at low-intermediate redshift. This holds even with the extreme and unrealistic assumption of strong dust production by Type Ia SNe in elliptical galaxies;

- by varying our model parameters ($f_{0,ell}$, α, Mag_V^* , n_*, K, $M_{l,X}$, $M_{u,X}$) over a reasonable range chosen from literature, we find that dust masses change by up to a factor of ~ 6 (up to ~ 3 most of the times). All these variations do not affect deeply our conclusions, confirming the robustness of the method adopted.

CHAPTER 4

The local Universe: Milky Way chemical evolution

OUR GALAXY, the Milky Way, is to date the most studied system from the point of view of the chemical evolution.
Even more, we are actually in a golden era for the study of our Galaxy: in the last decade many surveys and projects have been developed to study the formation and evolution of the Milky Way and this has pushed us towards a much more thorough understanding of the different components of this system. Nonetheless, many questions remain still open on the formation and evolution of the Milky Way.

Therefore, in this Chapter we want to focus on the modelling of our Galaxy. To introduce in more detail this system and the specific model framework in which we move throughout this Chapter, in the first section we give a general introduction about the Galaxy and on the main features of Milky Way chemical evolution models. Then, we present our analysis of the present-day radial gradients and [α/Fe] at different Galactic locations to constrain in detail the star formation history of the Galactic disc. The results of this Section have been published in Palla et al. (2020b). Finally, in the last Section we show the effects of the application of different Type Ia SN yields on the models for our Galaxy. These results are shown also in the published paper Palla (2021).

4.1 The Milky Way

Our Galaxy, the Milky Way (hereafter MW), is classified as a SBbc galaxy, namely a spiral barred galaxy in the Hubble sequence (see 1.3.1). It is a disc of gas and stars that rotates around a barred nucleus at its centre, surrounded by a spherical halo of stars. All this system of gas and stars is then surrounded by a large amount of dark matter (the dark matter halo, hereafter DM halo), which is supposed to dominate the mass content of the Galaxy at large distances.

The total stellar mass of the Galaxy is estimated to be $M_* = (5 \pm 1) \times 10^{10}$ $M_\odot$ (Bland-Hawthorn & Gerhard 2016 and references therein). As just mentioned, the MW stellar content consists of many different components/populations, which were likely assembled into the system at different epochs and at different timescales during the formation and evolution of our Galaxy.

The division of the MW into stellar components is performed by using chemical and kinematical criteria. Despite the fact that these different types of division can sometimes bring to contradictory results (see, e.g. Romano et al. 2021 and references therein), by means of such criteria we can divide the MW into four main stellar components :

- **stellar halo**: the stellar halo constitutes a little fraction of the Galactic stellar content (of the order of few percent) and includes globular cluster and field stars. Different studies point towards different estimates for the total stellar halo mass, from $M_* = (4 - 7) \times 10^8$ $M_\odot$ (Bland-Hawthorn & Gerhard 2016 and references therein) up to $M_* \simeq 1 \times 10^9$ $M_\odot$ (Deason et al. 2019; Mackereth & Bovy 2020).
  The halo stars constitute an extended spheroidal distribution, supported by random motions in eccentric orbits and with a small net rotation, which can be either prograde or retrograde[1] (e.g. Carollo et al. 2007, 2010). Indications of a dual (inner and outer) halo have been suggested from spatial distribution, kinematic and chemical studies (e.g. Hartwick 1987). The separation in the radial density distribution which identifies the two components was found at $\sim$25 kpc (Bland-Hawthorn & Gerhard 2016), even if some works challenge the presence of a real break in the density distribution (e.g. Mackereth & Bovy 2020). Most of the halo stars are older than 10 Gyr (e.g. Sneden et al. 1996; Cayrel de Strobel et al. 2001; Helmi 2008, 2020). These stars are metal-poor: the halo metallicity distribution is peaked at a value of [Fe/H]$\sim$-1.6 dex for the inner component and [Fe/H]$\sim$ -2.2 for the outer component and halo stars extends below [Fe/H]$\sim$-4 dex (e.g. Helmi 2008; Carollo et al. 2010; Helmi 2020 and references therein). Thanks to the combination of the data by *Gaia* mission (Gaia Collaboration et al. 2016b, 2018) and large spectroscopic surveys, in the last years it was discovered that a large fraction of the inner halo is built from the debris of an

[1] for prograde, we intend a sense of rotation which is the same as the disc; for retrograde, we intend an inverse sense of rotation.

ancient, quite massive dwarf galaxy, dubbed as Gaia-Encelaus (Helmi et al. 2018) or Gaia-Sausage (Belokurov et al. 2018). This is not the only merger discovered, since smaller stellar streams resembling accreted galaxies continue to be found (e.g. Myeong et al. 2019; Koppelman et al. 2019; Aguado et al. 2021; Martin et al. 2022);

- **bulge**: it is a massive component comprising about a quarter of the Galactic stellar mass ($M = (2.0 \pm 0.3) \times 10^{10}$ M$_\odot$, Valenti et al. 2013) located at the centre of the Galaxy.
  The bulge stars have random motions and span a metallicity range of -1.5≤[Fe/H] ≤+0.5 dex (Barbuy et al. 2018). Because of the heavy dust absorption towards the Galactic centre (see also Section 1.2), studies of this region have been difficult, but significant progress have been made thanks to new surveys looking at near infrared (NIR) wavelengths. The presence of a classical bulge (i.e. of spherical shape, formed quickly) is still debated, but its contribution has been constrained by the observed kinematics to be small ($< 8\%$ of the mass of the disc, e.g. Shen et al. 2010). Most of bulge stars form a rotating triaxial structure, the Galactic bar (e.g. Wylie et al. 2021). Concerning the chemistry, most of the studies found that bulge stars have a bimodal distribution with a metal-poor (peaking at [Fe/H]∼-0.30 dex) and a metal-rich (peaking [Fe/H]∼+0.32 dex) population (e.g. Hill et al. 2011; Rojas-Arriagada et al. 2017). Both the populations seem to host old stars, with age $\gtrsim$ 10 Gyr (e.g. Clarkson et al. 2011; Renzini et al. 2018). However, Bernard et al. (2018) found a non negligible fraction of bulge stars ($\sim 10\%$) is actually composed by stars younger than 5 Gyr, and this fraction rises to 20-25% for the metal-rich population. Moreover, other studies point towards more multi-modal distributions (e.g. Bensby et al. 2017) that imply more important fractions of relatively young stars, possibly associated to the inner thin disc (e.g. Haywood et al. 2016);

- **thin disc**: it is the component where most of the Galactic stellar mass is concentrated ($M_* = (4 \pm 1) \times 10^{10}$ M$_\odot$, Bland-Hawthorn & Gerhard 2016). It is also the site of ongoing star formation in the Galaxy, estimated at a rate between ∼1.5 and ∼2 M$_\odot$ yr^{-1} (Chomiuk & Povich 2011; Licquia & Newman 2015). Indeed, the majority of the gas, both atomic and molecular, resides in the thin disc.
  From the structural point of view, the thin disc constitutes a narrow (a few hundreds of parsec scaleheight) component above and below the Galactic plane, with an exponential decreasing density both in the vertical and in the radial direction (e.g. Bovy et al. 2016; Pouliasis et al. 2017). It is a rotationally supported component, where stars move on fairly circular orbits with a mean rotational velocities of the order of 210 km s^{-1} (Recio-Blanco et al. 2014). Thin disc stars are young relative to the other MW stellar components, with typical ages below 8 Gyr (e.g. Haywood et al. 2013; Silva Aguirre et al. 2018). Metallicities in these stars lie approximately from [Fe/H]∼-0.6 dex to [Fe/H]∼+0.5 dex, while their [α/Fe] ratios are roughly solar (e.g.

Table 4.1: *Properties of the different Milky Way stellar components.*

	M_* ($M_\odot$)	Age (Gyr)	[Fe/H] (dex)	ρ profile
Stellar halo	4×10^8-1.3×10^9 (1), (2)	>10 (3)	$\lesssim$-4 to -0.5 (4), (5)	$\rho \propto r^{-\beta}$ $r_{break} \sim 25$ kpc, $\beta_{in} \sim 2.5$, $\beta_{out} \sim 3.7$ (1)
Bulge	2×10^{10} (6)	>10 (most) (7)	-1.5 to +0.5 (7)	Boxy-peanut shape (1)
Thin disc	4×10^{10} (1)	$\lesssim$ 8 Gyr (8)	-0.6 to +0.5 (9)	$\rho \propto e^{-R/R_s}\, e^{-z/Z_s}$ $R_s \sim 2.6$ kpc, $Z_s \sim 0.3$ kpc (1)
Thick disc	6×10^9 (1)	$\gtrsim$ 8 Gyr (8)	-1 to $\gtrsim$0 (9)	$\rho \propto e^{-R/R_s}\, e^{-z/Z_s}$ $R_s \sim 2.0$ kpc, $Z_s \sim 0.9$ kpc (1)

References*: (1) Bland-Hawthorn & Gerhard (2016); (2) Mackereth & Bovy (2020); (3) Helmi (2008); (4) Helmi (2020); (5) Carollo et al. (2010); (6) Valenti et al. (2013); (7) Barbuy et al. (2018); (8) Haywood et al. (2013); (9) Hayden et al. (2015)*

Hayden et al. 2015; Ahumada et al. 2020);

- **thick disc**: relative to the thin disc, this component constitutes a thicker (almost a kpc scaleheight) volume above and below the Galactic plane, but it is more centrally concentrated in the radial direction. Its stellar mass is estimated to be much lower to that of the thin disc ($M_* = (6 \pm 3) \times 10^9$ $M_\odot$, Bland-Hawthorn & Gerhard 2016). Thick disc stars also differ from the thin disc ones in their kinematics, age distribution and chemistry. In particular, this population is made of field stars that, even if still rotationally supported, show hotter kinematics[2] than that of the thin disc stars. Thick disc stars span a range of metallicities from [Fe/H]$\sim$-1.0 dex up to solar values or even supersolar values, with [α/Fe] ratios systematically higher than those found at the correspondent metallicity in the thin disc (e.g. Hayden et al. 2015; Ahumada et al. 2020). For what concerns stellar ages, typical ages are larger than 8 Gyr (e.g. Haywood et al. 2013; Silva Aguirre et al. 2018).

The main features of the four MW stellar populations are summarized in Tab. 4.1. Furthermore, Fig. 4.1 gives a clear representation of the different kind of orbits experienced by the stars of the different populations.

Galactic archaeology: a golden era

Nowadays, it has became common to use the expression "Galactic archaeology" when referring to the study of the formation and evolution of the MW and its stellar populations. In particular, the idea behind this concept is to use the observed properties such as chemistry, age and kinematics of living stars to infer information on the history of the Galaxy,

[2] it means that the stars have higher velocity dispersion.

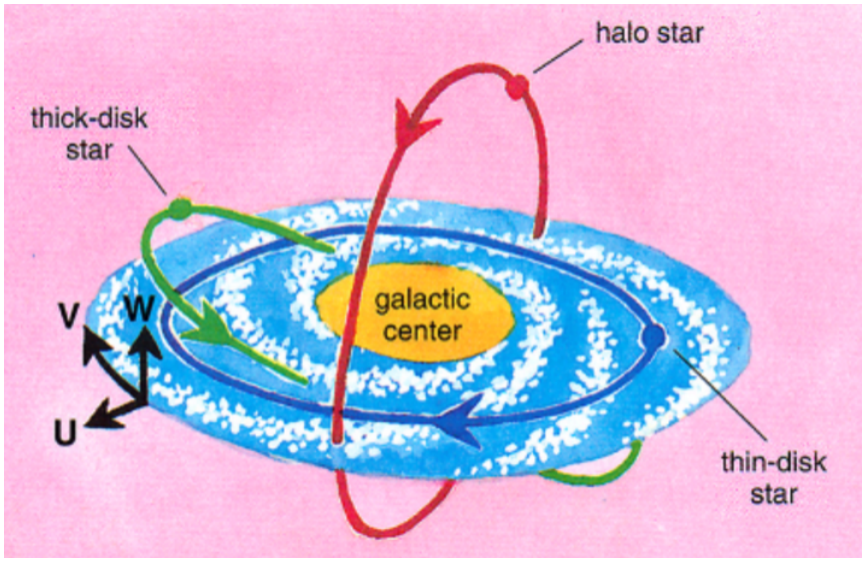

Figure 4.1: *From Chiappini (2001). Schematic view of the main stellar populations of the Milky Way.*

in the same way archaeologists use artifacts to learn about the past (Helmi 2020).

We are actually in a golden era for Galactic archaeology. As already mentioned, in the last decade many spectroscopic surveys and projects have been developed to study the formation and evolution of the MW. Just to give an example of the most important campaigns, we mention Gaia-ESO (Gilmore et al. 2012), APOGEE (Majewski et al. 2017), GALAH (De Silva et al. 2015), LAMOST (Zhao et al. 2012), RAVE (Steinmetz et al. 2020) and the AMBRE Project (de Laverny et al. 2013). These span different ranges of wavelengths (e.g. $\lambda s \sim 1.5 - 1.7$ μm APOGEE, $\lambda s \sim 0.4 - 0.8$ μm GALAH), resolution powers (e.g. $R \sim 4.7 \times 10^4$ Gaia-ESO for UVES targets, $R \sim 2 \times 10^3$ LAMOST-low resolution) and number of targets analysed (e.g. $\lesssim 10^5$ Gaia-ESO, $\sim 10^7$ LAMOST-low resolution), leading these surveys to assume complementary roles in the investigation of our Galaxy.

Furthermore, the launch of the *Gaia* mission (Gaia Collaboration et al. 2016a) is even enhancing the value of these surveys. In particular from its second data release (Gaia Collaboration et al. 2018, 2021), *Gaia* has provided us exquisite astrometrical and photometrical measurements for more than a billion of stars: this has allowed us not only to infer dynamical properties of MW stars with unprecedent accuracy, but also to improve the determination of stellar parameters and hence their spectroscopical analysis.
The cross match of the abundance data of spectroscopic surveys with that provided by *Gaia*, has helped us to obtain a much clearer picture of the evolution of our Galaxy. One of the most striking results was obtained with the discovery of the stellar relics of the MW

last major merger, dubbed as Gaia-Enceladus-Sausage[3] (Belokurov et al. 2018; Koppelman et al. 2018; Helmi et al. 2018).

In the very last years, also precise stellar age determinations have started to become part of the game. Up to recent times the determination of ages was based purely on spectroscopic or photometric information, and that was possible only for a very limited number of stars in the solar vicinity (e.g. Haywood et al. 2013; Bergemann et al. 2014). A step forward has become possible thanks to asteroseismology: by determining the frequency of oscillation of stellar interiors, we can derive information on stellar mass and thus on stellar ages by comparing the oscillation spectrum with stellar models predictions (e.g. Casagrande et al. 2014; Pinsonneault et al. 2018). In this way, for field red giant stars, we are capable to limit the uncertainties to a $\sim$20-25% level (e.g. Casagrande et al. 2016; Silva Aguirre et al. 2018; Miglio et al. 2021).

In order to couple the information coming from the different observational probes and enlarge as much as possible our data domain, a large number of value-added catalogues have been built by using Bayesian codes (e.g. ASTRONN, Leung & Bovy 2019, StarHorse, Queiroz et al. 2018). In this way, we can now work on detailed maps of the Galaxy containing various variables.
As for example, in Fig. 4.2 we show the APOGEE abundance ratios divided in Galactocentric radius and height bins, with the distances inferred by means of the StarHorse code coupled with *Gaia* DR2. We note that the maps go from the Galactic centre to the outermost regions of the disc. This has to be compared to our knowledge of the Galaxy just 20 years ago, where the majority of the available measurements were limited to samples of solar neighborhood stars.

Nonetheless, many questions remain still open on the formation and evolution of the MW. In fact, the wealth of data coming from observations has to be interpreted in terms of models of the Galaxy and its various components.
As for example, the [α/Fe] vs. [Fe/H] abundance diagrams of Fig. 4.2 show clearly the presence of two distinct sequences, i.e. the so-called high-α and low-α sequences. These sequences are associated to the thick disc (high-α) and the thin disc (low-α) stars. However, starting from the first theoretical works able to reproduce these two sequences (Calura & Menci 2009; Kobayashi & Nakasato 2011), different explanations have been proposed to explain the origin of the high and low-α stars: this is known as the [α/Fe] dichotomy/bimodality problem. Indeed, several models have suggested that the bimodality may be strictly connected to a delayed gas accretion episode (e.g. Grand et al. 2018; Spitoni et al. 2019; Buck 2020, see Section 4.2 for more on this), some others have proposed

[3] the different names indicate two different derivations of the merger. Belokurov et al. (2018) found that a high fraction of the halo stars had very large radial motions, dubbing the structure in the phase-space as Gaia-Sausage. On the other hand, Helmi et al. (2018) selected a blob of stars on slightly retrograde orbits, which show lower [α/Fe] than the stars of the thick disc sequence, naming the structure as Gaia-Enceladus. Actually, the two names indicate the same objects, since Belokurov et al. (2018) based its discovery on previous, less precise data (see Helmi 2020 for more information).

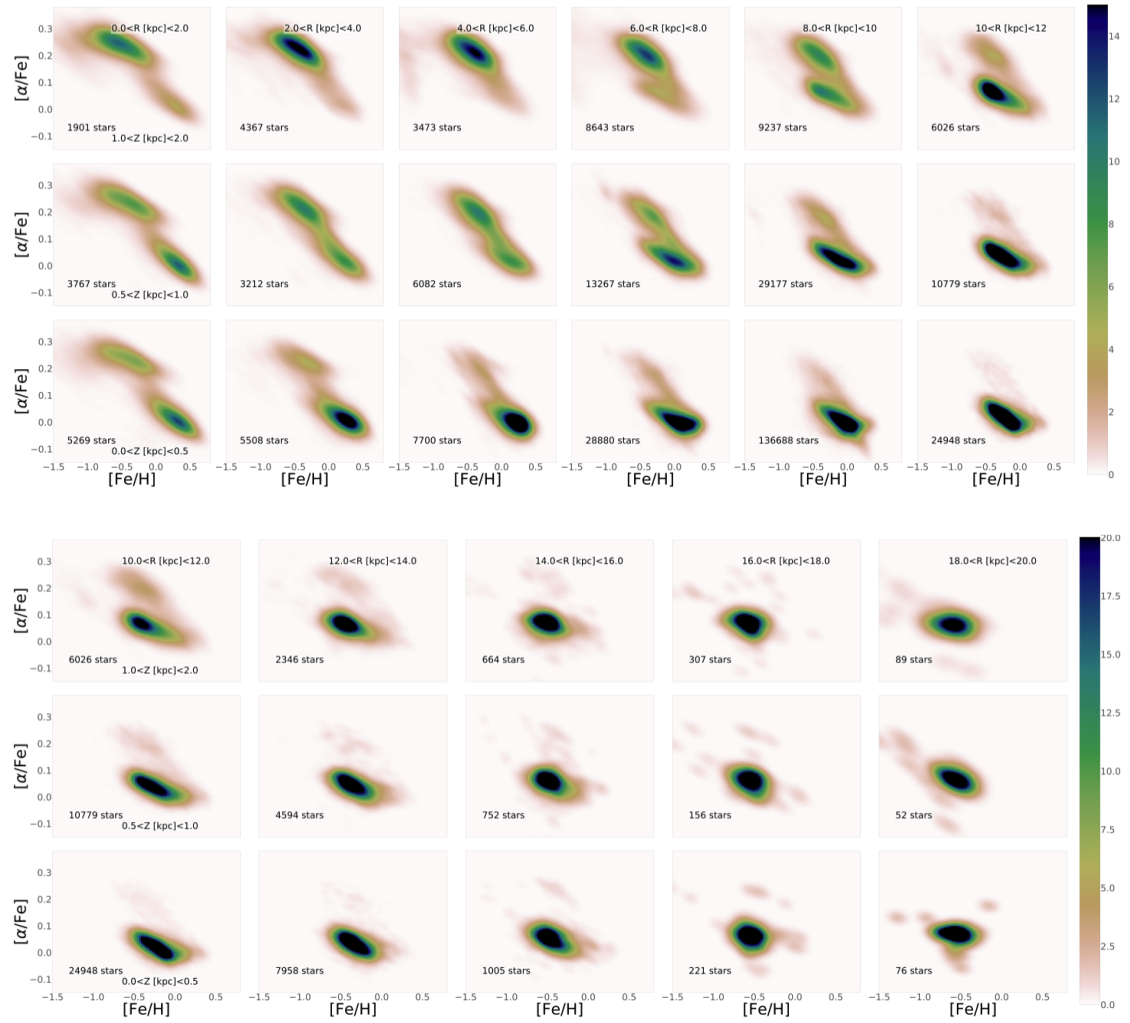

Figure 4.2: *Adapted from Queiroz et al. (2020). APOGEE DR16 [α/Fe] vs. [Fe/H] diagrams in bins of Galactocentric cylindrical coordinates (Galactocentric radius R_{gal} and height from the Galactic plane Z_{gal}). The right colorbars indicate the stellar density in the [α/Fe] vs. [Fe/H] plane.*

two separate and coeval evolutionary sequences as the origin of the observed abundances (e.g. Grisoni et al. 2017; Clarke et al. 2019), whereas other theoretical explanations invoke stellar migration from birthplace locations to explain the abundance patterns (e.g. Nidever et al. 2014; Sharma et al. 2021, but see e.g. Kubryk et al. 2015 for often ignored caveats) .

On the other side, the modelling of chemical abundance evolution is strictly connected to the stellar yields computed from stellar and SN models (see 2.1.3). As shown in Romano et al. (2010), different prescriptions for the stellar yields can give very different outcomes in the predicted chemical evolution of the Galaxy.
The uncertainties on the stellar yields still have a dominant effect especially on those elements whose nucleosynthetic origin is still not completely understood (e.g. F, V, Zn, Cu). Therefore, our view on the origin of such elements can completely change by using one prescription or another.

4.1.1 Modelling the Milky Way disc

As described in Section 1.3, chemical evolution models are powerful tools to constrain the formation and evolution of galaxies. This obviously holds also for the different MW components and in particular for the disc of the Galaxy.

Chemical evolution models of the MW have greatly evolved through the years, from the first suggesting gas infall for the system formation (Larson 1976; Chiosi 1980) to the most recent ones.
In particular, several models specifically built to describe the evolution of the MW disc have been proposed in the literature. Among these, we remind:

- **serial scenario/one-infall models** (e.g. Matteucci & Francois 1989): in this scenario, the Galaxy is modeled by means of one accretion episode lasting for the entire Galactic lifetime, where the halo, thick and thin disc form in sequence as a continuous process;
- **parallel scenario** (e.g. Ferrini et al. 1992; Grisoni et al. 2017): here, the different Galactic components start forming at the same time but evolve at different rates, with the halo and the thick disc experiencing a star formation episode on much shorter timescales relative to the thin disc;
- **sequential scenario/two-infall models** (e.g. Chiappini et al. 1997; Spitoni et al. 2019): in this scenario, the different components formed out of two separate infall episodes, with a first short episode at the beginning forming the halo-thick disc or the thick disc only and a subsequent longer one to form the thin disc. In the context of a sequential scenario, Micali et al. (2013) proposed also a three-infall model, where halo, thick and thin disc formed by means of three sequential star formation episodes.

Inside-out formation

For all the models mentioned above, it is assumed that the thin disc forms inside-out, i.e., that the disc forms by gas accretion occurring faster in the inner than in outermost regions.

This concept was first proposed by Larson (1976), who suggested this idea by means of chemo-dynamical models of the Galaxy. By adopting different timescale for gas infall at different radii, the inside-out formation allows us to obtain a good agreement between observational properties and models for the Galactic thin disc (e.g. Matteucci & Francois 1989; Boissier & Prantzos 1999; Chiappini et al. 2001; Pilkington et al. 2012).

In particular, in the model of Romano et al. (2000), the infall timescale for the thin disc gas accretion episode τ_2 was allowed to follow a simple linear relation:

$$\tau_2(\mathrm{R}) = \left(1.033\frac{\mathrm{R}}{\mathrm{kpc}} - 1.267\right)\mathrm{Gyr}, \tag{4.1}$$

where we remind that τ_2 is part of an exponentially decaying law (see Eq. (2.10)). With Eq. (4.1), it was possible to obtain an infall timescale of $\tau_2(8\text{ kpc})\sim 7$ Gyr for the solar vicinity, that allowed the authors to reproduce the G-dwarf metallicity distribution function (MDF) in the solar neighbourhood (see also 1.3.1).
Also other linear relations were proposed in the literature (e.g. Boissier & Prantzos 1999; Marcon-Uchida et al. 2010), being either flatter or steeper. However, most of them adopt a similar timescale of $\sim 6-8$ Gyr for the solar vicinity, as in Romano et al. (2000) and Chiappini et al. (2001).

For this reason, in this Thesis we basically assume Eq. (4.1) as inside-out law, but we also try to vary the slope of the relation in order to test its effect on several observables, such as present-day radial gradients and abundance ratios throughout the disc.

In this Thesis, we use the above prescriptions by applying them to the one-infall and two-infall models of chemical evolution.
One-infall models can be described by the same prescriptions listed in Chapter 2, with the addition of the inside-out law for the infall timescale at different radii (Eq. (4.1)). On the other hand, two-infall models also need different infall prescriptions for the two phases they represent.

It is also worth noting that, unlike the standard chemical evolution equation (Eq. (2.15)), for both these models we do not include galactic winds. Rather, it was found that galactic fountains more likely occur in galactic discs and several theoretical works (Melioli et al. 2009; Spitoni et al. 2009) demonstrated that fountains do not alter significantly the chemical evolution of the disc as a whole.

In the following, we go into detail of the two-infall model of chemical evolution. We remind that such a model can be framed in a scenario suggested by many dynamical (e.g. Noguchi 2018) and cosmological models (e.g. Calura & Menci 2009; Grand et al. 2018; Buck 2020), where a delayed gas infall episode forges the [α/Fe] dichotomy/bimodality in disc stars.

The two-infall model

The two-infall chemical evolution model was first proposed by Chiappini et al. (1997). In this model the Galaxy is assumed to form by means of two sequential gas infall episodes. In the first infall, the inner halo and the thick disc form on short timescales, whereas the thin disc is formed by the subsequent infall on much longer timescales.

For this reason, the infall term in the chemical evolution equation (Eq. (2.15)) can be written in this way:

$$\dot{G}_{i,inf}(\mathrm{R},t) = A(\mathrm{R})X_{i,1inf}\, e^{-t/\tau_1} + \theta(t-t_{max})B(\mathrm{R})X_{i,2inf}\, e^{(t-t_{max})/\tau_2(\mathrm{R})}, \qquad (4.2)$$

where A(R) and B(R) are two free parameters fixed by reproducing the present time total surface mass density for the halo-thick disc and thin discs at a certain radius R. $X_{i,Qinf}$ indicates the composition of the accreting gas for the Qth infall. The quantities τ_1 and $\tau_2(\mathrm{R})$ are the timescale for the formation of the halo-thick disk and the thin disk: for the latter, we make explicit the radial dependence due to the inside-out process. For what concerns t_{max}, it is the time for the maximum infall onto the Galactic disc and sets the starting time of the second infall episode: this is reminded by the argument of θ, namely the Heavyside step function.

From the first version by Chiappini et al. (1997), the two-infall scenario has been subsequently updated in the years (e.g. Romano et al. 2010; Spitoni et al. 2019) without changing drastically most of the basic prescriptions beneath the model.
The timescale of the first infall (τ_1) is set to be of the order of 1 Gyr at all radii while it varies according to the inside-out law for the second infall, imposing a τ_2 =7-8 Gyr for the solar neighbourhood (R= 8 kpc). A different efficiency of star formation (SFE) is also assumed for the two main accretion phases.. In particular, for the first infall it is usually assumed a value of $\nu_1 = 2$ Gyr^{-1}, whereas for the second infall a lower value is assumed, i.e. $\nu_2 = 1$ Gyr^{-1} (actually, in some works also the SFE of the second infall varies with Galactocentric radius, e.g. Colavitti et al. 2009; Mott et al. 2013). As it happens in most of the models of chemical evolution, both the infall episodes are assumed to be primordial.

Despite these similarities, we can divide the two-infall models in the literature in two subclasses, namely "classical" models (e.g. Chiappini et al. 1997; Romano et al. 2010; Grisoni et al. 2017) and revised models (e.g. Spitoni et al. 2019). The models differentiate basically for the delay between the first and the second infall episodes, set by t_{max}.

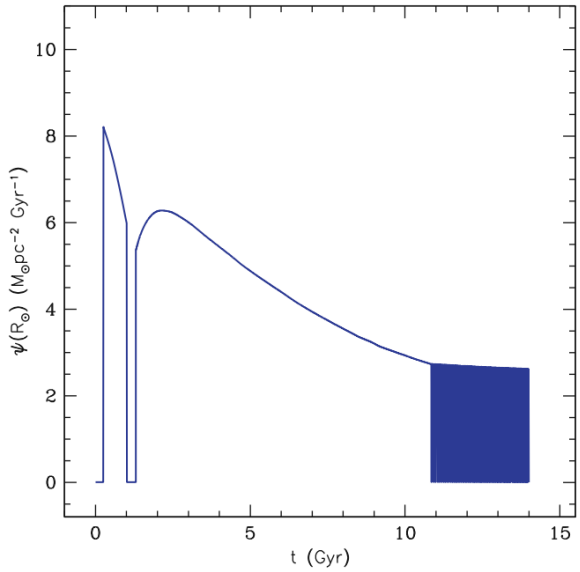

Figure 4.3: *From Matteucci (2012). SFR vs. evolutionary time of the Galaxy for the "classical" two-infall model for the solar neighbourhood.The gap in the SFR at around 1 Gyr and oscillating behavior in the SFR at late times is due to the assumed threshold density for star formation.*

"Classical" two-infall

This class of two-infall models follows the recipes adopted in Chiappini et al. (1997). Here the t_{max} parameter is typically set to 1 Gyr and in general the entire formation period of the halo-thick disc does not last more than 2 Gyr (see, e.g. Matteucci 2012).
In the original version, the authors also assumed a threshold in the gas surface mass density for star formation below which the SFE drops to zero. The existence of such a threshold has been suggested by optical studies (e.g. Kennicutt 1989); however its existence is quite uncertain since it has been challenged by UV results (GALEX, Martin 2004). In the two-infall model this threshold is set to $\Sigma_{thresh} = 4$ M$_\odot$ pc^{-2} in the inner halo-thick disc and 7 M$_\odot$ pc^{-2} in the thin disc (Chiappini et al. 1997, 2001, based on arguments by Elmegreen 1999).

In Fig. 4.3, we show the behaviour in the SFR with time typical of these models.
In this Figure, it is visible a clear gap in the star formation process at around 1 Gyr, just before the second infall/formation of the thin disc. This gap in the SFR has been suggested by some observational papers indicating a discontinuity in the [α/Fe] ratios between the thick and thin disc stars (e.g. Fuhrmann 1998; Gratton et al. 2000).

In the last years, Grisoni et al. (2017) proposed a slightly revised scenario in which the two-infall model is applied to the thick and thin disc only, but leaving most of the

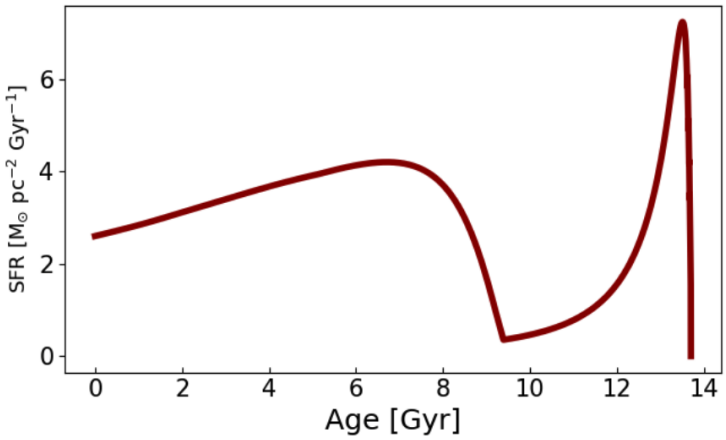

Figure 4.4: *From Spitoni et al. (2019). SFR vs. age (i.e. age of the universe - evolutionary time) of the Galaxy for the revised two-infall model for the solar neighbourhood.*

Chiappini et al. (1997, 2001) and Romano et al. (2010) set-up (e.g. t_{max}, gas threshold for SF) largely unchanged.

Revised (delayed) two-infall

Spitoni et al. (2019) applied the two-infall framework only to thick and thin disc stars as in Grisoni et al. (2017), but assumed a second infall episode much more delayed in time, setting $t_{max} \sim 4.3$ Gyr.
In Fig. 4.4, we show the behaviour in the SFR with time of the model by Spitoni et al. (2019). It is evident the prolonged hiatus in SFR is due to the large age gap between the two infall episodes. We also note that, at variance with Fig. 4.3, no gas density thresholds are assumed for the standard Kennicutt (1998) SFR law.

By means of such a set up, Spitoni et al. (2019) were able to reproduce the observed bimodality in [α/Fe] vs. [Fe/H] diagram as well as stellar ages from asteroseismology in the sample presented by Silva Aguirre et al. (2018).
This is shown in Fig. 4.5, where the revised and "classical" two-infall models are compared to the data discussed in Silva Aguirre et al. (2018). By looking at the Figure, it is clear that the "classical" two-infall prescriptions are not able to reproduce the high-α star sequence in the solar neighbourhood. Moreover, it has to be highlighted that the much larger gap in age between thick and thin disc stars relative to "classical" models has been strongly driven by the results of asteroseismic ages, highlighting the importance of this new data dimension.

It is worth mentioning that Spitoni et al. (2020) and Spitoni et al. (2021) confirmed the above scenario also quantitatively: in fact, they used a Bayesian framework based

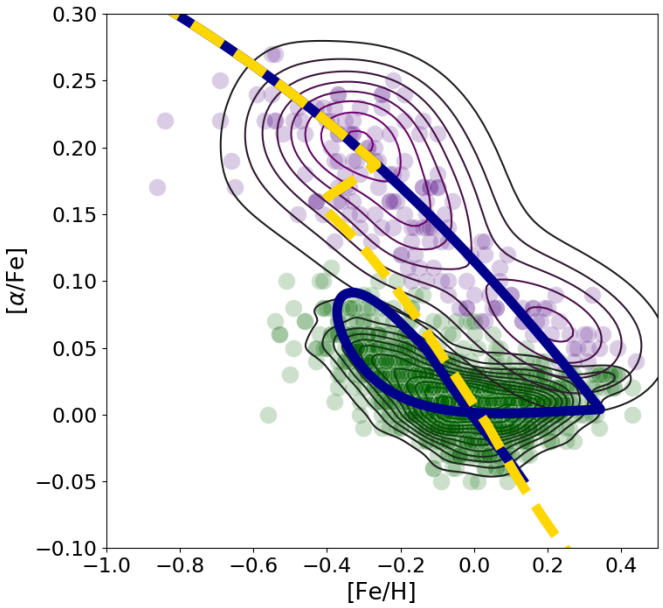

Figure 4.5: *From Spitoni et al. (2019). [α/Fe] vs. [Fe/H] for the revised two-infall model (solid blue) and the "classical" two-infall model (dashed yellow line). Purple and green filled circles represent the observed high-α and low-α stars in Silva Aguirre et al. (2018) solar neighbourhood sample.*

on Markov chain Monte Carlo (MCMC) methods to fit the two-infall chemical evolution models to the data of Silva Aguirre et al. (2018) and Leung & Bovy (2019), respectively. A scenario with a late time second accretion phase in a two-infall context was also derived by the dynamical models of Noguchi (2018), as well as in cosmological simulations (e.g. Grand et al. 2018 with AURIGA) to reproduce the [α/Fe] bimodality.

4.2 Constraints on the Milky Way disc formation from two-infall models

4.2.1 Introduction

As described at the beginning of this Chapter, we are living in a golden era for Galactic archaeology. In particular, a large number of spectroscopic surveys have been carried out in the last years, such as for example Gaia-ESO (Gilmore et al. 2012), APOGEE (Majewski et al. 2017), GALAH (De Silva et al. 2015), LAMOST (Zhao et al. 2012), RAVE (Steinmetz et al. 2020), while some other will be delivered in the next few years, such as 4MOST (de Jong et al. 2019) and WEAVE (Dalton et al. 2020). Furthermore, *Gaia* data releases (DR1, DR2 and EDR3, Gaia Collaboration et al. 2016b, 2018, 2021) are even enhancing the values of these surveys, providing dynamical properties with unprecedented accuracy.
The legacy of such data is reflected in our view of the [α/Fe] vs. [Fe/H] abundance diagram, in which a clear distinction between two sequences of disc stars, i.e. the so-called high-α (associated to the thick disc) and low-α (associated to the thin disc) sequences, was found (see, e.g. Fig. 4.2).

However, investigations of the MW evolution also benefit from different kinds of data. The last decade has seen a large increase in the number of data coming from nebular spectra (HII regions, e.g. Balser et al. 2015, planetary nebulae, e.g. Stanghellini & Haywood 2018, molecular clouds, e.g. Colzi et al. 2018) and particular classes of stars (Cepheids, e.g. Genovali et al. 2015, RR Lyrae, e.g. Crestani et al. 2021).
These data are fundamental, because they usually probe one of the most important constraints to study the formation and chemical evolution of the Galaxy: the radial abundance gradients along the Galactic thin disc.

Radial gradients

The distribution of the elements throughout the disc of spiral galaxies generally follows a radial gradient with metallicity decreasing outward from the Galactic Centre (Belfiore et al. 2019). The existence of radial abundance gradients in the MW and in the nearest disc galaxies has been known for years (e.g. D'Odorico et al. 1976; Diaz 1989; Zaritsky et al. 1994; Garnett et al. 1997) and the advent of Integral Field Unit (IFU) surveys of large samples of galaxies (e.g. CALIFA: Sánchez et al. 2012, MaNGA: Bundy et al. 2015; SAMI: Bryant et al. 2015) make possible to detect these gradients for thousands of galaxies.

For what concerns the MW Galaxy, a good agreement between observational properties and models is generally obtained by assuming that the Galaxy forms by infall of gas (e.g. Chiosi 1980; Matteucci & Francois 1989; Chiappini et al. 1997; Kobayashi et al. 2006; Spitoni & Matteucci 2011; Snaith et al. 2015; Prantzos et al. 2018). In addition, a common assumption for reproducing abundance gradients is that the formation timescale of the thin

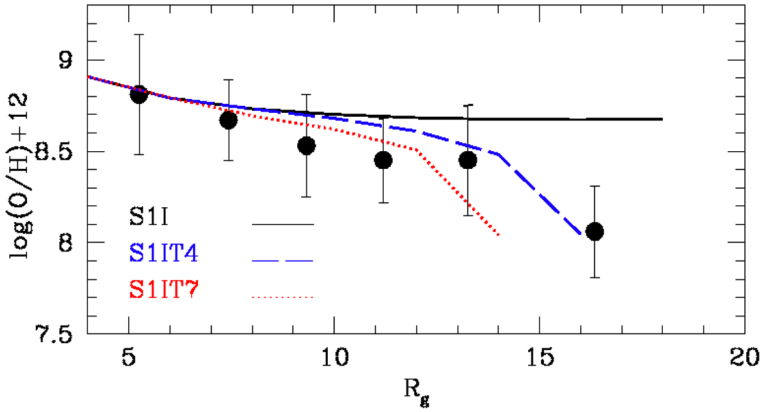

Figure 4.6: *From Spitoni & Matteucci (2011). Radial abundance gradient for oxygen. The black line refers to a model adopting only the inside-out law by Chiappini et al. 2001, while the other lines indicate models with gas density threshold for SF of 4 $M_{\odot}$ pc^{-2} (blue) and 7 $M_{\odot}$ pc^{-2} (red). The filled circles with error bars are the observed values from HII regions and planetary Nebulae.*

disc is a function of the Galactocentric radius (e.g. Matteucci & Francois 1989; Chiappini et al. 2001; Schönrich & McMillan 2017), i.e. the inside-out scenario (see 4.1.1).

Despite of its importance, the inside-out mechanism alone seems not enough to explain the gradients observed in the Galactic disc (e.g. Spitoni & Matteucci 2011; Mott et al. 2013; Grisoni et al. 2018). This can be seen in Fig. 4.6, where we show a plot from Spitoni & Matteucci (2011). It is clear from the Figure that the model adopting only an inside-out law (black line) is not able to achieve the slope needed to reproduce the observed radial gradient (see however Chiappini et al. 2001 for a discussion of the effects of thick disc evolution in shaping thin disc gradients in two-infall models).
To overcome this problem, Colavitti et al. (2009) suggested to add a threshold in the gas density for the SF or a variable SFE, i.e. higher in the inner regions than in the outer ones (see also Boissier & Prantzos 2000 for a radial dependence of the SFR related to the presence of density waves in the disc). Moreover, radial gas flows from outer to inner Galactic regions have been suggested to fit the disc constraints at the present time (e.g. Lacey & Fall 1985; Portinari & Chiosi 2000; Spitoni & Matteucci 2011; Bilitewski & Schönrich 2012; Cavichia et al. 2014). This explanation has a physical link with the MW formation via gas infall: the infalling gas may have a lower angular momentum than that of the gaseous disc, and the mixing between these two components may induce a net radial inflow to preserve angular momentum (Spitoni & Matteucci 2011). Other physical phenomena can also induce radial gas flows (e.g., gas viscosity, Lacey & Fall 1985, or gravitational interactions between gas and spiral density waves, Bertin & Lin 1996). Anyway, these phenomena have generally small flow speeds and their effects on the gradients

are assumed to be negligible (Portinari & Chiosi 2000).

[α/Fe] along the disc

A chemical distinction between a thick disc and a thin disc was already suggested by spectroscopic observations of small samples of stars well before the advent of the survey era (e.g. Fuhrmann 1998; Bensby et al. 2003). Evidences of a clear chemical distinction between a thick disc and a thin disc are now pointed out by multiple spectroscopic surveys (e.g. Hayden et al. 2014; Recio-Blanco et al. 2014; Mikolaitis et al. 2017; Rojas-Arriagada et al. 2017, see however caveats about pure chemical classification put forward by e.g. Bensby & Lind 2018; Franchini et al. 2020; Romano et al. 2021).

However, many surveys show some important limits in the analysis of our Galactic disc. On one hand, some campaigns have moderate to low spectral resolutions that do not allow us to catch precise abundances of individual elements. Another fundamental problem is the capability to target Galactic stars at very large distances, i.e., up to the outermost disc regions. The problem is even enhanced when we look at the most inner parts of the Galactic disc, since the optical extinction in the Galactic plane (especially towards the inner regions, see Section 1.2) can hamper the analysis of the targeted stars. Fig. 4.7 describe the above issues showing in the top panel surveys spectral resolution and in the bottom panel the survey depth including the effects of interstellar extinction for present and upcoming stellar surveys.

In spite of the fact that other campaigns will analyse the spectra of many more stars, APOGEE retain the best combination between spectral resolution ($R = 22500$) and distance range explored ($\gtrsim$ 10 kpc even at deep extinction values). In fact, APOGEE spectra are probing NIR wavelengths (1.51-1.70 μm), which are much less sensitive to extinction relative to optical ones. For this reasons, APOGEE results ideal to study in detail the behaviour of different abundance ratios throughout the disc of the Galaxy.
The analysis of APOGEE data actually confirms the division of the disc in high-α and low-α sequences at various radii. However, it is observed that the ratio between these populations changes with radius, with high-α/low-α ratio progressively decreasing to outer radii (Anders et al. 2014; Nidever et al. 2014). At the same time, the scale heights h_z of the two populations behave differently, with the low-α one showing a flaring towards outer regions, i.e. a h_z increasing with radius (Bovy et al. 2016). These findings point towards a thick disc concentrated in the inner Galactic regions, with very short scale length (e.g. Bovy et al. 2016; Haywood et al. 2016) and not forming in an inside-out manner (Haywood et al. 2018).

Haywood et al. (2016, 2018) and Miglio et al. (2021) also determined a quenching period after the thick disc formation, however, with uncertain origin. Some works (e.g. Khoperskov et al. 2018) suggest the formation of the Galactic bar as the responsible of

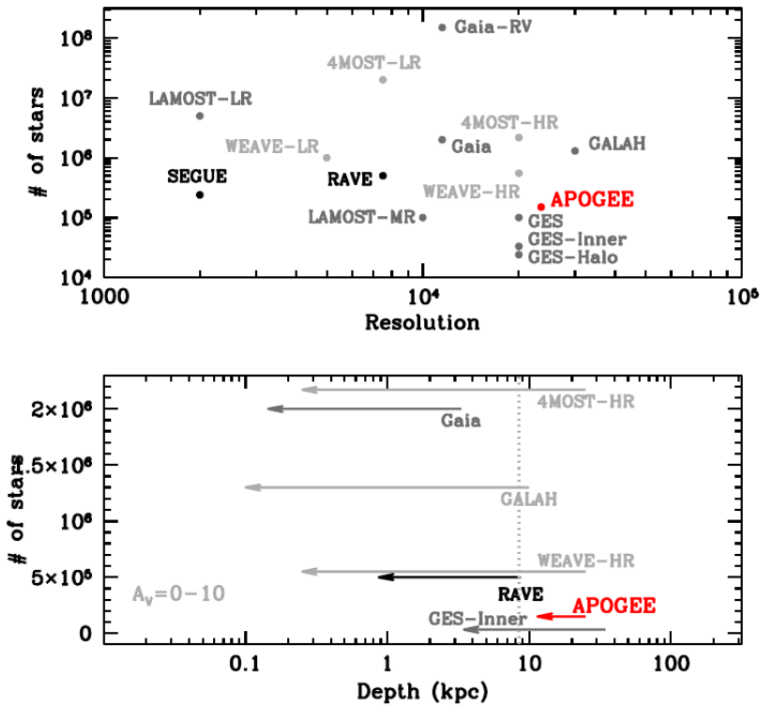

Figure 4.7: *From Anders (2017). Number of MW stars observed as function of survey spectral resolution (top panel) and of survey depth (bottom panel). The expected depth are computed for stars with* $M_V = -1$ *(e.g. giants of K4 spectral type), including the effect of interstellar extinction (arrows). In addition to APOGEE, in both panels are shown completed, ongoing and planned surveys.*

this quenching. However, the most frequent explanation of this gap in the SF at high redshift was the Gaia-Enceladus-Sausage (GES, Belokurov et al. 2018; Koppelman et al. 2018; Helmi et al. 2018) merger, where this major merger event (approximately 10 Gyr ago) heated up the gas in the dark matter halo (Chaplin et al. 2020), preventing the SF in the disc (Vincenzo et al. 2019).

All these observational hints have suggested some revision to the classical MW chemical evolution scenarios, i.e., the two-infall model of Chiappini et al. (1997, 2001).
In agreement with several theoretical models of Galactic disc evolution (e.g. Noguchi 2018; Grand et al. 2018) and analysis of *Gaia* DR2 colour-magnitude diagrams (e.g. Mor et al. 2019), Spitoni et al. (2019, 2020) suggested a revised two-infall model with a delayed formation of the thin disc (see 4.1.1). In this way, Spitoni et al. (2019, 2020) were able to fit nicely not only the bimodal distribution in the [α/Fe]-[Fe/H] plane, but also asteroseismic stellar ages of the APOKASC (APOGEE + *Kepler* Asteroseismology Science Consortium) sample (Silva Aguirre et al. 2018). On the other side, Grisoni et al. (2017)

proposed a picture where thick and thin discs are described by two separate and coeval evolutionary sequences, i.e. the parallel scenario. In particular, this model allows the author to obtain a better agreement with AMBRE data than "classical" two-infall models.

However, most of these works focus only on the solar vicinity, not accounting for the effects of their different prescriptions outside the "solar circle". An exception is represented by Grisoni et al. (2018), where radial abundance gradients and [α/Fe] vs.[Fe/H] relations over different Galactocentric radii were treated, but mostly in the framework of one-infall models.

In this Section we want to provide a global picture of the MW disc evolution in the framework of two-infall models of chemical evolution, taking into account both the constraints from recent abundance ratio relations throughout the disc of the Galaxy as well as abundance gradients in the Galactic plane.

To this aim, we start from "classical" MW two-infall models to reproduce present-day abundance, gas density and SFR gradients, testing also a detailed treatment of radial gas flows (see Spitoni & Matteucci 2011 and references therein). The models that better reproduce the gradients are then compared to APOGEE stellar abundances at various Galactocentric distances, allowing changes in the model prescriptions to better explain the observational trends. In the light of recent results about the impact of GES merger (e.g. Vincenzo et al. 2019; Buck 2020), we also explore the possibility of a sigificant contribution by GES gas to the MW gas accretion history. To this aim, we run a detailed chemical evolution model that reproduces the abundances observed in the stellar relics of the merged galaxy following the work of Vincenzo et al. (2019).

This Section is therefore organized as follows: in 4.2.2 we describe the observational data considered in this analysis. 4.2.3 is reserved to the description of the two-infall model setup and the chemical evolution model reproducing the GES progenitor (i.e., Enceladus dwarf galaxy). In 4.2.4, we present the comparison between model predictions and observations, discussing the implications of the obtained results. In particular, in the first part we aim at assessing the main mechanisms responsible for radial abundance gradients, while in the second we look at the comparison between observed and predicted [α/Fe] vs. [Fe/H] relations at different Galactocentric radii. Finally, in 4.2.5 we draw our main conclusions.

4.2.2 Observational data

In the following, we describe the adopted observational data for this work by dividing between present-day radial gradients and [α/Fe] vs. [Fe/H] abundance patterns at different Galactocentric distances, i.e. the two types of constraints that we adopt in this Section.

Radial gradients

To constrain the abundance gradients at the present time, we take advantage of the most used tracers in the literature, i.e. HII regions, Cepheids, open clusters (OCs) and planetary nebulae (PNe) originating from young stars.

The HII regions data are taken from Esteban et al. (2005); Rudolph et al. (2006) and Balser et al. (2015). We are aware that potential biases between these abundance measurements can be present. In fact, to infer the abundances, different techniques are adopted: i) recombination excited lines (RELs, Esteban et al. 2005), ii) collisionally excited lines (CELs, Rudolph et al. 2006), iii) radio recombination lines (RRLs, Balser et al. 2015). However, the abundances are all inferred with the direct method, without the adoption of any strong-line metallicity calibration (e.g. R_{23}, N_2, O_3N_2; see 3.2.2 for more information that might have major impacts on the final values (Kewley & Ellison 2008; Bresolin et al. 2016).

PNe data are taken from Costa et al. (2004) and Stanghellini & Haywood (2018). Since our focus is on the analysis of present time gradients, we consider only PNe whose progenitors are younger than 1 Gyr (YYPNe) from Stanghellini & Haywood (2018). At the same time, we take only objects classified as Type I (PNe with young progenitors) from Costa et al. (2004).

Regarding stellar data, the Cepheids abundances are taken from Luck & Lambert (2011) and Genovali et al. (2015), while the adopted open cluster data are from Magrini et al. (2017). From the Magrini et al. (2017) sample, we select the clusters with an age younger than 2 Gyr to consider only young-intermediate age OCs (YOCs[4]).

To give an estimate of the typical errors on the abundances, in the case of Cepheids they are of the order of ~ 0.1 dex. Of the same order are typical abundance errors for PNe. For HII regions, instead, typical errors are larger (~ 0.2 dex).

Concerning the errors on Galactocentric radius estimates, we note that the distance scale of PNe is much more uncertain than those of the other sources (Grisoni et al. 2018). For Cepheids, YOC, and HII regions the errors in radius are generally of the order of $\lesssim 1$ kpc.

In this Section, we also investigate SFR and gas mass density gradients along the disc. For the SFR we take estimates at different radial distances from Rana (1991) and Stahler & Palla (2005). In particular, the latter set is formed by weighted mean values (on individual data errors) of SFR from SN remnants, pulsars and HII regions. We also take advantage of the SFR-radius relation of Green (2014), a modified version of Lorimer et al. (2006) analytical fit to the pulsar distribution:

$$SFR(\mathrm{R})/SFR_{\odot} = \left(\frac{\mathrm{R}}{\mathrm{R}_0}\right)^b e^{-c\left(\frac{\mathrm{R}-\mathrm{R}_0}{\mathrm{R}_0}\right)}, \tag{4.3}$$

[4]actually, the acronym refers to young OCs only (age$\lesssim$0.2 Gyr, e.g. Baratella et al. 2021), but here we extend it also to intermediate age clusters.

where $\mathrm{R}_0 = 8$ kpc and parameters $b = 2$ and $c = 5.1$ (in Lorimer et al. 2006 $b = 1.9$ and $c = 5$). Eq. (4.3) fit is in very good agreement with SN remnants compilation by Green (2014), as well as for Urquhart et al. (2014) data on luminous massive stars (although with larger scatter).
Concerning the gas mass density, we compare our models with total surface gas density estimates from Dame (1993) and Nakanishi & Sofue (2003, 2006). It is worth mentioning that for these data we adopt the correction $\Sigma_{gas} = 1.4(\mathrm{HI+H_2})$, where the factor 1.4 accounts for the presence of He.

[α/Fe] along the disc

To investigate how the abundance pattern of [α/Fe] vs. [Fe/H] changes throughout the Galactic disc, we rely on APOGEE DR12 data by Hayden et al. (2015). In particular, Hayden et al. (2015) selected cool (3500 K$< T_{eff} <$5000 K) giant stars (1.0$< \log g <$3.8) with signal-to-noise ratio (S/N) >80 (see Hayden et al. 2015 for more details). All the stars are within 2 kpc of the midplane of the MW and have Galactocentric radii larger than 3 kpc.
Among the α-elements, here we focus on [Mg/Fe] measurements, the most reliable from an observational point of view (see Grisoni et al. 2017, 2018 and references therein).

Uncertainties on [X/H] abundance ratios are of $\sim$ 0.05 dex for both Fe and Mg (Holtzman et al. 2015). On average, distances (and hence radius estimatates) are accurate by 15%-20% level (for a more detailed discussion on the distances see Holtzman et al. 2015).

We also take advantage of stellar abundances combined with asteroseismic ages from the sample of Silva Aguirre et al. (2018). The data are from an updated APOKASC catalogue (Pinsonneault et al. 2014), composed by 1197 stars selected from the total APOKASC sample (see Spitoni et al. 2019 for a more complete discussion on the observations and selection criteria).
In the sample adopted here we have not taken into account the so called "young α rich" (YαR) stars, whose origin is still debated and attributed either to stars migrated from the Galactic bar (e.g. Chiappini et al. 2015) or more probably evolved blue stragglers (e.g. Martig et al. 2015; Jofré et al. 2016; Zhang et al. 2021).

Regarding the errors in stellar ages of Silva Aguirre et al. (2018) sample, these are dependent on the age value. In particular, the median uncertainty in the sample is 28.5% of the stellar age. On the other hand, the errors on the stellar metallicity are independent from stellar ages and they are about 0.1 dex.

4.2.3 Chemical evolution models set up

In the following, we briefly summarise the models adopted to infer the SFH of our Galactic disc.

The framework of the MW chemical evolution models adopted in this paper is based on the two-infall model (e.g. Chiappini et al. 1997; Romano et al. 2010). Even if the basic theory beneath this modelling is explained in 4.1.1, in the first part of 4.2.3 we better specify the adopted prescriptions, including the implementation of radial gas flows in the models.

Moreover, in order to test the possible effect of GES merger on gas accretion in the disc, we build a model for the galaxy relic based on Vincenzo et al. (2019). We reserve the second part of 4.2.3 to list and describe the main parameterizations of this model.

Two-infall model

The two-infall model assumes that the MW forms as a result of two main infall episodes. Here we base on the Grisoni et al. (2017); Spitoni et al. (2019) scenario, where the first episode forms the thick disc only, whereas the second (delayed and slower) infall gives rise to the thin disc (see 4.1.1).
In our model, we approximate the Galactic disc by rings 2 kpc wide.

The basic equations that follow the time evolution of G_i, namely the mass fraction of the element i in the ISM, in each ring are described by the usual chemical evolution equation (Eq. (2.15) without galactic winds, see 4.1.1).

According to the two-infall scenario, we adopt different SFE for the first and the second infall episodes. In particular, the SFE of the first infall (ν_1) is fixed to 2 Gyr^{-1}, whereas we allow variations for ν_2 at different Galactocentric radii. However, we always assume a second infall SFE of 1 Gyr^{-1} for the solar radius (R$=8$ kpc) according to previous studies (e.g. Grisoni et al. 2017).
The adopted IMF is the one by Kroupa et al. (1993), which was found to be preferred to explain MW observables (see 2.1.2).

For what concerns the gas infall term $\dot{G}_{i,inf}$ (Eq. (4.2)), we assume that the timescale for mass accretion in the Galactic thin disc $\tau_2(\mathrm{R})$ increases linearly with radius according to the inside-out scenario as in Eq. (4.1) (e.g. Chiappini et al. 2001; Cescutti et al. 2007). However, we perform also calculations with other inside-out laws, either flatter or steeper:

$$\tau_2(\mathrm{R}) = \left([0.75, 1.25]\frac{\mathrm{R}}{\mathrm{kpc}} + [0.997, -3.003]\right)\mathrm{Gyr}, \tag{4.4}$$

where in brackets are indicated the ranges of parameters explored. We remind that $\tau_2(8$ kpc$) \simeq 7$ Gyr is fixed by reproducing the G-dwarf metallicity distribution in the solar vicinity (Matteucci 2012). For what concerns the timescale of the thick disc τ_1, this is instead fixed at all radii to 1 Gyr (see also Haywood et al. 2018).
Regarding, t_{max}, i.e. the time for the maximum mass accretion onto the Galactic disc, in this work we let this parameter vary between "classical" prescriptions (i.e. 1 Gyr, Chiappini et al. 1997) and revised ones (i.e. > 3 Gyr, Spitoni et al. 2019) in order to reproduce

Table 4.2: *Fixed parameters for two-infall chemical evolution models. In the first column we list the variables that remain constant. In the last column, we show the adopted parameterization.*

Variable	Fixed parametrization
ν_1	2 Gyr^{-1}
$\nu_2(\mathrm{R}=8)$	1 Gyr^{-1}
τ_1	1 Gyr
$\Sigma_{thin}(\mathrm{R})$	$531e^{-\mathrm{R}/3.5}$ M$_\odot$ pc^{-2}
$\Sigma_{thick}(\mathrm{R}=8)$	12.3 M$_\odot$ pc^{-2}

Note*:* R *is expressed in kpc.*

the observational data.
In this Section, we assume that the present-day total surface mass density in the Galactic thin disc follows an exponential profile:

$$\Sigma(\mathrm{R}) = \Sigma_0\, e^{-\mathrm{R}/\mathrm{R_d}}, \tag{4.5}$$

where $\Sigma_0 = 531$ M$_\odot$ pc^{-2} is the central surface mass density and $\mathrm{R_d} = 3.5$ kpc is the disc scale length (see, e.g. Spitoni et al. 2017). For the thick disc instead, we explore different kind of surface profiles (inverse linear, exponentially decaying), fixing only the density in the solar neighborhood (R =8 kpc) at ~ 12 M$_\odot$ pc^{-2}. These parametrizations for the discs allow us to obtain: (i) a $\Sigma_{thin}(8$ kpc$) \sim 54$ M$_\odot$ pc^{-2}, which is in agreement with the values for thin disc given by e.g., Bovy & Rix (2013); Read (2014), and (ii) a ratio $\Sigma_{thin}(8$ kpc$)/\Sigma_{thick}(8$ kpc$)\sim 4$, in agreement with recent chemical evolution works on the solar neighbourhood (Spitoni et al. 2020).
Finally, also different composition $X_{i,Qinf}$ of the gas infall are tested. In particular, we try both primordial and pre-enriched chemical compositions for the two different infall episodes.

As a summary, the physical parameters which have been left constant in all models are listed in Tab. 4.2. For the other variable prescriptions, we refer to Tabs. 4.4 and 4.6.

Implementation of radial inflows

As previously mentioned, in our formulation the MW disc is divided in rings 2 kpc wide. These rings are usually assumed to be independent, without exchange of matter between them (e.g. Chiappini et al. 1997). However, in this work we also allow them to exchange gas due to radial flows (e.g. Spitoni & Matteucci 2011).

If radial flows are adopted, the chemical evolution equation (Eq. (2.15)) then becomes:

$$\dot{G}_i(\mathrm{R},t) = -\psi(\mathrm{R},t)X_i(\mathrm{R},t) + R_i(\mathrm{R},t) + \dot{G}_{i,inf}(\mathrm{R},t) + \dot{G}_{i,rf}(\mathrm{R},t), \tag{4.6}$$

where here we explicit the radial dependence of each term. The last term of this Equation refers to radial inflows of gas. In this work, we implement these flows using the prescriptions of Portinari & Chiosi (2000); Spitoni & Matteucci (2011).

In particular, we define the k_{th} shell in terms of the Galactocentric radius R_k, its inner and outer edges being labelled as $\mathrm{R}_{k-1/2}$ and $\mathrm{R}_{k+1/2}$. Through these edges, gas inflow occurs with velocities $\upsilon_{k-1/2}$ and $\upsilon_{k+1/2}$, respectively; the flow velocities are assumed to be positive outwards and negative inwards.
Radial inflows with a flux $F(\mathrm{R})$, alter the gas surface density in the k_{th} shell according to

$$\dot{\Sigma}_{gas,rf}(\mathrm{R}_k,t) = -\frac{1}{\pi(\mathrm{R}^2_{k+1/2}-\mathrm{R}^2_{k-1/2})}[F(\mathrm{R}_{k+1/2})-F(\mathrm{R}_{k-1/2})], \tag{4.7}$$

where

$$F(\mathrm{R}_{k+1/2}) = 2\pi \mathrm{R}_{k+1/2}\upsilon_{k+1/2}\Sigma_{gas}(\mathrm{R}_{k+1},t),$$
$$F(\mathrm{R}_{k-1/2}) = 2\pi \mathrm{R}_{k-1/2}\upsilon_{k-1/2}\Sigma_{gas}(\mathrm{R}_{k},t).$$

Since the edges $\mathrm{R}_{k-1/2}$ and $\mathrm{R}_{k+1/2}$ are taken respectively at the mid-point between the shells k, $k-1$ and k, $k+1$, we have that:

$$(\mathrm{R}^2_{k+1/2}-\mathrm{R}^2_{k-1/2}) = \frac{\mathrm{R}_{k+1}-\mathrm{R}_{k-1}}{2}\left(\mathrm{R}_k+\frac{\mathrm{R}_{k-1}+\mathrm{R}_{k+1}}{2}\right).$$

Inserting the latter expressions into Equation (4.7) we finally obtain:

$$\dot{G}_{i,rf}(\mathrm{R}_k,t) = -\beta_k G_i(\mathrm{R}_k,t)+\gamma_k G_i(\mathrm{R}_{k+1},t), \tag{4.8}$$

where

$$\beta_k = -\frac{2}{\mathrm{R}_k+\frac{\mathrm{R}_{k-1}+\mathrm{R}_{k+1}}{2}}\left[\upsilon_{k-1/2}\frac{\mathrm{R}_{k-1}+\mathrm{R}_k}{\mathrm{R}_{k+1}-\mathrm{R}_{k-1}}\right],$$
$$\gamma_k = -\frac{2}{\mathrm{R}_k+\frac{\mathrm{R}_{k-1}+\mathrm{R}_{k+1}}{2}}\left[\upsilon_{k+1/2}\frac{\mathrm{R}_k+\mathrm{R}_{k+1}}{\mathrm{R}_{k+1}-\mathrm{R}_{k-1}}\right]\frac{\Sigma_{k+1}}{\Sigma_k}.$$

Here, Σ_k and Σ_{k+1} are the present total surface mass density at the radius R_k and R_{k+1}, respectively. In our formulation, we assume that there are no flows from the outer parts of the disc where there is no star formation: flows start at radius 18 kpc and move inward.

In our models, we test different speed patterns. In particular, we see either the effects of radial flows with fixed velocity υ_{flow} (-1 km s^{-1}, e.g. Spitoni & Matteucci 2011), radius dependent velocity ($\upsilon_{flow} = -\left(\frac{R}{4}-1\right)$, e.g. Grisoni et al. 2018) or both radius and time dependent speed.
The latter formulation represents a novelty relative to previous Portinari & Chiosi (2000); Spitoni & Matteucci (2011) radial gas flows implementations. We adopt a velocity that in the thin disc phase follows the exponential behaviour of the second infall ($e^{-\frac{t-t_{max}}{\tau_2}}$). A flow speed that follows the infall is a simple but reasonable assumption: the ratio infall rate/gas density, which drives the variations in the flow speed (Eq. (28) of Pezzulli &

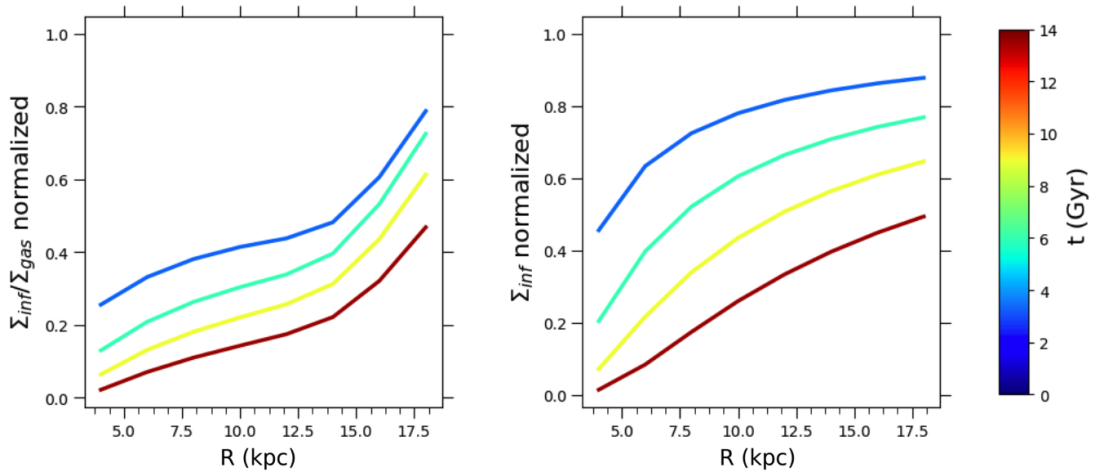

Figure 4.8: *Time evolution of the infall rate (right panel) and the ratio infall rate/gas density (left panel) as a function of radius for a typical two-infall model. Values in the two panel are normalized to the maximum. The right hand colorbar indicates the evolutionary time of the Galaxy.*

Fraternali 2016, see also Lacey & Fall 1985) decreases with time and radius, resembling infall rate behaviour in an inside-out scheme. This is shown in Fig. 4.8, where we present the variation with time of the infall rate (right panel) and the ratio infall rate/gas density (left panel) for a two-infall model: such a decrease of the flow velocity with time and radius is also supported by Bilitewski & Schönrich (2012), using a different flow implementation. Concerning the velocity range of all the radial flow prescriptions, they span the interval $0 - \sim 4$ km s^{-1}. This is in agreement with previous chemical evolution studies (e.g. Bilitewski & Schönrich 2012; Mott et al. 2013; Grisoni et al. 2018; Vincenzo & Kobayashi 2020) as well as observations of external galaxies (e.g. Wong et al. 2004).

Enceladus model

As mentioned in the Introduction of this Section, in this work we build a model for Enceladus dwarf galaxy itself.
We do this by assuming the same parameters as in Vincenzo et al. (2019): in such a work, a model characterised by a small star formation efficiency, fast infall time-scale and a mild outflow could nicely reproduce the observed [α/Fe] ratios as well as the metallicity distribution function (MDF) measured in Enceladus. They also predicted a stellar mass for the galaxy of $\sim 5 \times 10^9$ M$_\odot$ and suggested that the merging event could have been the cause for halting the star formation in the MW 10 Gyr ago, a fact already predicted by other models (e.g. Noguchi 2018).

The input parameters for Enceladus chemical evolution model are listed in Tab. 4.3. At variance with the two-infall model, here we allow the presence of galactic winds in the

Table 4.3: *Input parameters for the Enceladus chemical evolution model. In the first column we list the input variables of the model. In the second column, we show the adopted values.*

Input parameter	Adopted value
$M_{inf,Enc}$	10^{10} M$_\odot$
$\tau_{inf,Enc}$	0.24 Gyr
ν_{Enc}	0.42 Gyr^{-1}
ω_{Enc}	0.5

Eq. (2.12) formulation for which we remember ω, i.e. the wind mass loading factor. The adopted IMF is the one derived by Kroupa et al. (1993), in order to be consistent with the MW models of this Section. It is worth reminding that such an IMF was also adopted in Vincenzo et al. (2019) and allows to reproduce abundance and stellar mass constraints.

In this way, we simulate the formation of the MW discs by gas accretion episodes with the same chemical composition as predicted by our model and in agreement with the measured abundances in GES merger relics.

Nucleosynthesis prescriptions

For both the MW two-infall and Enceladus chemical evolution models, the contribution to chemical enrichment by LIMS, Type Ia and CC-SNe (Type II, Ib/c), is computed by taking advantage of detailed stellar yields for these stars (see 2.1.3).

In particular, the following mass and metallicity dependent stellar yields are adopted:

- for LIMS we use yields by Karakas (2010);
- for massive stars that explode as CC-SNe, we adopt yields by Kobayashi et al. (2006)/Nomoto et al. (2013);
- for Type Ia SNe we use the yields by Iwamoto et al. (1999).

4.2.4 Results

As mentioned in 4.2.3, we run several models based on the two-infall paradigm applied to the thick and thin discs only (e.g. Grisoni et al. 2017; Spitoni et al. 2019). Among the various model parameters, we keep fixed the IMF, the efficiency of star formation in the thick disc, the timescales for the formation of the thick and thin discs, the present time distribution of the surface mass density along the thin disc and the present time surface density for the thick disc in the solar neighbourhood (see Tab. 4.2).
These models are applied to the study of present-day radial gradients and [α/Fe] vs. [Fe/H]

Table 4.4: *Parameters for "classical" two-infall chemical evolution models adopted in this work. Fixed parameters (t_{max}, $\Sigma_{thick}(\mathrm{R})$, second infall gas abundances as in Chiappini et al. 2001; Colavitti et al. 2009; Romano et al. 2010) are shown in the upper Table. The parameters varied are indicated in the lower Table. For these latter, in the first column we write the name of the model. In the second column, we list the star formation efficiency of the thin disc ν_2 at different radii (4-6-8-10-12-14-16-18 kpc) from the Galactic center. In the last column, we indicate the radial flow speed pattern (where present).*

$\Sigma_{thick}(\mathrm{R})$ ($\mathrm{M}_\odot$ pc^{-2})	t_{max} (Gyr)	2^{nd} infall gas (dex)
$\propto \frac{1}{\mathrm{R}}$	1	primordial

Model	ν_2 (4-6-8-10-12-15-16-18 kpc) (Gyr^{-1})	Radial flows (km s^{-1})
MW A	1	-
MW B	$\nu(\mathrm{R})$ =5, 2, 1, 0.75, 0.5, 0.25, 0.15, 0.1	-
MW C	1	-1
MW D	1	$-\upsilon(\mathrm{R}) = -\left(\frac{\mathrm{R}}{4} - 1\right)$ if $t > t_{max}$ -1 ($t < t_{max}$)
MW E	1	$-\Theta(\mathrm{R}, t) = -\left[1 + \upsilon(\mathrm{R}) \cdot e^{-\frac{t - t_{max}}{\tau_2}}\right]$ ($t > t_{max}$) -1 ($t < t_{max}$)
MW F	$\nu(\mathrm{R})$	-1
MW G	$\nu(\mathrm{R})$	$-\upsilon(\mathrm{R})$ ($t > t_{max}$) -1 ($t < t_{max}$)

Notes*: R is expressed in kpc, t is expressed in Gyr. The minus sign in the last column means that the flow is an inflow.*

along the MW disc, allowing to vary the other parameters presented in the previous Subsection.

Present-day gradients

We first focus on the analysis of present-time abundance gradients along the thin disc.

We look in particular at the different results given by the models with "classical" two-infall prescriptions, i.e., t_{max}, $\Sigma_{thick}(\mathrm{R})$, second infall gas abundances, as in Chiappini et al. (2001); Colavitti et al. (2009); Romano et al. (2010). For these models, we vary the SFE at dfferent radii during the second infall (ν_2) and we test different radial gas flows speed patterns. To identify the different recipes, we name models from MW A to G. Both the fixed and the variable parameters for this set of models are presented in Tab. 4.4: in the

upper Table the fixed prescriptions are shown, whereas in the lower Table we list model names and the choice for the variable parameters.

For the analysis of present-day abundances we choose to show the abundances of oxygen, nitrogen, magnesium and iron. In this way, we analyse elements produced on different timescales and with different origin (primary or secondary origin).

The resulting abundance gradients from the models presented in Tab. 4.4 are presented in Fig. 4.9. On the left side, we show models that adopt different SFEs at different radii (B, F, and G). On the right side, we show the models which adopt only radial inflows (C, D, and E). In addition, in both sides, we show in black a standard model (Model A) with constant SFE, no radial gas flows, and inside-out formation for the thin disc (Eq. 4.1) by means of primordial gas.

The model results are compared with the data sets described in 4.2.2. In order to have a clearer view of the data trend with radius, we decide to bin the stellar (Cepheids and YOC) and nebular (HII regions and PNe) data in radius bins of 2 kpc of amplitude. To be more statistically consistent, within each bin we impose a minimum number of data of 10. In case this number is not reached, the bin is enlarged until this condition is satisfied.
As it can be seen from the first and second row panels, there is an offset between nebular and stellar data. This offset can be interpreted as a real observational bias in at least one of the two observational techniques. In fact, nitrogen is minimally depleted by dust in the MW ([N/H]$_{ISM}$-[N/H]$_{gas}$ $<$0.1 dex, see Jenkins 2009). In this way, the offset between nebular and stellar data for N and O can be interpreted in terms of a bias between the two observational techniques.
Still concerning nitrogen, we signal that adopting stellar yields with primary N production by all massive stars of all metallicities (Matteucci 1986) does not change significantly the model results on present-day abundances.

By looking at Fig. 4.9, we can see that only a few models can reasonably reproduce the abundance gradients. In particular, the Model MW A with only inside-out for the formation of the thin disc does not reproduce the observed gradients, since it predicts a very flat behaviour. Even adopting more extreme inside-out laws (see 4.2.3) the problem remains: in fact, we test different laws according to Eq. (4.4) and we find no substantial effects on the results. This can be seen in Fig. 4.10, where we show [Fe/H] radial gradients obtained with Eq. (4.4) values: it is clear from the Figure that the change in the results is marginal. Furthermore, variations are even less pronounced for the other abundance gradients.

Coming back to Fig. 4.9, we note that models with either variable efficiency of star formation or radial gas flows or both produce results in agreement with observations. In fact, a SFE decreasing with radius boosts the metal enrichment in the inner regions relative to the outer ones. Radial flows, instead, bring the material from the outer regions to the inner ones, providing an additional source of gas to enhance the SF (and so the metal

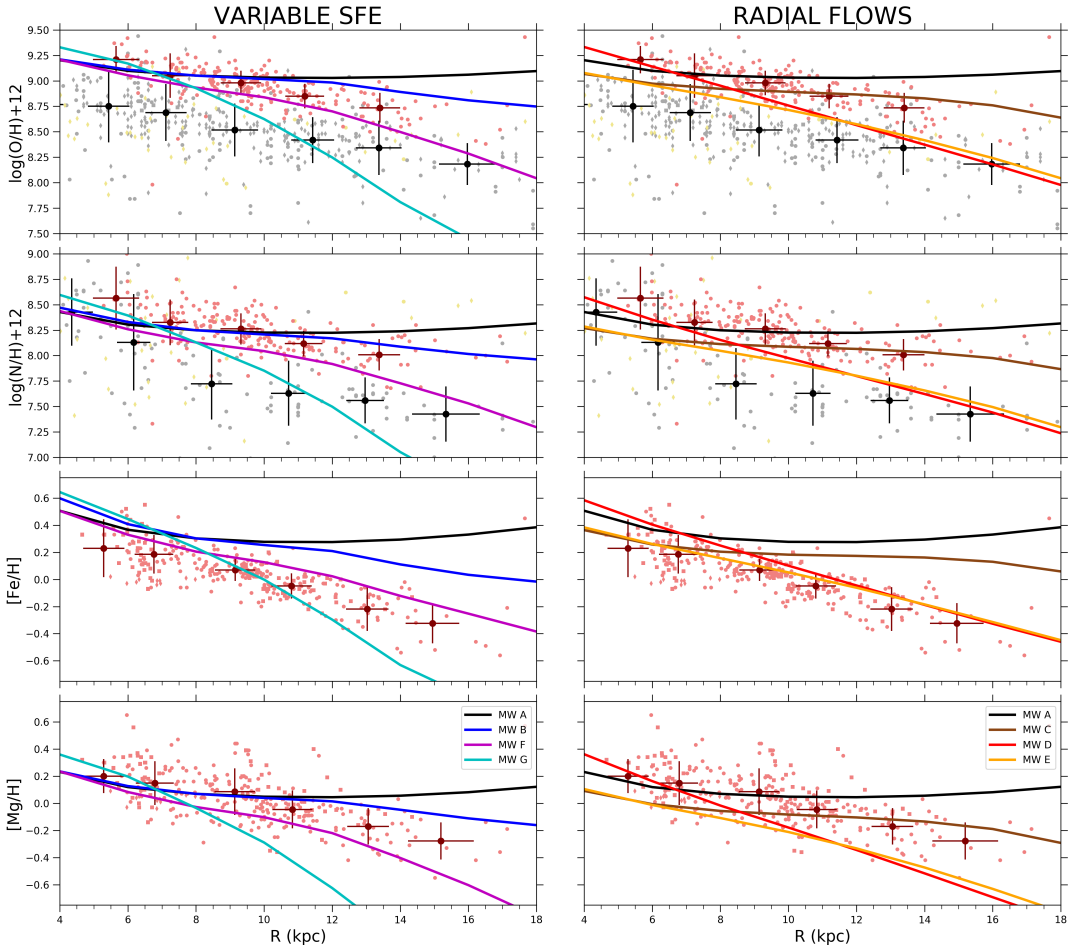

Figure 4.9: *Observed and predicted radial abundance gradients for models that adopt a variable SFE with radius (left panels) and models that adopt only radial flows (right panels). Abundances considered are oxygen (first row), nitrogen (second row), iron (third row) and magnesium (lower row). Data are from Esteban et al. (2005) (grey squares), Rudolph et al. (2006) (grey dots) and Balser et al. (2015) (grey diamonds) for HII regions, Luck & Lambert (2011) (light red dots) and Genovali et al. (2015) (light red squares) for Cepheids, Magrini et al. (2017) (light red diamonds) for YOC, Costa et al. (2004) (khaki dots) and Stanghellini & Haywood (2018) (khaki diamonds) for PNe. Black and dark red points with errorbars are data bins with associated rms for nebular and stellar data, respectively.*

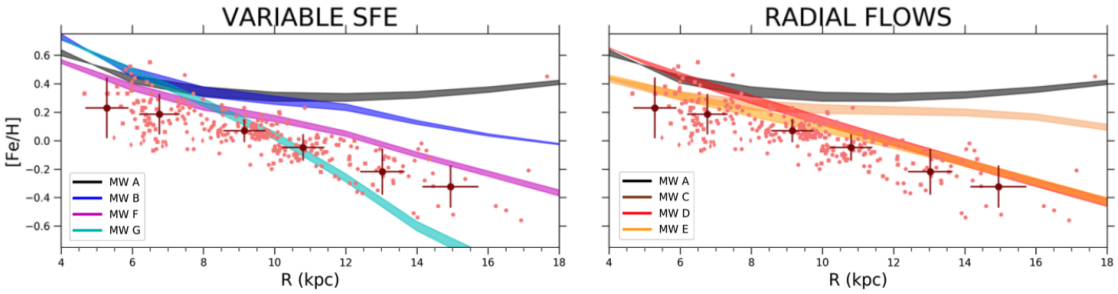

Figure 4.10: *Variations in [Fe/H] radial abundance gradients due to different inside-out law for models that adopt a variable SFE with radius (left panels) and models that adopt only radial flows (right panels). Shaded regions represent the spanned range of values for each model adopting Eq.* (4.4)*. Data and models color legends are the same of Fig. 4.9.*

enrichment).
Among the models of the left panel of Figure 4.9 Model MW F seems to be the best one, while Model MW E seems to be the best among those of the right panel. Model MW F assumes a variable efficiency of star formation along the disc plus radial gas flows with constant speed ($v_{flow} = -1$ km s^{-1}), whereas Model MW E assumes a constant efficiency of star formation but radial gas flows with speed variable with radius and time (see 4.2.3). These results are supported by previous findings (see, e.g. Colavitti et al. 2009; Grisoni et al. 2018) suggesting that either variable SFE or radial gas flows do reproduce the gradients along the thin disc of the Galaxy.
Looking at the other models, on the left side we see that the model with variable SFE only (MW B) predicts a steeper slope than the MW A model, in acceptable agreement with data from Cepheids and YOC (except for [Fe/H]). The agreement is absent instead for model MW G (variable SFE + $v_{flow} = \left(\mathrm{R}/4 - 1\right)$ km s^{-1}), which shows too steep gradients to be consistent with the observations. On the right side, we note that the model with constant inflow speed only (MW C) predicts too flat gradients to agree with the adopted data sets. MW D model instead predicts relatively too steep slopes in the inner regions of the Galaxy, and values very similar to model MW E in the outer regions.

In Tab. 4.5 we show the slopes obtained by means of the models in better agreement with observational data. In particular, we decide to compare the fits of the data with the ones of the models in the region 4-16 kpc. This choice is justified by the very limited amount of nebular and stellar data in the outer regions ($\mathrm{R} \gtrsim 16$ kpc).
As we can see from Tab. 4.5, the values predicted by the models with radius and time dependent radial flows (MW E) and combined variable SFE and radial flows (MW F) best agree with the fits to the data. The other two models in the Tab. 4.5 show larger (MW D) and smaller (MW B) negative gradients, respectively. Concerning MW D model, we have only marginal agreement with the N/H gradient slope from HII region data. However,

Table 4.5: *Present-day slopes for elemental abundance gradients from the best models of Figure 4.9 (MW B, MW F, MW D, MW E) and observed slopes from HII regions, Cepheids and YOC. In the first column, we write the elements considered in the analysis. From second to fifth column we list the results obtained by chemical evolution models. In the last two columns, we indicate the results coming from observations.*

	CHEMICAL EVOLUTION MODELS (4-16 kpc)				OBSERVATIONS	
$d(\mathrm{X/H})/dR$	MWD B (dex/kpc)	MW F (dex/kpc)	MW D (dex/kpc)	MW E (dex/kpc)	HII regions (dex/kpc)	Cepheids+YOC (dex/kpc)
O	-0.0305	-0.0734	-0.0961	-0.0688	-0.0539	- 0.0497
N	-0.0344	-0.0713	-0.0931	-0.0646	-0.0888	-0.0423
Fe	-0.0424	-0.0599	-0.0751	-0.0571	-	-0.0556
Mg	-0.0237	-0.0656	-0.0865	-0.0598	-	-0.0438

we take this data set with caution, because of the low number statistic together with the quite large observed data spread. We also note that the gradient predicted by model MW B is flatter than those obtained by other studies that adopt a variable SFE (e.g. Grisoni et al. 2018): this is due to the milder SFE-radius relation adopted here (see Tab. 4.4). In principle, the adoption of a steeper SFE gradient can produce a better agreement with the observed abundances: however, we will see later that the SFR-radius relation does not favour such an assumption (see Fig. 4.11).

For the model listed in Tab. 4.5, we compare the predicted present-day SFR rate gradient with available SFR estimates from the literature.

Most of the models shown (MW D, E, and F) do also well reproduce the SFR gradient along the thin disc, as shown in Fig. 4.11.
A general decrease of the SFR with Galactocentric radius is seen for all the models, in agreement with observations. However, Model MW B (variable SFE only) fails to reproduce the observed behaviour in the inner regions. This finding also excludes the adoption of steeper SFE-radius relations, which instead can give better agreement with abundance gradient data: larger SFEs produce lower gas consumption timescales, which tend to lower the SFR at late times. We also tested if the different infall rates of Eq. (4.4) can alleviate the tension between model MW B and data, finding no substantial improvements.
All the other models show a good agreement with Rana (1991) data set, which has however very large error bars. For this reason, the values taken from Stahler & Palla (2005) and Green (2014) are more indicative. The latter relation is very nicely reproduced by model MW D up to the solar radius, whereas stay in between MW F and MW D models in the inner Galactic radii. On the other hand, Stahler & Palla (2005) data seems to be better reproduced by MW E and MW F models.

We also analyse the predicted profiles of the gas density along the Galactic disc ac-

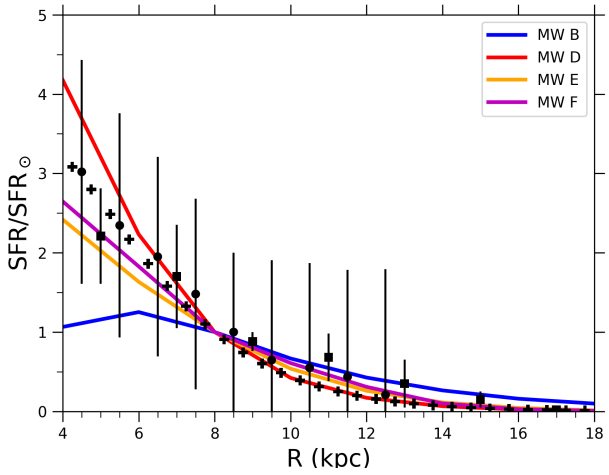

Figure 4.11: *Observed and predicted radial SFR density gradient relative to the solar neighbourhood. Lines are computed for the MW B model (solid blue), MW F (solid magenta), MW D (solid red) and MW E (solid orange). Data with errorbars are from Rana (1991) (black points) and Stahler & Palla (2005) (black squares). Black crosses with no error bars follow the analytical form suggested by Green (2014) for the MW SFR profile.*

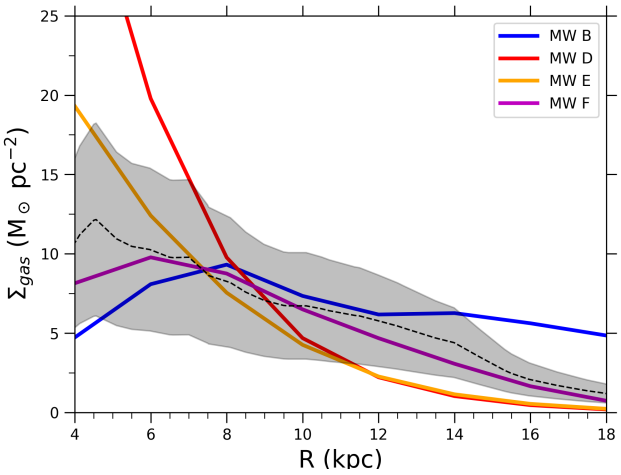

Figure 4.12: *Observed and predicted radial gas surface density gradient. Lines are computed for the MW B model (solid blue), MW F (solid magenta), MW D (solid red) and MW E (solid orange). The black dashed line is the average value between Dame (1993) and Nakanishi & Sofue (2003, 2006) datasets. The shaded region represents the typical uncertainty at each radius, for which we adopt either 50% of the average (see Nakanishi & Sofue 2006) or half the difference between the minimum and maximum values in each radial bin (if larger).*

cording to the different prescriptions adopted in this work. In particular, as for the SFR, we concentrate on the models showing a good agreement with the observed abundance gradients, i.e., those of Tab. 4.5. The results are shown in Fig. 4.12, where we compare the predictions with literature estimates at different radii.

We note that the models adopting only radial gas flows (MW D and MW E) underestimate the gas surface density for distances $\gtrsim 10$ kpc. Model MW D is also not able to reproduce the observed density in the more inner regions ($\mathrm{R} < 8$ kpc). For what concerns the models with variable SFE (MW B and MW F), they both fall inside the region covered by the observations in the inner regions. However, Model MW B overestimates the observed gas density in the more external part of the disc ($\mathrm{R} \gtrsim 14$kpc), whereas Model MW F shows a good agreement with data in the whole radial range.

The [α/Fe] vs. [Fe/H] relation along the thin disc

As a second step, we then consider only Model MW F, which well reproduces the abundance gradients as well as the SFR and gas density gradient along the thin disc, to predict the behaviour of the [α/Fe] vs. [Fe/H] at various Galactocentric radii, and compare it with APOGEE data (Hayden et al. 2015). In this way, we can test if our models are able not only to reproduce what happens at present, but also the evolution of abundances at different radii.

In Fig. 4.13 we show the predicted abundance ratios for model MW F computed for three different radii (4 kpc, 8 kpc, and 12 kpc), compared with the data of the corresponding disc regions (3-7 kpc, 7-11 kpc and 11-15 kpc). In this Figure, colour codes for models and data represent the stellar number density at a given model timestep and the normalised number of observed stars in a certain [Mg/Fe] vs. [Fe/H] bin, respectively. Such colour-coding helps in understanding the compatibility between models and data: regions with higher data density should broadly correspond to higher stellar density predictions by the models.

We see that the data shape for [Mg/Fe] vs. [Fe/H] relation is different for different regions. In particular, we note a diagonal shape for the inner regions, where the data seems to follow a unique sequence. Moving to the outer radii, the densest regions are progressively shifted at lower [Fe/H] and the diagonal shape is no more present. In particular, in central panels we see the presence of two distinct sequences, i.e., the so called high-α and low-α sequences, while for the outer regions we see only stars with low [α/Fe].
For what concerns the models, they exhibit the typical patterns of the "classical" two-infall model, with the gap marking the transition between the thick and thin disc phases (see Grisoni et al. 2017 for more details). This gap is not seen for the model at 4 kpc due to the high SFE in the second infall phase that produce an overabundance of α-elements (for the "time-delay model": see Matteucci 2001, 2012).

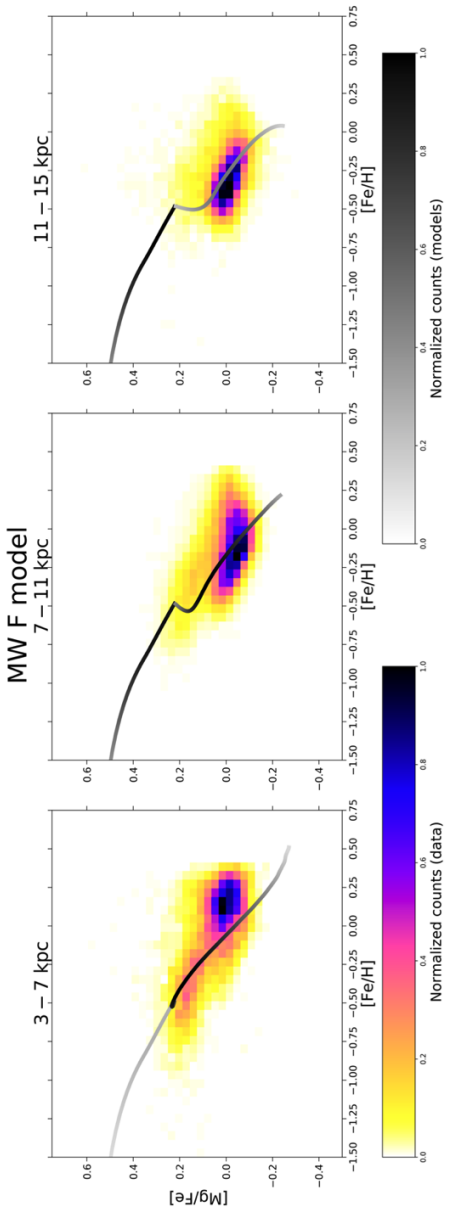

Figure 4.13: *[α/Fe] vs. [Fe/H] abundance ratios of model MW F with "classical" two-infall prescriptions ($t_{max} = 1$ Gyr, $\Sigma_{thick} \propto 1/\mathrm{R}$). Data are from Hayden et al. (2015). Left, central and right panels show the models and data in the ranges 3 < R/kpc <7, 7 < R/kpc < 11 and 11 < R/kpc < 15, respectively. Left colorbar indicates the normalised counts of data in a certain bin of the plot (the area of each bin is fixed at the value of 0.056 dex×0.031 dex), while right colorbar indicates the normalised counts of stars formed in the model at a certain time t (and hence at certain [Mg/Fe] and [Fe/H]).*

Table 4.6: *Variable parameters for revised two-infall chemical evolution models (t_{max}, $\Sigma_{thick}(\mathrm{R})$, second infall gas abundances different from Chiappini et al. 2001; Colavitti et al. 2009; Romano et al. 2010) adopted in this work. In the first column, we write the name of the model. In the second column, there is the density profile for the thick disc $\Sigma_{thick}(\mathrm{R})$. In the third column, we indicate the time of maximum infall on the thin disk t_{max}. In the fourth column we show the level of enrichment of the second infall episode.*

Model	$\Sigma_{thick}(\mathrm{R})$ ($\mathrm{M}_\odot$ pc^{-2})	t_{max} (Gyr)	2^{nd} infall gas (dex)
MW F1	$\propto \frac{1}{\mathrm{R}}$	3.25	primordial
MW F2	$\propto \frac{1}{\mathrm{R}}$	4.5	primordial
MW F3	$\propto e^{-\mathrm{R}/4}$	3.25	primordial
MW F4	$\propto e^{-\mathrm{R}/2.3}$	3.25	primordial
MW F5	$\propto e^{-\mathrm{R}/2.3}$	3.25	[Fe/H]=-1 ($\mathrm{R} < 8$)
MW F6	$\propto e^{-\mathrm{R}/2.3}$	3.25	[Fe/H]=-0.5 ($\mathrm{R} < 8$)
MW F7	$\propto e^{-\mathrm{R}/2.3}$	3.25	[Fe/H]=0 ($\mathrm{R} < 8$)

Notes*:* R *is expressed in kpc.*

The comparison with APOGEE data shows that the models fail in reproducing the data, especially in the outer and inner regions. In the left panel (3< R/kpc < 7), we see that the model track fails to pass in the densest data region. Regarding the right panel (11< R/kpc <15), the model is able to cover the densest regions of the diagram; however, it seems to predict a too low number of stars in correspondence of this abundance region. Moreover, it is clear from both the right panels that the models predict a significant amount of stars forming at high [α/Fe] and low [Fe/H], which are not observed.

Due to the difficulties encountered in reproducing the data at different radii, we run models varying the fixed parameters shown in Tab. 4.4, i.e. t_{max} (time for the maximum mass accretion onto the thin disc), Σ_{thick} (surface mass density profile in the thick disc) and second infall gas (metal enrichment of the second infall episode).
The adopted set-up for these revised models is shown in Tab. 4.6: we start from the SFE and radial flow speed pattern of model MW F and we distinguish with numbers the models adopting different t_{max}, Σ_{thick} and second infall enrichment.

Effects of t_{max} and Σ_{thick} variations

We start by looking at the effect of t_{max} and Σ_{thick} parameters on the abundance patterns. These are shown in Fig. 4.14, where the results of Model MW F, F1, F2, F3 and F4 are plotted.

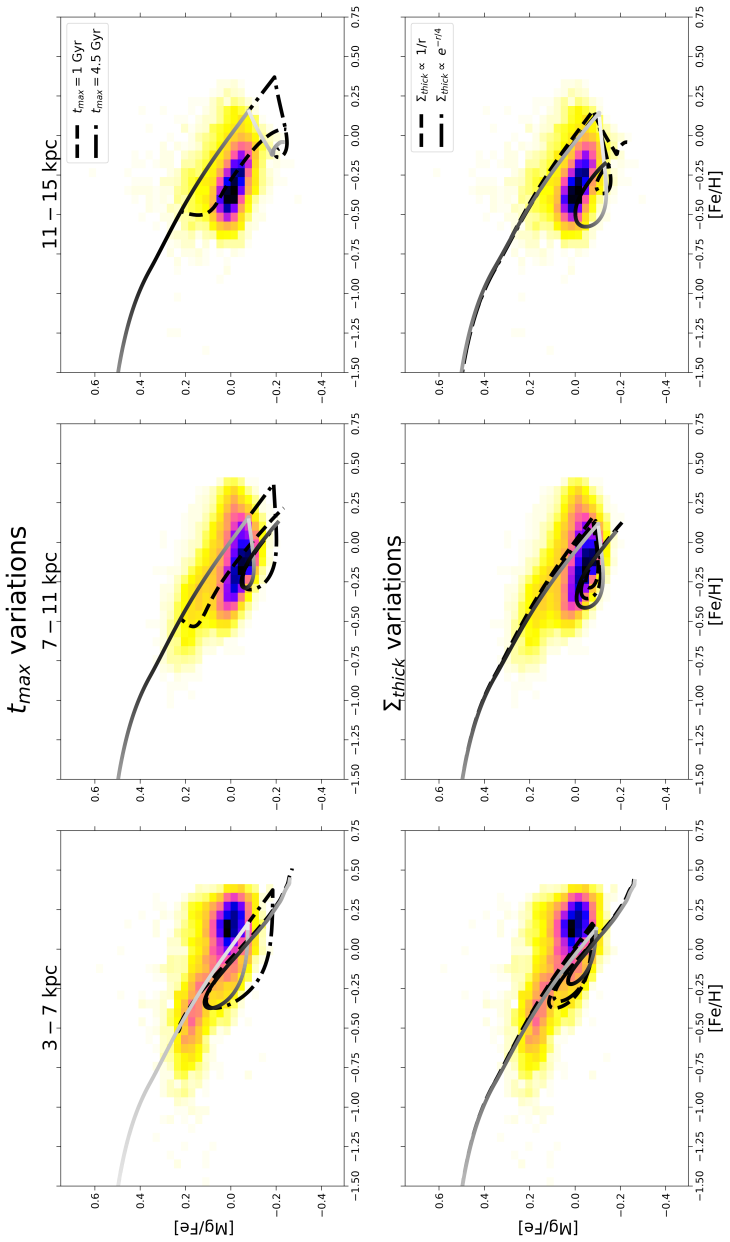

Figure 4.14: *[α/Fe] vs. [Fe/H] abundance ratios for variations of t_{max} and Σ_{thick}. Upper panels show the effects of t_{max} variations: Model MW F ($t_{max} = 1$ Gyr, black dashed line), Model MW F1 ($t_{max} = 3.25$ Gyr, solid colour coded as in Figure 4.13) and Model MW F2 ($t_{max} = 4.5$ Gyr, black dash-dotted). Lower panels show the effects of Σ_{thick} variations: Model MW F1 ($\Sigma_{thick} \propto 1/\mathrm{R}$, black dashed), Model MW F3 ($\Sigma_{thick} \propto e^{-\mathrm{R}/4}$, black dash-dotted) and Model MW F4 ($\Sigma_{thick} \propto e^{-\mathrm{R}/2.3}$, solid colour coded as in Figure 4.13). Data are from Hayden et al. (2015). Left, central and right panels show the models and data in the ranges 3 < R/kpc <7, 7 < R/kpc < 11 and 11 < R/kpc < 15, respectively.*

In the upper panels of Fig. 4.14, we see that the agreement between model results and data in the region between 7 and 11 kpc slightly improves if we assume a longer time for maximum infall onto the thin disc (i.e. t_{max} from 1 to 4.5 Gyr), and this corresponds to enlarging the time during which there is a gap in the star formation between the assembly of the two discs. In particular, the model with t_{max} =3.25 Gyr (MW F1) fits quite nicely the high density regions of stars at Galactocentric distances between 7 and 11 kpc. Larger values of t_{max} produce instead a too large loop which does not agree with the density distribution of stars. On the other hand, at outer radii the models with larger t_{max} completely fail to pass for the region covered by the largest number of stars. At inner radii, instead, a longer t_{max} creates a loop which is not consistent with the observed diagonal sequence of denser data regions.

Our modification in the second infall delay time is justified by results found in previous works. A large t_{max} was also suggested by Spitoni et al. (2019, 2020) who well reproduced chemical abundances and stellar ages in the solar neighbourhood from APOKASC data (Silva Aguirre et al. 2018) by imposing a large delay ($\gtrsim$ 4 Gyr) in the second infall episode.

In Fig. 4.14 lower panel, we show the effect of assuming a Σ_{thick} variable with Galactocentric distance, but in a different way than $\propto 1/\mathrm{R}$ (see Model MW F3 and MW F4 in Tab. 4.6).

Recent works proposed a more centrally peaked density for the thick disc (Bensby et al. 2011; Bovy et al. 2012; Haywood et al. 2016), with scale length of the order of 2 kpc (e.g. Pouliasis et al. 2017). The variation in the thick disc profile reflects in the ratio between thin and thick disc densities ($\Sigma_{thin}/\Sigma_{thick}$), which have a great influence on the chemical evolution patterns at different radii.
This can be clearly seen in Fig. 4.14, where we test three different surface density profiles for the thick disc: in particular, we look at the profiles $\Sigma_{thick} \propto 1/\mathrm{R}$ (Colavitti et al. 2009; Romano et al. 2010, model F1), $\Sigma_{thick} \propto e^{-\mathrm{R}/4}$ (Cautun et al. 2020, model F3) and $\Sigma_{thick} \propto e^{-\mathrm{R}/2.3}$ (Pouliasis et al. 2017, model F4). We remind that we fix $\Sigma_{thin}(8$ kpc$)/\Sigma_{thick}(8$ kpc$) \sim 4$ for all the models, according to Spitoni et al. (2020). The different profiles are plotted in Fig. 4.15, together with the density profile of the thin disc (dashed line in the Figure).

Coming back to Fig. 4.14, we observe that a higher $\Sigma_{thin}/\Sigma_{thick}$ ratio produces more evident loops. This allows the model with $\Sigma_{thick} \propto e^{-\mathrm{R}/2.3}$ to reproduce the data density distribution at R$>$ 11 kpc. The obtained result suggests a ratio $\Sigma_{thin}/\Sigma_{thick} \sim 8$ in the outer disc region, hence a ratio increasing with radius, in agreement with what noted in Anders et al. (2014). This is exactly the opposite of what is found with "classical" prescriptions, where the ratio in the outer regions is halved rather than doubled relative to the solar neighbourhood (see Fig. 4.15). In the inner regions (R$<$ 7 kpc), the most centrally peaked thick disc profile contributes to alleviate the problem of the prominent loop. This latter feature still prevents to cover the region with the highest density of stellar data.

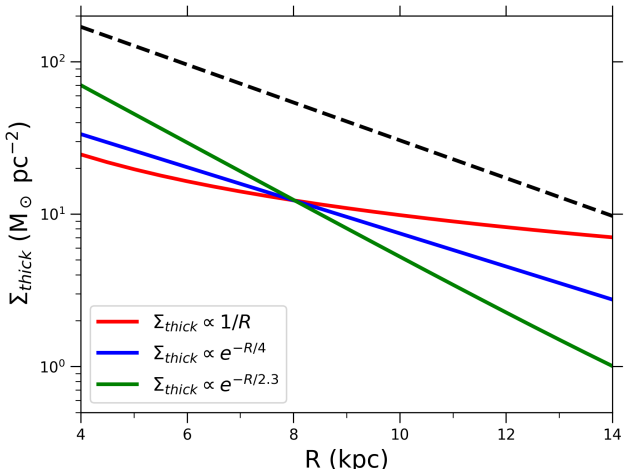

Figure 4.15: *Assumed total surface mass density profiles for the thick disc adopted in this work. Solid lines are computed for* $\Sigma_{thick} \propto 1/\mathrm{R}$ *(red),* $\Sigma_{thick} \propto e^{-\mathrm{R}/4}$ *(blue) and* $\Sigma_{thick} \propto e^{-\mathrm{R}/2.3}$ *(green). The black dashed line indicates the assumed density profile for the thin disc,* $\Sigma_{thin} \propto e^{-\mathrm{R}/3.5}$.

Nonetheless, the Model MW F4 results the best among the models shown in Fig. 4.14. Moreover, this model maintains a good agreement with present-day abundance, SFR, and gas density gradients: the variations resulted from the different t_{max} and $\Sigma_{thick}(\mathrm{R})$ are in fact limited ($\lesssim 0.015$ dex/kpc in abundance gradients slopes), allowing us to maintain a good agreement with the data.

Effects of enriched gas infall

Because of the problems found for the [α/Fe] ratios, we further investigate the evolution of the inner regions. In particular, we test whether a metal enriched second infall can explain the observed behaviour. This is done by adopting a second infall with the abundances that we obtain from the model of the thick disc corresponding to some specific [Fe/H] values.

The adoption of the abundance patterns of the thick disc does not mean that the gas is enriched only by the gas lost from the thick disc, but rather that this enriched infall is due partly to the gas lost from the formation of the thick disc, Galactic halo or the Galactic bar which then gets mixed with a larger amount of infalling primordial gas. We should note that this was already proposed by Gilmore & Wyse (1986). However, in this work we can address data sets which were not available at that time, thus providing more stringent constraints.

The results of such analysis are shown in Fig. 4.16. In particular, we test three levels of pre-enrichment for the second infall: [Fe/H]=-1,-0.5 and 0 dex (Models MW F5, F6

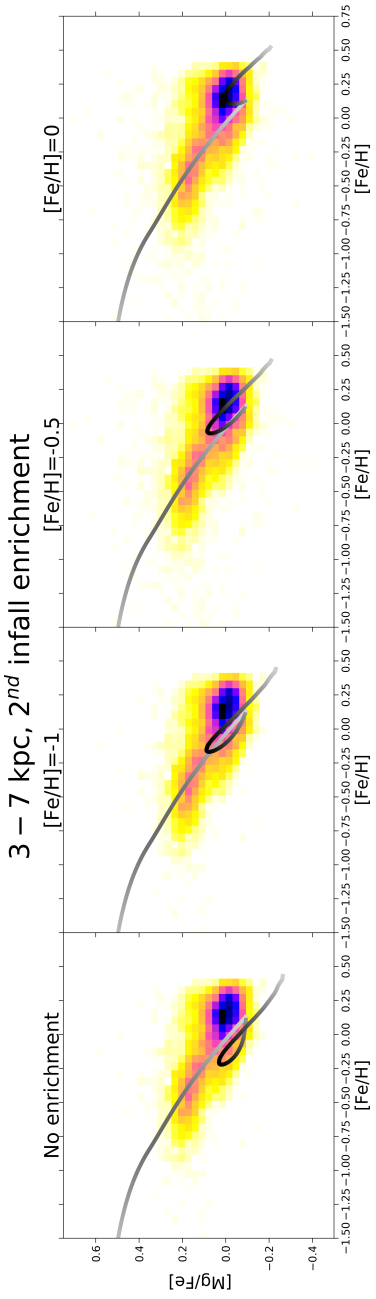

Figure 4.16: *Effects on the chemical evolution at 4 kpc in the [α/Fe] vs. [Fe/H] abundance ratios in varying the enrichment of the second infall episode. Panels show the models with pre-enrichment (from left to right): primordial (Model MW F4), [Fe/H]=-1 (Model MW F5), [Fe/H]=-0.5 (Model MW F6), [Fe/H]=0 (Model MW F7). Data are from Hayden et al. (2015).*

and F7). Lower metallicities for the infall imply too little variation relative to a primordial infall; moreover, such metallicities are reproduced by halo models only at $t \lesssim 1$ Gyr (e.g. Spitoni et al. 2016b). A supersolar infall, instead, would produce too large abundance values at present, which are not consistent with present-day gradient observations.

In Fig. 4.16, we see that a significant gas enrichment is necessary to explain APOGEE data of the thin disc in the inner regions. Going more into detail, we obtain a good agreement for Model MW F6, with [Fe/H]=-0.5 dex enriched infall. In fact, the high [Fe/H] enrichment prevents a too low [Fe/H] at the beginning of the thin disc accretion, while the high [α/Fe] in the infall gas boosts the model track to higher [Mg/Fe] values in the thin disc.
At a first sight, the Model MW F7 ([Fe/H]=0 dex) seems to have an even higher data-model agreement, with densest data region covered by the model. However, the high level of enrichment in the second infall totally prevents to explain the large number of data at moderate metallicity (-0.2 dex<[Fe/H]<0.1 dex, see the data of inner region MDF in Fig. 4.17).

Discussion

In Fig. 4.17 we summarise the results for the best model (MW F6) in reproducing the data. This model assumes a variable SFE, radial gas flows with constant speed, a time for the maximum infall onto the disc of 3.25 Gyr, an enriched infall ([Fe/H]$= -0.5$ dex) and a distribution of the total surface mass density of the thick disc $\Sigma_{thick} \propto e^{-\mathrm{R}/2.3}$.

For this model, we show the [Mg/Fe] vs. [Fe/H] plots (upper panels), the [Fe/H] MDFs (middle panels) and the [Mg/Fe] MDFs (lower panels); we also plot the median $\langle[\mathrm{Fe/H}]\rangle$ and $\langle[\mathrm{Mg/Fe}]\rangle$ resulting from data (red dashed line) and models (blue dashed line). The median abundances, together with their uncertainties, are presented in Tab. 4.7. We point out that model MDFs and median abundances in each disc region (3-7 kpc, 7-11 kpc, 11-15 kpc) are calculated considering the results of all the rings included in each region (4 kpc and 6 kpc in the range 3-7 kpc; 8 kpc and 10 kpc in the range 7-11 kpc; 12 kpc and 14 kpc in the range 11-15 kpc).

As can be seen from the upper panels, the MW F6 model predicts [Mg/Fe] vs. [Fe/H] in good agreement with the data, with the peaks in the data density nicely reproduced by the predicted stellar number densities.
This is also visible from the [Fe/H] MDFs in the central row of panels of Fig. 4.17. In particular, the model [Fe/H] MDFs at median and outer radii in general reproduce very well the observational data, although the number of metal rich ([Fe/H]$\gtrsim$0 dex) stars is slightly underestimated at radii > 11 kpc. This underestimation may have been caused by radial migration of stars (e.g. Schönrich & Binney 2009; Minchev et al. 2018). In fact, Vincenzo & Kobayashi (2020) showed that a non negligible fraction of outer radii stars

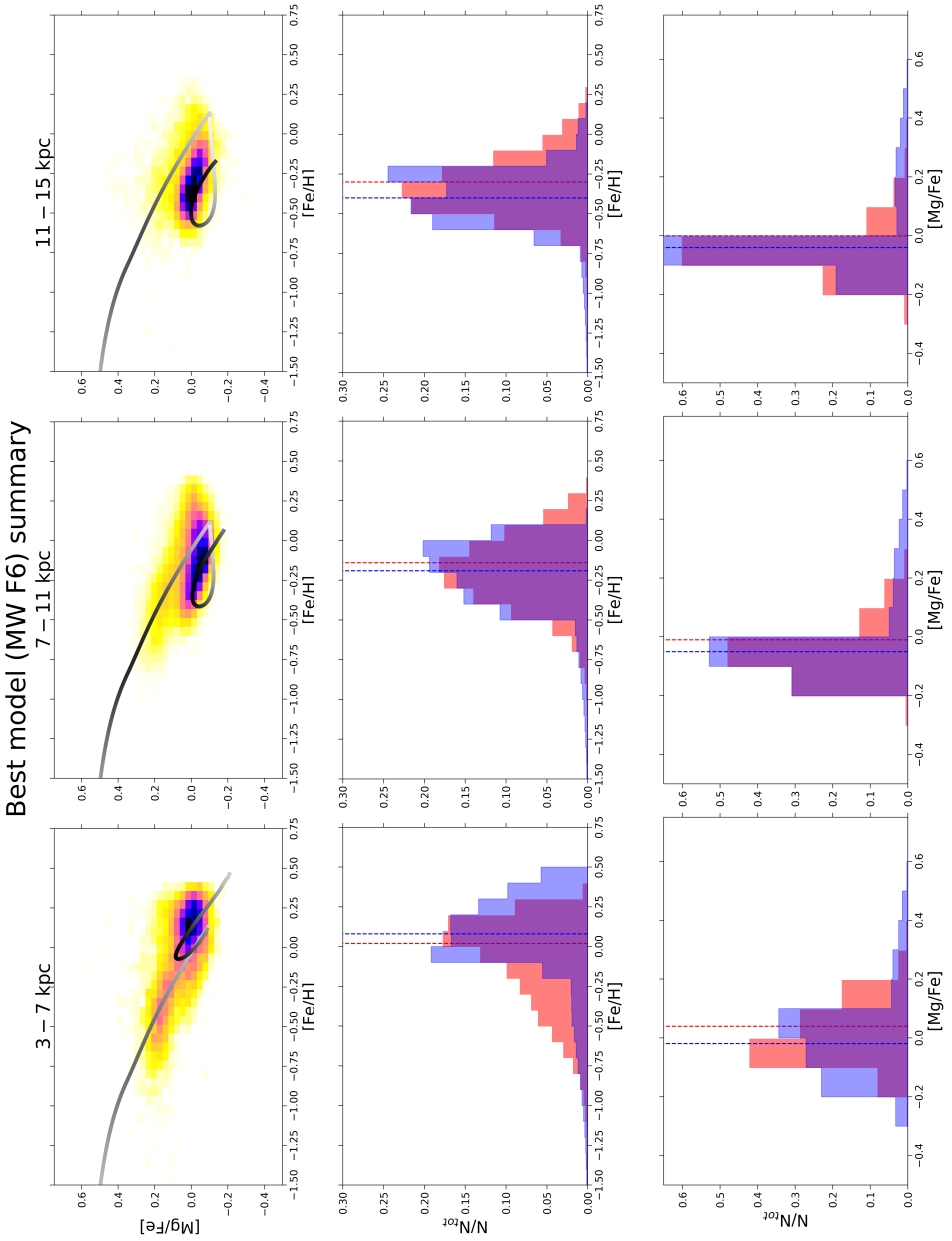

Figure 4.17: *Summary for the resulting best model MW F6. Data are from Hayden et al. (2015). Left, central and right panels show the models and data in the ranges 3 < R/Kpc <7, 7 < R/kpc < 11 and 11 < R/Kpc < 15, respectively. Upper panels: [α/Fe] vs. [Fe/H] abundance ratios. Middle panels: [Fe/H] MDFs. Lower panels: [Mg/Fe] MDFs. Blue and red dashed lines are the median [X/Y] ratios for models and data, respectively.*

Table 4.7: *Median abundance ratios obtained from APOGEE data of Hayden et al. (2015) and the best model MW F6. In the first column, we write the elements and the source considered (model or data). In the second, third and fourth column we list the obtained median abundance ratios (with $\pm\sigma$ errors) in the radius ranges 3-7 kpc, 7-11 kpc and 11-15 kpc, respectively.*

	3-7 kpc	7-11 kpc	11-15 kpc
$\langle$[Fe/H]$\rangle$ data	$0.02^{+0.21}_{-0.39}$	$-0.14^{+0.22}_{-0.22}$	$-0.30^{+0.20}_{-0.16}$
$\langle$[Fe/H]$\rangle$ model	$0.08^{+0.22}_{-0.21}$	$-0.19^{+0.17}_{-0.21}$	$-0.40^{+0.18}_{-0.17}$
$\langle$[Mg/Fe]$\rangle$ data	$0.04^{+0.13}_{-0.07}$	$-0.01^{+0.10}_{-0.06}$	$0.00^{+0.07}_{-0.05}$
$\langle$[Mg/Fe]$\rangle$ model	$-0.01^{+0.10}_{-0.13}$	$-0.05^{+0.05}_{-0.08}$	$-0.04^{+0.04}_{-0.06}$

may have been born in the Galaxy inner regions (see Fig. 8 of Vincenzo & Kobayashi 2020). However, Vincenzo & Kobayashi (2020) also found that in general less than 10% of stars have been migrated outward for more than 2 kpc. The model at inner radii instead predicts a low number of stars with metallicity [Fe/H]$\leq$-0.2 dex. This latter feature is more or less common to all the models with delayed second infall (i.e. larger t_{max}). This low number of low metallicity stars can be possibly solved by adopting an even denser thick disc profile for the inner regions (model MW F6 already adopts the most centrally peaked profile tested). Also stronger radial gas flows in the inner regions can help to alleviate the observed discrepancy, although to a lesser extent.
Concerning [Mg/Fe] MDFs, we have a good agreement from solar to outer radii (7-15 kpc), where the sharp peaks in the data MDFs are exactly reproduced. The broader MDF observed in the inner radii is also predicted by the model. However, the model MDF seems to show an offset of $\sim$0.1 dex relative to the observed one. This offset (which is however roughly compatible with APOGEE uncertainties) can be in part attributed to the model underestimation of low [Fe/H] stars. On the other hand, some recent works claimed some systematics in APOGEE abundance determinations (Jönsson et al. 2020). In particular, such problems seem to affect α-elements, where too large [α/Fe] are observed at high [Fe/H] (Matteucci et al. 2020, see also Santos-Peral et al. 2020).

In any case, the general good agreement between the model results and data is evident by looking at Tab. 4.7. In fact, the median abundances obtained from the models are well within the 1σ range obtained from the data, for both [Fe/H] and [Mg/Fe].

Having established the best model in reproducing the Hayden et al. (2015) data set, we decide to test the dependence on radius of the age-metallicity relation for this model.

In particular, we compare the predictions of the MW F6 model to abundances and ages from the updated APOKASC sample by Silva Aguirre et al. (2018). In that paper, the authors chemically separated the high-α and low-α disc populations. They used a sample of red giant stars spanning out to $\sim$2 kpc in the solar annulus and provided precise stellar

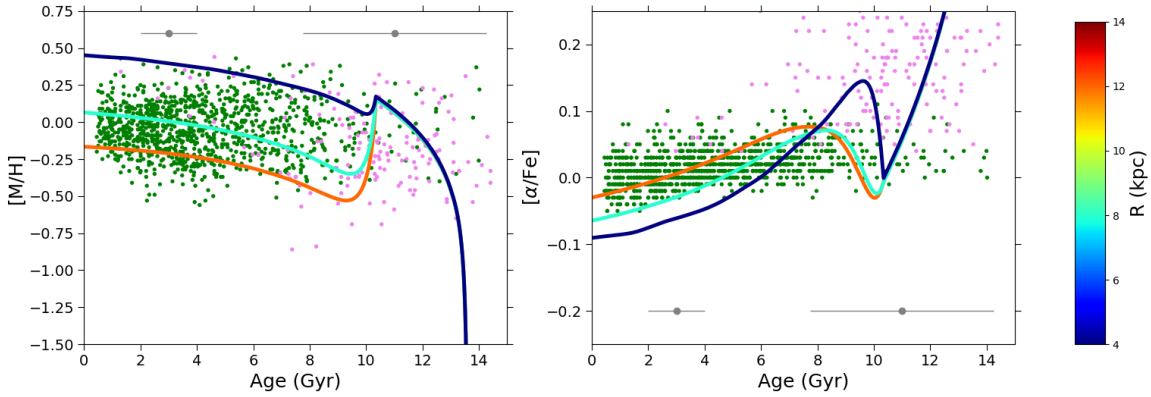

Figure 4.18: *Time evolution of [M/H] (left panel) and [α/Fe] (right panel) ratios for the stellar sample presented by Silva Aguirre et al. (2018), compared with the predictions of the best model MW F6. Pink points depict the high-α population defined as in Silva Aguirre et al. (2018), whereas green points represent the low-α one. As in Spitoni et al. (2019, 2020), we have not taken into account YαR stars. The grey symbols in the two panels indicate median age uncertainties for 3 and 11 Gyr old stars of the sample. The right colorbar indicates the radius at which each model line is computed.*

ages by means of asteroseismology.
The comparison is shown in Fig. 4.18, where we see the time evolution of [M/H] (upper panel) and [α/Fe] (lower panel) at different radii. In order to be consistent with available abundances associated with asteroseismic data, we compute the metallicity adopting the expression introduced by Salaris et al. (1993):

$$[\mathrm{M/H}] = [\mathrm{Fe/H}] + \log(0.638 \times 10^{[\alpha/\mathrm{Fe}]} + 0.362) \tag{4.9}$$

where for [α/Fe] we mean [(Si+Mg)/Fe].

In Fig. 4.18 left panel, we note that the chemical evolution tracks show progressively decreasing [M/H] with radius during the second infall phase. This behaviour is caused by the increasing SFE with decreasing radius and radial gas flows. At the same time, we see that for the most internal radius (4 kpc) the drop in metallicity between the end of the first infall and the beginning of the second one almost vanishes due to the enriched infall. The comparison with the age and [M/H] data shows that our best model at 8 kpc generally reproduces the trend of both high and low-α data. The other two lines of Fig. 4.18 left panel can be instead regarded as genuine predictions by the best model. In fact, the guiding radii of the low-α sample are comprised between $\sim$6 and $\sim$9 kpc (see Fig. 13 of Silva Aguirre et al. 2018). Nonetheless, the suggestion of an enriched infall for the most internal radii (R$<$ 8 kpc) could explain the most metal rich stars.
Concerning the right panel of Fig. 4.18, we note in this case that our model well fits the age of the high-α sequence stars, as defined in Silva Aguirre et al. (2018) (pink points).

The model is also able to explain the relatively young ($\sim 6-8$ Gyr), high-α stars as a consequence of the enriched second-infall assumed for the most internal radii. In fact, the high-α sample exhibits lower average radii than the low-α one ($\sim$6 kpc instead of $\sim$8 kpc). At the same time, the model reproduces the bulk of low-α data, although the [α/Fe] ratio in young stars seems be to be underestimated by the model. However, we already pointed out that APOGEE (and so also APOKASC) abundances may overestimate the [α/Fe] ratios at high metallicities (Matteucci et al. 2020).

Enceladus

Since we tested that enriched infall allows us to better fit APOGEE data in the inner (3-7 kpc) Galactic thin disc, we investigate the possibility that the infall episodes are related to the GES merger event occurred in the inner halo (Helmi et al. 2018; Koppelman et al. 2018; Belokurov et al. 2018). In particular, we test if some gas from Enceladus galaxy can contribute to the first or the second infall episode.

To see whether GES plays a significant contribution to the MW disc evolution, we run a chemical evolution model for Enceladus progenitor itself (see 4.2.3) based on the best model of Vincenzo et al. (2019) (see Tab. 4.3).
As can be seen from Fig. 4.19, the predicted [α/Fe] ratios for Enceladus agree very well with the stellar data from Helmi et al. 2018, which show lower values than found in the MW disc, as suggested by the "time-delay model" (see Matteucci 2001, 2012). In this formalism, if the SFR of Enceladus is lower than in the solar vicinity (and in MW inner radii), we expect a steeper decrease of the [α/Fe] ratios as functions of [Fe/H]. The evolution of Enceladus is in fact assumed to be similar to that of a dwarf spheroidal galaxy.

Having built the model for Enceladus, we test a possible contribution to the second infall episode from the galaxy relic by assuming its measured gas abundances at the start of the second infall assumed to occur at 3.25 Gyr, as in model MW F4. Since our MW models start ~ 13.5 Gyr ago, the above assumptions on the accreting gas are reasonable: in fact, Helmi et al. (2018) placed the merger approximately 10 Gyr ago, while Chaplin et al. (2020) found that the 68% confidence upper age limit was of 11.6 Gyr.

The lower [α/Fe] ratios of a dwarf galaxy gas relative to the MW disc prevent the agreement between two-infall models with a second infall enriched by Enceladus and data, even adopting a partial contribution to the enrichment of the infalling gas. In fact, the low [Mg/Fe] in the infalling gas (which does not vary significantly changing the contribution of Enceladus to the infall) causes a significant lowering in the predicted [Mg/Fe] evolution relative to previous models. This is shown in Fig. 4.20 upper left panel, where 15% of the second infall is constituted by Enceladus enriched gas.
We choose this contribution from Enceladus in order to have a consistent picture in the mass budget. Our Enceladus model predicts a $M_{gas} \sim 2 \times 10^9$ M$_\odot$ at $t = 3.25$ Gyr, which

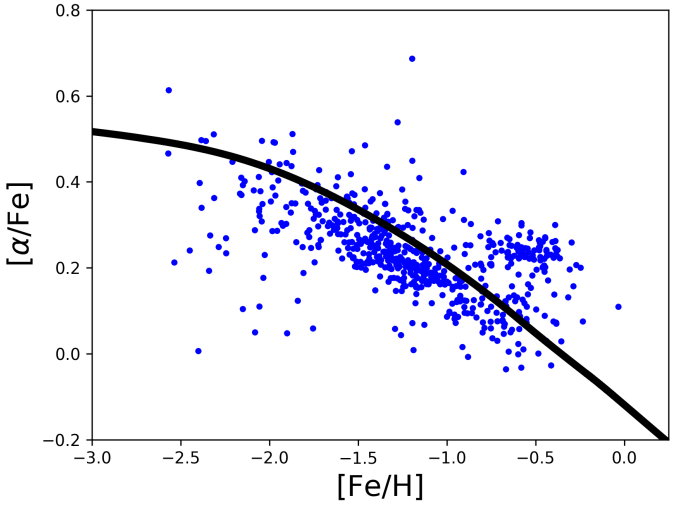

Figure 4.19: *[α/Fe] vs. [Fe/H] abundance ratios for Enceladus chemical evolution model (black solid line) compared with data from Helmi et al. (2018) (blue dots).*

is $\simeq 15$ % the mass accreted during the second infall episode by inner regions (3-7 kpc). We highlight that our result is robust against the different mass estimates for Gaia-Enceladus (Helmi et al. 2018; Vincenzo et al. 2019: $\sim 10^9$ $M_\odot$, Mackereth & Bovy 2020: $\sim 3 \cdot 10^8$ $M_\odot$). Even limiting the enriched accretion within 1 Gyr from the start of the second infall (coherently with Mackereth & Bovy 2020 mass estimate), we obtain results inconsistent with data. Inconsistent results are also obtained by adopting a higher Enceladus contribution to the infall (e.g. 25%, 50%).

Recent papers (e.g. Grand et al. 2020) also suggest that the Enceladus merger contribute 10-50% of gas to a centrally concentrated starburst. For this reason, we simulate an Enceladus induced starburst by reducing significantly the second infall timescale in the inner regions of the galaxy (< 7 kpc). In particular, we adopt $\tau_2 = 1$ Gyr and an infall pattern where Enceladus gas contributes for 15%.
However, as it can be seen in Fig. 4.20 lower left panel, the very short infall timescale does not solve the problem of too low [Mg/Fe] ratios predicted by the model in the upper panel.

Similar conclusions are reached also varying the input parameters for the Enceladus enriched infall. In particular, we test what happens with a second infall starting at 2 Gyr, i.e., coincident with the age upper limit suggested by Chaplin et al. (2020) for the start of Enceladus accretion to the Galaxy. We also try to change the infall patterns of Enceladus gas (e.g., [Fe/H]=-1 dex). However, all these models are not able to explain the observed data trend.

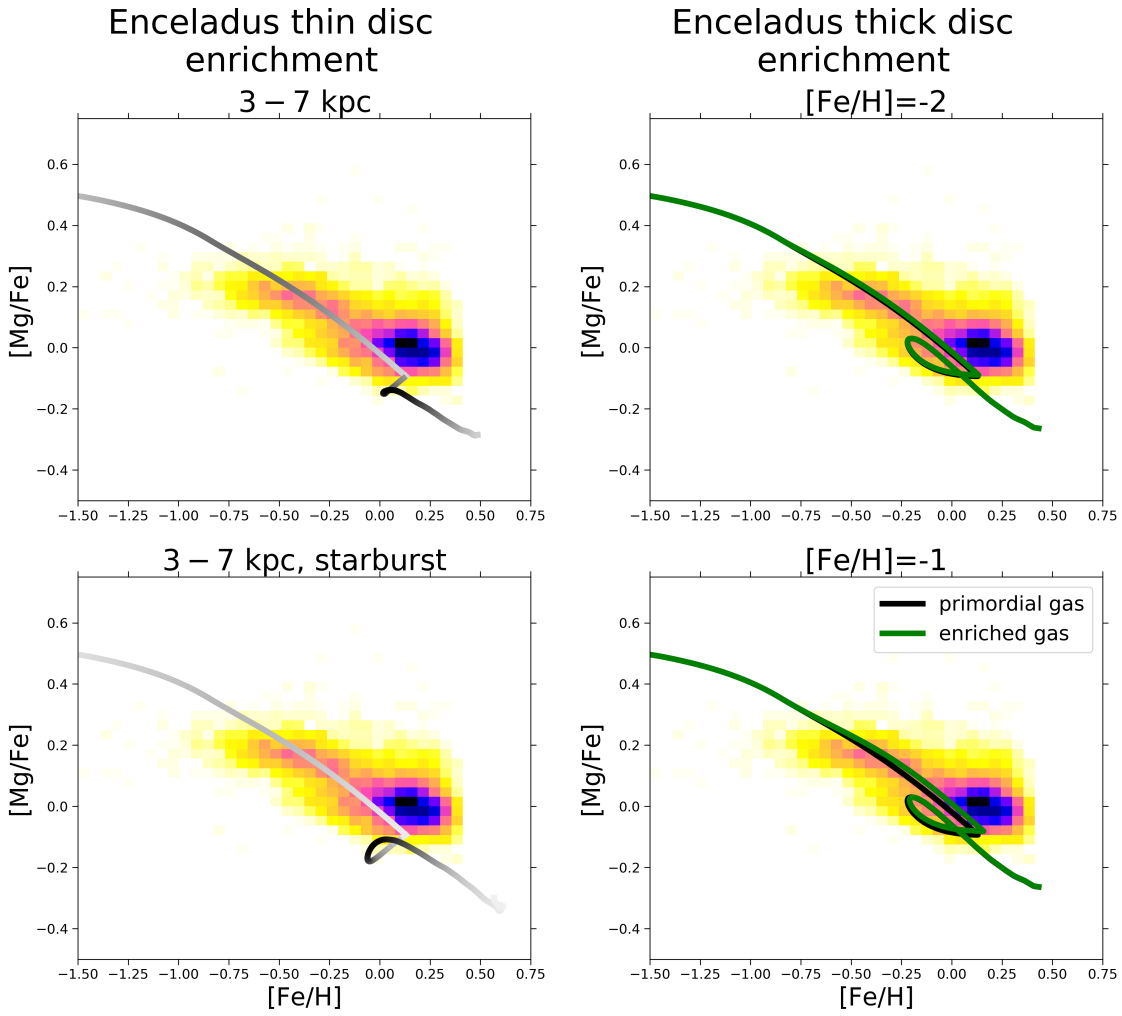

Figure 4.20: *Effects on the chemical evolution at 4 kpc in the [α/Fe] vs. [Fe/H] abundance ratios in adopting a second infall enriched by Enceladus gas at 15% (left side) and a first infall fully enriched by Enceladus gas from $t > 0.5$ Gyr (right side). All panels refer to MW F4 based models. Data are from Hayden et al. (2015).*

We also explore the possibility that Enceladus gas contributes to the first infall giving rise to the thick disc. To this scope, we try different levels of enrichment ([Fe/H]=-2,-1,-0.5 dex, adopting the abundance pattern seen in Fig. 4.19), as well as different times for the start of the infall enrichment (0, 0.5, 1, 2 Gyr).

On the right side of Fig. 4.20, we show the results for a thick disc infall enrichment starting at 0.5 Gyr. In the upper panel, we see that a low metal enriched gas ([Fe/H]=-2 dex) does not bring any evident change in the predicted abundance track. Concerning the lower panel, the moderate enrichment (1/10 solar in iron) has little effect in enhancing the [α/Fe] ratio but it is still not able to explain the abundance trend.
Nonetheless, the marginal effect of an Enceladus driven thick disc accretion on the abundance patterns does not exclude the possibility that gas lost from Enceladus could have contributed to the formation of the thick disc.

4.2.5 Conclusions

In this Section, we have computed the chemical evolution of the thick and thin discs of the MW by adopting the two-infall model paradigm. In other words, we have assumed that the thick and thin discs form by means of two infall episodes separated by a period in which star formation decreases and then increases again thanks to the second infall episode.

We run several models by varying physical parameters such as the presence or absence of radial gas flows, constant or variable efficiency of star formation along the thin disc as well as different inside-out schemes for the formation of the thin disc and we have compared the results with abundance, SFR and gas density gradients along the thin disc, selecting the best models to reproduce the gradients.
Then we varied the duration of the interval between the formation of the thick and thin discs, expressed as the time of maximum gas infall onto the disc, the total present time surface gas density of the thick disc, and finally the thin disc infalling gas chemical composition in the innermost radii. For all the models, we did not change the IMF (Kroupa et al. 1993), the timescale of the infall and the efficiency of star formation for the thick disc (1 Gyr and 2 Gyr^{-1}). We showed the predictions of these models concerning the [Mg/Fe] vs. [Fe/H] relations along the disc compared with APOGEE data (Hayden et al. 2015). We also computed the metallicity distribution functions at different Galactocentric radii, selecting the best model in reproducing the majority of the observational constraints.

Moreover, we computed the evolution of a dwarf galaxy resembling the progenitor of the Gaia-Enceladus-Sausage stars (Belokurov et al. 2018; Helmi et al. 2018) and adopted the predicted abundance pattern as the chemical composition of the infalling gas either in the thick or thin disc.

Our main conclusions can be summarized as follows:

- it is not possible to reproduce the observed abundance gradients along the thin disc only assuming an inside-out formation as the main mechanism for gradient formation. We need to assume either radial gas flows and/or efficiency of star formation varying with the Galactocentric distance, in agreement with Grisoni et al. (2018). However, too strong radial gas flows produce too steep abundance and gas density gradients and models adopting only variable star formation efficiency and no radial gas flows do not reproduce the gradient of the SFR and gas density along the thin disc. Our best models for reproducing abundance and SFR gradients are Model MW E, assuming radial flows with variable speed progressively decreasing with radius and time, and Model MW F, with constant, moderate radial gas flows and variable star formation efficiency. In addition, the latter model well matches the observed gas density gradient;
- for the model MW F, we allow to vary the maximum timescale for infall onto the disc t_{max} and the profiles for the thick disc surface mass density Σ_{thick}. In fact, "classical" two infall model prescriptions (e.g. Chiappini et al. 1997; Romano et al. 2010) does not produce very good agreement with the observed [Mg/Fe] vs. [Fe/H] relations especially in the inner (3-7 kpc) and outer (11-15 kpc) Galactic disc regions. Better agreement is reached if $t_{max} = 3.25$ Gyr, in accord (even if larger values are found) with previous suggestions by Spitoni et al. (2019, 2020). Results for the outer regions suggest also the adoption of a small scale length ($R_d \sim 2$ kpc) exponential profile for the thick disc, in agreement with recent findings (e.g. Anders et al. 2014; Haywood et al. 2016; Ciucă et al. 2021);
- even better agreement with data is reached if the infall onto the inner thin disc is enriched at the level of [Fe/H]=-0.5 dex. This can be the effect of mixing between the gas leftover from the formation of the thick disc, Galactic halo, or Galactic bar and the more abundant primordial extragalactic infalling gas. Finally, after analysing the metallicity distribution functions at different radii, we conclude that the best model is Model MW F6, with moderate gas flows, variable SF efficiency, $t_{max} = 3.25$ Gyr and centrally peaked exponential distribution for the total surface density of the thick disc, plus enriched gas infall along the inner thin disc;
- the chemical evolution of Enceladus is computed by adopting the same parameters shown in Tab. 4.3, as in Vincenzo et al. (2019) and we do reproduce the observed abundances by Helmi et al. (2018). The models assuming gas infall enriched as the abundance pattern derived for Enceladus at 3.25 Gyr (starting time for the thin disc infall) fail in reproducing the [Mg/Fe] vs. [Fe/H] relation for the inner Galactic regions. Enceladus enriched infall during the thick disc formation instead does not alter significantly the chemical evolution pattern. Therefore, we can conclude that

the gas lost by Enceladus or a part of it could have concurred to the formation of the thick disc but not to that of the thin disc and that the origin of the metal enrichment in the second infall for inner regions (see above) is unknown.

4.3 The effect of Type Ia SN nucleosynthesis in MW chemical evolution

4.3.1 Introduction

Type Ia supernovae (hereafter, SNe Ia) are one of the most important phenomena in Astrophysics. For example, they are used as "standard candles" for measuring cosmological distances (Phillips 1993) and they are beneath the discovery of the accelerating expansion of the Universe (Riess et al. 1998; Perlmutter et al. 1999). SNe Ia are also the origin of the majority of the iron in galaxies and play a fundamental role in galactic chemical evolution (e.g. Nomoto et al. 1984; Matteucci 2012).

The SN Ia events are assumed to be originated to be thermonuclear explosions by white dwarfs (WDs) in binary systems. In fact, Nomoto et al. (1984) realised that if a WD star is incinerated on a similar timescale to its dynamical time[5], the resulting ejecta give rise to a transient that has spectral features characteristic of a SN Ia.

Nonetheless, the physics governing SNe Ia is still largely debated (see Hillebrandt & Niemeyer 2000; Hillebrandt et al. 2013; Maoz et al. 2014; Ruiter 2020 for a review). In particular, the main problems reside in the progenitor system and the explosion mechanism.

In the last decades, the most popular proposed scenarios for the explosion mechanisms of SNe Ia have been: (i) deflagration or delayed detonation of a near-Chandrasekhar mass (near-M_{Ch}) carbon-oxygen (CO) WD in a single degenerate system (e.g. Whelan & Iben 1973), (ii) near-Chandrasekhar mass explosion in a double degenerate system (e.g. Iben & Tutukov 1984), (iii) double detonations of sub-Chandrasekhar mass (sub-M_{Ch}) WD in a single or double degenerate system (e.g. Nomoto 1982; Iben & Tutukov 1991), (iv) violent merger in double degenerate sub-M_{Ch} WDs (e.g. Pakmor et al. 2012), (v) weak deflagration of a near-M_{Ch} WD in a single degenerate system giving rise to low mass WD remnant. The latter scenario could correspond to a Type Iax supernova (SN Iax, see e.g., Kromer et al. 2015).

Nearly all classes of explosions are supported by lightcurve and abundance observations of several individual SN explosions and remnants (see Kirby et al. 2019; de los Reyes et al. 2020), suggesting that SNe Ia explode through multiple channels (e.g. Mannucci et al. 2006).

Type Ia SN nucleosynthesis

As said above, SNe Ia dominate the Fe budget in the chemical evolution of galaxies. SNe Ia are also supposed to be the most important players in the production of some of the Fe-peak elements (e.g. de los Reyes et al. 2020). In particular, Mn is often used as an

[5] measure of the time scale on which a star would expand or contract if the balance between pressure and gravity is suddenly disrupted.

abundance tracer for SN Ia. Furthermore, a non negligible fraction of some α-elements (i.e. Si, S, Ca) is produced in these thermonuclear explosions.

However, different progenitor channels produce characteristic abundance patterns. While the nucleosynthetic distinction between single and double degenerate channels may not be large enough to be constrained with current data, the mass of the WD (i.e. near-M_{Ch} or sub-M_{Ch}) has a large effect on the production of certain elements (Kobayashi et al. 2020a): this happens in particular for neutron rich isotopes (e.g. ^{54}Cr, ^{55}Mn, ^{58}Ni), whose production is closely related to the WD density and hence mass[6].
In addition, important roles in element production are also played by other WD features. As for example, different explosion mechanisms for near-M_{Ch} SNe Ia lead to significant differences in ejecta masses (Kobayashi et al. 2020a). On the other hand, the explosion pattern of the WD (within models adopting the same explosion mechanism) leaves a significant imprint on several abundance ratios resulting from SNe Ia (e.g. Seitenzahl et al. 2013a; Leung & Nomoto 2020a).

Owing to the different conditions before and during the explosion, different SN Ia can reach differences even larger than an order of magnitude in the chemical abundance ratios (see Fig. 2.4).

In the last decade, a great number of simulations devoted to study the nucleosynthesis of the different SN Ia channels have become available in the literature, with a broad exploration of the parameter space. Therefore, it is the right time to consider the abundances of chemical elements as a valuable tool to constrain the dominant SN Ia channels.

Type Ia SNe in chemical evolution models

Since SNe Ia are central in the production of several chemical elements, they play a key role in galactic chemical evolution.

So far, however, most of the papers treating chemical evolution still adopt old 1D simulations, in particular the W7 model (e.g. Nomoto et al. 1984; Iwamoto et al. 1999) or less frequently the WDD2 model (Iwamoto et al. 1999). In fact, the yields obtained from these simulations reasonably reproduce the Galactic chemical evolution in the solar neighbourhood for most of the elements.
Nonetheless, these yields show some problems. As for example, Ni is overproduced in W7 model, while Cr is overproduced in WDD2 model (Leung & Nomoto 2018). Another crucial issue is that these models actually suffer from substantial limitations in the physical treatment of the explosion.

[6] more massive WD have lower radius than less massive ones. In fact, WD have a mass-radius relationship $r_{WD} \propto M_{WD}^{-1/3}$.

Up to now, only few studies of chemical evolution have been devoted to asses the impact of different SN Ia progenitor yields on the evolution of the abundance ratios (e.g. Cescutti & Kobayashi 2017; Kobayashi et al. 2020a).
However, most of these studies look at single elements (e.g. Eitner et al. 2020; de los Reyes et al. 2020; Gronow et al. 2021) or external galaxies (mainly MW satellites and other dwarfs, e.g. Kobayashi et al. 2015; Cescutti & Kobayashi 2017; Kirby et al. 2019). An exception is represented by Kobayashi et al. (2020a), where O, Mn, Cr and Ni abundances in the Galaxy are compared with chemical evolution models adopting updated near-M_{Ch} and sub-M_{Ch} yields.

Therefore, the aim of this work is to compare the yields of a large compilation of SN Ia models for different nucleosynthesis channels (i.e. near-M_{Ch}, sub-M_{Ch}, SNe Iax), by adopting detailed models for the chemical evolution of the MW. In particular, we test more than 20 SN Ia models from the literature sampling different progenitor masses, explosion mechanisms and other features. We also explore models with different dimensional treatment of the SN Ia simulations (1D, 2D, 3D).
To include the SN Ia in our chemical evolution models, we adopt a fixed delay time distribution function (DTD) and in particular the one pertaining to the single degenerate model. The possible effects of different DTDs are beyond the scope of this work, since our focus is on the SN Ia nucleosynthetic yields and in particular on the different progenitors and different parameters affecting chemical abundance ratios. However, it is worth reminding that other DTDs, such as that of double degenerate systems or observationally inferred ones, are similar to the one adopted here (see Matteucci et al. 2009).

To include the results of this work, we organise this Section as follows. In 4.3.2, we give a detailed overview of SN Ia modelling and we list the SN Ia models considered. In 4.3.3, we present the chemical evolution models adopted in this work. In 4.3.4, we describe the results of the application of the yield sets to our chemical evolution models. In particular, we reserve the first part to the analysis of the abundance patterns obtained with the individual yield sets. In the second part, instead, we present a comparison between model predictions and MW observations: in doing this, we allow our chemical evolution models to have contributions from multiple SN Ia progenitor channels, in order to test the role of the different subclasses of these events. Finally, in 4.3.5, we draw our conclusions.

4.3.2 SN Ia models and yields

As mentioned in 4.3.1, in this work we sample different explosion mechanisms and progenitor masses for SNe Ia. In particular, we look at delayed detonation/deflagration-to-detonation transition (hereafter DDT) and pure deflagrations (PTD) models for near-M_{Ch} WD, while for sub-M_{Ch} WD we adopt double-detonation (DD) models.

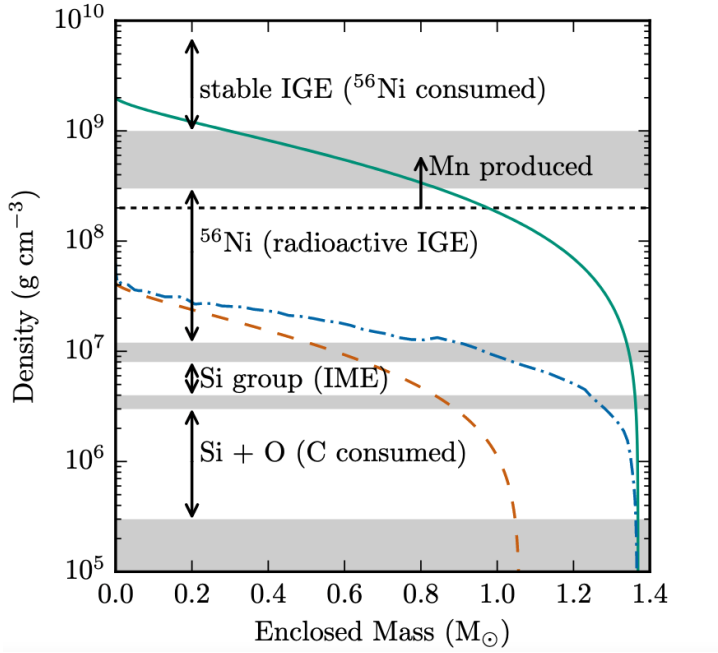

Figure 4.21: *From Seitenzahl & Townsley (2017). Profiles of WD density and correspondent main nucleosynthetic products for different SN Ia progenitor models. Lines are shown for a near-M_{Ch} WD without expansion, i.e. without initial deflagration (green solid), a near-M_{Ch} WD after expansion (blue dash-dotted) and a sub-M_{Ch} WD (orange dashed).*

Below, we introduce these SN Ia explosion mechanism. In particular, we describe the basic theory beneath the different models, highlighting the main differences.

Fig. 4.21 shows how the products of the explosive burning depend on the local fuel density in different SN Ia models.

From the Figure, we see that at high densities we have more complete processing to Fe-group elements (hereafter, IGE)[7], whereas at lower densities the nuclear processing ends with the production of intermediate mass elements (hereafter IME)[8]. It is thus immediately clear that the hydrostatic state of the WD at the time the burning takes place has a direct role in the nucleosynthetic yield produced.

The green line in Fig. 4.21 represent the typical density structure of a near-M_{Ch} WD, which are usually identified with masses of $\sim$1.38-1.39 M$_\odot$ (e.g. Nomoto et al. 1984; Seitenzahl et al. 2013a; Leung & Nomoto 2018), before the explosion. If the explosion occurs on a timescale that is lower than the dynamical time of the star (around 1 second), i.e., the WD is burned by a detonation, the burning is supersonically propagated by a shock

[7] elements with atomic number adjacent to iron.
[8] elements with atomic number between that of Na and Ca.

that is self-sustained by the energy release. With this mechanism at play, the star has no opportunity to expand and will produce nearly all stable IGE. This is not in agreement with what is observed in SN Ia ejecta, where IGE production is well below the mass of the WD and where large amounts of radioactive ^{56}Ni are detected.
Yields favoring more IME can be obtained if the beginning of the incineration occurs slightly more slowly than the dynamical time: in this way, the WD can expand so that the lowered densities lead to a realistic production of IME, as well as ^{56}Ni amount able to power the observed bright transient. For this reason, a deflagration explosion mode is invoked: here a flame driven by heat conduction burns the fuel more slowly (i.e., at subsonic speeds) and allows the star to globally respond and expand. The density profile after the deflagration is shown with the blue, dash-dotted line in Fig. 4.21: here, we see that the central density is lowered by at least 1 order of magnitude relative to the initial WD configuration.
Therefore, models explaining near-M_{Ch} SN Ia always assume an initial deflagration for the WD.

On the other side, sub-M_{Ch} WDs have masses of around 1 M$_\odot$ (e.g. Shen et al. 2018; Leung & Nomoto 2020a, even if less or more massive models are also computed). These lower masses imply lower initial WD densities (central values below 10^8 g cm^{-3}), that do not need any reduction to produce an amount of ^{56}Ni needed to enlight SN Ia lighcurves. This is shown by the orange, dashed line in Fig. 4.21, which represents the profile of a 1.05 M$_\odot$ WD.
For this reason, no deflagration mechanisms are invoked to explain sub-M_{Ch} SN Ia, which burning is the result of a detonation.

In the following, we describe in more detail the different explosion mechanisms adopted throughout this work. In doing this, we also present the SN Ia yield that we apply to chemical evolution models, listing their main physical parameters. However, the reader is referred to the source papers for a more thorough discussion on the adopted input physics of the individual models.

Near-M_{Ch} DDT models

With this explosion mechanism the initial WD deflagration is followed by a detonation that burns the remaining fuel. This transition happens after some time delay, under suitable conditions.

The DDT formulation was introduced by Khokhlov (1991) to overcome the shortcomings of pure detonation (no IMEs production) and pure deflagration models (e.g., overprodution of neutron-rich nuclear species).
In fact, the expansion of the star prior to the detonation results in the desired nuclear burning at densities $\sim$10^7 g cm^{-3}, where IMEs are synthetised. At the same time, the initial

deflagration contribute to the production of neutron-rich isotopes, such as Mn. In fact, these elements need high densities to be produced, typically above 10^8 g cm^{-3} (Seitenzahl et al. 2013a). The lower limit for a consistent Mn production regime can be identified by the horizontal dashed line in Fig. 4.21, which represents the border between α-rich freeze-out of nuclear statistical equilibrium (NSE[9]) at lower densities and normal, i.e. with larger Fe-group element production, NSE freeze-out at higher densities (see Seitenzahl & Townsley 2017 for more information).

For what concerns models with the DDT mechanism at play, we consider two recent studies that sample a variety of different WD initial conditions in multi-dimensional SN Ia simulations. In particular, we test the yields from Seitenzahl et al. (2013a) and Leung & Nomoto (2018).
It worth noting that the consideration of more than one spatial dimension is necessary to obtain realistic simulations, in particular during the deflagration phase. During this phase, the burning front is highly textured due to convection mechanism for the heat transfer: thus non-spherical effects need to be considered (e.g. Niemeyer et al. 1996).

Seitenzahl et al. (2013)

Seitenzahl et al. (2013a) completed the first study in the literature in which detailed nucleosynthesis for DDT in 3D was performed.
The authors computed the results for twelve 3D models with different number of initial deflagration sites (from 1 to 1600) at solar metallicity and with a WD central density of $\sim 3 \times 10^9$ g cm^{-3}. For the case of 100 ignition points (N100), the set includes the results for a range of metallicities ($0.01 \leq Z/Z_\odot \leq 1$) and central densities for the CO WD ($1 \times 10^9 \leq \rho_c/\mathrm{g\ cm^{-3}} \leq 5.5 \times 10^9$).

We consider as benchmark models the N100 ones with $\rho_c \sim 3 \times 10^9$ g cm^{-3} at different metallicities (see Tab. 4.8). Throughout this Section, we also explore the effects on the yields of different WD central densities. We do not consider instead the results for the models with a different number of ignition sites: in fact, in most of them the nucleosynthesis is not in line with that of typical SNe Ia (e.g. $M_{^{56}\mathrm{Ni}} \gtrsim 1$ M$_\odot$ or Si/Fe$\sim$1).

Leung & Nomoto (2018)

In Leung & Nomoto (2018) more than twenty 2D DDT models with central point ignition were computed, exploring broadly the parameter space.
In particular, the effects of WD central density ($0.5 \times 10^9 \leq \rho_c/\mathrm{g\ cm^{-3}} \leq 5 \times 10^9$), metallicity ($0 \leq Z/Z_\odot \leq 5$), flame shape and turbulent flame formula were tested. It has to be

[9] at the temperatures of the burning, radiation is energetic enough to knock protons and α-particles off of nuclei (photodisintegration): nuclei continually gain and loose particles, setting up a statistical equilibrium. However, α-captures slightly predominate over photodisintegration favouring the presence of heavier nuclei at the end of this phase.

noted that in Leung & Nomoto (2018) the WD progenitor masses are extended down to the range of 1.30-1.35 $M_\odot$, which may be considered as sub-Chandrasekhar masses (Leung & Nomoto 2018). The C ignition in such progenitors would be possible by shock compression due to surface He detonation (e.g. Arnett 1996), that however may not produce a C detonation (as in DD models) due to the relatively large WD mass.

In our work, we consider the models with the full metallicity range ($0 \leq Z/Z_\odot \leq 5$) covered, i.e. the low density ($\rho_c = 10^9$ g cm^{-3}, $M_{WD} = 1.33 M_\odot$), benchmark ($\rho_c = 3 \times 10^9$ g cm^{-3}, $M_{WD} = 1.38 M_\odot$) and high density ($\rho_c = 5 \times 10^9$ g cm^{-3}, $M_{WD} = 1.39 M_\odot$) models. In particular, we focus on the outcomes of their benchmark model (see Tab. 4.8 for the main parameters), showing the results of the other models where the differences in the abundances are important.

Near-M_{Ch} PTD models

Since a direct detonation of a near-M_{Ch} CO WD would burn most of the star at high density to ^{56}Ni and other IGE (Arnett 1969), pure deflagration (PTD) had been considered for long time as the favoured models in explaining SN Ia nucleosynthesis (Seitenzahl & Townsley 2017). Here, the deflagration flame allows the WD to respond to the nuclear energy release with expansion to lower densities. In this way, the burning can also produce IMEs and not only IGEs as for a purely detonating WD.

However, recent multi-dimensional models of PTD explosion seem to exclude that this scheme is one of the responsible of "normal" SNe Ia (e.g. Röpke et al. 2007; Fink et al. 2014): the explosions are too faint and chemically mixed to explain transient colors and spectra.
Nonetheless, PTD mechanism provide excellent models for peculiar subluminous SNe Ia, i.e. SNe Iax (e.g. Kromer et al. 2015; Leung & Nomoto 2018; Kirby et al. 2019). In this scenario, the weak explosion only partially unbind the star and leave a bound remnant behind it: this leads to a lower amount of ^{56}Ni. At the same time, large amounts of neutron-rich stable iron group isotopes are produced as a signature of the burning at high densities.

As for DDT models, also for PTD models we consider two studies from the literature where multi-dimensional treatment of the system is adopted. In particular, we test the yields from Fink et al. (2014) and Leung & Nomoto (2018).

Fink et al. (2014)

In this paper, the authors computed PTD simulations based on the code adopted by Seitenzahl et al. (2013a). Fink et al. (2014) also simulated between 1 and 1600 sites of ignition for the WD, but the models do not experience a transition to detonation (as for Seitenzahl et al. 2013a). For the N100def model (100 ignition sites), variations in WD central density

($1 \times 10^9 \leq \rho_c/\mathrm{g\ cm^{-3}} \leq 5.5 \times 10^9$) are also explored. The metallicity is solar for all the fourteen models presented in the paper.

We decide to take the N100def simulation as our benchmark model. In this way, we can directly see the effects of a missing detonation relative to Seitenzahl et al. (2013a) yields. We note that Fink et al. (2014) stated that models with lower number of ignition sites are more suitable to explain typical SN Iax lightcurves (e.g. SN 2005hk). For this reason we also consider the outcomes of the N10def (10 ignition sites) model. However, despite of the lower Fe production, the variations relative to the N100def model are limited ($\lesssim 0.1$ dex) for most of the abundance ratios.

Leung & Nomoto (2018)

Together with the DDT models presented above, in this paper are also considered four 2D models in which the detonation transition trigger is "switched-off". These models can be seen as approximations of a failed DDT caused by some external effects (see Leung & Nomoto 2018).
The models examine how the WD central density (and hence its mass) influences the nucleosynthesis. This is done in the same range of densities explored for the Leung & Nomoto (2018) DDT models ($0.5 \times 10^9 \leq \rho_c/\mathrm{g\ cm^{-3}} \leq 5 \times 10^9$). The metallicity of all the models is solar.

In our work, we mainly show the results for the model 300-1-C3-1P ($\rho_c = 3 \times 10^9$g cm^{-3}, see Tab. 4.8). However, we also look at the impact of WD mass variation on the chemical evolution where the differences between the models are important.
We point out that in Leung & Nomoto (2020b) PTD models for CO WDs are tested specifically on SNe Iax. In these models the mass trapped by the WD remnant, that may be originated by Type Iax subclass, was also computed. However, the resulting abundance patterns are generally very similar to those of the PTD models of Leung & Nomoto (2018) that we consider in this work.

Sub-M_{Ch} DD models

As mentioned earlier, SNe Ia originating from sub-M_{Ch} WD do not need any initial deflagration: here, C detonation is the responsible of the observed ^{56}Ni mass.
In most of sub-M_{Ch} models, the C detonation is triggered by a surface detonation of He, which can accumulate from direct He accretion (either from a He WD, Tutukov & Yungelson 1996, or a non-degenerate He star, Iben & Tutukov 1987) or slow accretion of H reprocessed into He (e.g. Taam 1980). In fact, multi-dimensional simulations have shown that detonations in the He-layer compress the core and likely (at least for CO cores with sufficient mass) initiate a second C detonation there (e.g. Woosley & Weaver 1994; Shen & Bildsten 2014). For this reason, we refer to sub-M_{Ch} models as double-detonation (DD) models.

In such a scenario, the lower central density ($\lesssim 10^8$ g cm^{-3}) of the progenitor leads the C detonating WD to produce an amount of ^{56}Ni generally consistent with what observed in typical SN Ia spectra ($\sim 0.5 - 0.7$ M$_\odot$). On the other side, the explosive nuclear burning at densities above $\sim 10^8$ g cm^{-3} does not contribute to the yields, implying a much lower production of neutron-rich nuclear species (Seitenzahl & Townsley 2017).

To explore the impact of sub-M_{Ch} SN Ia progenitors on the chemical evolution, we test the yield sets from Shen et al. (2018) and Leung & Nomoto (2020a).
In particular, the two papers reflect two different frameworks for sub-M_{Ch} WD progenitors. Shen et al. (2018) adopted the dynamically driven double-detonation (DD) process. In this framework, when two WDs pass by each other, a very small amount of helium from one WD to another is sufficient to ignite He shell detonation that subsequently triggers a C core detonation (due to the tidal forces from the secondary WD). Therefore, this scenario requires a very small He shell mass, which can be approximated by a bare CO WD detonation, as it was done in Shen et al. (2018). In Leung & Nomoto (2020a) instead, the WD encloses a low but non negligible ^{4}He mass (≥ 0.05 M$_\odot$). At the contrary of the dynamically driven DD, this latter scenario allows for both single and double degenerate progenitors, as explained in Leung & Nomoto (2020a).

Shen et al. (2018)

In Shen et al. (2018) 1D, spherically symmetric, centrally ignited detonations of bare CO WDs were simulated. Different models were run for different metallicities (0$\leq Z/Z_\odot \leq$2) and different WD masses (0.8$\leq M_{WD}$/M$_\odot \leq$1.1). Variations in the C/O ratio are also explored.
It has to be noted that the adoption of 1D models in the case of detonation only is not an issue as for models experiencing deflagration: in the case of pure detonation we are not dealing with a heat transfer due to diffusion or convection, which are responsible for a highly textured burning front.

In the remainder of the Section, we mainly consider the metallicity dependent, 1M$_\odot$, C/O=1 model. However, we also see the effects on the nuclesoynthesis of different WD masses. We do not discuss instead the impact of different C/O ratios, since we found it negligible (always $<< 0.1$ dex on the resulting abundance ratios).

Leung & Nomoto (2020a)

Using the same code as for 2D DDT models, Leung & Nomoto (2020a) exploded the simulated WDs using double detonation (DD). In this work, Leung & Nomoto (2020a) studied the effects of different metallicities (0$\leq Z/Z_\odot \leq$5), WD masses ($0.9 \leq M_{WD}$/M$_\odot \leq 1.2$), as well as He shell masses ($0.05 \leq M_{He}$/M$_\odot \leq 0.2$) and shape of the initial He detonation configuration (bubble, ring, spherical).

In our work, we focus on the three metallicity dependent models with different He detonation configurations. In particular, we show mainly the outcomes for the model with spherical detonation (see Tab. 4.8), extending to the other models where the results are not similar.
For Leung & Nomoto (2020a) models, we do not focus on mass variation effects, since these are similar to the ones produced by Shen et al. (2018) models.

W7 and WDD2 models

As aforementioned in 4.3.1, most of galactic chemical evolution studies still adopt W7 or WDD2 models. These models were the first able to describe with success the SNe Ia contribution to chemical evolution (e.g. Matteucci & Tornambe 1985; Matteucci & Greggio 1986; Kobayashi et al. 2006) as well as the features of Type Ia SN light curves and spectra (e.g. Hoeflich & Khokhlov 1996).
The models differentiate by the presence or absence of the detonation transition: the W7 model (e.g. Nomoto et al. 1984; Thielemann et al. 1986; Iwamoto et al. 1999) adopts a PTD scheme, while WDD2 (Iwamoto et al. 1999) is a DDT model.

Despite of their success, these models suffer substantial physical limitations. In fact, some model parameters (i.e., propagation flame speed, density at the detonation transition) are fine-tuned to reproduce the observables in both W7 and WDD2. Moreover, the 1D modelling represents an important limitation, since non-sphericity have to be considered in modelling deflagration burning (e.g. Niemeyer et al. 1996).
For these reasons more realistic multi-dimensional models have to be preferred. In fact, in these models different outcomes can be imposed only by different initial conditions (e.g. WD structure and first ignition place).

Anyway, we adopt the outcome of W7 and WDD2 models for comparison with the other yields used in this work. In particular, we show the results obtained with the updated W7 and WDD2 models presented in Leung & Nomoto (2018), with a refined nuclear reaction network relative to the most used version by Iwamoto et al. (1999).

As a summary, in Tab. 4.8 we provide a compilation of the models adopted in this work. In particular, we list the references, the explosion mechanisms and main features of the models introduced in this Subsection.

4.3.3 Chemical evolution models set up

In the following, we describe the models adopted in this work. To understand the influence of SN Ia in the chemical evolution, we adopt models that follow the chemical evolution of the solar neighbourhood.

Table 4.8: *SN Ia models. Horizontal lines divide the standard models adopted in chemical evolution (W7 and WDD2), deflagration-to-detonation transition models (DDT), pure deflagration models (PTD) and double detonation models (DD). For each set, the main parameters of the benchmark model are listed.*

Model	Study	Explosion	Main properties
W7 L18	Leung & Nomoto (2018)	near-M_{Ch} PTD	1D, parameters fine-tuned to match observation, different Z available
WDD2 L18	Leung & Nomoto (2018)	near-M_{Ch} DDT	1D, parameters fine-tuned to match observation
DDT S13	Seitenzahl et al. (2013a)	near-M_{Ch} DDT	3D, different number of ignition sites, WD ρ_c and Z available M_{WD}=1.40 | ρ_c=2.9 $\cdot 10^9$ | C/O$\simeq$1 | ignit. sites=100 | Z=0.01,0.1,0.5,1
DDT L18	Leung & Nomoto (2018)	near-M_{Ch} DDT	2D, centred ignition, different WD ρ_c and Z available M_{WD}=1.38 | ρ_c=3 $\cdot 10^9$ | C/O=1 | Z=0,0.1,0.5,1,2,5
PTD F14	Fink et al. (2014)	near-M_{Ch} PTD	3D, different number of ignition sites and WD ρ_c available M_{WD}=1.40 | ρ_c=2.9 $\cdot 10^9$ | C/O$\simeq$1 | ignit. sites=100 | Z=1
PTD L18	Leung & Nomoto (2018)	near-M_{Ch} PTD	2D, centred ignition, different WD ρ_c available M_{WD}=1.38 | ρ_c=3 $\cdot 10^9$ | C/O=1 | Z= 1
DD S18	Shen et al. (2018)	sub-M_{Ch} DD	1D, bare CO WD, different WD masses, Z and C/O available M_{WD}=1.00 | M_{He}=0.00 | C/O=1 | Z=0,0.25,0.5,1
DD L20	Leung & Nomoto (2020a)	sub-M_{Ch} DD	2D, different WD masses, He shell masses, detonation patterns and Z available M_{WD}=1.00 | M_{He}=0.05 | C/O=1 | det. pattern=spheric | Z=0,0.1,0.5,1,2,5

Notes*: M_{WD}, M_{He} are expressed in $M_\odot$. ρ_c is expressed in g cm^{-3}. Z is expressed in $Z_\odot$.*

In particular, we adopt two different two different models, i.e., the one-infall model (Matteucci & Francois 1989; Grisoni et al. 2018) and the revised two-infall model (Palla et al. 2020b). We make this choice depending on the goal of the discussion. In the first case, we want to stress the differences between SN Ia yields, whereas with the latter model our aim is to reproduce the observational trend for solar vicinity stars.

One-infall model

The one-infall model assumes that the MW disc in the solar vicinity forms by means of a single gas infall episode, forging the thick and thin disc in sequence as a continuous process.

The basic equation that follow the time evolution of G_i, namely the mass fraction of the element i in the ISM, is the usual chemical evolution equation (Eq. (2.15) without galactic winds, see 4.1.1).

In the framework of this model, we fix the SFE ν to 1 Gyr^{-1}, according to previous studies (e.g. Grisoni et al. 2018). For what concerns the IMF, we adopt the one by Kroupa et al. (1993) that allows us to explain most of MW observables (see 2.1.2).

In the gas infall term, we assume a timescale of mass accretion $\tau \simeq 7$ Gyr. This timescale is chosen to reproduce the G-dwarf metallicity distribution in the solar vicinity (Matteucci 2012). For the infall normalisation, we fix the surface mass density of the thin disc in the solar neighbourhood to 54 M$_\odot$ pc^{-2}, in agreement with the values proposed by Bovy & Rix (2013); Read (2014).

Two-infall model

In the two-infall model the solar neighbourhood is assumed to form by means of two distinct infall episodes. In our picture, the first one forms the thick disc, whereas the second (delayed and slower) infall gives rise to the thin disc (see 4.2.3).

The basic equation that describe the time evolution of the elements in the ISM are the same as for the one-infall model, i.e. Eq. (2.15) without galactic winds.

As for the SFR, we adopt different SFE for the first and second infall episodes. In particular, we assume $\nu_1 = 2$ Gyr^{-1} for the first infall and $\nu_2 = 1$ Gyr^{-1} for the second infall, as done in Section 4.2 for models at the solar radius (R$= 8$ kpc). Also for this model, the adopted IMF is the one by Kroupa et al. (1993).

In the gas infall term (Eq. (4.2)), the infall timescales for the thick and thin disc are assumed to be $\tau_1 \simeq 1$ Gyr and $\tau_2 \simeq 7$ Gyr. For what concerns the total surface mass densities that are reproduced by setting A and B parameters, we fix them to 12 M$_\odot$ pc^{-2} for the thick disc and 54 M$_\odot$ pc^{-2} for the thin disc, as those adopted in Section 4.2 for the solar vicinity (R$= 8$ kpc).

Regarding t_{max}, i.e. the time for the maximum mass accretion onto the Galactic disc, we adopt a revised value of 3.25 Gyr for this parameter. In fact, the assumption of a delayed second infall allows us to reproduce APOGEE abundance data (e.g. Palla et al. 2020b; Spitoni et al. 2021) as well as asteroseismic ages (e.g. Spitoni et al. 2020) in the solar neighbourhood.

It is worth reminding that for both the models, we assume a single degenerate (SD) scenario formulation for the SN Ia explosions. In particular, we adopt the SD DTD function by Matteucci & Recchi (2001) (see 2.2.1).
The adoption of Matteucci & Recchi (2001) DTD is made because i) it represents a more than acceptable compromise to describe the delayed pollution from the entire SN Ia population (see, e.g. Matteucci et al. 2009) and ii) allows us to well reproduce the observed SN Ia rate in the MW disc (Cappellaro et al. 1997) within our model framework. Moreover, we remind that our focus in this work is on SN Ia nucleosynthesis rather than on the different DTDs, whose analysis is beyond the scope of this Section.

Nucleosynthesis prescriptions

We extensively talk about SN Ia yields in 4.3.2. However, in the evolution of individual chemical elements yields from other stellar sources have to be considered.
Therefore, the contribution to chemical enrichment by LIMS and CC-SNe (Type II, Ib/c) is computed by taking advantage of detailed stellar yields for these stars.

In particular, the following mass and metallicity dependent stellar yields are adopted:

- for LIMS we use yields by Karakas (2010);
- for massive stars that explode as CC-SNe, we adopt yields by Kobayashi et al. (2006)/ Nomoto et al. (2013). For V and Mn, in some cases we allow the yields to be multiplied by a 1.75 and 3 factor, respectively. This is because the severe uncertainties in the stellar yields (for V, see Kobayashi et al. 2020b) or in the determination of the observed abundances (for Mn, see e.g. Bergemann et al. 2019; Eitner et al. 2020).

4.3.4 Results

In the following we discuss, element by element, the behaviour of several abundance ratios as functions of metallicity ([X/Fe] vs. [Fe/H]) for the different yield sets presented in 4.3.2.

In particular, we show the results for α-element and Fe-peak element abundances. For these latter, which are the main focus of this work, we show the results for the elements in which SNe Ia production is important, i.e., V, Cr, Mn, and Ni.
In addition, we also see which combinations of different SN Ia progenitor yields could

explain the observed abundance ratios involving Fe-peak elements in the solar neighbourhood.

Tracing the different abundance patterns by individual models

Here we show the contribution to the chemical evolution of the different yield sets presented in Tab. 4.8.
The Section is divided into two parts: in the first one, we test the effects of different SN Ia yield sets on [α/Fe] ratios, in which we can directly see the SNe Ia contribution to Fe production (α-elements are underproduced by this SN class). In the second part, instead, we concentrate on the Fe-peak abundances for which the SN Ia production is also relevant.

For this first analysis, we adopt the one-infall model presented in 4.3.3. In fact, this model allows us to highlight and explain better the effects produced by the different SN Ia yields on the abundance patterns, which is the aim of this part. The finding of the best models to fit the observational data is reserved to following discussion, where the more realistic two-infall model is adopted.

However, the one-infall model is able to explain pretty well the observed [α/Fe] vs. [Fe/H] behaviour in the solar neighbourhood stars. This is shown in Fig. 4.22, where a model adopting the standard W7 Iwamoto et al. (1999) yield set is compared to the data from Cayrel et al. (2004); Lai et al. (2008); Yong et al. (2013) (metal poor stars) and Chen et al. (2000); Adibekyan et al. (2012); Bensby et al. (2014) (moderate to metal rich stars). Actually, we note a large spread in low metallicity data, falling both below and above the model track. This can be explained by two facts. Low [α/Fe] data are probably accreted stars from MW satellites that merged with the Galaxy during its first phase of formation (Helmi 2020). The spread around the model track is instead due to the inhomogeneous mixing that affect MW evolution at high redshift (e.g. Cescutti 2008). Nevertheless, this plot shows clearly the so-called "time-delay model" (Matteucci 2001, 2012, see 1.3.1). In fact, Fe pollution from SNe Ia is evident for [Fe/H]$\gtrsim -1$ dex, where the contribution of SNe Ia to chemical enrichment starts to be comparable to that of CC-SNe.

α-elements

For the α-elements, we choose to show the results for magnesium and silicon, since they are two elements where SN Ia contribution is different.
Mg is negligibly produced by SN Ia, since its production comes from hydrostatic carbon burning and explosive neon burning in massive stars (e.g. Woosley & Weaver 1995): in this way, the [Mg/Fe] ratio can be used as a direct indicator of Fe pollution from SNe Ia. On the other hand, Si receives a non negligible contribution from SNe Ia.

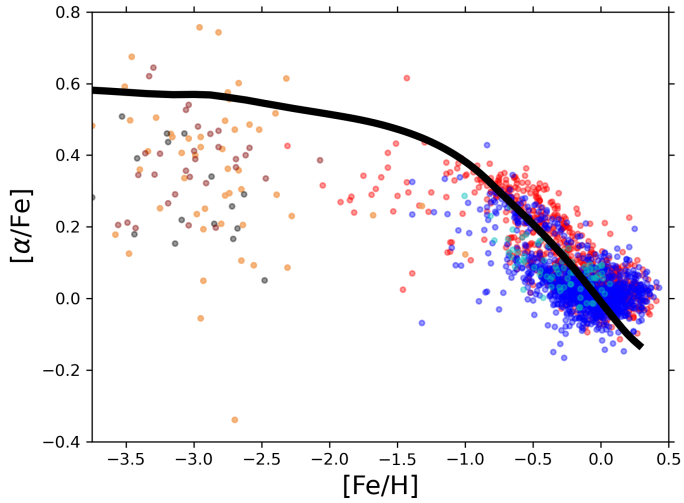

Figure 4.22: *[α/Fe] vs. [Fe/H] predicted by our one-infall chemical evolution model adopting standard W7 Iwamoto et al. (1999) SN Ia yields. Data are from Chen et al. (2000) (cyan points), Cayrel et al. (2004) (maroon points), Lai et al. (2008) (grey points), Adibekyan et al. (2012) (blue points), Yong et al. (2013) (orange points) and Bensby et al. (2014) (red points).*

Magnesium In Fig. 4.23 we show the chemical evolution results for one near-M_{Ch} DDT model (Leung & Nomoto 2018), one near-M_{Ch} PTD model (Fink et al. 2014) and one sub-M_{Ch} DD model (Leung & Nomoto 2020a). In addition, we also plot the abundance pattern obtained using the revised W7 L18 model.
The choice of plotting just few of the model results is made to avoid overcrowding of lines in the Figure. We also plot the results only for [Fe/H]> -1.75 dex since for lower metallicities the effect of SNe Ia on abundance ratios is negligible. The line colors, styles, and thicknesses are organised to simply identify the explosion mechanism, the geometry and the other parameters affecting SN Ia yields. In particular, we plot the PTD models in blue, the DDT models in green and the DD models red, whereas the geometry is treated by plotting solid lines for 1D models, dashed lines for 2D models and dash-dotted lines for 3D ones. In addition, we consider the effect of different central densities (for DDT and PTD models) and explosion patterns (for DD models) by varying the thickness of the lines and giving a shaded effect to the lines not belonging to benchmark sets. The same organisation is adopted for the subsequent Figures.

In Fig. 4.23 we see that the different yield sets provide negligible variations in the abundance ratios, except for the model adopting yields with pure deflagration explosion (blue dashed line). For this latter, we see slightly higher [Mg/Fe] at a certain [Fe/H]: this

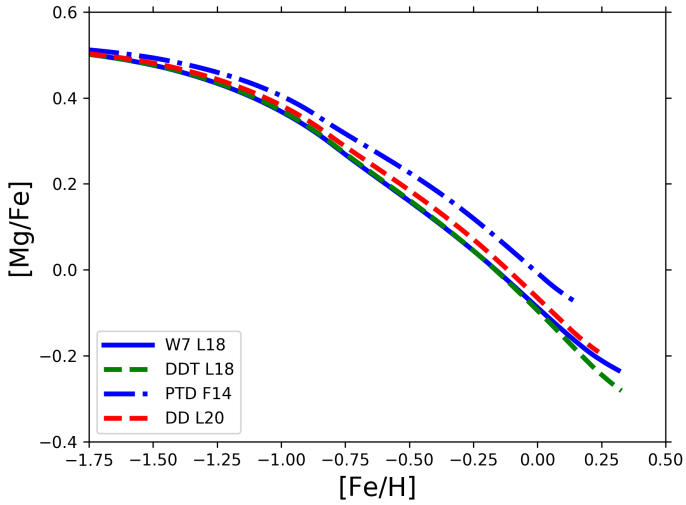

Figure 4.23: *[Mg/Fe] vs. [Fe/H] ratios predicted by our one-infall chemical evolution model adopting different SN Ia benchmark yield sets. Results are shown for W7 L18 (blue solid line), DDT L18 (green dashed), PTD F14 (blue dash-dotted) and DD L20 (red dashed) yields.*

is due to the lower Fe production in PTD models, in which large amounts of C and O remain unburnt (Leung & Nomoto 2018). A similar behaviour is also seen for the other PTD yields tested in this work (Fink et al. 2014; Leung & Nomoto 2018).
On the other side, all the SN Ia yields tested show negligible Mg production: this rules out (or at least make it very unlikely) the hypothesis that larger contributions to Mg production from SN Ia could explain the Mg underestimation at high metallicity in chemical evolution models (see, e.g. Magrini et al. 2017; Grisoni et al. 2018).

The differences in iron production can be also seen by looking at Tab. 4.9, where we list Fe and other Fe-peak elements solar abundances predicted by the revised two-infall model adopting the different yield sets tested in this work. We choose to compare the two-infall model to solar photospheric abundances since, as explained in 4.3.3, this model reproduces in detail the features observed in the solar vicinity.
For Fe, we see that the benchmark near-M_{Ch} DDT and sub-M_{Ch} DD models agree well within 0.1 dex relative to the observed solar abundance (taken from Asplund et al. 2009), whereas PTD yields give lower predicted abundances. However, we have to remind that pure deflagration models are usually considered to be not representative of the whole SN Ia population, but rather of the peculiar SN Iax class (e.g. Kromer et al. 2015). Still regarding the predicted Fe abundance, it must be pointed out that Shen et al. (2018) low-mass sub-M_{Ch} models (0.8 $M_{\odot}$) produce extremely low amount of iron (<0.1 $M_{\odot}$) to be considered as valuable SN Ia progenitor candidates. At the same time, high-mass WD

Table 4.9: *Observed* $\log$*(X/H)+12 solar abundances for Fe-peak elements and predicted abundances by our two-infall model using the different SN Ia yield sets tested. In the upper Table we show the observed photospheric solar abundances by Asplund et al. (2009). In the lower Table we show chemical evolution models abundances taken at* $t = 9.25$ *Gyr in order to take the time at which the protosolar cloud was formed. Horizontal lines divide the standard models adopted in chemical evolution (W7 and WDD2), DDT, PTD, and DD models. The assumed benchmark models are written in bold.*

Observation	Fe/H	V/H	Cr/H	Mn/H	Ni/H
Asplund et al. (2009)	7.50±0.04	3.93±0.08	5.64±0.04	5.43±0.04	6.22±0.04

Model	Fe/H	V/H	Cr/H	Mn/H	Ni/H
W7 L18	7.50	3.64	5.58	5.52	6.36
WDD2 L18	7.48	3.77	5.79	5.35	6.25
DDT S13	**7.48**	**3.64**	**5.64**	**5.46**	**6.37**
DDT S13 (low ρ_c)	7.43	3.69	5.62	5.55	6.24
DDT S13 (high ρ_c)	7.52	3.79	5.74	5.57	6.45
DDT L18	**7.50**	**3.64**	**5.61**	**5.40**	**6.38**
DDT L18 (low ρ_c)	7.50	3.59	5.54	5.18	6.28
DDT L18 (high ρ_c)	7.52	3.96	5.85	5.52	6.42
PTD F14	**7.37**	**3.53**	**5.46**	**5.45**	**6.36**
PTD F14 (low ρ_c)	7.33	3.48	5.41	5.26	6.21
PTD F14 (high ρ_c)	7.38	3.68	5.62	5.49	6.38
PTD F14 (10 ignit. sites)	7.26	3.44	5.36	5.18	6.19
PTD L18	**7.37**	**3.52**	**5.48**	**5.37**	**6.34**
PTD L18 (low ρ_c)	7.30	3.43	5.32	5.10	6.20
PTD L18 (high ρ_c)	7.44	3.92	5.79	5.50	6.39
DD L20 (spheric det.)	**7.44**	**3.61**	**5.43**	**4.85**	**6.13**
DD L20 (bubble det.)	7.45	4.23	5.78	4.95	6.18
DD L20 (ring det.)	7.48	3.97	5.41	4.78	6.17
DD S18 (1 $M_\odot$)	**7.42**	**3.55**	**5.61**	**5.04**	**6.11**
DD S18 (0.8 $M_\odot$)	7.13	3.48	5.36	4.80	5.95
DD S18 (1.1 $M_\odot$)	7.51	3.51	5.54	4.96	6.22
DD S18 (1 $M_\odot$,C/O=0.3)	7.41	3.56	5.63	5.06	6.08

models (1.1 $M_\odot$) show too large ^{56}Ni feedback ($> 0.8\ M_\odot$). Similar results for low and high mass sub-M_{Ch} WD are found for Leung & Nomoto (2020a) models (see also Fig. 9 of Kobayashi et al. 2020a). For this reason, in the rest of the Section we will not consider mass variations for the sub-Chandrasekhar models.

Silicon In Fig. 4.24 we can see the effects of the different yield sets on the [Si/Fe] vs. [Fe/H] plot. At variance with Mg, in this case there is not a distinction on the results based on the explosion mechanism. Sub-M_{Ch} yields of Shen et al. (2018) provide a larger [Si/Fe] yield relative to those from Leung & Nomoto (2020a) (for all the different He detonation trigger). The reason of a higher Si yield can be found in a more incomplete burning that leads to larger production of IMEs and light Fe-peak elements (Leung & Nomoto 2020a; Kobayashi et al. 2020a). Also DDT and PTD models show visible differences in the resulting [Si/Fe] vs. [Fe/H] relations. However, the described variations in the final abundance ratios are limited to the order of $\sim$0.1 dex.
For what concerns PTD models, we note that [Si/Fe] abundance tracks are similar, where not lower, to those of the models with other explosion mechanisms. This means that the [Si/Fe] yields for PTD models are similar to those of DDT or sub-M_{Ch} DD models: this means that the lack of Fe is compensated by a smaller Si production.

A similar general picture can be found for other IMEs (e.g., S, Ca), since most of the IME isotopes are produced during the detonation phase (see Fig. 7 of Leung & Nomoto 2018).

Fe-peak elements

SNe Ia have a central role in Fe-peak elements pollution. In fact, for some of these elements SNe Ia represent the main site of production. In this study, we consider Fe-peak elements for which SN Ia production has a significant impact on the abundance patterns. These elements are vanadium, chromium, manganese, and nickel.

The ranges of values for [X/^{56}Fe] (where X is the most abundant isotope for V, Cr, Mn, and Ni) covered by the different SN Ia yields tested in this work for solar metallicity have been already presented in Fig. 2.4. Reminding that Figure, it is worth noting that not only the SN Ia pollution is important for these elements, but also that yields are spanning even more than an order of magnitude in the abundance ratios.
Fig. 2.4 shows also model yields for other Fe-peak elements, which generally present lower [X/^{56}Fe] fractions. In fact, for some of the Fe-peak elements it is claimed a predominant CC-SN production (e.g., Cu, Co; see Ernandes et al. 2020). Moreover, for some other elements severe problems are encountered in reproducing the observed trends (e.g. Ti, Sc; see Romano et al. 2010; Prantzos et al. 2018). For these reasons, we decide to not consider other Fe-peak elements than V, Cr, Mn, and Ni in our analysis.

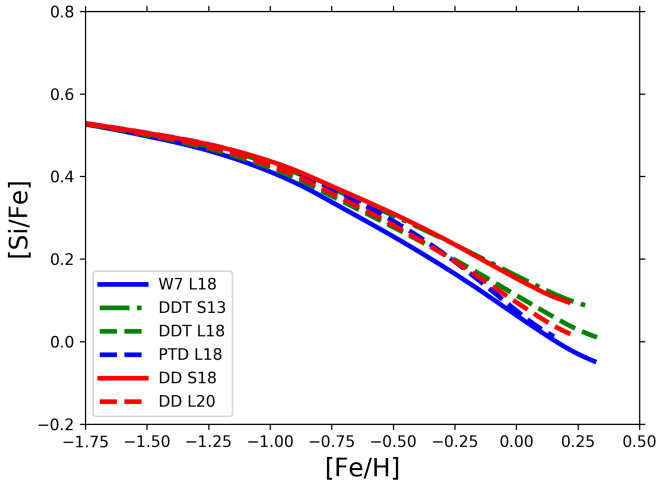

Figure 4.24: *Same of Fig. 4.23, but for [Si/Fe]. Results are shown for W7 L18 (blue solid line), DDT S13 (green dash-dotted), DDT L18 (green dashed), PTD L18 (blue dashed), DD S18 (red solid) and DD L20 (red dashed) yields.*

Vanadium The contribution of different SN Ia yield sets to [V/Fe] vs. [Fe/H] is shown in Fig. 4.25. As can be seen in the upper panel, all our benchmark models show a first decreasing and then an almost flat trend with metallicity, with only the WDD2 model showing slightly larger [V/Fe] values. We also see that the models shown in Fig. 4.25 upper panel exhibit subsolar trends for [V/Fe]. These trends are reflected in the predicted solar abundances for the benchmark yields in Tab. 4.9 (bold lines).
However, part of this results may be due to the uncertain CC-SN contribution to V chemical enrichment (we will come back later on this).

In Fig. 4.25 lower panel we show the results for different yield sets from the benchmark ones. In particular, we plot the near-M_{Ch} DDT L18 model with larger WD central density (5×10^9 g cm^{-3}) than the benchmark model, the PTD L18 model also with larger central density and the sub-M_{Ch} DD L20 model with bubble He detonation trigger (i.e., with an aspherical detonation pattern).
As we can see, not all the SN Ia yields tested have subsolar [V/Fe]. Rather, highly supersolar [V/Fe] (by $\simeq 0.4$ dex at solar metallicity, see Tab. 4.9) are obtained adopting sub-M_{Ch} DD yields with an aspherical He detonation: spherical symmetry in the He detonation pattern tends to produce less V. This is also a common feature with other light Fe-peak elements (e.g. Cr). By adopting the high density L18 DDT and PTD models (and also the S13 and F14 ones, even if in much less extent) we still see a larger V production than in the benchmark models, although not as much as for DD yields with bubble He detona-

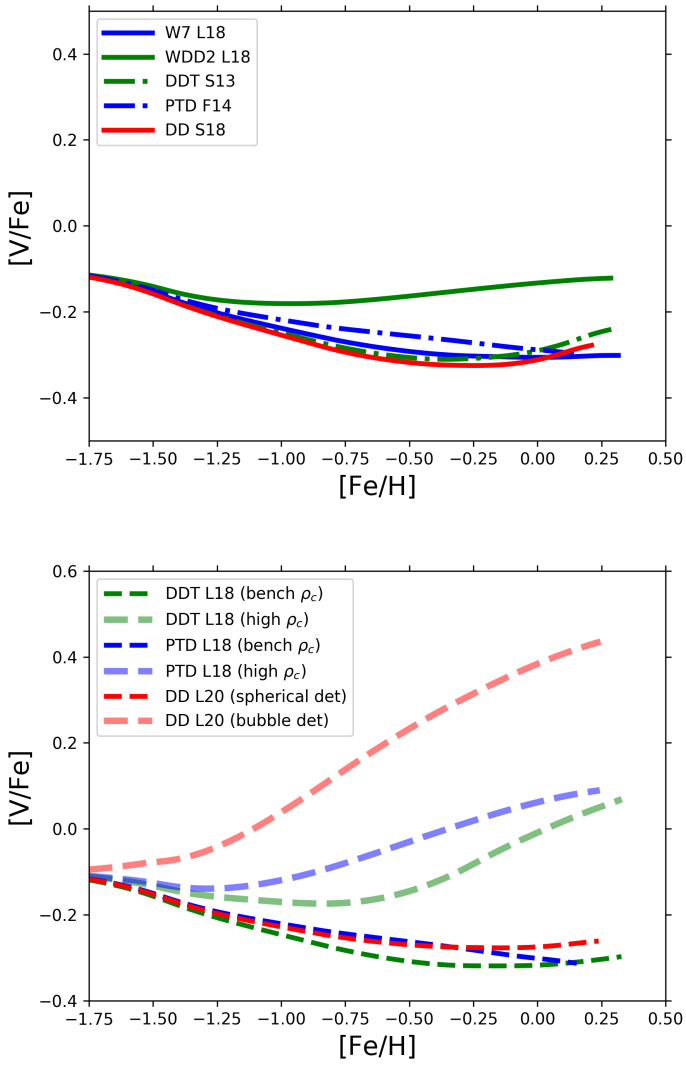

Figure 4.25: *Upper panel: same of Fig. 4.23, but for [V/Fe]. Results are shown for W7 L18 (blue solid line), WDD2 L18 (green solid), DDT S13 (green dash-dotted), PTD F14 (blue dash-dotted) and DD S18 (red solid) yields. Lower panel: variations in [V/Fe] vs. [Fe/H] diagram by adopting SN Ia yields with different initial conditions from benchmark models. Results are shown for DDT L18 high density model (shaded green thick dashed line), PTD L18 high density model (shaded blue thick dashed) and DD L20 bubble detonation model (shaded red thick dashed). Results for the correspondent benchmark yields are shown with the usual color code.*

tion. In this case, the larger V production is caused by the much lager zone incinerated by deflagration in high density near-M_{Ch} WD models.

Chromium In Fig. 4.26 we plot the model results for [Cr/Fe] vs. [Fe/H]. Looking at the benchmark SN Ia yield sets in the upper panel, we see that the near-M_{Ch} DDT S13 yields cause a nearly flat chemical track up to supersolar metallicity. The same happens for the S18 sub-M_{Ch} yields. Near-solar but slightly decreasing [Cr/Fe] values with metallicity are obtained by DDT L18 benchmark model, the F14 and L18 PTD models, as well as for the W7 model.
However, we remind that the result coming from W7 yields (also in the updated Leung & Nomoto 2018 calculation) is influenced by a severe overestimation of the ^{54}Cr isotope. In fact, the models predict that almost 10% of the solar Cr is in the form of ^{54}Cr, a factor 4 more than required to reproduce solar abundance ratio of Cr isotopes (Bergemann & Cescutti 2010). A general underestimation of the observed ^{54}Cr/^{52}Cr ratio is instead seen for the sub-M_{Ch} models tested.
For the other yield sets shown in Fig. 4.26 upper panel, the [Cr/Fe] ratio tends to be overestimated (WDD2 L18) or underestimated (sub-M_{Ch}, DD L20) at solar metallicity. This can be also seen by looking at Tab. 4.9.

To check if the WD initial conditions in the simulated SN Ia have an important impact on the nucleosynthesis of Cr, in Fig. 4.26 lower panel we show the model results for near-M_{Ch}, DDT L18 models with different WD central density, and a sub-M_{Ch}, DD L20 model with different He detonation pattern (bubble configuration).
As it happens for V, we see an increment in [Cr/Fe] due to the overproduction of Cr at higher densities (by $\sim$0.25 dex, see also Tab. 4.9). Conversely, a lower Cr production is obtained at lower densities. We highlight that the same behaviour with WD central density is obtained with pure deflagration models. Concerning the sub-M_{ch} DD models, we see that the Cr production is favoured for an aspherical detonation pattern (as for the others light Fe-peak elements).
However, we note that the behaviour of [Cr/Fe] with the WD central density or initial detonation pattern are not the same for different studies. Models with Shen et al. (2018) and Leung & Nomoto (2020a) (benchmark) sub-M_{Ch} yields show a variation of $\gtrsim 0.2$ dex in their solar Cr abundances despite of the same symmetric detonation structure (see also Fig. 39 of Leung & Nomoto 2020a). At the same time, WD central density variations in Seitenzahl et al. (2013a) (and partly in Fink et al. 2014) do not produce a significant [Cr/Fe] enhancement/decrease as in Leung & Nomoto (2018). For these latter cases, the slightly different initial conditions can explain the different behaviour of the yields.

Manganese Manganese has been extensively studied in the astronomical literature. However, the contribution to its production from different types of SNe is still uncertain (e.g. Seitenzahl et al. 2013b; Eitner et al. 2020).

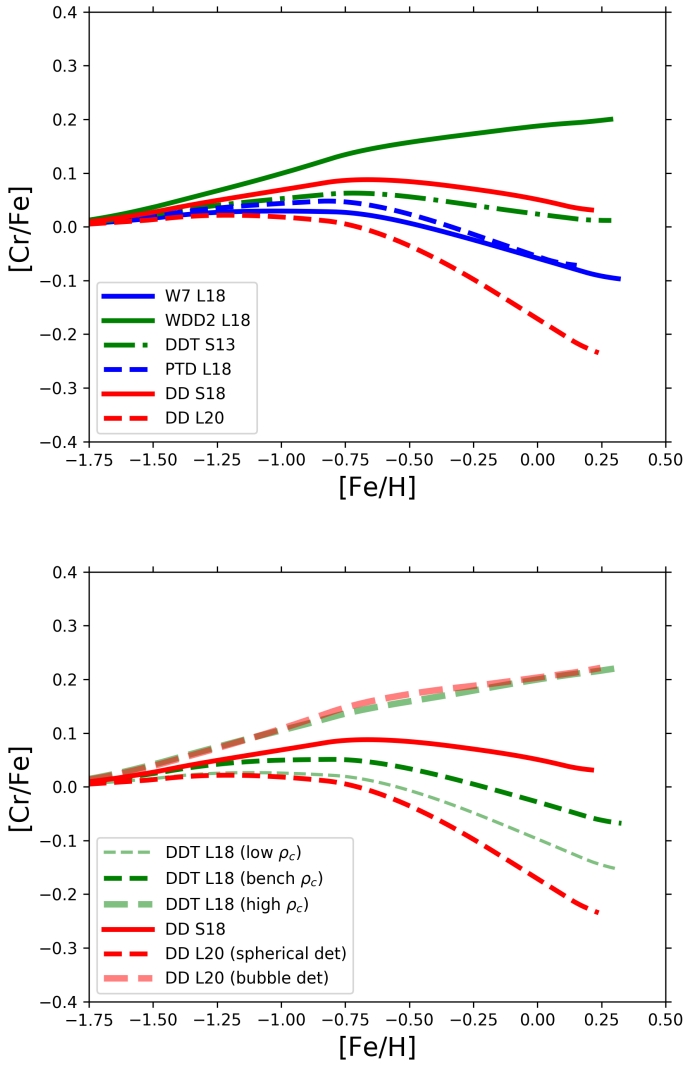

Figure 4.26: *Upper panel: same of Fig. 4.23, but for [Cr/Fe]. Results are shown for W7 L18 (blue solid line), WDD2 L18 (green solid), DDT S13 (green dash-dotted), PTD L18 (blue dashed), DD S18 (red solid) and DD L20 (red dashed) yields. Lower panel: variations in [Cr/Fe] vs. [Fe/H] diagram by adopting SN Ia yields with different initial conditions from the benchmark models. Results are shown for DDT L18 low density model (shaded green thin dashed line), DDT L18 high density model (shaded green thick dashed) and DD L20 bubble detonation model (shaded red thick dashed). Results for the correspondent benchmark yields are shown with the usual color code. DD S18 model (red solid line) is also plotted for comparison with DD L20 benchmark model.*

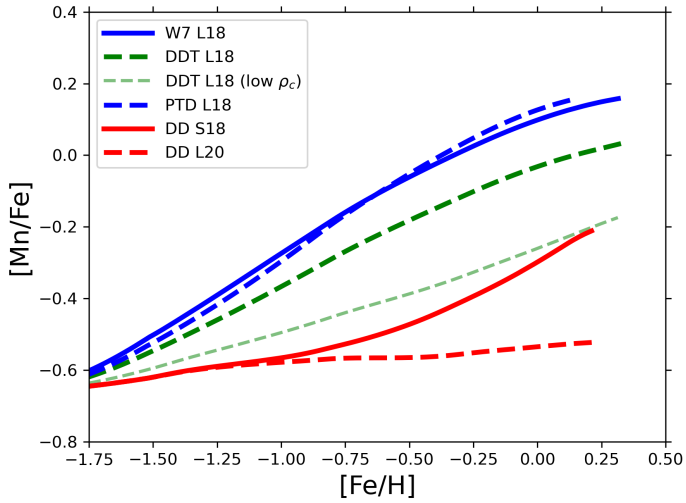

Figure 4.27: *Same of Figure 4.23, but for [Mn/Fe]. Results are shown for W7 L18 (blue solid line), DDT L18 (green dashed), PTD L18 (blue dashed), DD S18 (red solid) and DD L20 (red dashed) yields. In addition, results are shown for the DDT L18 low density model yields (shaded green thin dashed line) for direct comparison with DDT L18 benchmark yields.*

As we can see from Fig. 4.27, the models applying multi-D benchmark yields for near-M_{Ch} DDT and PTD explosion mechanisms show a qualitatively similar behaviour, with [Mn/Fe] jumping from highly subsolar values to solar ones. This is caused by the fact that Mn is mainly synthesised during the deflagration phase in near-M_{Ch} SN Ia (see Fig. 7 of Leung & Nomoto 2018). The same of multi-D models happens for W7 and WDD2 yields, where a similar jump to solar values is seen.
For what concerns sub-M_{Ch} DD models, [Mn/Fe] at solar metallicities is lowered by at least ~ 0.25 dex (see also Tab. 4.9). A similar offset is expected, since the limited electron capture in sub-Chandrasekhar WD explosions (Leung & Nomoto 2020a). An offset is also present between different sub-M_{Ch} yields, with Shen et al. (2018) showing larger [Mn/Fe] values relative to Leung & Nomoto (2020a) (especially when adopting the benchmark/-spherical He detonation configuration).

For what concerns DDT L18 models, we see in Fig. 4.27 that a lower WD central density (i.e. 10^9 g cm^{-3}, that imply a WD mass of 1.33M$_\odot$) leads to subsolar [Mn/Fe] at solar metallicity (see also Tab. 4.9). A similar decrease of [Mn/Fe] with central density is found for PTD L18 models, that however still show larger abundance ratios due to the lack of Fe production.
This deficit in Mn pollution (roughly 0.2 dex) relative to the benchmark models is due to the more massive zones incinerated by detonation instead of deflagration in low density

models. However, as for Cr, this behaviour with WD central density does not hold if we consider Seitenzahl et al. (2013a) yields due to the different conditions in the simulated SNe.

Nickel Nickel is another key element to understand the contribution to the chemical enrichment of the different SN Ia channels (e.g. Kirby et al. 2019). Ni is also one of the main concerns for the W7 model by Iwamoto et al. (1999) in chemical evolution, predicting Ni/Fe ratios much higher than what observed at [Fe/H]$\gtrsim$-1 (Kobayashi et al. 2006; Romano et al. 2010; Prantzos et al. 2018).

In Fig. 4.28, we show the chemical evolution tracks obtained by applying the SN Ia models described in 4.3.2. By looking at the Figure, we note that pure deflagration yields (Fink et al. 2014; Leung & Nomoto 2018) lead the chemical evolution to a rapid increase in [Ni/Fe] between [Fe/H]$\sim$-1.25 and [Fe/H]$\sim$-0.75. The enhancement in Ni is less prominent for the benchmark DDT models, similarly to W7 L18 yields.
Regarding the W7 yields, we note that the chemical evolution model adopting the Leung & Nomoto (2018) yield computation (with an updated nuclear reaction network) shows an offset of ~ 0.2 dex at solar metallicity relative to the model adopting the old W7 Iwamoto et al. (1999) version. The difference can be explained by the lower electron capture rates in the updated version (Kobayashi et al. 2020a).
On the contrary, Fig. 4.28 highlights that sub-M_{Ch} yields (Shen et al. 2018; Leung & Nomoto 2020a) are not able to produce supersolar [Ni/Fe] in the chemical evolution pattern, placing the [Ni/Fe] at subsolar values at [Fe/H]=0.

Even if we do not show it in Fig. 4.28, we highlight that DDT and PTD L18 low density models show lower Ni pollution relative to the correspondent benchmark yields, revealing a behaviour that is similar to that of Mn. In this case, however, this fact holds also for the models by Seitenzahl et al. (2013a) and Fink et al. (2014), as can be seen in Tab. 4.9 for the predicted solar abundances.

It is worth noting that the different behaviour seen in the models is due to fact that the Ni yield is strongly dependent on the electron fraction Y_e (and hence on the efficiency of electron capture), as it happens for Mn. As said above for the W7 model, Ni production is disfavoured for higher Y_e (approaching 0.5), a condition that is found in sub-M_{Ch} models due to their lower densities. This dependence on Y_e also allows the DDT L18 low density model to have a lower [Ni/Fe] yield.
In the case of multi-D PTD models instead, the [Ni/Fe] yield is enhanced relative to DDT models, since ^{58}Ni tend to be overproduced because of the lower ^{56}Fe mass.

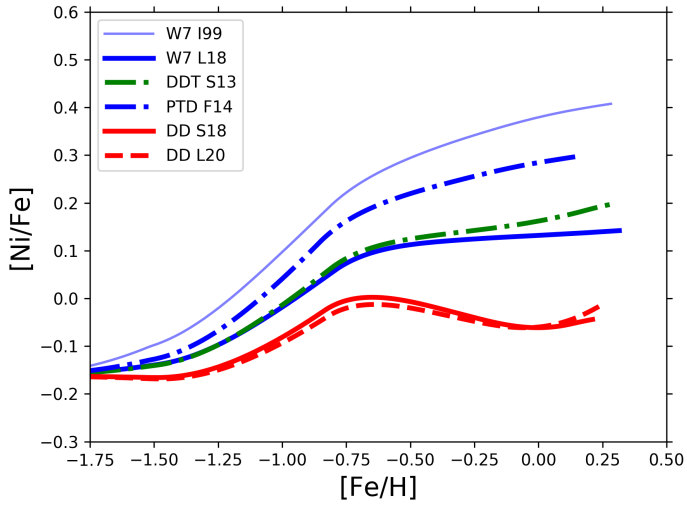

Figure 4.28: *Same of Figure 4.23, but for [Ni/Fe]. Results are shown for W7 L18 (blue solid line), WDD2 L18 (green solid), DDT S13 (green dash-dotted), PTD F14 (blue dash-dotted) and DD S18 (red solid) yields. In addition, results are shown for W7 Iwamoto et al. (1999) yields (W7 I99, shaded blue thin solid line) for direct comparison with the updated Leung & Nomoto (2018) version.*

Reproducing MW observations

Having tested how the nucleosynthesis of different SN Ia explosion mechanisms affects the chemical evolution, it is of great interest to study if a combination of them can improve the agreement between chemical evolution models and observed abundances.

Lightcurve and abundance observations of individual SNe Ia show characteristics typical of different subclasses (e.g. Kirby et al. 2019; de los Reyes et al. 2020), suggesting that SNe Ia explode through different mechanisms. Moreover, studies on SN Ia rate (e.g. Maoz et al. 2014) and on WDs population in the solar vicinity (Gentile Fusillo, private communication) advocate similar conclusions, with some fraction of sub-M_{Ch} progenitors that seems necessary to explain the inferred features.
Some recent works aimed at assessing the role of different SN Ia progenitors in the framework of chemical evolution, but most of them focused only at single elements, such as manganese (e.g. Seitenzahl et al. 2013b; Eitner et al. 2020), or looked at other systems, mostly dwarf MW satellites (e.g. Kobayashi et al. 2015; Cescutti & Kobayashi 2017).

Here we concentrate our analysis on Fe-peak elements, and in particular to V, Mn, Cr and Ni, which show the most significant variations between different SN Ia models (remember Fig. 2.4).
The different progenitor combinations tested are shown in Tab. 4.10, where in the first

Table 4.10: *Combination of near-M_{Ch} and sub-M_{Ch} SN Ia progenitors tested in this work. The rightmost column shows the suffix placed to indicate variations from near-M_{Ch} DDT L18 and sub-M_{Ch} DD L20 benchmark models.*

Model	Combination	Variation suffix
100n	100% near-M_{Ch} DDT	
75n-25s	75% near-M_{Ch} DDT - 25% sub-M_{Ch} DD	l=low ρ_c DDT L18 model
50n-50s	50% near-M_{Ch} DDT - 50% sub-M_{Ch} DD	h=high ρ_c DDT L18 model
25n-75s	25% near-M_{Ch} DDT - 75% sub-M_{Ch} DD	b=bubble detonation DD L20 model
100s	100% sub-M_{Ch} DD	

column we list the model names for the specific progenitor combinations, indicated in the second column. As we can see in the Table, we look at the combinations of near-M_{Ch}, DDT yields with sub-M_{Ch}, DD yields. As mentioned in 4.3.2, multi-dimensional near-M_{Ch} PTD models are likely to be representative of SNe Iax, which very likely leave a remnant, have weak explosions and low ejecta masses. Therefore, this peculiar may not be important for chemical enrichment compared to other explosion models (e.g. Leung & Nomoto 2018; Kobayashi et al. 2020b).

For this analysis, we adopt the yields by Leung & Nomoto (2018) (for DDT models) and Leung & Nomoto (2020a) (DD models), due to their deep exploration of the parameter space.
In fact, in Leung & Nomoto (2018) the WD central density/mass was varied in different DDT models. Such variations are consistent, for example, with those allowed for the SD scenario, where the WD central density/mass are strictly connected to the accretion rate from the non-degenerate companion star (e.g. Nomoto et al. 1994; Leung & Nomoto 2018). At the same time, in Leung & Nomoto (2020a) DD models multiple types of detonation-triggers were investigated. These models leave abundance patterns of most characteristic iron-peak elements for sub-M_{Ch} SNe Ia (Mn, Ni) which are compatible with the sub-M_{Ch} scenario, but also show very different patterns for other Fe-peak elements. The adoption of these different yield sets is indicated with a suffix in the model name, for which a list in the third column of Tab. 4.10 is shown.

At variance with the previous analysis on individual yield sets, here we apply the yields to the revised two-infall model presented and adopted in Section 4.2.
It is worth reminding that this model describes the abundances, as well as stellar ages, observed in the solar neighbourhood. In particular, such a model is able to explain recent APOGEE (Hayden et al. 2015) and APOKASC (Silva Aguirre et al. 2018) data (see Section 4.2). Moreover, the revised two-infall model predicts a present-day star formation rate (SFR) density in line with that observed in the solar vicinity. In particular, the predicted value for SFR is:

$$SFR_{predicted} = 4.34\,\mathrm{M_\odot\,pc^{-2}\,yr^{-1}},$$

which is in good agreement with the range of values given by Prantzos et al. (2018):

$$SFR_{observed} = 2 - 5\,\mathrm{M}_\odot\,\mathrm{pc}^{-2}\,\mathrm{yr}^{-1}.$$

To reach our goal of understanding if and in case which combination of different SN Ia progenitors could explain the observed MW abundance trends, our two-infall model results are compared with several literature abundance ratios. We adopt as for α-elements (Fig. 4.22) the abundances of Chen et al. (2000) (for Mn we adopt a subsample of Nissen et al. 2000 corresponding to Chen et al. 2000 stars); Adibekyan et al. (2012) and Bensby et al. (2014) for moderate to high [Fe/H] stars. For metal poor halo-thick disc stars we use instead the measurements from Lai et al. (2008) and Ou et al. (2020).
In addition, we consider non-LTE (NLTE) corrected measurements from Bergemann & Cescutti (2010); Battistini & Bensby (2015) and Eitner et al. (2020). In fact, for several Fe-peak elements, NLTE effects in neutral lines were found to be large, especially in the metal-poor regime. This may cause a substantial change in the chemical evolution picture of the element.

To assess quantitatively the best models in reproducing the abundance data trend, we perform a statistical test. In this way, we determine the best yield combinations to reproduce each abundance diagram (V, Cr, Mn, Ni) as well as the overall best yield set for the Fe-peak elements tested here.

In particular, we run a quasi-χ^2 diagnostic, defined in this way:

$$\chi^2 = \frac{1}{N}\sum_{n=1}^{N}\sum_{i=1}^{I}\left(\frac{X_{dat;n,i} - X_{mod;n,i}}{\sigma_{dat;n,i}}\right)^2, \tag{4.10}$$

where the sum is calculated over the N data points in the abundance diagram (index n) and the observables [X/Fe] and [Fe/H] (index i). Since there is more than one [X/Fe] value for a certain [Fe/H] (see, e.g. Fig. 4.17 upper panels), it becomes ambiguous to associate an observed data point in the abundance space to a point on the model track. As in Spitoni et al. (2020), we associate a data point to the closest point in the curve. Given a data point $X_{dat;n,i}$, this is done by defining this function:

$$S_n = \min_j\left\{\sqrt{\sum_{i=1}^{I}\left(\frac{X_{dat;n,i} - X_{mod;n,i,j}}{\sigma_{dat;n,i}}\right)^2}\right\} = \\ = \sqrt{\sum_{i=1}^{I}\left(\frac{X_{dat;n,i} - X_{mod;n,i,j'}}{\sigma_{dat;n,i}}\right)^2}, \tag{4.11}$$

where j are the runs over the different points on the curve. Hence, the closest point on the curve is $X_{mod;n,i} = X_{mod;n,i,j'}$.

Having computed the quasi-χ^2 for each abundance diagram, the results are then summed to obtain the overall data-model agreement.

Since the severe uncertainties for V and Mn determination at low metallicity (see later), we repeat the process for two times, one time adopting standard CC-SN yields (from Kobayashi et al. 2006) and another time using modified CC-SN yield values that account for the observed behaviour at low metallicity. For the same reason, we decide to consider in the calculation only stars from moderate to high metallicity samples. In particular, we adopt the samples of Chen et al. (2000) (Nissen et al. 2000); Adibekyan et al. (2012) and Bensby et al. (2014). In addition, we use Battistini & Bensby (2015) instead of Nissen et al. (2000) and Adibekyan et al. (2012) data in the comparison with the models adopting modified CC-SN yields for Mn.

Vanadium As we have seen in Fig. 4.25, the largest variations in the chemical evolution of vanadium are not driven by the different types of explosion mechanisms (i.e., PTD, DDT, DD). The main reason of the spread of the models in [V/Fe] is due to the initial condition of the exploding WD.
This is particularly evident for sub-M_{Ch}, DD models, where different He detonation patterns can produce variations in the abundance patterns up to ~ 0.6 dex. In this way, we can use [V/Fe] as an indicator of the asphericity in He detonation in sub-M_{Ch} progenitors (Leung & Nomoto 2020a).

In Fig. 4.29 we show the results for different combinations of SN Ia progenitors. In particular, in the upper panel we look at the V evolution adopting standard CC-SN yield from the literature (Kobayashi et al. 2006), which agree well with [VI/Fe] measurements at low-metallicity (Ou et al. 2020, light grey area). However, the vanadium abundance from VI lines is probably underestimated by at least ~ 0.1 dex (Scott et al. 2015): for this reason, in Fig. 4.29 lower panel we provide the results for models with vanadium CC-SNe yields multiplied by a 1.75 factor. This change provide better agreement with [V/Fe] inferred from VII lines at low metallicity (Ou et al. 2020, grey area), that should be less affected by NLTE effects. Unfortunately, no NLTE measurements are at disposal for V to confirm what just said; however, we know that V should be predominantly singly-ionised in stellar atmosphere due to its low ionisation energy (Scott et al. 2015) and hence VII abundances should not suffer of particular underestimation.
In both panels, we note the characteristic loop feature of the models presented in Section 4.2. It is worth reminding that this behaviour is the consequence of a delayed second infall, which dilutes the local ISM of primordial gas lowering the [Fe/H] ratio and leaving the [X/Fe] unchanged. The metal abundance is then restored thanks to the star formation (see also Spitoni et al. 2019).

Coming back to the effect of SN Ia yields on V chemical evolution, we see that both

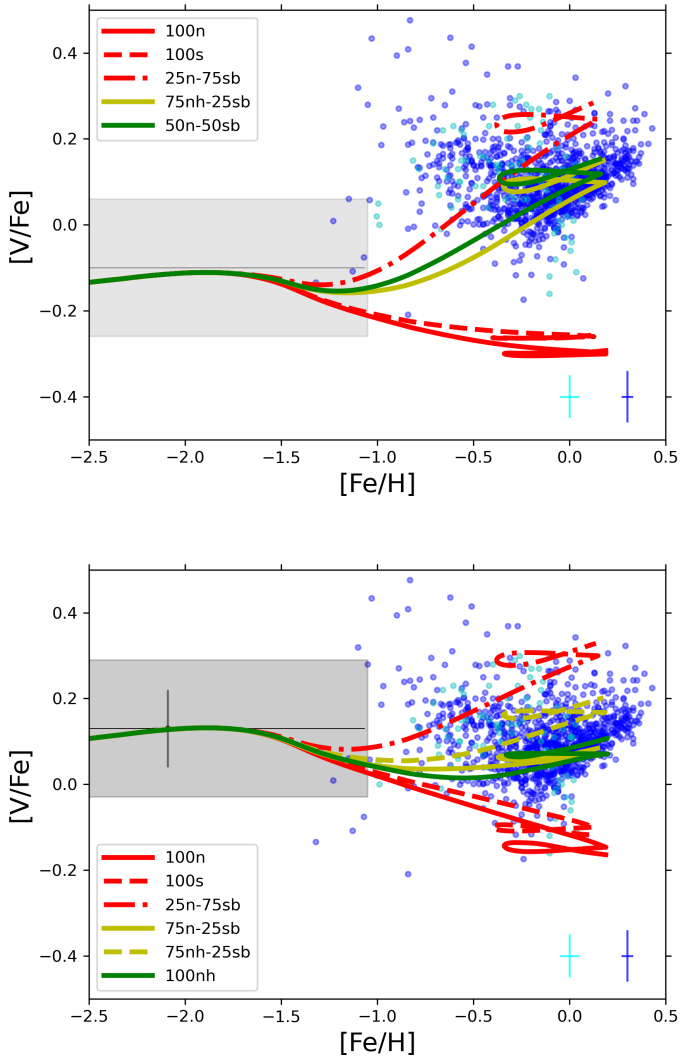

Figure 4.29: *[V/Fe] vs. [Fe/H] ratios predicted by our two-infall chemical evolution model adopting different combinations of different SN Ia progenitor yield sets (see Tab. 4.10). Green lines stand for the best models obtained by the statistical test; yellow lines indicate other models able to explain the observed data trend; red lines represent models with bad agreement with the observations. Upper panel: results for model with standard CC-SN yields from Kobayashi et al. (2006). Lower panel: results for model with vanadium CC-SN yields multiplied by a 1.75 factor. Both panels show VI LTE data are Chen et al. (2000) (cyan points) and Adibekyan et al. (2012) (blue points). Cyan and blue errorbars indicate the typical uncertainties in Chen et al. (2000) and Adibekyan et al. (2012) samples. Upper panel shows also VI LTE Ou et al. (2020) sample average value with correspondent rms (light grey line with shaded area). VII LTE data from Lai et al. (2008) (grey points) and Ou et al. (2020) sample average value with correspondent rms (grey line with shaded area) are shown in the lower panel.*

near-M_{Ch} (100n) and sub-M_{Ch} (100s) benchmark yields are not able to reproduce the bulk of the data in both panels of Fig. 4.29. At the same time, a large fraction of sub-M_{Ch} progenitors with aspherical detonation trigger (i.e. bubble detonation) is unlikely, since it raises too much the V abundance. Therefore, models adopting moderate fraction (up to 0.5) of this latter progenitor subclass assure a good agreement with data. In particular, this can be seen for Fig. 4.29 upper panel, where the best model (green line) exhibit a sub-M_{Ch}, bubble detonating SN Ia fraction of 0.5. We also note that a significant contribution from near-M_{Ch} SN Ia progenitors with high WD central density (in particular when we adopt L18 yields) increases the [V/Fe] ratio at high metallicity. In fact, the near-M_{Ch}, high central density set (100nh) results the best to explain the [V/Fe] behaviour when applied to a model with higher V production by CC-SN (lower panel of Fig. 4.29). However, a contribution from sub-M_{Ch} progenitors with aspherical detonation cannot be left out also in this case.

However, all these considerations have to be taken with caution: the severe uncertainties on V abundances at low metallicity do not well constrain the V enrichment from CC-SNe, providing limits on the analysis of SN Ia contribution. Nonetheless, by running models for two different scenarios at low metallicity, we should be able to provide the global picture for this element.

Chromium As for vanadium, the initial conditions for the simulated SN Ia have an important impact on the nucleosynthesis of chromium (Fig. 4.26). For this reason, we can use Cr as an indicator of the detonation pattern for sub-M_{Ch} progenitors (Leung & Nomoto 2020a) and of the WD central density (and hence WD mass) for near-M_{Ch} progenitors (Leung & Nomoto 2018).

Concerning [Cr/Fe] observations, we adopt abundances inferred from LTE CrI lines only for moderate to high metallicities, where NLTE effects are found to be less prominent (~ 0.1 dex, Prochaska et al. 2000). In fact, LTE calculations have revealed severe problems in determining the Cr abundance in metal poor stars, due to the very large offset between values inferred from CrI and CrII (up to 0.5 dex, e.g. Gratton et al. 2003; Lai et al. 2008, see also Figs. 20 and 21 of Kobayashi et al. 2006). For this reason, for [Fe/H]< -1.5 dex, we consider only CrI NLTE abundances or CrII LTE abundances (whose LTE-NLTE offset is much lower than for CrI, Bergemann & Cescutti 2010).
Such data selection provides a good agreement with our chemical evolution model at low metallicity, indicating the reliability of the adopted CC-SN yields for Cr.

Looking at Fig. 4.30, we note that an important fraction (> 0.25) of sub-M_{Ch} progenitors with aspherical detonation is not favoured by the observational constraints (red solid line). At the same time, a little but not negligible fraction of this progenitor class is likely contributing to the enrichment, since the low [Cr/Fe] yield for sub-M_{Ch}, spherical detonation models by Leung & Nomoto (2020a) (red dash-dotted line). However, we must

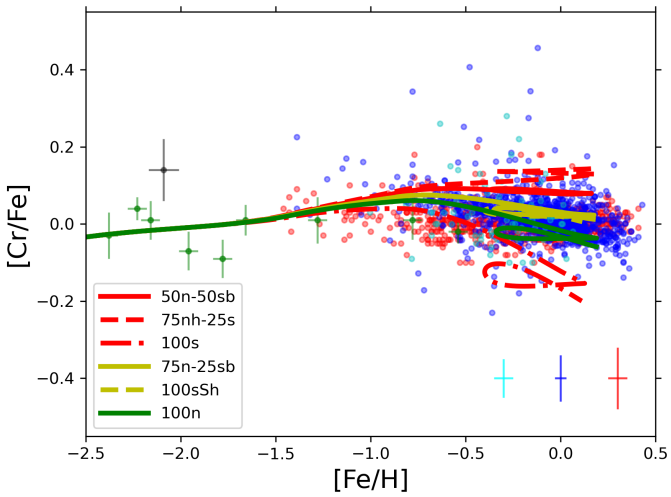

Figure 4.30: *Same of Fig. 4.29, but for [Cr/Fe]. CrI LTE data are from Chen et al. (2000) (cyan points). Mediated CrI+CrII LTE data are from Bensby et al. (2014) (red points). CrII LTE data are from Lai et al. (2008) (grey points with errorbars) Adibekyan et al. (2012) (blue points). Cr NLTE data are from Bergemann & Cescutti (2010) (green points with errorbars). Cyan, blue and red errorbars indicate the typical uncertainties in Chen et al. (2000); Adibekyan et al. (2012) and Bensby et al. (2014) samples. Dashed yellow line (100sSh) adopt DD S18 yields for sub-M_{Ch} progenitors.*

say that sub-M_{Ch}, spherical detonation models by Shen et al. (2018) (indicated as 'sSh' in Fig. 4.30) produces a good agreement with the observations (remember Fig. 4.26).
Concerning near-M_{Ch} progenitors, the data do not favour the scenario in which a considerable fraction of them are high central density/mass WD. Their presence does not allow to reproduce the observational trend, as we can note from Fig. 4.30 (red dashed line). On the contrary, the near-M_{Ch} benchmark model is in very good agreement with the data: this yield set results the best from the statistical test for the [Cr/Fe] vs. [Fe/H] diagram. We have to remember that these considerations about initial conditions for near-M_{Ch} WDs are valid in the case we are adopting Leung & Nomoto (2018) yields. In fact, if we use the yields of Seitenzahl et al. (2013a), we do not see any particular variation in changing the WD density.

Manganese We already saw in Fig. 4.27 that we have substantially different [Mn/Fe] yields for different SN Ia explosion mechanisms. Higher [Mn/Fe] values are obtained using PTD yields relative to DDT ones, which in turn give much larger Mn production relative to DD explosions.
For these differences between different classes of models, Mn is considered one of or

even the most promising element to identify the contributions to chemical enrichment of different SN Ia progenitor classes (e.g. Cescutti & Kobayashi 2017; Eitner et al. 2020; de los Reyes et al. 2020). However, the very different [Mn/Fe] values inferred by the observations over the whole metallicity range limit the conclusions of many of the previous works (e.g. Seitenzahl et al. 2013b). Up to recent years LTE abundances suggested that the [Mn/Fe] is highly sub-solar in low metallicity stars (e.g. Bonifacio et al. 2009). However, in the last years NLTE studies show that Mn lines are severely affected by NLTE effects, suggesting a [Mn/Fe] much closer to solar at low metallicity (Bergemann & Gehren 2008; Bergemann et al. 2019; Eitner et al. 2020, but see also Amarsi et al. 2020).

In Fig. 4.31, we consider the effect of combining near-M_{Ch} DDT and sub-M_{Ch} DD yields. In the upper panel, we show the results of the two-infall model adopting standard CC-SN yields from the literature (Kobayashi et al. 2006). In this panel, low metallicity Mn data obtained in LTE approximation (e.g. Eitner et al. 2020, maroon crosses; Lai et al. 2008, grey crosses) are considered. With these data, [Mn/Fe] exhibits a $\sim$-0.6 dex plateau at low metallicity, with a steep rise after [Fe/H]$\sim$-1 dex.
This trend favours the models in which the majority of SN Ia progenitors are near-M_{Ch} WDs. In fact, the best model from the statistical test (green line), as well as the other models with good data-model agreement (yellow lines), adopt a near-M_{Ch} fraction $\geq$0.75. This is in agreement with Kobayashi et al. (2020a), who claimed a low-to-negligible contribution by sub-M_{Ch} WDs for Mn by using only LTE abundances for Mn analysis.
Finally, we have to say that these results are not particularly affected by the slight underestimation of [Mn/Fe] at low metallicity by the model. In fact, we test whether an increment of 25% of adopted Mn CC-SN yields (which give a better agreement between the models and the observed low metallicity plateau) can change our conclusion, finding no substantial differences.

The situation changes instead in the lower panel of Fig. 4.31, where we consider both Mn data with NLTE corrections (Battistini & Bensby 2015; Eitner et al. 2020) or LTE data from MnII lines (Lai et al. 2008). The choice to include MnII measurements in LTE finds support in the fact that these abundances results very similar to the ones derived in NLTE (e.g. Eitner et al. 2020).
To reproduce the almost solar trend of NLTE data at low metallicity, in Fig. 4.31 lower panel Mn yields from CC-SNe are multiplied by a factor of 3: this operation is actually equivalent to adopt Kobayashi et al. (2006) yields with hypernova fraction ϵ_{HY} =0 (in this work we adopt ϵ_{HY} =1, as in Romano et al. 2010 best model), suggested by Eitner et al. (2020) to reproduce Mn NLTE data. Moreover, we see a difference between the LTE and NLTE observed trends also at moderate to high metallicity ([Fe/H]$\gtrsim -0.5$ dex): the steep rise in [Mn/Fe] up to supersolar metallicities of Fig. 4.31 upper panel is no longer present in the lower panel, thus claiming caution for that trend.
Coming to the prediction of our models, we see that the behaviour of the observational data is followed by models with a majority of sub-M_{Ch}, DD progenitors (50-75%), in

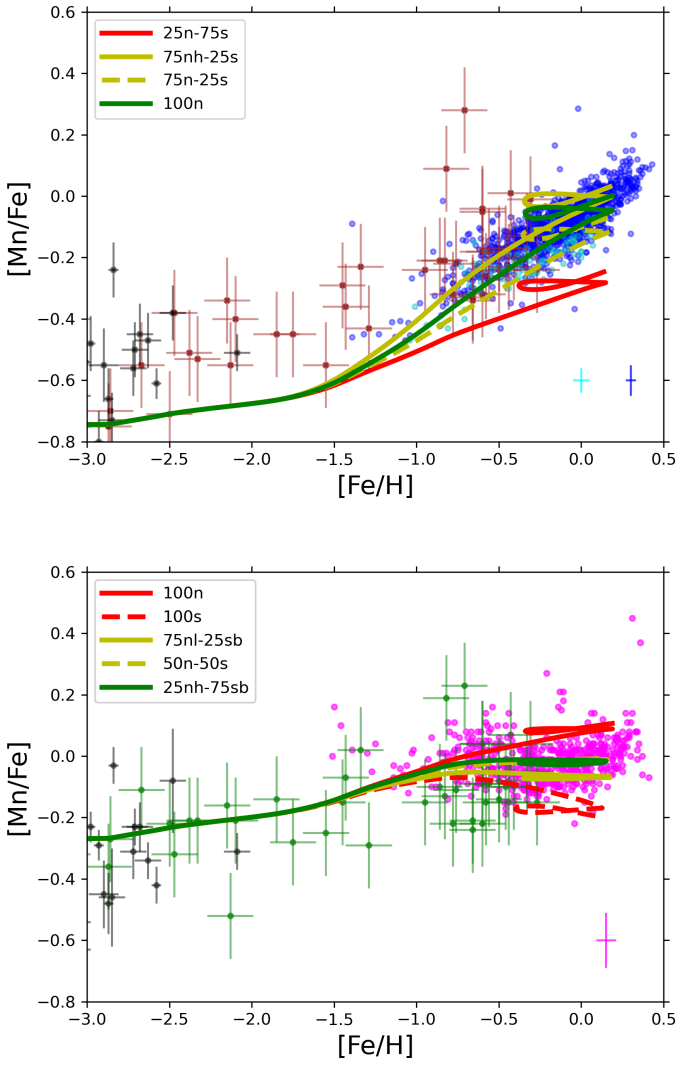

Figure 4.31: *Same of Fig. 4.29, but for [Mn/Fe]. Upper panel: results for model with standard CC-SN yields from Kobayashi et al. (2006). Mn LTE data from Nissen et al. (2000) (cyan points), Adibekyan et al. (2012) (blue points), Lai et al. (2008) (grey crosses with errorbars) and Eitner et al. (2020) (brown dots with errorbars). Cyan and blue errorbars indicate the typical uncertainties in Nissen et al. (2000) and Adibekyan et al. (2012) samples. Lower panel: results for model with manganese CC-SN yields multiplied by a 3 factor. Mn NLTE data are from Battistini & Bensby (2015) (magenta points) and Eitner et al. (2020) (green points with errorbars). MnII LTE data from Lai et al. (2008) (grey points with errorbars). Magenta errorbar indicates the typical uncertainties in Battistini & Bensby (2015) sample.*

agreement with recent results for the MW (Eitner et al. 2020). In fact, the best model resulting from the statistical analysis (green line in Fig. 4.31 lower panel) claims that more than half of SN Ia come from sub-M_{Ch} WD progenitors.
Despite of this, we cannot exclude a larger contribution from SNe exploding via DDT mechanism for two reasons. First, the spread and the uncertainties[10] for NLTE data at low metallicity (see also Amarsi et al. 2020) does not allow to exclude a larger fraction of near-M_{Ch} SNe Ia, even if Battistini & Bensby (2015) data seem also to point towards a significant sub-M_{Ch} SNe Ia contribution. On the other hand, the adoption of a predominant fraction (75%) of SNe Ia exploding via DDT, but with low WD central density and mass (i.e., 10^9 g cm^{-3}, $M_{WD} = 1.33$ M$_\odot$), still assure good agreement with the data of Fig. 4.31 lower panel (see yellow solid line).
However, this is not necessarily against the conclusion of predominant sub-M_{Ch} contribution to explain Mn evolution (e.g. Eitner et al. 2020). DDT L18 models with low WD central density correspond to WD with masses < 1.35 M$_\odot$, which can be in a certain sense still considered as sub-Chandrasekhar masses (Leung & Nomoto 2018). In fact, at masses ~ 1.30 M$_\odot$ the surface He detonation may trigger a C deflagration via shock compression of the central region (Leung & Nomoto 2018). Moreover, as explained before, the abundance pattern of these low density models is much more similar to those of sub-M_{Ch} DD models than of others near-M_{Ch} DDT models. The fact that DDT, low density model by Seitenzahl et al. (2013a) does not show a marked decrease in [Mn/Fe] relative to the benchmark model may worry about what just said. However, it is worth reminding that Seitenzahl et al. (2013a) model is not directly comparable with the scenario seen with Leung & Nomoto (2018) models because of the different WD mass (> 1.35M$_\odot$) and conditions in Seitenzahl et al. (2013a) simulations.

Nickel As happens for Mn, the evolution of [Ni/Fe] vs. [Fe/H] can be also used to identify the relative contribution of the different SN Ia progenitor classes (e.g. Seitenzahl et al. 2013b; Kirby et al. 2019).
In fact, the lower [Ni/Fe] yields for sub-M_{Ch} explosions relative to near-M_{Ch} DDT yields are evident (see Figs. 2.4, 4.28). In turn, these latter are lower than those from pure deflagration models that are indicative of SNe Iax.

From the observational point of view, Ni abundances at disposal are all inferred assuming LTE approximation. Unfortunately, there is little known on departures from LTE of Ni in stellar atmospheres. However, significant variations (> 0.1 dex) from LTE are not expected for Ni lines in the optical range (Scott et al. 2015; Jofré et al. 2015).

[10] it should be noted however that at variance with other works, Eitner et al. (2020) errobars consider not only the error due to the uncertainties in stellar parameters. In fact, they sum in quadrature also the statistical error (reflecting the imperfection in the observational data). Without this latter source of error, the errorbars in Fig. 4.31 would be similar to those of Nissen et al. (2000); Adibekyan et al. (2012) and Battistini & Bensby (2015).

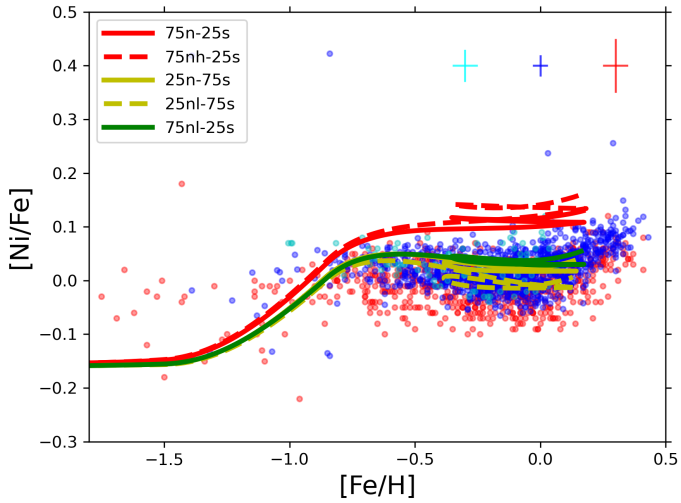

Figure 4.32: *Same of Fig. 4.29, but for [Ni/Fe]. Ni LTE data are from Chen et al. (2000) (cyan points), Adibekyan et al. (2012) (blue points) and Bensby et al. (2014) (red points). Cyan, blue and red errorbars indicate the typical uncertainties in Chen et al. (2000), Adibekyan et al. (2012) and Bensby et al. (2014) samples.*

In Fig. 4.32, we note that models assuming a predominant contribution from benchmark near-M_{Ch} models (e.g., solid and dashed red lines) are not able to reproduce the flat [Ni/Fe] trend from the observations. For this reason, it is suggested a large contribution ($\gtrsim$50%) from sub-M_{Ch} progenitors. This is actually against the recent results by Kobayashi et al. (2020a) on MW Ni evolution, suggesting a much lower contribution by sub-M_{Ch} WD progenitors to the SN Ia population. However, the different result can be explained by the different initial WD chemical composition in the near and sub-M_{Ch} models of Kobayashi et al. (2020a) relative to those of L18; L20[11]. In this way, the models by Kobayashi et al. (2020a) produce less Ni (see Figs. 10, 11 and 24 of Kobayashi et al. 2020a) and this explains why sub-M_{Ch} SNe Ia are not needed.
Coming back to our models, the contribution to the chemical enrichment from sub-M_{Ch}, DD progenitors can be lower if a large fraction of DDT SNe Ia has lower WD progenitor density, as demonstrated by the best model for the [Ni/Fe] vs. [Fe/H] diagram (green line in Fig. 4.32). This is driven by the fact that abundance patterns produced by low density DDT models are similar to those of DD models, as seen for Mn. Nonetheless, we noted in the previous paragraph that this does not alter significantly the conclusion of at least a non marginal role of sub-M_{Ch} progenitors in the chemical enrichment of our Galaxy.

[11] L18; L20 assumed only ^{22}Ne for the Z component of the initial composition, at variance with Kobayashi et al. (2020a) models that adopted a more realistic chemical mixture. For the rest, L18; L20 and Kobayashi et al. (2020a) models share analogous setups.

At variance with Cr and Mn, a decreasing Ni/Fe ratio in the yields is seen also for Seitenzahl et al. (2013a) DDT models. However, we remind that we cannot use Seitenzahl et al. (2013a) low density yields as an additional argument for a sub-M_{Ch} predominance in the SN Ia population. In fact, the conditions in the simulated WD are different than in Leung & Nomoto (2018).

Having performed the analysis on the individual Fe-peak elements, we conclude by looking at the how the chemical evolution models testing different combinations of SN Ia yields behave in a more global picture.
In particular, we show in Fig. 4.33 the overall best models from the statistical test described in this Subsection in comparison with the abundance data shown in previous Figures. The predicted solar abundances for these model are shown instead in Tab. 4.11.

As mentioned earlier, we perform the statistical test twice. First, we determine the best model adopting standard CC-SN yields from the literature (Kobayashi et al. 2006). Then, we apply the test to models adopting enhanced CC-SN yields for V and Mn, that allow us to better reproduce the low metallicity trends found for VII LTE and Mn NLTE data. For the latter element we perform the test with a different sample from that adopted for the models with standard CC-SNe yields (Battistini & Bensby 2015 instead of Nissen et al. 2000; Adibekyan et al. 2012), since the different abundance behavior between LTE and NLTE data even at moderate to high metallicities.

We find in the end that the best model adopting standard CC-SN yields assume an equal distribution of near-M_{Ch} and sub-M_{Ch} SNe Ia. When we adopt the modified CC-SN yields for V and Mn, instead, we find a combination with 75% of near-M_{Ch} and 25% of sub-M_{Ch} models as our preferred scenario. Both the best models suggest the adoption of the sub-M_{Ch} model with bubble He detonation pattern. In the case of the model with modified CC-SN yields, however, we have to note that the near-M_{Ch} fraction is constituted by low central density/mass DDT models by Leung & Nomoto (2018). As explained in this Subsection, these models have very similar yields to sub-M_{Ch} DD ones: this happens in particular for Mn and Ni, which are the most characteristic elements to distinguish between the near-M_{Ch} and the sub-M_{Ch} scenarios. For this reason, the low density DDT model by Leung & Nomoto (2018) can be be also interpreted theoretically in terms of an "alternative" sub-M_{Ch} channel and therefore a very important contribution by the sub-M_{Ch} channel can be seen as very reliable.

The analysis of Fig. 4.33 and Tab. 4.11 gives important insights not only on the side of SN Ia yields but also on the LTE-NLTE matter. We observe in Fig. 4.33 that the best model with modified CC-SN yields, which are tuned to reproduce VII and Mn NLTE data at low metallicity, fits quite well the observed abundance for all the elements considered. This happens at variance with the best model with standard CC-SN yields, for which a ‘golden combination’ to reproduce the observations is not really found. This fact is also seen in

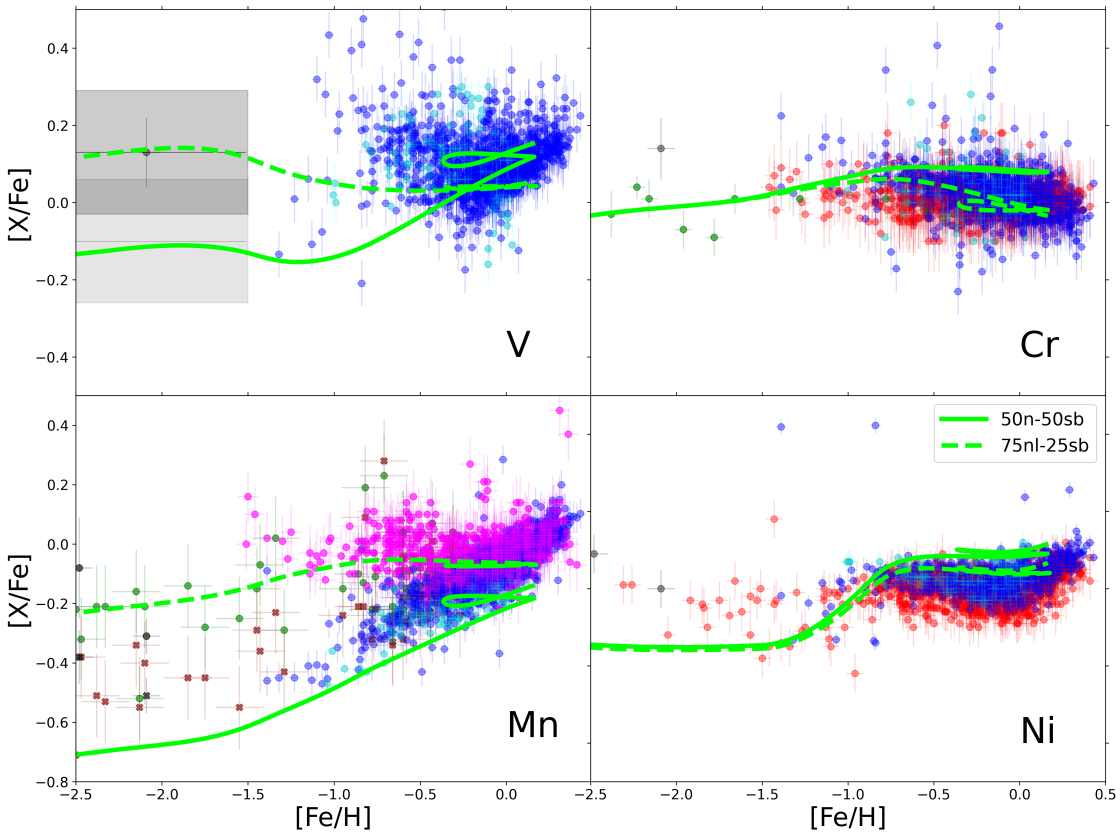

Figure 4.33: *[X/Fe] vs. [Fe/H] ratios predicted by the overall best models obtained adopting the statistical test described in 4.3.4. Light green solid lines indicate the best model for standard Kobayashi et al. (2006) CC-SN yields, while light green dashed lines stand for the best model obtained with modified CC-SN yields for V and Mn tuned to reproduce low-metallicity VII and Mn NLTE data. For the observational data, the colour code is the same as described in Figures 4.29, 4.30, 4.31, 4.32.*

Table 4.11: *Observed* log*(X/H)+12 solar abundances for Fe-peak elements and predicted abundances by our two-infall best models using combinations of SN Ia yield sets. In the upper Table we show the observed photospheric solar abundances by Asplund et al. (2009). In the lower Table we show chemical evolution models abundances taken at* $t = 9.25$ *Gyr in order to take the time at which the protosolar cloud was formed.*

Observation	Fe/H	V/H	Cr/H	Mn/H	Ni/H
Asplund et al. (2009)	7.50±0.04	3.93±0.08	5.64±0.04	5.43±0.04	6.22±0.04

Model	Fe/H	V/H	Cr/H	Mn/H	Ni/H
50n-50sb	7.48	4.03	5.71	5.24	6.31
75nl-25sb$^{(1)}$	7.49	3.95	5.61	5.35	6.26

Notes*:* $^{(1)}$ *values for V and Mn are given adopting modified CC-SN yields tuned to reproduce low-metallicity data (see 4.3.3).*

Tab. 4.11, where the best model for modified CC-SN yields shows better agreement with the observed solar abundances by Asplund et al. (2009).
The obtained results may perhaps indicate that NLTE and singly ionised (XII, with X being a chemical element) abundances at low metallicity should be definitely preferred for Fe-peak elements. In turn, this can also provide tighter constraints on V and Mn CC-SN yields, which behaviour is far to be completely understood (see, e.g. Eitner et al. 2020).

4.3.5 Conclusions

In this Section, we have investigated the effects of a broad compilation of Type Ia SN (SN Ia) yield sets available in the literature on the MW chemical evolution.
In particular, we test the near-Chandrasekhar (near-M_{Ch}) WD, delayed detonation (DDT) yields from Seitenzahl et al. (2013a) and Leung & Nomoto (2018), the near-M_{Ch}, pure deflagration (PTD) yields from Fink et al. (2014) and Leung & Nomoto (2018) (which can be representative of SNe Iax) and the sub-Chandrasekhar (sub-M_{Ch}), double detonation (DD) yields from Shen et al. (2018) and Leung & Nomoto (2020a). These yields are also compared with the "standard" yields adopted in chemical evolution, i.e. the W7 and WDD2 models (in the updated Leung & Nomoto 2018 version). Moreover, we have combined the yields from different progenitor classes (i.e. near-M_{Ch} WD with sub-M_{Ch} WD) to asses the dominant SN Ia class in terms of chemical enrichment.

We have assumed a specific delay-time-distribution function (DTD) for SN Ia, i.e., the single degenerate from Matteucci & Recchi (2001). The results would not have changed if a double degenerate DTD (e.g. Greggio 2005) or a $t^{-\sim 1}$ DTD (e.g. Totani et al. 2008; Maoz & Graur 2017) would have been adopted, since they predict very similar SN Ia rates. The different yield sets and the adopted DTD have been applied to detailed MW chemical

evolution models. In particular, we have run one-infall and two-infall models for MW chemical evolution, in order to highlight the differences between yields in the first case and to better reproduce the observations in the second one.

We have mostly concentrated on elements whose production by SNe Ia is important. In particular, we have looked at vanadium, chromium, manganese, and nickel, where the differences among the SN Ia yield sets adopted in this work are important.
In order to test the results obtained by means of different sets/combination of yields, we have adopted recent observational data from the literature, exploiting NLTE corrected measurements when possible. The best models arising from the comparison between theory and observations are determined also quantitatively by adopting a statistical test.

The main results of this work can be summarised as follows:

- despite of being less physical than more recent multi-dimensional models, W7 and WDD2 models can still be safely adopted in chemical evolution models if the goal of the study is the total abundance of iron or the [α/Fe] vs. [Fe/H] diagram. In fact, Fe yields (and so [α/Fe] ratios) are not particularly different for most of multi dimensional near-M_{Ch} and sub-M_{Ch} yields tested in this work.
  In addition, we substantially rule out the hypothesis of a larger Mg production by SN Ia, as suggested by several works to explain the Mg underestimation at high metallicity by models (e.g. Magrini et al. 2017; Grisoni et al. 2018): all the tested yields predict negligible production of this element;

- only Mn and Ni show a clear distinct behaviour in the abundance ratio vs. metallicity diagram for all the three explosion mechanisms investigated in this work. In particular, pure deflagration (PTD) models produce higher [Mn,Ni/Fe] ratios relative to delayed detonation (DDT) models, which in turn produce higher ratios than double detonation (DD) models.
  In the case of Cr and V, the main differences can be instead caused by the different initial conditions of the exploding WD (WD central density for near-M_{Ch} models, He detonation pattern for sub-M_{Ch} models) or by the different results obtained by different SN Ia simulations sharing similar conditions (e.g. Shen et al. 2018; Leung & Nomoto 2020a);

- by adopting combinations of different SN Ia progenitor classes, we note that the [Ni/Fe] abundance diagram suggests an important contribution ($\gtrsim$50%) by sub-M_{Ch} SNe Ia to Galactic chemical evolution. A similar suggestion can be found for [Mn/Fe] if we consider enhanced CC-SN Mn yields, which best fit NLTE measurements at low metallicity. A minor contribution by double detonating sub-M_{Ch} WD to Ni and Mn can be achieved by adopting DDT yields by Leung & Nomoto (2018) with lower WD central density. The results in this case are almost indistinguishable from the scenario

in which we have a large fraction of sub-M_{Ch} WD combined with benchmark near-M_{Ch} WD models.
In any case, the results for Mn with enhanced yields are in fair agreement with previous work by Eitner et al. (2020). On the other hand, Kobayashi et al. (2020a) claimed a low-to-negligible contribution by sub-M_{Ch} WDs for Mn and Ni. Concerning Mn, we actually found similar results when we adopt standard CC-SN yields, which best fit low metallicity LTE abundances, as done in their paper. For Ni instead, Kobayashi et al. (2020a) different result can be explained by the different (and more realistic) initial WD chemical composition in their SN Ia models, which leave lower [Ni/Fe] yields;

- concerning V and Cr, the comparison with observations suggests that for these two elements a low but non negligible fraction ($\sim$25%) of SNe Ia may come from sub-M_{Ch} WD with an aspherical He detonation pattern (i.e. bubble detonation in the models of Leung & Nomoto 2020a). Even if different near-M_{Ch} models are able to explain the behaviour of the two elements separately, the general picture is better explained by a combination of progenitors including sub-M_{Ch} WDs with bubble detonation.
However, we remind that uncertainties in the abundances observed at low metallicity (for V, Ou et al. 2020) as well as in the SN Ia yields themselves (for Cr, Shen et al. 2018; Leung & Nomoto 2020a) place limits on our analysis of SNe Ia contribution to these elements;

- we see that overall best models for the four Fe-peak elements analysed obtained adopting standard CC-SN yields (Kobayashi et al. 2006) is an equal distribution of near-M_{Ch} and sub-M_{Ch} SNe Ia. When we adopt modified CC-SN yields for V and Mn (to fit low metallicity data), instead, we find a combination with 75% of near-M_{Ch} and 25% of sub-M_{Ch} models. In this case, however, the near-M_{Ch} fraction is constituted by low central density/mass DDT models, which have similar yields to sub-M_{Ch} DD models. Therefore, we obtain very similar results to the case in which we have a predominant fraction of sub-M_{Ch} DD models combined with near-M_{Ch} benchmark DDT models. Concerning the sub-M_{Ch} fraction, both the best models suggest the adoption of models with bubble He detonation pattern.
It is worth noting that the best model with modified CC-SN yields fits quite well the observed abundance for all the elements considered at variance with the best model with standard CC-SN yields. This may indicate that NLTE and XII abundances should be definitely preferred and can provide constraints for V and Mn CC-SN yields.

In conclusion, in this Section we have provided a view of the influence of different SN Ia yields on the chemical evolution of the solar neighbourhood.

It would be natural to extend this study to other environments, such as dwarf MW

satellites (e.g. Kirby et al. 2019; de los Reyes et al. 2020; Kobayashi et al. 2020a) or the Galactic bulge. In this way, we can study in more detail the metallicity dependence of the different SN Ia yields, which in the solar vicinity is limited to a restricted range ($0.1 \lesssim Z/Z_{\odot} \lesssim 2$). Moreover, these objects could be very useful to understand if different environments lead to a different contribution from SN Ia channels or not.

CHAPTER 5

Final remarks

In this Thesis, we have investigated the chemical and dust evolution of the different galactic environments encountered during the cosmic history, from the high-redshift Universe to the Milky Way.
To this aim, in the first part of the Thesis we have concentrated on the study of distant galaxies. In particular, we have focused our attention to high-redshift starburst galaxies and galaxy clusters. Since one of the main issues in studying these systems is accounting for interstellar dust, we have implemented in the models detailed dust treatment in order to unveil the observed properties of these objects. After having considered what happens in moderate to high-redshift environments, in the second part of the Thesis we have moved to the study of the local Universe and in particular of the Milky Way Galaxy. In particular, we have concentrated on the study of the Galactic disc by means of specific chemical evolution models thought to describe the Milky Way disc, aiming at constraining the star formation history and the stellar nucleosynthesis features in our Galaxy.

In the following Sections, we summarize the main results and conclusions of this Thesis and we outline some possible future perspectives.

5.1 Summary and conclusions

As just mentioned, the main results of this Thesis have been splitted in those concerning local objects such as the Milky Way and those regarding moderate to high-redshift systems.

Elements and dust through cosmic evolution

In Chapter 3, we have focused on the chemical and dust evolution of high-redshift starburst galaxies and the dust evolution in galaxy clusters.

To study these objects, dust treatment has been implemented by taking into account different processes that regulate the amount of dust present in the interstellar medium (ISM), i.e., dust formation by stars, dust accretion in cold and dense media and dust destruction by SN shocks. Accounting for interstellar dust is especially important in studies of high-redshift systems and deeply influences our view of the distant universe (e.g. Hauser & Dwek 2001).

High-redshift starbursts are extreme systems with very high star formation rates and thus a turbulent, strongly pressurized ISM. These extreme conditions pose questions on the shape of their initial mass function (IMF), which could deviate from that observed in our local, relatively quiet environment, as well as on the processes regulating the dust cycle in the ISM. For these reasons, we have applied the so-called Integrated Galactic IMF (IGIMF) from Weidner et al. (2011) to chemical evolution models specifically suited to study starburst galaxies and tested the interplay between the IMF and dust in shaping the observed gas abundance patterns, as well as global dust quantities, such as the dust mass (Palla et al. 2020a).
On the other hand, we have a poor knowledge of dust properties within clusters of galaxies, especially in the diffuse intracluster medium (ICM) component. To overcome this, at least partly, we have presented a novel method to compute the redshift evolution of dust mass in galaxy clusters, based on the approach presented by Matteucci & Vettolani (1988) to calculate the galactic contribution to the metals in the ICM. Following this new method, we integrate the predictions of chemical and dust evolution models for individual galaxies over the galaxy cluster luminosity function, assuming suitable cosmological scenarios for the luminosity function evolution (Gjergo, Palla et al. 2020).

IGIMF and dust in high-redshift starbursts

In Section 3.3 we have studied the effects of the Weidner et al. (2011) IGIMF as well as dust condensation of gas metals on the chemical evolution of high-redshift starburst galaxies.

In our analysis we have looked at the effects of the IGIMF on the star formation history and the abundance patterns in these peculiar objects.
In order to test our predictions, we compared the abundance patterns predicted by our models with the abundances observed in high quality spectra of high-redshift starburst galaxies, mainly Lyman Break Galaxies and Lyman-α Emitters.
To this aim, our models take into account dust evolution in the ISM. In fact, the effects of dust depletion can have a strong impact on interstellar abundances and therefore are fundamental to interpret the observed patterns.

It is worth noting that this is the first time that chemical evolution models including a detaild treatment of dust are computed assuming also the IGIMF theory.

The main results obtained can be summarised as follows:

- in all our models, the adoption of the IGIMF causes the increase of the rate of star formation with respect to the "standard" Salpeter (1955) IMF. In particular, the highest SFRs are obtained with the lowest values for the slope of the embedded cluster mass function β, which is a free parameter of the IGIMF. This is a consequence of the behaviour of the IGIMF: the lower is β, the more top-heavy is the IMF.
  On the other hand, we have found a longer duration of the star formation phase for low β values, due to the later occurrence of galactic winds;

- the different star formation histories obtained with different IMFs affect the evolution of chemical abundances. For a given galaxy mass, the more top-heavy the IMF, the faster the growth of the metal content. As for the [α/Fe] vs. [Fe/H] diagram, the lower the β, the higher the overabundance of α-elements, and the higher the metallicity at which the [α/Fe] starts to deviate from the initial plateau (i.e., the knee point);

- the chemical abundances measured in high-redshift, strong star forming galaxies of volatile elements (i.e., those less affected by dust depletion: N, O) are in agreement with our results in which the IGIMF is adopted. However, the large scatter in the available data and the large uncertainties in some of the stellar yields (N in particular) have prevented us from reaching firm conclusions;

- to interpret the observed abundances for refractory elements (C, Mg, Si, Fe), we have used models which can account for differential dust depletion (i.e., different elements depleted into dust in different proportions), and we have tested various assumptions regarding the processes that regulate the evolution of dust grains.
  All the models with minimal dust production tend to underestimate the observed [α/Fe] ratio in the [α/Fe] vs. [Fe/H] diagrams and an extremely top-heavy IGIMF is in better agreement with the observations. On the other hand, if the effects of dust are assumed to be important, our analysis suggests a Salpeter or an IGIMF with $\beta \geq 2$,

i.e. only slightly top-heavier than the Salpeter. In other words, either we need a very top-heavy IMF or a strong dust depletion to reproduce the data;

- we have predicted the evolution of the dust mass with time for galaxies of different stellar mass and IMF, showing that the IGIMF is a possible way to solve the "dust budget crisis" problem, i.e., the lack of dust mass predicted by models in high-redshift galaxies (e.g. Valiante et al. 2014).

Dust in galaxy clusters

In Section 3.3, we have aimed at computing the total cluster dust mass produced by elliptical, spiral, and irregular galaxies, separating the dust residing within galaxies from the dust ejected into the ICM.

In order to do this, we have revised the integration method developed by Matteucci & Vettolani (1988) for metals in galaxy clusters by integrating galaxy-born dust over a parametrization of the cluster luminosity function (LF).
We have tested the cluster dust evolution both in a "monolithic" (where galaxies evolve independently of other galaxies and preserve their number density across cosmic epochs) and in a "hierarchical" scenario of galaxy formation (where the number density of galaxies evolves with redshift). Our model predictions have been then compared to the latest observations of dust in galaxy clusters.

Our main conclusions can be summarised as follows:

- spiral galaxies account for most of the dust contained within clusters in any assumed galaxy formation scenario. Both scenarios provide a present-day dust-to-gas ratio of $\sim 5 \times 10^{-4}$ in galaxy clusters. In particular, most of the dust resides within galaxies, with the ICM component accounting for less than one percent of the total dust mass. In any case, ICM dust estimates are consistent with the dust abundance upper limits measured in the ICM of local (Stickel et al. 2002) and moderate-redshift galaxy clusters (Gutiérrez & López-Corredoira 2017). This suggests that galaxy-born dust is likely the main source of the ICM dust;
- without any need for model parameter calibration, we have been able to produce dust abundances in agreement with observational data. In addition to ICM dust measurments, our integration method is able to reproduce total (ISM+ICM) dust masses and their redshift evolution, as observed by Planck Collaboration (XLIII) et al. (2016). We also have found a marginal improvement of the dust mass redshift dependence by letting our model evolve according to a hierarchical scenario;
- galaxies close to the break of the LF dominate the cluster dust mass. A similar result was found in Gibson & Matteucci (1997) for the gas-phase metals in the ICM.

However, at variance with gas phase metals where early-type galaxies (elliptical/S0) dominate the chemical enrichment, here spiral galaxies govern the dust mass budget. This holds also under the not realistic assumption (see 2.3.1) of strong dust production by Type Ia SNe in elliptical galaxies;

- by varying our model parameters over a reasonable range chosen from literature, we have found that dust masses change by up to a factor of ~ 6 (up to 3 most of the times). All these variations do not affect deeply our conclusions, confirming the robustness of the adopted method.

The local Universe: Milky Way chemical evolution

In the second part of the Thesis (Chapter 4) we have studied the Milky Way (MW) Galaxy, whose investigation is now living a golden era. In particular, we have looked at the evolution of the Galactic discs, devoting our attention to the study of radial gradients and abundance patterns throughout the disc and then to a deeper understanding of the effects of Type Ia SN nucleosynthesis in the model results of the solar vicinity.

On the one hand, the understanding of the star formation history of the MW thick and thin discs is still object of intense debate. Indeed, theoretical models have suggested very different scenarios for the evolution of the MW disc, proposing either a delayed gas accretion episode for the thin disc, two separate and coeval evolutionary sequences for thick and thin discs or stellar migration to explain the observed abundance patterns. In this Thesis, we have tested a scenario based on the two-infall paradigm (e.g. Chiappini et al. 1997), discussing the formation of radial gradients and the so-called [α/Fe] dichotomy/bimodality in the MW disc (Palla et al. 2020b).
On the other side, the modelling of chemical abundance evolution is strictly connected to the stellar yields computed from stellar and SN models and uncertainties on these yields have important effects on the final results. This holds especially for those elements whose origin is not yet fully understood. Therefore, we have decided to probe Type Ia SNe nucleosynthesis in the light of the new Type Ia SN yield outcomes in the last decade (e.g. Seitenzahl et al. 2013a; Leung & Nomoto 2018, 2020a). In particular, we have tested different Type Ia SN progenitors in chemical evolution models for the solar vicinity in order to obtain a more thorough understanding of the "Type Ia SN zoo" (Palla 2021).

Constraints on the Milky Way disc formation

The first results obtained for the MW galaxy (Section 4.2) concern the investigation of the Galactic thick and thin discs by adopting the two-infall model paradigm, i.e., assuming that the thick and thin discs form by means of two infall episodes separated by a period in which star formation decreases.

We have run several models by varying several physical parameters and explored their effects on the present-day gradients along the disc, [α/Fe] vs. [Fe/H] relations, metallicity distribution functions and stellar ages at different Galactocentric distances.
We have compared the model results with abundance gradients from HII regions, young planetary nebulae, Cepheids and young-intermediate age open clusters. Abundance ratios and metallicity distribution functions from APOGEE survey and stellar ages from an APOKASC stellar sample have also been considered.

Moreover, we have computed the evolution of a dwarf galaxy resembling the progenitor of the Gaia-Enceladus-Sausage stars (Belokurov et al. 2018; Helmi et al. 2018) and adopted the predicted abundance pattern as the chemical composition of the infalling gas either for the thick or thin disc.

Our main conclusions can be summarized as follows:

- within our model framework, it is not possible to reproduce the observed abundance gradients along the thin disc only assuming an inside-out formation: besides the inside-out mechanism, we need to assume either radial gas flows and/or efficiency of star formation varying with the Galactocentric distance, in agreement with Grisoni et al. (2018). In particular, our best model assumes constant, moderate radial gas flows and variable star formation efficiency, that also allow us to well match the observed SFR and gas density gradient;

- starting from the above best model, we have allowed the maximum timescale for the infall onto the disc t_{max} to vary as well as the profiles for the thick disc surface mass density Σ_{thick}, since the "classical" two-infall model prescriptions (e.g. Romano et al. 2010) do not produce very good agreement with the recently observed [α/Fe] vs. [Fe/H] abundance patterns throughout the MW disc. Better agreement is reached if $t_{max} = 3.25$ Gyr and the thick disc has a small scale length ($R_d \sim 2$ kpc) exponential profile, in agreement with previous suggestions (e.g. Spitoni et al. 2019; Ciucă et al. 2021);

- even better agreement with data is reached if the infall onto the inner thin disc is enriched at the level of [Fe/H]=-0.5 dex. This can be the effect of mixing between the gas leftover from the formation of the thick disc, Galactic halo, or Galactic bar and the more abundant primordial extragalactic infalling gas;

- the models assuming gas infall for the thin disc enriched as the abundance pattern derived for Gaia-Enceladus-Sausage progenitor (see also Vincenzo et al. 2019) fail in reproducing the abundance relations for the inner Galactic regions. On the other hand, enriched infall during the thick disc formation does not alter significantly the

chemical evolution, opening the possibility that the gas lost by Enceladus or a part of it could have concurred to the formation of the thick disc.

Type Ia SNe in Galactic chemical evolution

Finally, in Section 4.3 we have investigated the effects of a large compilation of Type Ia SN yields available in the literature on the MW chemical evolution.
We have concentrated on elements whose production by Type Ia SNe is important. Besides iron, we have looked at vanadium, chromium, manganese, and nickel, where the differences among the Type Ia SN yield sets adopted in this work are large.

We have tested yields for the near-Chandrasekhar (near-M_{Ch}) WD, delayed detonation (DDT, from Seitenzahl et al. 2013a and Leung & Nomoto 2018), for the near-M_{Ch}, pure deflagration (PTD, which can be representative of peculiar Type Ia SNe, from Fink et al. 2014 and Leung & Nomoto 2018) and yields for the sub-Chandrasekhar (sub-M_{Ch}), double detonation (DD, from Shen et al. 2018 and Leung & Nomoto 2020a) channels. These yields have been also compared with the "standard" Type Ia SN yields adopted in the literature, i.e. the W7 and WDD2 models.

Moreover, we have combined the yields from different progenitor classes (i.e. near-M_{Ch} WD with sub-M_{Ch} WD) in order to asses the dominant Type Ia SN class in terms of chemical enrichment. To this aim, we also compared the model results with recent observations.

The main results of this work can be summarised in this way:

- despite of being less physical than more recent models, W7 and WDD2 models can still be safely adopted in chemical evolution models if the goal of the study is the total abundance of iron or the [α/Fe] vs. [Fe/H] relation. In other words, Fe production in recent yields is similar to previous studies.

- only Mn and Ni show a clear distinct behaviour in the abundance ratio vs. metallicity diagram for the three different explosion mechanisms investigated in this work. In particular, PTD models produce higher [Mn,Ni/Fe] ratios relative to DDT models, which in turn produce higher ratios than DD models.
  In the case of Cr and V, the main differences can be instead caused by the different initial conditions of the exploding WD or by the different results obtained by different Type Ia SN simulations sharing similar conditions (e.g. Shen et al. 2018; Leung & Nomoto 2020a);

- the [Ni/Fe] abundance diagram suggests an important contribution ($\gtrsim$50%) by sub-M_{Ch} Type Ia SNe to Galactic chemical evolution (even if Type Ia SN models with more realistic initial composition indicate a lower contribution, see Kobayashi et al.

2020a). A similar suggestion can be found for [Mn/Fe] if we consider enhanced CC-SN Mn yields relative to the literature ones, which best fit non LTE (NLTE) abundances at low metallicity.
Concerning V and Cr, the comparison with observations suggests that for these two elements a low but non negligible fraction ($\sim$25%) of Type Ia SNe may come from sub-M_{Ch} WD with peculiar initial detonation pattern (see Leung & Nomoto 2020a);

- depending on the assumed CC-SN yields for Fe-peak elements (either from Kobayashi et al. 2006 or with "ad hoc" prescriptions to fit low-metallicity data), the overall best models for the studied Fe-peak elements (V, Cr, Mn, and Ni) need to assume different fractions of near-M_{Ch} and sub-M_{Ch} Type Ia SNe.
The analysis of the best models also suggests that NLTE and singly ionised abundances should be preferred when dealing with the elements studied in Section 4.3.

5.2 Future prospects

Despite of the results obtained in this Thesis, much work is still necessary to better understand the evolution of dust and chemical elements in galaxies.

In the following, we list future perspectives that are intimately linked to the results of this Thesis work.

- The dust evolution models developed in this Thesis rely on literature prescriptions to describe the processes affecting the so-called "dust cycle". However, these prescriptions are not definitive.
  In the last years, a great number of works related to the description of the different dust processes have appeared. For what concerns the stellar dust yields, Marassi et al. (2019) and Ventura et al. (2020, 2021) published new sets of dust masses produced by massive stars and AGB stars, respectively. New prescriptions for ISM dust processes have been also recently presented. As for example, Jones et al. (in prep, see De Vis et al. 2021) obtained new analytical formulae for dust accretion in molecular clouds and the cold neutral medium, whereas Priestley et al. (2022) recently presented new prescriptions for the dust destruction timescale. In addition, chemical evolution models with dust are starting to include other dust processes, such as dust fragmentation (e.g. De Vis et al. 2021) in order to differentiate between small and large grains.
  Therefore, it would be natural to probe all these new prescriptions in consistent chemical and dust evolution models, both for local and high-redshift environments.

- Concerning the IGIMF topic, it is worth noting that some other works support a top-heavy IMF in high-redshift starbursts. In particular, this has been suggested by few studies based on the interpretation of the abundances ratios of rare isotopes such as ^{13}C, ^{17}O and ^{18}O (Romano et al. 2017 and references therein; Zhang et al. 2018).
  In the future it will be important to take into account the latest IGIMF formulation (including the dependence on both the SFR and the metallicity) in models to interpret such measures, and possibly better assess the role of downsizing in the star formation histories of starbursting systems.

- The new IGIMF formulations can be also tested for the MW in the light of recent developments.
  In fact, the clear appearance of a double sequence in the [α/Fe] vs. [Fe/H] diagram even in the most central regions of the Galaxy (see Fig. 4.2, Queiroz et al. 2020) has opened up the possibility of a sort of "continuous" evolution between the MW bulge and disc regions. This is perhaps supported by the results of several authors, who have suggested that the presence of a classical bulge in the MW is minimal (see Wylie et al. 2021). On the other hand, chemical abundance studies of the bulge

have revealed that a top-heavier IMF than those used for the solar neighbourhood is needed to reproduce the observed metallicity distribution and abundance patterns of bulge stars (e.g. Matteucci & Brocato 1990; Ballero et al. 2007; Matteucci et al. 2019).
The study of the IGIMF effects in the MW environment is interesting not only for the pure chemical evolution, but also in the context of dynamical and feedback processes. Therefore, the implementation of the IGIMF on already well-developed hydrodynamical simulations of MW-like galaxies is needed, also for better testing the IGIMF formulation.

- Recently, Bayesian frameworks based on Markov Chain Monte Carlo (MCMC) have been used to test more quantitatively chemical evolution models of galaxies (e.g. Côté et al. 2017; Belfiore et al. 2019). In particular, Spitoni et al. (2020, 2021) applied Bayesian analysis based on MCMC methods to fit two-infall chemical evolution models to stellar abundance and age data for the Galactic disc.
  With the new data progressively coming out thanks to ground-based (e.g. APOGEE; GALAH) and satellite surveys (*Gaia* chemical abundances, even if obtained only with low-intermediate resolution spectroscopy, will be available from DR3) it will be natural to adopt such an approach for future works.

- MCMC methods can be also very useful for dust evolution modelling.
  In fact, Bayesian frameworks have started to be developed for dust evolution models in the analysis of local dust data in the very last years (De Looze et al. 2020; Galliano et al. 2021; De Vis et al. 2021). However, different works have adopted very diverse approaches for likelihood calculations, since the connection between dust data and model predictions is not trivial as for chemical abundances (see, e.g. De Vis et al. 2021).
  This kind of studies will be also encouraged by the new dust survey data (e.g., from JINGLE, DustPedia) expected in the next few years. Moreover, they will be central to asses with a high degree of confidence the roles of the different dust processes in the dust cycle, thus allowing a robust dust implementation in more physical but computationally expensive simulations.

- Concerning our work on Type Ia SNe, it would be natural to extend such a comparative study on stellar yields to other galactic environments. As for example, dwarf MW satellites (see, e.g. Kirby et al. 2019; de los Reyes et al. 2020; Kobayashi et al. 2020a) or the Galactic bulge would be ideal candidates to perform studies of this kind.
  As for example, the metallicity dependence of different Type Ia SN yields can be probed in such different environments: in fact, the metallicity regimes experienced by these systems are much different than that of the solar vicinity. Moreover, the

study of different objects could be very useful to understand if different environments lead to a different contribution from Type Ia SN channels or not.

These are just possible examples of immediate future perspectives related to this Thesis work. However, the panorama is much broader than what written in these few pages.

Next years will bring huge excitement to the astronomical community thanks to the launch of the *James Webb Space Telescope* (JWST, Gardner et al. 2006). Among the fields that will benefit from JWST data, the study of galaxy chemical evolution will become vital to understand the new data coming from the high-redshift Universe. In fact, the particular wavelengths caught by JWST detectors, i.e. from the long visible to the mid-infrared ($\lambda s \sim 0.6 - 28.3$ μm), will allow us to look at the most redshifted object and thus to the formation and evolution of the first primordial galaxies.
On the other side, the wavelengths observed by JWST will be also important on the side of dust modelling for relatively nearby ($z \lesssim 0.5$) galaxies (e.g. Pappalardo et al. 2021), and this will allow further improvements in the dust data to be compared to our models.

Concerning the MW, new large spectroscopic surveys are starting to collect data (e.g. WEAVE, Dalton et al. 2020) or are planned for the next few years (e.g. 4MOST, de Jong et al. 2019). In addition, *Gaia* will continue providing the beautiful dynamical data that are revolutionising our study of the Galaxy for more and more stars. Moreover, the design of extremely high-resolution instruments on future 30m-class telescopes ($R \gtrsim$100000, e.g. HIRES at ELT) will bring further advancement to the field of Galactic archaeology, by delivering abundance data with unprecedent precision, even for the faintest stellar sources.

List of Publications

THE RESULTS shown in this Thesis are part of the product of the research activity that I have carried out during my PhD at the University of Trieste, under the supervision of Prof. Francesca Matteucci.

In particular, the work accomplished during my PhD period yielded the publications listed below:

- Vladilo, G.; Gioannini, L.; Matteucci, F.; **Palla, M.**, "Evolution of the Dust Composition in Damped Ly-α Systems", 2018, ApJ, 868, 13.

- **Palla, M.**; Matteucci, F.; Calura, F.; Longo, F., "Galactic Archaeology at High Redshift: Inferring the Nature of GRB Host Galaxies from Abundances", 2020, ApJ, 889, 4.

- Gjergo, E.; **Palla, M**.; Matteucci, F.; Lacchin, E.; Biviano, A.; Fan, X., "On the origin of dust in galaxy clusters at low-to-intermediate redshift", 2020, MNRAS, 493, 2782.

- Lacchin, E.; Matteucci, F.; Vincenzo, F.; **Palla, M.**, "Chemical evolution of ultra-faint dwarf galaxies: testing the IGIMF", 2020, MNRAS, 495, 3276.

- **Palla, M.**; Calura, F.; Matteucci, F.; Fan, X. L.; Vincenzo, F.; Lacchin, E., "The influence of a top-heavy integrated galactic IMF and dust on the chemical evolution of high-redshift starbursts", 2020, MNRAS, 494, 2355.

- **Palla, M.**; Matteucci, F.; Spitoni, E.; Vincenzo, F.; Grisoni, V., "Chemical evolution of the Milky Way: constraints on the formation of the thick and thin discs ", 2020, MNRAS, 498, 1710.

- Spitoni, E.; Verma, K.; Silva Aguirre, V.; Vincenzo, F.; Matteucci, F.; Vaičekauskaité, B.; **Palla, M.**; Grisoni, V.; Calura, F., "APOGEE DR16: a multi-zone chemical evolution model for the Galactic disc based on MCMC methods", 2021, A&A, 647, A73.

- **Palla, M.**, "The effects of different Type Ia SN yields on Milky Way chemical evolution", 2021, MNRAS, 503, 3216.

List of Figures

List of Tables

Bibliography

Adibekyan V. Z., Sousa S. G., Santos N. C., Delgado Mena E., González Hernández J. I., Israelian G., Mayor M., Khachatryan G., 2012, A&A, 545, A32

Aguado D. S., et al., 2021, MNRAS, 500, 889

Ahn C. P., et al., 2012, ApJS, 203, 21

Ahumada R., et al., 2020, ApJS, 249, 3

Allam S. S., Lin H., Tucker D., Buckley-Geer E., Kubik D., Diehl T., Annis J., Frieman J., 2007, in American Astronomical Society Meeting Abstracts. p. 99.02

Alpher R. A., Bethe H., Gamow G., 1948, Physical Review, 73, 803

Altobelli N., Kempf S., Krüger H., Landgraf M., Roy M., Grün E., 2005, Journal of Geophysical Research (Space Physics), 110, A07102

Amarsi A. M., et al., 2020, A&A, 642, A62

Anders F., 2017, PhD thesis, Doctoral School of Physics, University of Potsdam

Anders F., et al., 2014, A&A, 564, A115

Annunziatella M., et al., 2017, ApJ, 851, 81

Aoyama S., Hou K.-C., Shimizu I., Hirashita H., Todoroki K., Choi J.-H., Nagamine K., 2017, MNRAS, 466, 105

Arendt R. G., et al., 2010, ApJ, 725, 585

Arnett W. D., 1969, Ap&SS, 5, 180

Arnett D., 1996, Supernovae and Nucleosynthesis: An Investigation of the History of Matter from the Big Bang to the Present

Asano R. S., Takeuchi T. T., Hirashita H., Nozawa T., 2013, MNRAS, 432, 637

Asplund M., Grevesse N., Sauval A. J., Scott P., 2009, ARA&A, 47, 481

Baade W., 1951, Publications of Michigan Observatory, 10, 7

Bacchini C., Fraternali F., Iorio G., Pezzulli G., 2019, A&A, 622, A64

Bacon R., et al., 2010, in McLean I. S., Ramsay S. K., Takami H., eds, Society of Photo-Optical Instrumentation Engineers (SPIE) Conference Series Vol. 7735, Ground-based and Airborne Instrumentation for Astronomy III. p. 773508, doi:10.1117/12.856027

Bai L., Rieke G. H., Rieke M. J., 2007, ApJ, 668, L5

Baker A. J., Tacconi L. J., Genzel R., Lehnert M. D., Lutz D., 2004, ApJ, 604, 125

Ballero S. K., Matteucci F., Origlia L., Rich R. M., 2007, A&A, 467, 123

Balser D. S., Wenger T. V., Anderson L. D., Bania T. M., 2015, ApJ, 806, 199

Baratella M., et al., 2021, A&A, 653, A67

Barbuy B., Chiappini C., Gerhard O., 2018, ARA&A, 56, 223

Bastian N., 2008, MNRAS, 390, 759

Battistini C., Bensby T., 2015, A&A, 577, A9

Baugh C. M., Lacey C. G., Frenk C. S., Granato G. L., Silva L., Bressan A., Benson A. J., Cole S., 2005, MNRAS, 356, 1191

Bayliss M. B., Rigby J. R., Sharon K., Wuyts E., Florian M., Gladders M. D., Johnson T., Oguri M., 2014, ApJ, 790, 144

Becklin E. E., Neugebauer G., 1968, ApJ, 151, 145

Bekki K., 2015, MNRAS, 449, 1625

Belfiore F., Vincenzo F., Maiolino R., Matteucci F., 2019, MNRAS, 487, 456

Belokurov V., et al., 2007, ApJ, 671, L9

Belokurov V., Erkal D., Evans N. W., Koposov S. E., Deason A. J., 2018, MNRAS, 478, 611

Bensby T., Lind K., 2018, A&A, 615, A151

Bensby T., Feltzing S., Lundström I., 2003, A&A, 410, 527

Bensby T., Alves-Brito A., Oey M. S., Yong D., Meléndez J., 2011, ApJ, 735, L46

Bensby T., Feltzing S., Oey M. S., 2014, A&A, 562, A71

Bensby T., et al., 2017, A&A, 605, A89

Berg D. A., et al., 2012, ApJ, 754, 98

Bergemann M., Cescutti G., 2010, A&A, 522, A9

Bergemann M., Gehren T., 2008, A&A, 492, 823

Bergemann M., et al., 2014, A&A, 565, A89

Bergemann M., et al., 2019, A&A, 631, A80

Bernard E. J., Schultheis M., Di Matteo P., Hill V., Haywood M., Calamida A., 2018, MNRAS, 477, 3507

Bertin G., Lin C. C., 1996, Spiral structure in galaxies a density wave theory

Bethe H. A., Critchfield C. L., 1938, Physical Review, 54, 248

Bianchi S., Schneider R., 2007, MNRAS, 378, 973

Biermann P., Harwit M., 1980, ApJ, 241, L105

Bilitewski T., Schönrich R., 2012, MNRAS, 426, 2266

Blair W. P., Ghavamian P., Long K. S., Williams B. J., Borkowski K. J., Reynolds S. P., Sankrit R., 2007, ApJ, 662, 998

Bland-Hawthorn J., Gerhard O., 2016, ARA&A, 54, 529

Bocchio M., Jones A. P., Slavin J. D., 2014, A&A, 570, A32

Bocchio M., Marassi S., Schneider R., Bianchi S., Limongi M., Chieffi A., 2016, A&A, 587, A157

Boggess N. W., et al., 1992, ApJ, 397, 420

Boissier S., Prantzos N., 1999, MNRAS, 307, 857

Boissier S., Prantzos N., 2000, MNRAS, 312, 398

Bonifacio P., et al., 2009, A&A, 501, 519

Bonnell I. A., Larson R. B., Zinnecker H., 2007, in Reipurth B., Jewitt D., Keil K., eds, Protostars and Planets V. p. 149 (arXiv:astro-ph/0603447)

Bovy J., Rix H.-W., 2013, ApJ, 779, 115

Bovy J., Hogg D. W., Moustakas J., 2008, ApJ, 688, 198

Bovy J., Rix H.-W., Liu C., Hogg D. W., Beers T. C., Lee Y. S., 2012, ApJ, 753, 148

Bovy J., Rix H.-W., Schlafly E. F., Nidever D. L., Holtzman J. A., Shetrone M., Beers T. C., 2016, ApJ, 823, 30

Bradamante F., Matteucci F., D'Ercole A., 1998, A&A, 337, 338

Bresolin F., Kudritzki R.-P., Urbaneja M. A., Gieren W., Ho I. T., Pietrzyński G., 2016, ApJ, 830, 64

Bryant J. J., et al., 2015, MNRAS, 447, 2857

Buck T., 2020, MNRAS, 491, 5435

Bundy K., et al., 2015, ApJ, 798, 7

Burbidge E. M., Burbidge G. R., Fowler W. A., Hoyle F., 1957, Reviews of Modern Physics, 29, 547

Calura F., Menci N., 2009, MNRAS, 400, 1347

Calura F., Pipino A., Matteucci F., 2008, A&A, 479, 669

Calura F., Pipino A., Chiappini C., Matteucci F., Maiolino R., 2009a, A&A, 504, 373

Calura F., Dessauges-Zavadski M., Prochaska J. X., Matteucci F., 2009b, ApJ, 693, 1236

Calura F., Recchi S., Matteucci F., Kroupa P., 2010, MNRAS, 406, 1985

Calura F., Gilli R., Vignali C., Pozzi F., Pipino A., Matteucci F., 2014, MNRAS, 438, 2765

Calura F., et al., 2017, MNRAS, 465, 54

Calzetti D., 2001, PASP, 113, 1449

Calzetti D., Armus L., Bohlin R. C., Kinney A. L., Koornneef J., Storchi-Bergmann T., 2000, ApJ, 533, 682

Cameron A. G. W., 1957, PASP, 69, 201

Cameron A. G. W., 1982, in Barnes C. A., Clayton D. D., Schramm D. N., eds, Essays in Nuclear Astrophysics. p. 23

Cappellaro E., Turatto M., Tsvetkov D. Y., Bartunov O. S., Pollas C., Evans R., Hamuy M., 1997, A&A, 322, 431

Carollo D., et al., 2007, Nature, 450, 1020

Carollo D., et al., 2010, ApJ, 712, 692

Casagrande L., et al., 2014, ApJ, 787, 110

Casagrande L., et al., 2016, MNRAS, 455, 987

Casasola V., et al., 2017, A&A, 605, A18

Casey C. M., 2016, ApJ, 824, 36

Cautun M., et al., 2020, MNRAS, 494, 4291

Cava A., et al., 2017, A&A, 606, A108

Cavichia O., Mollá M., Costa R. D. D., Maciel W. J., 2014, MNRAS, 437, 3688

Cayrel de Strobel G., Soubiran C., Ralite N., 2001, A&A, 373, 159

Cayrel R., et al., 2004, A&A, 416, 1117

Ceccarelli C., Viti S., Balucani N., Taquet V., 2018, MNRAS, 476, 1371

Cenarro A. J., Gorgas J., Vazdekis A., Cardiel N., Peletier R. F., 2003, MNRAS, 339, L12

Cernuschi F., Marsicano F., Codina S., 1967, Annales d'Astrophysique, 30, 1039

Cescutti G., 2008, A&A, 481, 691

Cescutti G., Kobayashi C., 2017, A&A, 607, A23

Cescutti G., Matteucci F., François P., Chiappini C., 2007, A&A, 462, 943

Chabrier G., 2003, PASP, 115, 763

Chabrier G., Hennebelle P., Charlot S., 2014, ApJ, 796, 75

Chamberlain J. W., Aller L. H., 1951, ApJ, 114, 52

Chaplin W. J., et al., 2020, Nature Astronomy, 4, 382

Chelouche D., Koester B. P., Bowen D. V., 2007, ApJ, 671, L97

Chen Y. Q., Nissen P. E., Zhao G., Zhang H. W., Benoni T., 2000, A&AS, 141, 491

Cheng T., et al., 2019, MNRAS, 490, 3840

Chiappini C., 2001, American Scientist, 89, 506

Chiappini C., Matteucci F., Gratton R., 1997, ApJ, 477, 765

Chiappini C., Matteucci F., Romano D., 2001, ApJ, 554, 1044

Chiappini C., Romano D., Matteucci F., 2003, MNRAS, 339, 63

Chiappini C., et al., 2015, A&A, 576, L12

Chiosi C., 1980, A&A, 83, 206

Chokshi A., Tielens A. G. G. M., Hollenbach D., 1993, ApJ, 407, 806

Chomiuk L., Povich M. S., 2011, AJ, 142, 197

Christensen L., et al., 2012a, MNRAS, 427, 1953

Christensen L., et al., 2012b, MNRAS, 427, 1973

Ciucă I., Kawata D., Miglio A., Davies G. R., Grand R. J. J., 2021, MNRAS, 503, 2814

Clark C. J. R., et al., 2018, A&A, 609, A37

Clarke F. W., 1889, Philisophical Society of Washington Bulletin, 11, 131

Clarke A. J., et al., 2019, MNRAS, 484, 3476

Clarkson W. I., et al., 2011, ApJ, 735, 37

Clayton D. D., 1979, Ap&SS, 65, 179

Clayton D. D., Nittler L. R., 2004, ARA&A, 42, 39

Clayton G. C., Green J., Wolff M. J., Zellner N. E. B., Code A. D., Davidsen A. F., WUPPE Science Team HUT Science Team 1996, ApJ, 460, 313

Clayton G. C., Wolff M. J., Gordon K. D., Smith P. S., Nordsieck K. H., Babler B. L., 2004, AJ, 127, 3382

Clemens M. S., et al., 2010, A&A, 518, L50

Colavitti E., Cescutti G., Matteucci F., Murante G., 2009, A&A, 496, 429

Colzi L., Fontani F., Rivilla V. M., Sánchez-Monge A., Testi L., Beltrán M. T., Caselli P., 2018, MNRAS, 478, 3693

Conroy C., van Dokkum P., 2012a, ApJ, 747, 69

Conroy C., van Dokkum P. G., 2012b, ApJ, 760, 71

Cooray A., et al., 2014, ApJ, 790, 40

Costa R. D. D., Uchida M. M. M., Maciel W. J., 2004, A&A, 423, 199

Côté B., O'Shea B. W., Ritter C., Herwig F., Venn K. A., 2017, ApJ, 835, 128

Crestani J., et al., 2021, ApJ, 914, 10

Cristallo S., Straniero O., Gallino R., Piersanti L., Domínguez I., Lederer M. T., 2009, ApJ, 696, 797

Cristallo S., et al., 2011, ApJS, 197, 17

Cui Y., Xiang Y., Rong K., Feris R., Cao L., 2014, in IEEE Winter Conference on Applications of Computer Vision. pp 213–219, doi:10.1109/WACV.2014.6836098

D'Odorico S., Peimbert M., Sabbadin F., 1976, A&A, 47, 341

Dalton G., et al., 2020, in Society of Photo-Optical Instrumentation Engineers (SPIE) Conference Series. p. 1144714, doi:10.1117/12.2561067

Dame T. M., 1993, in Holt S. S., Verter F., eds, American Institute of Physics Conference Series Vol. 278, Back to the Galaxy. pp 267–278, doi:10.1063/1.43985

Danziger I. J., Lucy L. B., Bouchet P., Gouiffes C., 1991, in Woosley S. E., ed., Supernovae. p. 69

Davé R., 2008, MNRAS, 385, 147

Davies J. I., et al., 2019, A&A, 626, A63

De Cia A., Ledoux C., Mattsson L., Petitjean P., Srianand R., Gavignaud I., Jenkins E. B., 2016, A&A, 596, A97

De Looze I., Barlow M. J., Swinyard B. M., Rho J., Gomez H. L., Matsuura M., Wesson R., 2017, MNRAS, 465, 3309

De Looze I., et al., 2020, MNRAS, 496, 3668

De Masi C., Matteucci F., Vincenzo F., 2018, MNRAS, 474, 5259

De Masi C., Vincenzo F., Matteucci F., Rosani G., La Barbera F., Pasquali A., Spitoni E., 2019, MNRAS, 483, 2217

De Silva G. M., et al., 2015, MNRAS, 449, 2604

De Vis P., et al., 2017a, MNRAS, 464, 4680

De Vis P., et al., 2017b, MNRAS, 471, 1743

De Vis P., Maddox S. J., Gomez H. L., Jones A. P., Dunne L., 2021, MNRAS, 505, 3228

Deason A. J., Belokurov V., Sanders J. L., 2019, MNRAS, 490, 3426

Dell'Agli F., García-Hernández D. A., Schneider R., Ventura P., La Franca F., Valiante R., Marini E., Di Criscienzo M., 2017, MNRAS, 467, 4431

Dessauges-Zavadsky M., D'Odorico S., Schaerer D., Modigliani A., Tapken C., Vernet J., 2010, A&A, 510, A26

Diaz A. I., 1989, in Beckman J. E., Pagel B. E. J., eds, Evolutionary Phenomena in Galaxies. p. 377

Döbereiner J. W., 1829, Annalen der Physik, 91, 301

Doherty C. L., Gil-Pons P., Lau H. H. B., Lattanzio J. C., Siess L., 2014a, MNRAS, 437, 195

Doherty C. L., Gil-Pons P., Lau H. H. B., Lattanzio J. C., Siess L., Campbell S. W., 2014b, MNRAS, 441, 582

Dong H., et al., 2014, ApJ, 785, 136

Dopita M. A., Seitenzahl I. R., Sutherland R. S., Vogt F. P. A., Winkler P. F., Blair W. P., 2016, ApJ, 826, 150

Draine B. T., 2003, ApJ, 598, 1017

Draine B. T., 2009, in Henning T., Grün E., Steinacker J., eds, Astronomical Society of the Pacific Conference Series Vol. 414, Cosmic Dust - Near and Far. p. 453 (arXiv:0903.1658)

Draine B. T., Lee H. M., 1984, ApJ, 285, 89

Draine B. T., Li A., 2007, ApJ, 657, 810

Dressler A., 1980, ApJ, 236, 351

Dwek E., 1998, ApJ, 501, 643

Dwek E., 2004, ApJ, 611, L109

Dwek E., 2016, ApJ, 825, 136

Dwek E., Scalo J. M., 1980, ApJ, 239, 193

Dwek E., Rephaeli Y., Mather J. C., 1990, ApJ, 350, 104

Dye S., Evans N. W., Belokurov V., Warren S. J., Hewett P., 2008, MNRAS, 388, 384

Eitner P., Bergemann M., Hansen C. J., Cescutti G., Seitenzahl I. R., Larsen S., Plez B., 2020, A&A, 635, A38

Elmegreen B. G., 1999, ApJ, 527, 266

Ernandes H., Barbuy B., Friaça A. C. S., Hill V., Zoccali M., Minniti D., Renzini A., Ortolani S., 2020, A&A, 640, A89

Esteban C., García-Rojas J., Peimbert M., Peimbert A., Ruiz M. T., Rodríguez M., Carigi L., 2005, ApJ, 618, L95

Fabian A. C., 2012, ARA&A, 50, 455

Fasano G., et al., 2006, A&A, 445, 805

Ferrara A., Viti S., Ceccarelli C., 2016, MNRAS, 463, L112

Ferrarotti A. S., Gail H.-P., 2006, A&A, 447, 553

Ferreras I., La Barbera F., Vazdekis A., 2016, Astronomy and Geophysics, 57, 2.32

Ferrini F., Matteucci F., Pardi C., Penco U., 1992, ApJ, 387, 138

Field G. B., 1974, ApJ, 187, 453

Fink M., et al., 2014, MNRAS, 438, 1762

Finkelstein S. L., Papovich C., Rudnick G., Egami E., Le Floc'h E., Rieke M. J., Rigby J. R., Willmer C. N. A., 2009, ApJ, 700, 376

Fontanot F., De Lucia G., Hirschmann M., Bruzual G., Charlot S., Zibetti S., 2017, MNRAS, 464, 3812

François P., Matteucci F., Cayrel R., Spite M., Spite F., Chiappini C., 2004, A&A, 421, 613

Franchini M., et al., 2020, ApJ, 888, 55

Fraternali F., Marasco A., Armillotta L., Marinacci F., 2015, MNRAS, 447, L70

Fuhrmann K., 1998, A&A, 338, 161

Gaia Collaboration et al., 2016a, A&A, 595, A1

Gaia Collaboration et al., 2016b, A&A, 595, A2

Gaia Collaboration et al., 2018, A&A, 616, A1

Gaia Collaboration et al., 2021, A&A, 649, A1

Gail H. P., Zhukovska S. V., Hoppe P., Trieloff M., 2009, ApJ, 698, 1136

Gall C., Hjorth J., 2018, ApJ, 868, 62

Gall C., Hjorth J., Andersen A. C., 2011a, A&A Rev., 19, 43

Gall C., Hjorth J., Andersen A. C., 2011b, A&A Rev., 19, 43

Galliano F., et al., 2011, A&A, 536, A88

Galliano F., Galametz M., Jones A. P., 2018, ARA&A, 56, 673

Galliano F., et al., 2021, A&A, 649, A18

Gardner J. P., et al., 2006, Space Sci. Rev., 123, 485

Garnett D. R., Shields G. A., Skillman E. D., Sagan S. P., Dufour R. J., 1997, ApJ, 489, 63

Geller M. J., Diaferio A., Kurtz M. J., 1999, ApJ, 517, L23

Genovali K., et al., 2015, A&A, 580, A17

Giard M., Montier L., Pointecouteau E., Simmat E., 2008, A&A, 490, 547

Gibson B. K., Matteucci F., 1997, MNRAS, 291, L8

Gilmore G., Wyse R. F. G., 1986, Nature, 322, 806

Gilmore G., et al., 2012, The Messenger, 147, 25

Ginolfi M., Graziani L., Schneider R., Marassi S., Valiante R., Dell'Agli F., Ventura P., Hunt L. K., 2018, MNRAS, 473, 4538

Gioannini L., 2017, PhD thesis, Doctoral School of Physics, University of Trieste

Gioannini L., Matteucci F., Vladilo G., Calura F., 2017a, MNRAS, 464, 985

Gioannini L., Matteucci F., Calura F., 2017b, MNRAS, 471, 4615

Gjergo E., Granato G. L., Murante G., Ragone-Figueroa C., Tornatore L., Borgani S., 2018, MNRAS, 479, 2588

Gjergo E., Palla M., Matteucci F., Lacchin E., Biviano A., Fan X., 2020, MNRAS, 493, 2782

Gomez H. L., et al., 2012, ApJ, 760, 96

Gordon K. D., Clayton G. C., Misselt K. A., Landolt A. U., Wolff M. J., 2003, ApJ, 594, 279

Gould R. J., Salpeter E. E., 1963, ApJ, 138, 393

Granato G. L., Lacey C. G., Silva L., Bressan A., Baugh C. M., Cole S., Frenk C. S., 2000, ApJ, 542, 710

Grand R. J. J., et al., 2018, MNRAS, 474, 3629

Grand R. J. J., et al., 2020, MNRAS, 497, 1603

Gratton R. G., Carretta E., Matteucci F., Sneden C., 2000, A&A, 358, 671

Gratton R. G., Carretta E., Claudi R., Lucatello S., Barbieri M., 2003, A&A, 404, 187

Graziani L., Schneider R., Ginolfi M., Hunt L. K., Maio U., Glatzle M., Ciardi B., 2020, MNRAS, 494, 1071

Green D. A., 2014, in Ray A., McCray R. A., eds, IAU Symposium Vol. 296, Supernova Environmental Impacts. pp 188–196 (arXiv:1309.3072), doi:10.1017/S1743921313009459

Greggio L., 2005, A&A, 441, 1055

Grieco V. L., 2015, PhD thesis, Doctoral School of Physics, University of Trieste

Grieco V., Matteucci F., Meynet G., Longo F., Della Valle M., Salvaterra R., 2012, MNRAS, 423, 3049

Grieco V., Matteucci F., Calura F., Boissier S., Longo F., D'Elia V., 2014, MNRAS, 444, 1054

Grisoni V., Spitoni E., Matteucci F., Recio-Blanco A., de Laverny P., Hayden M., Mikolaitis Ŝ., Worley C. C., 2017, MNRAS, 472, 3637

Grisoni V., Spitoni E., Matteucci F., 2018, MNRAS, 481, 2570

Gronow S., Cote B., Lach F., Seitenzahl I. R., Collins C. E., Sim S. A., Roepke F. K., 2021, arXiv e-prints, p. arXiv:2103.14050

Grun E., et al., 1993, Nature, 362, 428

Gunawardhana M. L. P., et al., 2011, MNRAS, 415, 1647

Gutiérrez C. M., López-Corredoira M., 2014, A&A, 571, A66

Gutiérrez C. M., López-Corredoira M., 2017, ApJ, 835, 111

Hainline K. N., Shapley A. E., Kornei K. A., Pettini M., Buckley-Geer E., Allam S. S., Tucker D. L., 2009, ApJ, 701, 52

Hartwick F. D. A., 1987, in Gilmore G., Carswell B., eds, NATO Advanced Study Institute (ASI) Series C Vol. 207, The Galaxy. p. 281

Hauser M. G., Dwek E., 2001, ARA&A, 39, 249

Hayden M. R., et al., 2014, AJ, 147, 116

Hayden M. R., et al., 2015, ApJ, 808, 132

Haywood M., Di Matteo P., Lehnert M. D., Katz D., Gómez A., 2013, A&A, 560, A109

Haywood M., Lehnert M. D., Di Matteo P., Snaith O., Schultheis M., Katz D., Gómez A., 2016, A&A, 589, A66

Haywood M., Di Matteo P., Lehnert M., Snaith O., Fragkoudi F., Khoperskov S., 2018, A&A, 618, A78

Helmi A., 2008, A&A Rev., 15, 145

Helmi A., 2020, ARA&A, 58, 205

Helmi A., Babusiaux C., Koppelman H. H., Massari D., Veljanoski J., Brown A. G. A., 2018, Nature, 563, 85

Henkel C., Mauersberger R., 1993, A&A, 274, 730

Hildebrand R. H., 1983, Quarterly Journal of the Royal Astronomical Society, 24, 267

Hill V., et al., 2011, A&A, 534, A80

Hillebrandt W., Niemeyer J. C., 2000, ARA&A, 38, 191

Hillebrandt W., Kromer M., Röpke F. K., Ruiter A. J., 2013, Frontiers of Physics, 8, 116

Hirashita H., 2000, PASJ, 52, 585

Hirashita H., 2012, MNRAS, 422, 1263

Hirashita H., Kuo T.-M., 2011, MNRAS, 416, 1340

Hirashita H., Hunt L. K., Ferrara A., 2002, MNRAS, 330, L19

Hoeflich P., Khokhlov A., 1996, ApJ, 457, 500

Höfner S., Olofsson H., 2018, A&A Rev., 26, 1

Holland W. S., et al., 1999, MNRAS, 303, 659

Holtzman J. A., et al., 2015, AJ, 150, 148

Hopkins P. F., 2013, MNRAS, 433, 170

Hoyle F., 1946, MNRAS, 106, 343

Hoyle F., 1954, ApJS, 1, 121

Hoyle F., Wickramasinghe N. C., 1962, MNRAS, 124, 417

Hoyle F., Wickramasinghe N. C., 1970, Nature, 226, 62

Hubble E. P., 1926, ApJ, 64, 321

Iben I. J., Tutukov A. V., 1984, ApJS, 54, 335

Iben Icko J., Tutukov A. V., 1987, ApJ, 313, 727

Iben Icko J., Tutukov A. V., 1991, ApJ, 370, 615

Indebetouw R., et al., 2014, ApJ, 782, L2

Israelian G., Ecuvillon A., Rebolo R., García-López R., Bonifacio P., Molaro P., 2004, A&A, 421, 649

Iwamoto K., Brachwitz F., Nomoto K., Kishimoto N., Umeda H., Hix W. R., Thielemann F.-K., 1999, ApJS, 125, 439

James B. L., Koposov S., Stark D. P., Belokurov V., Pettini M., Olszewski E. W., 2015, MNRAS, 448, 2687

Jenkins E. B., 2009, ApJ, 700, 1299

Jenkins E. B., Wallerstein G., 2017, ApJ, 838, 85

Jeřábková T., Hasani Zonoozi A., Kroupa P., Beccari G., Yan Z., Vazdekis A., Zhang Z. Y., 2018, A&A, 620, A39

Jofré P., et al., 2015, A&A, 582, A81

Jofré P., et al., 2016, A&A, 595, A60

Jones A., 2014, arXiv e-prints, p. arXiv:1411.6666

Jones A. P., Tielens A. G. G. M., Hollenbach D. J., McKee C. F., 1994, ApJ, 433, 797

Jones A. P., Köhler M., Ysard N., Bocchio M., Verstraete L., 2017, A&A, 602, A46

Jönsson H., et al., 2020, AJ, 160, 120

Kaiser N., 1986, MNRAS, 222, 323

Kapteyn J. C., 1909, ApJ, 29, 46

Karakas A. I., 2010, MNRAS, 403, 1413

Kawabata K. S., et al., 2014, ApJ, 795, L4

Kellogg E., Gursky H., Tananbaum H., Giacconi R., Pounds K., 1972, ApJ, 174, L65

Kemper F., Vriend W. J., Tielens A. G. G. M., 2004, ApJ, 609, 826

Kennicutt Robert C. J., 1989, ApJ, 344, 685

Kennicutt Robert C. J., 1998, ApJ, 498, 541

Kennicutt R. C., et al., 2011, PASP, 123, 1347

Kessler M. F., et al., 1996, A&A, 500, 493

Kewley L. J., Ellison S. L., 2008, ApJ, 681, 1183

Khokhlov A. M., 1991, A&A, 245, 114

Khoperskov S., Haywood M., Di Matteo P., Lehnert M. D., Combes F., 2018, A&A, 609, A60

Kirby E. N., et al., 2019, ApJ, 881, 45

Kitayama T., et al., 2009, ApJ, 695, 1191

Knapp G. R., 1985, ApJ, 293, 273

Knudsen K. K., Watson D., Frayer D., Christensen L., Gallazzi A., Michałowski M. J., Richard J., Zavala J., 2017, MNRAS, 466, 138

Kobayashi C., Nakasato N., 2011, ApJ, 729, 16

Kobayashi C., Umeda H., Nomoto K., Tominaga N., Ohkubo T., 2006, ApJ, 653, 1145

Kobayashi C., Karakas A. I., Umeda H., 2011, MNRAS, 414, 3231

Kobayashi C., Nomoto K., Hachisu I., 2015, ApJ, 804, L24

Kobayashi C., Leung S.-C., Nomoto K., 2020a, ApJ, 895, 138

Kobayashi C., Karakas A. I., Lugaro M., 2020b, ApJ, 900, 179

Kodama T., 1997, PhD thesis, Institute of Astronomy, Univ.ersity of Tokyo

Koppelman H., Helmi A., Veljanoski J., 2018, ApJ, 860, L11

Koppelman H. H., Helmi A., Massari D., Price-Whelan A. M., Starkenburg T. K., 2019, A&A, 631, L9

Kromer M., et al., 2015, MNRAS, 450, 3045

Kroupa P., 2001, MNRAS, 322, 231

Kroupa P., 2002, Science, 295, 82

Kroupa P., Weidner C., 2003, ApJ, 598, 1076

Kroupa P., Tout C. A., Gilmore G., 1993, MNRAS, 262, 545

Kroupa P., Weidner C., Pflamm-Altenburg J., Thies I., Dabringhausen J., Marks M., Maschberger T., 2013, The Stellar and Sub-Stellar Initial Mass Function of Simple and Composite Populations. p. 115, doi:10.1007/978-94-007-5612-0_4

Krumholz M. R., Klein R. I., McKee C. F., 2011, ApJ, 740, 74

Kubryk M., Prantzos N., Athanassoula E., 2015, A&A, 580, A126

La Barbera F., Ferreras I., Vazdekis A., de la Rosa I. G., de Carvalho R. R., Trevisan M., Falcón-Barroso J., Ricciardelli E., 2013, MNRAS, 433, 3017

Lacchin E., Matteucci F., Vincenzo F., Palla M., 2020, MNRAS, 495, 3276

Lacey C. G., Fall S. M., 1985, ApJ, 290, 154

Lada C. J., Lada E. A., 2003, ARA&A, 41, 57

Lai D. K., Bolte M., Johnson J. A., Lucatello S., Heger A., Woosley S. E., 2008, ApJ, 681, 1524

Landgraf M., Müller M., Grün E., 1999, Planet. Space Sci., 47, 1029

Lanfranchi G. A., Matteucci F., 2003, MNRAS, 345, 71

Laporte N., et al., 2017, ApJ, 837, L21

Larson R. B., 1976, MNRAS, 176, 31

Larson R. B., 1998, MNRAS, 301, 569

Larson R. B., 2005, MNRAS, 359, 211

Leroy A., Bolatto A., Stanimirovic S., Mizuno N., Israel F., Bot C., 2007, ApJ, 658, 1027

Leśniewska A., Michałowski M. J., 2019, A&A, 624, L13

Leung H. W., Bovy J., 2019, MNRAS, 489, 2079

Leung S.-C., Nomoto K., 2018, ApJ, 861, 143

Leung S.-C., Nomoto K., 2020a, ApJ, 888, 80

Leung S.-C., Nomoto K., 2020b, ApJ, 900, 54

Li Y., Bryan G. L., Quataert E., 2019, ApJ, 887, 41

Licquia T. C., Newman J. A., 2015, ApJ, 806, 96

Limongi M., Chieffi A., 2003, ApJ, 592, 404

Limongi M., Chieffi A., 2018, ApJS, 237, 13

Lodders K., 2003, ApJ, 591, 1220

Lorimer D. R., et al., 2006, MNRAS, 372, 777

Luck R. E., Lambert D. L., 2011, AJ, 142, 136

Lynden-Bell D., 1975, Vistas in Astronomy, 19, 299

Mac Low M.-M., Ferrara A., 1999, ApJ, 513, 142

Mackereth J. T., Bovy J., 2020, MNRAS, 492, 3631

Madden S. C., et al., 2013, PASP, 125, 600

Magrini L., et al., 2017, A&A, 603, A2

Maiolino R., et al., 2015, MNRAS, 452, 54

Majewski S. R., et al., 2017, AJ, 154, 94

Mamon G. A., Cava A., Biviano A., Moretti A., Poggianti B., Bettoni D., 2019, A&A, 631, A131

Mancini M., Schneider R., Graziani L., Valiante R., Dayal P., Maio U., Ciardi B., Hunt L. K., 2015, MNRAS, 451, L70

Mannucci F., Della Valle M., Panagia N., 2006, MNRAS, 370, 773

Maoz D., Graur O., 2017, ApJ, 848, 25

Maoz D., Mannucci F., Nelemans G., 2014, ARA&A, 52, 107

Marassi S., Schneider R., Limongi M., Chieffi A., Graziani L., Bianchi S., 2019, MNRAS, 484, 2587

Marcon-Uchida M. M., Matteucci F., Costa R. D. D., 2010, A&A, 520, A35

Marconi G., Matteucci F., Tosi M., 1994, MNRAS, 270, 35

Marrone D. P., et al., 2018, Nature, 553, 51

Martig M., et al., 2015, MNRAS, 451, 2230

Martin C., 2004, in CfA Colloquium Lecture Series Talk. p. 26

Martin C. L., Shapley A. E., Coil A. L., Kornei K. A., Bundy K., Weiner B. J., Noeske K. G., Schiminovich D., 2012, ApJ, 760, 127

Martin N. F., et al., 2022, Nature, 601, 45

Massey P., Hunter D. A., 1998, ApJ, 493, 180

Mathis J. S., Rumpl W., Nordsieck K. H., 1977, ApJ, 217, 425

Matsuda T., Satō H., Takeda H., 1969, Progress of Theoretical Physics, 42, 219

Matsuura M., et al., 2009, MNRAS, 396, 918

Matsuura M., et al., 2011, Science, 333, 1258

Matteucci F., 1986, MNRAS, 221, 911

Matteucci F., 1992, ApJ, 397, 32

Matteucci F., 1994, A&A, 288, 57

Matteucci F., 2001, The chemical evolution of the Galaxy. Vol. 253, Kluwer Academic Publishers, Dordrecht, doi:10.1007/978-94-010-0967-6

Matteucci F., 2012, Chemical Evolution of Galaxies. Springer-Verlag, Berlin Heidelberg, doi:10.1007/978-3-642-22491-1

Matteucci F., Brocato E., 1990, ApJ, 365, 539

Matteucci F., Francois P., 1989, MNRAS, 239, 885

Matteucci F., Greggio L., 1986, A&A, 154, 279

Matteucci F., Pipino A., 2002, ApJ, 569, L69

Matteucci F., Recchi S., 2001, ApJ, 558, 351

Matteucci F., Tornambe A., 1985, A&A, 142, 13

Matteucci F., Tornambe A., 1987, A&A, 185, 51

Matteucci F., Vettolani G., 1988, A&A, 202, 21

Matteucci F., Spitoni E., Recchi S., Valiante R., 2009, A&A, 501, 531

Matteucci F., Romano D., Arcones A., Korobkin O., Rosswog S., 2014, MNRAS, 438, 2177

Matteucci F., Grisoni V., Spitoni E., Zulianello A., Rojas-Arriagada A., Schultheis M., Ryde N., 2019, MNRAS, 487, 5363

Matteucci F., Vasini A., Grisoni V., Schultheis M., 2020, MNRAS, 494, 5534

Mattsson L., 2011, MNRAS, 414, 781

Mattsson L., 2015, arXiv e-prints, p. arXiv:1505.04758

McGee S. L., Balogh M. L., 2010, MNRAS, 405, 2069

McKee C., 1989, in Allamandola L. J., Tielens A. G. G. M., eds, Vol. 135, Interstellar Dust. p. 431

McKinnon R., Torrey P., Vogelsberger M., Hayward C. C., Marinacci F., 2017, MNRAS, 468, 1505

McKinnon R., Vogelsberger M., Torrey P., Marinacci F., Kannan R., 2018, MNRAS, 478, 2851

Megeath S. T., et al., 2016, AJ, 151, 5

Melin J. B., Bartlett J. G., Cai Z. Y., De Zotti G., Delabrouille J., Roman M., Bonaldi A., 2018, A&A, 617, A75

Melioli C., Brighenti F., D'Ercole A., de Gouveia Dal Pino E. M., 2009, MNRAS, 399, 1089

Mendeleev D. I., 1869, Zeitschrift für Chemie, 12, 405

Meneghetti M., et al., 2017, MNRAS, 472, 3177

Merrill P. W., 1952, ApJ, 116, 21

Meurer G. R., et al., 2009, ApJ, 695, 765

Meynet G., Maeder A., 2002, A&A, 390, 561

Micali A., Matteucci F., Romano D., 2013, MNRAS, 436, 1648

Michałowski M. J., Murphy E. J., Hjorth J., Watson D., Gall C., Dunlop J. S., 2010, A&A, 522, A15

Miglio A., et al., 2021, A&A, 645, A85

Mikolaitis Š., de Laverny P., Recio-Blanco A., Hill V., Worley C. C., de Pascale M., 2017, A&A, 600, A22

Millán-Irigoyen I., Mollá M., Ascasibar Y., 2020, MNRAS, 494, 146

Miller G. E., Scalo J. M., 1979, ApJS, 41, 513

Minchev I., et al., 2018, MNRAS, 481, 1645

Miville-Deschênes M.-A., Lagache G., 2005, ApJS, 157, 302

Mollá M., Cavichia O., Gavilán M., Gibson B. K., 2015, MNRAS, 451, 3693

Montier L. A., Giard M., 2004, A&A, 417, 401

Mor R., Robin A. C., Figueras F., Roca-Fàbrega S., Luri X., 2019, A&A, 624, L1

Moretti A., et al., 2015, A&A, 581, A11

Morgan W. W., 1956, PASP, 68, 509

Moseley H. G. J., 1913, Proceedings of the Royal Society of London Series A, 88, 471

Mott A., Spitoni E., Matteucci F., 2013, MNRAS, 435, 2918

Muller S., Wu S. Y., Hsieh B. C., González R. A., Loinard L., Yee H. K. C., Gladders M. D., 2008, ApJ, 680, 975

Murakami H., et al., 2007, PASJ, 59, S369

Myeong G. C., Vasiliev E., Iorio G., Evans N. W., Belokurov V., 2019, MNRAS, 488, 1235

Nakanishi H., Sofue Y., 2003, PASJ, 55, 191

Nakanishi H., Sofue Y., 2006, PASJ, 58, 847

Nanni A., Bressan A., Marigo P., Girardi L., 2013, MNRAS, 434, 2390

Nanni A., Cristallo S., van Loon J. T., Groenewegen M. A. T., 2021, Universe, 7, 233

Navarro J. F., Frenk C. S., White S. D. M., 1996, ApJ, 462, 563

Neugebauer G., et al., 1984, ApJ, 278, L1

Newlands J. A. R., 1865, Chemical News, 12, 83

Nidever D. L., et al., 2014, ApJ, 796, 38

Niemeyer J. C., Hillebrandt W., Woosley S. E., 1996, ApJ, 471, 903

Nissen P. E., Chen Y. Q., Schuster W. J., Zhao G., 2000, A&A, 353, 722

Nittler L. R., O'D. Alexander C. M., Liu N., Wang J., 2018, ApJ, 856, L24

Noguchi M., 2018, Nature, 559, 585

Nomoto K., 1982, ApJ, 257, 780

Nomoto K., Thielemann F. K., Yokoi K., 1984, ApJ, 286, 644

Nomoto K., Yamaoka H., Shigeyama T., Kumagai S., Tsujimoto T., 1994, in Bludman S. A., Mochkovitch R., Zinn-Justin J., eds, Supernovae. p. 199

Nomoto K., Kobayashi C., Tominaga N., 2013, ARA&A, 51, 457

Nozawa T., Maeda K., Kozasa T., Tanaka M., Nomoto K., Umeda H., 2011, ApJ, 736, 45

Oort J. H., 1970, A&A, 7, 381

Ostriker J. P., Heisler J., 1984, ApJ, 278, 1

Ota K., et al., 2014, ApJ, 792, 34

Ou X., Roederer I. U., Sneden C., Cowan J. J., Lawler J. E., Shectman S. A., Thompson I. B., 2020, ApJ, 900, 106

Pagel B. E. J., 2009, Nucleosynthesis and Chemical Evolution of Galaxies

Pagel B. E. J., Patchett B. E., 1975, MNRAS, 172, 13

Pakmor R., Kromer M., Taubenberger S., Sim S. A., Röpke F. K., Hillebrandt W., 2012, ApJ, 747, L10

Palla M., 2018, Master's thesis, University of Trieste, Italy

Palla M., 2021, MNRAS, 503, 3216

Palla M., Calura F., Matteucci F., Fan X. L., Vincenzo F., Lacchin E., 2020a, MNRAS, 494, 2355

Palla M., Matteucci F., Spitoni E., Vincenzo F., Grisoni V., 2020b, MNRAS, 498, 1710

Palla M., Matteucci F., Calura F., Longo F., 2020c, ApJ, 889, 4

Papadopoulos P. P., et al., 2014, ApJ, 788, 153

Pappalardo C., Bendo G. J., Boquien M., Baes M., Viaene S., Bianchi S., Fritz J., 2021, arXiv e-prints, p. arXiv:2110.00022

Perlmutter S., et al., 1999, ApJ, 517, 565

Pettini M., Steidel C. C., Adelberger K. L., Dickinson M., Giavalisco M., 2000, ApJ, 528, 96

Pettini M., Shapley A. E., Steidel C. C., Cuby J.-G., Dickinson M., Moorwood A. F. M., Adelberger K. L., Giavalisco M., 2001, ApJ, 554, 981

Pettini M., Ellison S. L., Bergeron J., Petitjean P., 2002, A&A, 391, 21

Pettini M., Zych B. J., Steidel C. C., Chaffee F. H., 2008, MNRAS, 385, 2011

Pezzulli G., Fraternali F., 2016, MNRAS, 455, 2308

Pflamm-Altenburg J., Weidner C., Kroupa P., 2007, ApJ, 671, 1550

Phillips M. M., 1993, ApJ, 413, L105

Pilbratt G. L., et al., 2010, A&A, 518, L1

Pilkington K., et al., 2012, A&A, 540, A56

Pinsonneault M. H., et al., 2014, ApJS, 215, 19

Pinsonneault M. H., et al., 2018, ApJS, 239, 32

Piovan L., Chiosi C., Merlin E., Grassi T., Tantalo R., Buonomo U., Cassarà L. P., 2011, preprint, (arXiv:1107.4541)

Pipino A., Matteucci F., 2004, MNRAS, 347, 968

Pipino A., Matteucci F., Borgani S., Biviano A., 2002, New A, 7, 227

Pipino A., Fan X. L., Matteucci F., Calura F., Silva L., Granato G., Maiolino R., 2011, A&A, 525, A61

Pitrou C., Coc A., Uzan J.-P., Vangioni E., 2018, Phys. Rep., 754, 1

Planck Collaboration (XLIII) et al., 2016, A&A, 596, A104

Polikarpova O. L., Shchekinov Y. A., 2017, Astronomy Reports, 61, 89

Pollack J. B., Hubickyj O., Bodenheimer P., Lissauer J. J., Podolak M., Greenzweig Y., 1996, Icarus, 124, 62

Popescu C. C., Tuffs R. J., Fischera J., Völk H., 2000, A&A, 354, 480

Popesso P., Biviano A., Böhringer H., Romaniello M., 2006, A&A, 445, 29

Popesso P., Biviano A., Böhringer H., Romaniello M., 2007, A&A, 464, 451

Popping G., Somerville R. S., Galametz M., 2017, MNRAS, 471, 3152

Portinari L., Chiosi C., 2000, A&A, 355, 929

Portinari L., Sommer-Larsen J., Tantalo R., 2004, MNRAS, 347, 691

Pouliasis E., Di Matteo P., Haywood M., 2017, A&A, 598, A66

Pozzi F., Calura F., Zamorani G., Delvecchio I., Gruppioni C., Santini P., 2020, MNRAS, 491, 5073

Prantzos N., Abia C., Limongi M., Chieffi A., Cristallo S., 2018, MNRAS, 476, 3432

Prgomet M., Rey M. P., Andersson E. P., Segovia Otero A., Agertz O., Renaud F., Pontzen A., Read J. I., 2021, arXiv e-prints, p. arXiv:2107.00663

Priestley F. D., De Looze I., Barlow M. J., 2022, MNRAS, 509, L6

Prochaska J. X., Naumov S. O., Carney B. W., McWilliam A., Wolfe A. M., 2000, AJ, 120, 2513

Queiroz A. B. A., et al., 2018, MNRAS, 476, 2556

Queiroz A. B. A., et al., 2020, A&A, 638, A76

Quider A. M., Pettini M., Shapley A. E., Steidel C. C., 2009, MNRAS, 398, 1263

Rana N. C., 1991, ARA&A, 29, 129

Read J. I., 2014, Journal of Physics G Nuclear Physics, 41, 063101

Recchi S., Matteucci F., D'Ercole A., 2001, MNRAS, 322, 800

Recchi S., Calura F., Kroupa P., 2009, A&A, 499, 711

Recio-Blanco A., et al., 2014, A&A, 567, A5

Rémy-Ruyer A., et al., 2014, A&A, 563, A31

Rémy-Ruyer A., et al., 2015, A&A, 582, A121

Renzini A., et al., 2018, ApJ, 863, 16

Riess A. G., et al., 1998, AJ, 116, 1009

Rigby J. R., Wuyts E., Gladders M. D., Sharon K., Becker G. D., 2011, ApJ, 732, 59

Rodrigues C. V., Magalhães A. M., Coyne G. V., Piirola S. J. V., 1997, ApJ, 485, 618

Rojas-Arriagada A., et al., 2017, A&A, 601, A140

Romano D., Matteucci F., Salucci P., Chiappini C., 2000, ApJ, 539, 235

Romano D., Chiappini C., Matteucci F., Tosi M., 2005, A&A, 430, 491

Romano D., Tosi M., Chiappini C., Matteucci F., 2006, MNRAS, 369, 295

Romano D., Karakas A. I., Tosi M., Matteucci F., 2010, A&A, 522, A32

Romano D., Bellazzini M., Starkenburg E., Leaman R., 2015, MNRAS, 446, 4220

Romano D., Matteucci F., Zhang Z. Y., Papadopoulos P. P., Ivison R. J., 2017, MNRAS, 470, 401

Romano D., Matteucci F., Zhang Z.-Y., Ivison R. J., Ventura P., 2019, MNRAS, 490, 2838

Romano D., et al., 2021, A&A, 653, A72

Roncarelli M., Pointecouteau E., Giard M., Montier L., Pello R., 2010, A&A, 512, A20

Röpke F. K., Hillebrandt W., Schmidt W., Niemeyer J. C., Blinnikov S. I., Mazzali P. A., 2007, ApJ, 668, 1132

Rosswog S., Liebendörfer M., Thielemann F. K., Davies M. B., Benz W., Piran T., 1999, A&A, 341, 499

Rowlands K., Gomez H. L., Dunne L., Aragón-Salamanca A., Dye S., Maddox S., da Cunha E., van der Werf P., 2014, MNRAS, 441, 1040

Rubele S., et al., 2015, MNRAS, 449, 639

Rudolph A. L., Fich M., Bell G. R., Norsen T., Simpson J. P., Haas M. R., Erickson E. F., 2006, ApJS, 162, 346

Ruiter A. J., 2020, arXiv e-prints, p. arXiv:2001.02947

Safronov V. S., Zvjagina E. V., 1969, Icarus, 10, 109

Saglia R. P., Maraston C., Thomas D., Bender R., Colless M., 2002, ApJ, 579, L13

Saintonge A., et al., 2018, MNRAS, 481, 3497

Salaris M., Chieffi A., Straniero O., 1993, ApJ, 414, 580

Salpeter E. E., 1955, ApJ, 121, 161

Salvador-Rusiñol N., Vazdekis A., La Barbera F., Beasley M. A., Ferreras I., Negri A., Dalla Vecchia C., 2019, Nature Astronomy, p. 1

Sánchez S. F., et al., 2012, A&A, 538, A8

Sandford S. A., 1987, Fund. Cosmic Phys., 12, 1

Santos-Peral P., Recio-Blanco A., de Laverny P., Fernández-Alvar E., Ordenovic C., 2020, A&A, 639, A140

Sarazin C. L., 1988, S&T, 76, 639

Savage B. D., Sembach K. R., 1996, ARA&A, 34, 279

Scalo J. M., 1986, Fund. Cosmic Phys., 11, 1

Schaller G., Schaerer D., Meynet G., Maeder A., 1992, A&AS, 96, 269

Schechter P., 1976, ApJ, 203, 297

Schmidt M., 1963, ApJ, 137, 758

Schneider R., Valiante R., Ventura P., dell'Agli F., Di Criscienzo M., Hirashita H., Kemper F., 2014, MNRAS, 442, 1440

Schneider R., Valiante R., Ventura P., dell'Agli F., di Criscienzo M., 2015, in Kerschbaum F., Wing R. F., Hron J., eds, Astronomical Society of the Pacific Conference Series Vol. 497, Why Galaxies Care about AGB Stars III: A Closer Look in Space and Time. p. 369

Schneider F. R. N., et al., 2018, A&A, 618, A73

Schoenberg E., Jung B., 1934, Astronomische Nachrichten, 253, 261

Schönrich R., Binney J., 2009, MNRAS, 396, 203

Schönrich R., McMillan P. J., 2017, MNRAS, 467, 1154

Scott P., Asplund M., Grevesse N., Bergemann M., Sauval A. J., 2015, A&A, 573, A26

Seitenzahl I. R., Townsley D. M., 2017, Nucleosynthesis in Thermonuclear Supernovae. p. 1955, doi:10.1007/978-3-319-21846-5_87

Seitenzahl I. R., et al., 2013a, MNRAS, 429, 1156

Seitenzahl I. R., Cescutti G., Röpke F. K., Ruiter A. J., Pakmor R., 2013b, A&A, 559, L5

Seitz S., Saglia R. P., Bender R., Hopp U., Belloni P., Ziegler B., 1998, MNRAS, 298, 945

Sembach K. R., Howk J. C., Savage B. D., Shull J. M., Oegerle W. R., 2001, ApJ, 561, 573

Shapley A. E., Steidel C. C., Pettini M., Adelberger K. L., 2003, ApJ, 588, 65

Sharma S., Hayden M. R., Bland-Hawthorn J., 2021, MNRAS, 507, 5882

Shen K. J., Bildsten L., 2014, ApJ, 785, 61

Shen J., Rich R. M., Kormendy J., Howard C. D., De Propris R., Kunder A., 2010, ApJ, 720, L72

Shen K. J., Kasen D., Miles B. J., Townsley D. M., 2018, ApJ, 854, 52

Siana B., Teplitz H. I., Chary R.-R., Colbert J., Frayer D. T., 2008, ApJ, 689, 59

Silk J., 1995, ApJ, 438, L41

Silva Aguirre V., et al., 2018, MNRAS, 475, 5487

Silva L., Granato G. L., Bressan A., Danese L., 1998, ApJ, 509, 103

Snaith O., Haywood M., Di Matteo P., Lehnert M. D., Combes F., Katz D., Gómez A., 2015, A&A, 578, A87

Sneden C., McWilliam A., Preston G. W., Cowan J. J., Burris D. L., Armosky B. J., 1996, ApJ, 467, 819

Sollima A., 2019, MNRAS, 489, 2377

Spiniello C., Trager S. C., Koopmans L. V. E., Chen Y. P., 2012, ApJ, 753, L32

Spiniello C., Trager S., Koopmans L. V. E., Conroy C., 2014, MNRAS, 438, 1483

Spite M., et al., 2005, A&A, 430, 655

Spitoni E., 2015, MNRAS, 451, 1090

Spitoni E., Matteucci F., 2011, A&A, 531, A72

Spitoni E., Matteucci F., Recchi S., Cescutti G., Pipino A., 2009, A&A, 504, 87

Spitoni E., Vincenzo F., Matteucci F., Romano D., 2016a, MNRAS, 458, 2541

Spitoni E., Vincenzo F., Matteucci F., Romano D., 2016b, MNRAS, 458, 2541

Spitoni E., Gioannini L., Matteucci F., 2017, A&A, 605, A38

Spitoni E., Silva Aguirre V., Matteucci F., Calura F., Grisoni V., 2019, A&A, 623, A60

Spitoni E., Verma K., Silva Aguirre V., Calura F., 2020, A&A, 635, A58

Spitoni E., et al., 2021, A&A, 647, A73

Spolaor M., Kobayashi C., Forbes D. A., Couch W. J., Hau G. K. T., 2010, MNRAS, 408, 272

Stahler S. W., Palla F., 2005, The Formation of Stars

Stanghellini L., Haywood M., 2018, ApJ, 862, 45

Steidel C. C., et al., 2014, ApJ, 795, 165

Steidel C. C., Strom A. L., Pettini M., Rudie G. C., Reddy N. A., Trainor R. F., 2016, ApJ, 826, 159

Steigman G., Romano D., Tosi M., 2007, MNRAS, 378, 576

Steinmetz M., et al., 2020, AJ, 160, 82

Stickel M., Lemke D., Mattila K., Haikala L. K., Haas M., 1998, A&A, 329, 55

Stickel M., Klaas U., Lemke D., Mattila K., 2002, A&A, 383, 367

Struve F. G. W., 1847, Etudes d'Astronomie Stellaire: Sur la voie lactee et sur la distance des etoiles fixes

Taam R. E., 1980, ApJ, 242, 749

Talbot Raymond J. J., Arnett W. D., 1971, ApJ, 170, 409

Tamura Y., et al., 2019, ApJ, 874, 27

Temim T., Dwek E., 2013, ApJ, 774, 8

Teplitz H. I., et al., 2000, ApJ, 533, L65

Thielemann F. K., Nomoto K., Yokoi K., 1986, A&A, 158, 17

Thies I., Pflamm-Altenburg J., Kroupa P., Marks M., 2015, ApJ, 800, 72

Thomas D., Maraston C., Schawinski K., Sarzi M., Silk J., 2010, MNRAS, 404, 1775

Tinsley B. M., 1979, ApJ, 229, 1046

Tinsley B. M., 1980, Fund. Cosmic Phys., 5, 287

Tosi M., Greggio L., Marconi G., Focardi P., 1991, AJ, 102, 951

Totani T., Morokuma T., Oda T., Doi M., Yasuda N., 2008, PASJ, 60, 1327

Trimble V., 1996, in Holt S. S., Sonneborn G., eds, Astronomical Society of the Pacific Conference Series Vol. 99, Cosmic Abundances. p. 3

Trumpler R. J., 1930, PASP, 42, 214

Tsai J. C., Mathews W. G., 1995, ApJ, 448, 84

Tutukov A., Yungelson L., 1996, MNRAS, 280, 1035

Urquhart J. S., Figura C. C., Moore T. J. T., Hoare M. G., Lumsden S. L., Mottram J. C., Thompson M. A., Oudmaijer R. D., 2014, MNRAS, 437, 1791

Vaduvescu O., McCall M. L., Richer M. G., 2007, AJ, 134, 604

Valenti E., Zoccali M., Renzini A., Brown T. M., Gonzalez O. A., Minniti D., Debattista V. P., Mayer L., 2013, A&A, 559, A98

Valiante R., Schneider R., Salvadori S., Bianchi S., 2011, MNRAS, 416, 1916

Valiante R., Schneider R., Salvadori S., Gallerani S., 2014, MNRAS, 444, 2442

Vanzella E., et al., 2017, MNRAS, 467, 4304

Veilleux S., Cecil G., Bland-Hawthorn J., 2005, ARA&A, 43, 769

Ventura P., et al., 2012, MNRAS, 424, 2345

Ventura P., Dell'Agli F., Lugaro M., Romano D., Tailo M., Yagüe A., 2020, A&A, 641, A103

Ventura P., et al., 2021, A&A, 655, A6

Vernon H. M., 1890, Chemical News, 61, 51

Vincenzo F., Kobayashi C., 2020, MNRAS, 496, 80

Vincenzo F., Matteucci F., Vattakunnel S., Lanfranchi G. A., 2014, MNRAS, 441, 2815

Vincenzo F., Matteucci F., Recchi S., Calura F., McWilliam A., Lanfranchi G. A., 2015, MNRAS, 449, 1327

Vincenzo F., Belfiore F., Maiolino R., Matteucci F., Ventura P., 2016, MNRAS, 458, 3466

Vincenzo F., Spitoni E., Calura F., Matteucci F., Silva Aguirre V., Miglio A., Cescutti G., 2019, MNRAS, 487, L47

Vincoletto L., Matteucci F., Calura F., Silva L., Granato G., 2012, MNRAS, 421, 3116

Vladilo G., 2004, A&A, 421, 479

Vladilo G., Gioannini L., Matteucci F., Palla M., 2018, ApJ, 868, 127

Vogelsberger M., McKinnon R., O'Neil S., Marinacci F., Torrey P., Kannan R., 2019, MNRAS, 487, 4870

Voshchinnikov N. V., Henning T., 2010, A&A, 517, A45

Wakker B. P., van Woerden H., 1997, ARA&A, 35, 217

Watson D., Christensen L., Knudsen K. K., Richard J., Gallazzi A., Michałowski M. J., 2015, Nature, 519, 327

Watts A. B., Meurer G. R., Lagos C. D. P., Bruzzese S. M., Kroupa P., Jerabkova T., 2018, MNRAS, 477, 5554

Weidner C., Kroupa P., 2004, MNRAS, 348, 187

Weidner C., Kroupa P., 2005, ApJ, 625, 754

Weidner C., Kroupa P., Larsen S. S., 2004, MNRAS, 350, 1503

Weidner C., Kroupa P., Pflamm-Altenburg J., 2011, MNRAS, 412, 979

Weingartner J. C., Draine B. T., 2001, ApJ, 548, 296

Werner M. W., et al., 2004, ApJS, 154, 1

Werner N., Durret F., Ohashi T., Schindler S., Wiersma R. P. C., 2008, Space Sci. Rev., 134, 337

Whelan J., Iben Icko J., 1973, ApJ, 186, 1007

Wickramasinghe N. C., Wickramasinghe A. N., 1993, Ap&SS, 200, 145

Williams B. J., Borkowski K. J., Reynolds S. P., Ghavamian P., Blair W. P., Long K. S., Sankrit R., 2012, ApJ, 755, 3

Wolfe A. M., Gawiser E., Prochaska J. X., 2005, ARA&A, 43, 861

Wong T., Blitz L., Bosma A., 2004, ApJ, 605, 183

Woosley S. E., Weaver T. A., 1994, ApJ, 423, 371

Woosley S. E., Weaver T. A., 1995, ApJS, 101, 181

Wootten A., Thompson A. R., 2009, IEEE Proceedings, 97, 1463

Wuyts E., et al., 2010, ApJ, 724, 1182

Wylie S. M., Gerhard O. E., Ness M. K., Clarke J. P., Freeman K. C., Bland-Hawthorn J., 2021, A&A, 653, A143

Yan Z., Jerabkova T., Kroupa P., 2017, A&A, 607, A126

Yan Z., Jerabkova T., Kroupa P., Vazdekis A., 2019, A&A, 629, A93

Yan Z., Jerabkova T., Kroupa P., 2020, A&A, 637, A68

Yee H. K. C., Ellingson E., Bechtold J., Carlberg R. G., Cuillandre J. C., 1996, AJ, 111, 1783

Yin J., Matteucci F., Vladilo G., 2011, A&A, 531, A136

Yong D., et al., 2013, ApJ, 762, 26

Zaritsky D., Kennicutt Robert C. J., Huchra J. P., 1994, ApJ, 420, 87

Zavala J. A., et al., 2015, MNRAS, 453, L88

Zavala J. A., et al., 2018, Nature Astronomy, 2, 56

Zhang Z.-Y., Romano D., Ivison R. J., Papadopoulos P. P., Matteucci F., 2018, Nature, 558, 260

Zhang M., et al., 2021, arXiv e-prints, p. arXiv:2109.00746

Zhao G., Zhao Y.-H., Chu Y.-Q., Jing Y.-P., Deng L.-C., 2012, Research in Astronomy and Astrophysics, 12, 723

Zhukovska S., 2014, A&A, 562, A76

Zhukovska S., Gail H. P., Trieloff M., 2008, A&A, 479, 453

Zhukovska S., Dobbs C., Jenkins E. B., Klessen R. S., 2016, ApJ, 831, 147

Zhukovska S., Henning T., Dobbs C., 2018, ApJ, 857, 94

Zinner E., 2014, Presolar Grains. pp 181–213

Zubko V., Dwek E., Arendt R. G., 2004, ApJS, 152, 211

de Jong R. S., et al., 2019, The Messenger, 175, 3

de Laverny P., Recio-Blanco A., Worley C. C., De Pascale M., Hill V., Bijaoui A., 2013, The Messenger, 153, 18

de los Reyes M. A. C., Kirby E. N., Seitenzahl I. R., Shen K. J., 2020, ApJ, 891, 85

van den Hoek L. B., Groenewegen M. A. T., 1997, A&AS, 123, 305